UNIVERSIDADE TÉCNICA DE LISBOA
INSTITUTO SUPERIOR TÉCNICO

Characterisation of On-Body Communications

Carla Sofia Carita Castelo Grilo de Oliveira

Supervisor: Doctor Luís Manuel de Jesus Sousa Correia

Thesis approved in public session to obtain the

PhD Degree in Electrical and Computer Engineering

Jury Final Classification: *Pass with Merit*

Jury

Chairperson: Chairman of the IST Scientific Board

Members of the Committee:

Doctor Narcis Cardona

Doctor Carlos António Cardoso Fernandes

Doctor Filipe Duarte dos Santos Cardoso

Doctor Luís Manuel de Jesus Sousa Correia

Doctor Custódio José de Oliveira Peixeiro

2013

UNIVERSIDADE TÉCNICA DE LISBOA
INSTITUTO SUPERIOR TÉCNICO

Characterisation of On-Body Communications

Carla Sofia Carita Castelo Grilo de Oliveira

Supervisor: Doctor Luís Manuel de Jesus Sousa Correia

Thesis approved in public session to obtain the

PhD Degree in Electrical and Computer Engineering

Jury Final Classification: *Pass with Merit*

Jury

Chairperson: Chairman of the IST Scientific Board

Members of the Committee:

Doctor Narcis Cardona, Full Professor, Universitat Politécnica de Valência, Espanha

Doctor Carlos António Cardoso Fernandes, Professor Catedrático do Instituto Superior Técnico, da Universidade Técnica de Lisboa

Doctor Filipe Duarte dos Santos Cardoso, Professor Coordenador da Escola Superior de Tecnologia de Setúbal, do Instituto Politécnico de Setúbal

Doctor Luís Manuel de Jesus Sousa Correia, Professor Associado (com Agregação) do Instituto Superior Técnico, da Universidade Técnica de Lisboa

Doctor Custódio José de Oliveira Peixeiro, Professor Auxiliar do Instituto Superior Técnico, da Universidade Técnica de Lisboa

2013

This work is dedicated to my beloved family

Acknowledgements

This Thesis is the outcome of five demanding years of research, during which different people assisted me. To all of them, I express my gratitude.

My main acknowledgement goes to my supervisor, Prof. Luís M. Correia, who guided me in this challenge with his leadership excellence. Thank you very much for your absolute support, obstinacy, and for the unique opportunity provided. Thank you for your friendship.

I would also like to express my profound gratitude to my colleague, and friend, Michał Maćkowiak, for his unconditional support. Our brainstorming and cooperation were essential for this work.

To Instituto de Telecomunicações, to Instituto Superior Técnico, and to INOV – INESC Inovação, I would like to acknowledge for the exceptional working conditions. I am particularly thankful to the support given by Eduardo Lima, Prof. Custódio Peixeiro, Prof. Jorge Costa, Prof. Carlos Fernandes, Carla Medeiros, António Almeida, Carlos Brito and José Moreira.

I am also grateful for the assistance given by the *CST* support team, namely by Jerome Mollet.

Part of this work was developed within the framework of NEWCOM++, COST 2100 and COST IC1004 European Projects, to whose colleagues I am grateful for the stimulating sharing of knowledge.

I also want to express gratitude to my friends for their continuous encouragement, principally to my dear GROW team: Daniel Sebastião, Mónica Branco, Lúcio Ferreira, Ema Catarré, and Vera Almeida, among others.

To conclude, a special recognition to my beloved family, to whom I dedicate this work. I am particularly thankful to my dear parents, as well as to my husband, for their unconditional daily support.

Abstract

This Thesis characterises the on-body radio channel, developing strategies to enable effective on-body communications using MIMO. The antenna-body interaction is analysed, and the concept of a statistical model for on-body antennas is introduced. Analytical models are firstly used for the general understanding of the behaviour of elementary radiation sources near the user. Full wave simulations with a real patch antenna are performed with *CST Microwave Studio*, being complemented with measurements. Different studies are conducted to characterise the on-body channel, starting with a static user in free space (via simulations and measurements). The complexity of the problem is then increased, and novel models are developed to include the mobility of the user, as well as the operating scattering environment. Based on simulations, values for the channel correlation and power imbalance are estimated, along with the MIMO capacity for selected 2×2 configurations. The best performance is obtained when the sink nodes are on front and back of the body, and the sensors are on the head, with a relative capacity gain to SISO of roughly 2. When the sensors are on the arms, the best sink placements are on the sides of the head, with a relative gain of 1.9.

Keywords

Body Area Networks. Antenna-Body Interaction. Statistical Modelling. On-Body Channel Models. Body Dynamics. Numerical Simulations. Channel Gain. Correlation. Power Imbalance. MIMO Capacity.

Resumo

Nesta Tese caracteriza-se o canal rádio das redes de sensores corporais, desenvolvendo-se estratégias que permitam uma comunicação eficiente entre sensores usando MIMO. Analisa-se a interação entre a antena e o utilizador, obtendo-se um modelo estatístico de uma antena colocada junto ao corpo. A análise preliminar baseia-se em modelos analíticos com fontes de radiação básicas, evoluindo para simulações numéricas com o *CST Microwave Studio* usando uma antena real. A análise é complementada com uma campanha de medidas. Desenvolvem-se vários estudos para observar o canal rádio das redes de sensores corporais, começando com o utilizador estático em espaço livre (através de medidas e simulações). A complexidade é aumentada com a introdução da mobilidade do utilizador, e também do ambiente de propagação. Com base em simulações, estimam-se valores para a correlação e balanço de potência dos vários canais, bem como para a capacidade do sistema MIMO. O melhor desempenho obtido para uma configuração 2×2, contém os sensores colocados na cabeça (frente/trás), e os recetores no tronco (frente/trás), com um ganho de capacidade cerca de 2 vezes superior ao de um sistema SISO. Se os sensores estiverem nos braços, o melhor desempenho é obtido para os recetores na cabeça (esquerda/direita), obtendo-se um ganho relativo de 1.9.

Palavras-Chave

Redes de Sensores Corporais. Interacção Antena/Corpo. Modelação Estatística. Modelação do Canal Rádio. Mobilidade do Utilizador. Simulações Numéricas. Ganho de Canal. Correlação. Balanço de Potência. Capacidade MIMO.

Table of Contents

List of Figures

List of Tables

List of Acronyms

AB_L	Left Side of the Arm's Bottom Part (left wrist)
AB_R	Right Side of the Arm's Bottom Part (right wrist)
ABACK	Arms on back of the body
ABEND	Arms bend
ADOWN	Arms down
AFRONT	Arms on front of the body
APDP	Average Power Delay Profile
AUP	Arms up
BAN	Body Area Network
BER	Bit Error Ratio
CDF	Cumulative Distribution Function
CIR	Channel Impulse Response
COST	Co-Operation in the Field of Scientific and Technical Research
ECG	Electrocardiogram
FDTD	Finite-Difference Time-Domain
FEM	Finite Element Method
FIT	Finite Integration Technique
FP7	7*th* Framework Programme
GBSC	Geometrically Based Statistical Channel
GBSC_B	GBSC model for BANs
HE_B	Back Side of the Head
HE_F	Front Side of the Head
HE_L	Left Side of the Head
HE_R	Right side of the Head
ISM	Industrial, Scientific and Medical

KNEE	Military surveillance posture with flexed knee
LOS	Line-of-Sight
LW	Lines per Wavelength
MAC	Medium Access Control
MGE	Maxwell's Grid Equations
MIL	Military posture
MIMO	Multiple-Input Multiple-Output
MoM	Method of Moments
MPC	Multipath Component
MS-MIMO	Multi-Sensor MIMO
NLOS	Non Line-of-Sight
PAD	Pattern Average Difference
PAN	Personal Area Network
PDF	Probability Density Function
PDP	Power Delay Profile
PWD	Pattern Weighted Difference
QLOS	Quasi Line-Of-Sight
QoS	Quality of Service
RL	Mesh Line Ratio Limit
RMS	Root Mean Square
RT	Ray-Tracing Techniques
RX	Receiver
SAR	Specific Absorption Rate
SISO	Single-Input Single-Output
SIT	Sitting posture
SNR	Signal to Noise Ratio
STD	Standing posture
STEP	Military surveillance posture
SYM	Symmetric
TO_B	Back side of the torso
TO_F	Front side of the torso
TX	Transmitter

UTD	Uniform Theory of Diffraction
UWB	Ultra Wide Band
WA_F	Front side of the Waist
WLAN	Wireless Local Area Network

List of Symbols

α	Path loss exponent
α_B	Shape parameter of the Beta Distribution
α_{3dB}	Half-power beam width
α_m	Dispersion distribution for each dispersion region m
α_K	Shape parameter of the Kumaraswamy Distribution
β_B	Shape parameter of the Beta Distribution
β_K	Shape parameter of the Kumaraswamy Distribution
δ	Pulse
δ_r	Changes of output parameters in meshing assessment
∂A	Closed contour
ΔE	Variation of the E field
$\overline{\Delta E^d}$	Average relative difference between E field patterns taken at different distances
$\overline{\Delta E^d_{max}}$	Maximum average relative difference between E field patterns taken at different distances
Δf_r	Relative changes of f_r
$\overline{\Delta G}$	Radiation pattern average difference
$\overline{\Delta G_w}$	Radiation pattern weighted difference
ΔG^d	Relative difference between patterns taken at different distances
$\Delta G_{n,m}$	Radiation pattern difference at direction (θ_n, φ_m)
ΔH	Variation of the H field
Δ_{L_p}	Signal fluctuation around the mean (fading)

ΔP	Power imbalance
$\overline{\Delta P}$	Mean power imbalance
Δs_{11}	Relative changes of s_{11}
Δs_{12}	Range of s_{12}
Δt	Time step
Δt_n	Range of time frames
$\Delta\eta_{rad}$	Relative changes of η_{rad}
ε	Complex permittivity
ε_∞	Permittivity of a given tissue at THz frequency
ε_0	Free-space permittivity
ε_1	Permittivity inside of the cylinder
ε_r	Relative permittivity
ε_s	Permittivity of a given tissue at low frequencies
η_{rad}	Radiation efficiency
θ	Co-Elevation angle
λ	Wavelength
λ_n	Wavelength inside tissue n
μ	Outside medium permeability
μ_0	Free space permeability
μ_1	Permeability inside of the cylinder
μ_{EE}	Exponential Distribution (inverse) rate parameter
$\mu_{s_{11}}$	Average return loss
$\mu_{s_{12}}$	Average transmission
μ_{TN}	Mean of the Truncated Normal Distribution
ρ	Correlation
$\bar{\rho}$	Mean correlation
ρ_e	Electric charge volume density

ρ_N	SNR at the receiver
$\overline{\rho_N}$	Mean SNR
$\sigma_{95\%}$	Maximum likelihood estimates for standard deviation of a Normal Distribution with 95% confidence
σ	Electric Conductivity
$\sigma_{\Delta P}$	Standard deviation of power imbalance
σ_{ρ}	Standard deviation of correlation
σ_C	Standard deviation of MIMO capacity
$\sigma_{\bar{C}}$	Standard deviation of the average MIMO capacity
$\overline{\sigma_C}$	Average standard deviation of the MIMO capacity
$\sigma_{\overline{h_{GBSC\_B}}}$	Standard deviation of the MPCs channel gain
$\sigma_{\overline{h_T}}$	Standard deviation of the average total channel gain
$\overline{\sigma_{h_T}}$	Average standard deviation of the total channel gain
σ_E	Standard deviation of the radiation pattern (E field)
σ_E^N	Maximum likelihood estimate (95%) for the standard deviation of a Normally distributed E field
σ_G	Standard deviation of the radiation pattern
$\sigma_{\overline{h_{kl}}}$	Standard deviation of the on-body channel gain
σ_i	Ionic conductivity
$\sigma_{s_{11}}$	Standard deviation of return loss
$\sigma_{s_{12}}$	Standard deviation of transmission
σ_{TN}	Variance of the Truncated Normal Distribution
τ_m	Relaxation time of each dispersion region m
τ_n	Delay of the nth MPC
Φ	PDF of the Normal Distribution
Φ_N	CDF of the Normal Distribution
φ	Azimuth angle
$\chi^2_{th95\%}$	χ^2 test threshold for a 95% confidence interval

χ^2	Result from χ^2 test
ω	Angular frequency
a	Radius of cylinder
A	Amplitude of signal
$\mathbf{A}$	Surface vector
$\mathbf{b}$	Magnetic facet fluxes matrix
$\mathbf{B}$	Magnetic induction field vector
B_{α_B}	Normalisation constant for the Beta Distribution
B_{β_B}	Normalisation constant for the Beta Distribution
$\mathbf{C}$	Discrete curl operator
$\tilde{\mathbf{C}}$	Dual discrete curl operator
$c_{\{1,2,3\}}$	Linear relation between the $\mathbf{H}$ matrix entries and h_{11}
C	MIMO capacity
$\overline{C(t_n)}$	Average MIMO capacity at each time frame t_n
$\overline{C(\Delta t_n)}$	Average MIMO capacity in a Δt_n time frame range
C_G	Relative MIMO capacity gain
$C_{G_{BAN}}$	BAN MIMO capacity gain
C_{lower}	Lower bound of MIMO capacity
C_{MIMO}	Theoretical capacity of a MIMO radio channel
C_{SISO}	Capacity of a SISO radio channel
C_{upper}	Upper bound of MIMO capacity
d	Distance between the antenna and the body
d_0	Reference distance
d_{max}	*CST* highest distance between mesh lines
d_{min}	*CST* smallest distance between mesh lines
d_n	Distance between mesh lines for tissue n
$\mathbf{d}$	Dielectric facet fluxes matrix

$\mathbf{D}$	Electric displacement field
$\mathbf{e}$	Electric grid voltages matrix
$\mathbf{E}$	Electric field vector
E	Electric field strength
E_{max}	Maximum E field strength
E_{min}	Minimum E field strength
$\mathbf{E^i}$	Incident electric field
$E_n(t)$	Electric field of each n-component wave
$\mathbf{E^s}$	Scattered electric field
$\overline{E^N}$	Maximum likelihood estimate (95%) for the mean of a Normally Distributed E field
$\mathbf{E_t}$	Total electric field
$\mathbf{E}_{\boldsymbol{\phi}}$	Electric field component over $\boldsymbol{\phi}$ plane
f	Frequency
f_r	Resonant frequency
G	Radiation pattern in terms of gain
$\mathbf{G}$	*CST* primary grid
$\widetilde{\mathbf{G}}$	*CST* dual primary grid
G_h	Gain of the horn antenna
G_{min}	Minimum gain of the radiation patterns
G_{max}	Maximum gain of the radiation patterns
$\bar{G}_{max}$	Maximum average value of radiation pattern G
G_r	Gain of the RX antenna
G_{ref}	Reference radiation pattern
G_t	Gain of the TX antenna
G_μ	Average radiation pattern
$\mathbf{H}$	Magnetic field vector

$\mathbf{H_c}$	Channel matrix
H_{max}	Maximum H field strength
H_{min}	Minimum H field strength
$h(t)$	Channel impulse response
$\mathbf{h}$	Magnetic grid voltages matrix
h_{GBSC_B}	Channel impulse response from GBSC_B simulator (MPCs)
$\overline{h_{GBSC\_B}}$	Average MPCs channel gain
h_{kj}	Transfer functions from the j-th transmit antenna to the k-th receive antenna
$\overline{h_{kl}}$	Average on-body channel gain
$H_n^{(2)}()$	n-th order Hankel function of 2nd kind
h_n	Channel impulse response of each n component
h_T	Total channel impulse response obtained from the sum of the on-body component and of the MPCs
$\overline{h_T}$	Average total channel gain
H_t	Total magnetic field
$\mathbf{I}_{N_R}$	$N_R \times N_R$ identity matrix
$\mathbf{I}_{N_T}$	$N_T \times N_T$ identity matrix
j	Imaginary unit
$\mathbf{J}$	Current density vector
$\mathbf{j_c}$	Current density flux matrix
$J_n()$	n-th order Bessel function
$\mathbf{j_s}$	Surface current density flux matrix
$\mathbf{J}_s$	Surface current density
K_{α_K}	Normalisation constant for the Kumaraswamy Distribution
K_{β_K}	Normalisation constant for the Kumaraswamy Distribution
K	Rician distribution factor
l	Distance between transmission and reception antenna

L_p	Path loss
L_{p_0}	Free space path loss
$L_{p_{d_0}}$	Path loss at a reference distance d_0
$\mathbf{M}_{\boldsymbol{\mu}}$	Permeability matrix
m_R	Mode of the Rayleigh Distribution
$\mathbf{M}_{\boldsymbol{\varepsilon}}$	Permittivity matrix
$\mathbf{M}_{\boldsymbol{\sigma_c}}$	Conductivities matrix
$\mathbf{n}$	Noise vector
N_φ	Number of discrete elevation angle samples
N_θ	Number of discrete azimuth angle samples
N_c	Number of mesh cells
$N_{c_{max}}$	Maximum number of mesh cells
N_d	Number of distance samples
N_f	Number of time frames
N_{mc}	Number of multipath components
N_p	Number of antenna placements
N_R	Number of receiving antennas
N_{LW}	Number lines per wavelength
N_{RL}	Mesh line ratio limit
N_s	Number of simulations
N_T	Number of transmitting antennas
p_B	PDF of the Beta Distribution
p_K	PDF of the Kumaraswamy Distribution
p_{TN}	PDF of the Truncated Normal Distribution
P_h	Received power of the horn antenna
P_r	Received power
P_t	Transmitted power

P_{test}	Received power of the test antenna
$\mathbf{q}$	Electric charges matrix
R^2	Result from correlation test
s	RX time signal
$\mathbf{s}$	Infinitesimal vector element
$\mathbf{S}$	Discrete divergence matrix
$\tilde{\mathbf{S}}$	Dual discrete divergence matrix
s_{11}	Input return loss
s_{12}	Transmission
t	Time
t_m	Firs time frame
t_M	Last time frame
t_n	n-th time frame
u_φ	Orientation of elementary source over φ coordinate
u_z	Orientation of elementary source over z coordinate
u_ρ	Orientation of elementary source over ρ coordinate
v	Speed of the user
V	Volume of integration
$\mathbf{x}$	Transmitted signal vector
$\mathbf{y}$	Received signal vector

Chapter 1

Introduction

This chapter gives a general overview of the Thesis. The scope and a brief state of the art are brought up in Section 1.1. Then, the work motivation and main targets are identified in Section 1.2. Section 1.3 highlights the original contributions given by this work. The strategy of investigation is described in Section 1.4, stressing the published work. Section 1.5 concludes the chapter, providing the Thesis structure.

1.1 Scope

Body Area Networks (BANs) are one of the very last advances in "anywhere, anytime" communications, and will play a key role in future mobile communication systems. Their main objective is to connect personalisation and convergence of systems into a single one, through a network of sensors located on the human body, or in its close proximity. Figure 1.1 depicts the concept of body centric communications. BANs arise as an extension of Wireless Local Area Networks (WLANs) to the personal sphere [HaHa06]:

- *Body Area Networks* – Communications ranging from the human body to a distance of around 3 m, incorporating devices worn on, or implanted in, the body.
- *Personal Area Networks* (PANs) – Communications ranging from 3 to 10 m, incorporating all wearable devices.

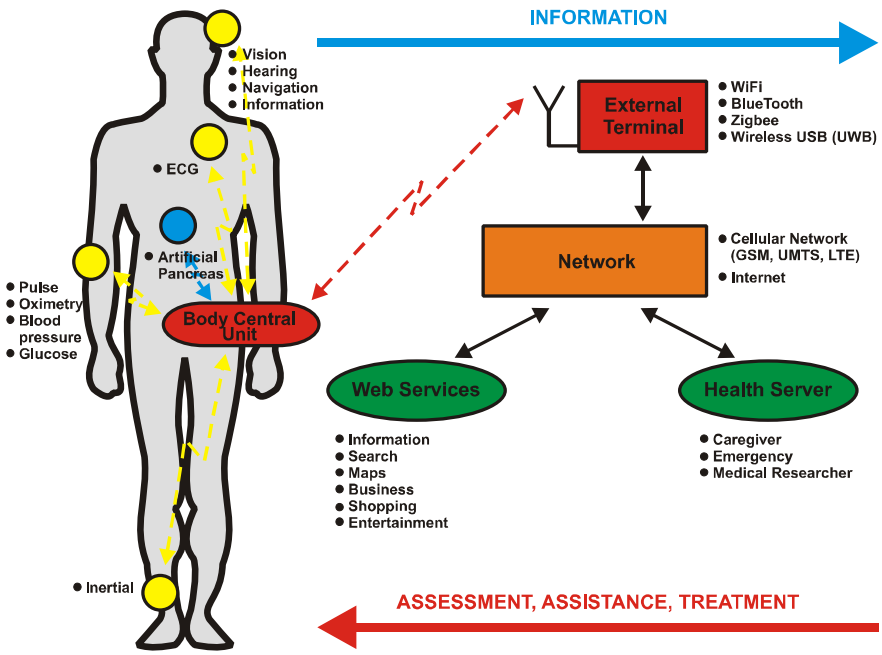

Figure 1.1. Body centric communications.

A practical arrangement often used for characterising communications in BANs [HaHa06], regarding the transmission channel, is:

- *Body-Body:* Communications occur among wearable devices on two independently users. The propagation channel is similar to the off-body one, but, in this case, antennas on both sides of the radio link are influenced by the presence of the user.
- *Off-body:* Communications from off-body to an on-body device or system. Only one antenna of the communication link is on the body, and most of the channel is off the

body and in the surrounding space.

- *On-body:* Communications within on-body networks and wearable systems. Most of the channel will be on the surface of the body, with both transmitter (TX) and receiver (RX) antennas located very near the body.
- *In-body:* Communications to medical implants and sensor networks. A significant part of the channel is inside the body, and implanted sensors are used.

This Thesis deals with the BANs domain and, in particular, with on-body communication systems. In-body communications are not exploited here, as it would involve a profound investigation insight the human body, which is clearly out the scope of this work. Off-body communications are also not covered.

BANs have a plentiful range of potential applications, summarised in Table 1.1. The major interests are health care and patient monitoring, sports monitoring, security/military/space applications, business and multimedia entertainment, among others.

Table 1.1. Summary of potential applications in BANs (adapted from [HaHa06]).

Application	Description
Healthcare	Smart diagnosis, treatment and drug delivery system, patient monitoring, aging care
Business	Wireless transactions, identification of individual peripheral devices
Entertainment	Wireless Digital Video Disc, wearable computing
Military and space	Smart suits, battlefield personnel care and intelligence, astronaut monitoring
Other	Tourism, security, intelligent transportation systems

In *healthcare*, BANs can be applied for typical monitoring of vital parameters purposes, providing real time readings that need to be monitored and analysed (*i.e.*, electrocardiogram (ECG), heart sound, heart rate, electroencephalography, respiratory rate, temperature of body). BANs may allow the detection of the early signs of a disease, and the monitoring of transient or infrequent events. The security, the reliability and schedule of the transmission are of top importance. Patient and elderly people monitoring at home is another attractive area of application, assisting people in maintaining independent mobility and day life activities and preventing injuries. This application demands for low bandwidth networks, reliable links and intolerance to delays.

In *sports*, BANs may be used to monitor fitness-related activities, including several sensors for measuring different physiological parameters, like heart rate, energy consumption, fat percentage (bio-resistance meter), body water content or galvanic skin response. These sensors can measure and display on-time information and/or follow-up reports to a control entity (*e.g.*, professional well-being and caring personnel). Sport applications demand for high capacity

systems to deliver real time information.

Security and military applications comprise smart suits for fire fighters, soldiers and support personnel in battlefields. Smart clothes use special sensors to detect bullet wounds or to monitor the body's vital signals during combat conditions [PaJa03]. For these cases, the communication link ought to be reliable, as vital information is involved. *Space* applications include biosensors for monitoring the physiological parameters of astronauts during space flights (*e.g.*, ECG and temperature biotelemetry, sensor pills), in order to understand the impact of space flight on living systems [Hine96].

In *business*, BAN devices can be used in numerous ways, such as touch-based authentication services using the human body as a transmission channel (*e.g.*, data deliver on handshake). Several applications are possible, like electronic payment service, e-business card service, auto-lock or login systems. User identification/authentication, associated to biometrics, play a key role in here. Business applications have to ensure secure communications, and, in this case, the most important thing is high level security, which eliminates the risk of a third person attack.

In *entertainment*, wireless applications are multimedia oriented, and many times require the high speed transfer of voice, video and data together in real time. But, contrary to applications from the previous groups, these ones tolerate some errors and, what is more important, they do not put high demands on communication security. Personal video is an example application, where the central device is a video camera, which can stream video content and connect to a personal storage device, a playback device with large display, or a home media server. Another example of an entertainment application is wearable audio, where the central device is a headset (stereo audio, microphone), connecting to various devices as a cellular phone, an MP3 player, a CD audio player, or a hands-free car device.

BANs can be classified according to the flow categories depending on the application: streaming, monitoring, authentication, and alarm. In order to provide certain Quality of Service (QoS) requirements for the application, traffic and communication requirements have to be taken into account, like data rate, delay, target Bit Error Ratio (BER), security and class of service. Table 1.2 merges the flow categories for BANs with the QoS requirements [OlMC11].

An increased research on the different layers of BANS has risen recently, as these networks are quite different from traditional wireless ones. Some of their general requirements merged together with protocol design goals are interoperability and reliability (at system and cross-system levels), low complexity and small devices, security and privacy, and energy efficiency.

At the upper layers, compression and aggregation of data ought to be exploited under a power aware strategy, but taking the application into account (*e.g.*, aggregation is not reasonable for

streaming, but it is suitable for monitoring applications). A substantial reduction of energy could be made by intelligent processing at the transmission, compressing the signal or extracting only its significant features, while removing the characteristic artefacts caused by (inevitable) body influence (absorption and antenna displacement). Exploiting temporal and spatial correlation is likewise pertinent, *e.g.*, observed signals might vary only slowly in time, so there is no need to transmit all data at full rate all the time, which is useful for monitoring and alarm applications. Also, signals of neighbouring nodes are often quite similar, thus, only the differences should be transmitted. A careful trade-off between communication and computation is crucial for an optimal node design [Jova05], which should be applied at both sensor and sink (body central unit) nodes.

Table 1.2. Summary of data flow categories for BANs (adapted from [OlMC11]).

	Streaming	**Monitoring**	**Authentication**	**Alarm**
Application	leisure, entertainment, data transfer	monitoring of body parameters for healthcare and sport	business and authentication systems	medicine and battlefields
Data rate	high	low	medium	low
Delay	tolerable	low	tolerable	very low
Target BER	10^{-2}	10^{-6}	10^{-4}	10^{-9}
Security	medium	high	very high	medium
Class of Service	variable bit rate	minimum bit rate	available bit rate	minimum bit rate

Regarding the transport layer, advanced error detection schemes for on- or on-off body communications should account for the highly dynamic changes, not only from the body itself, but also from the neighbouring environment. The work in [DFVH09] observes that it is extremely difficult to reach a security level of 90% without a transmission control protocol. The transport layer is of extreme importance for secure applications.

At the network layer, bottlenecks resulting from sudden increases of the network load ought to be avoided, such as after an emergency event. If the network throughput suffers, there is no guarantee that all the critical information is going through the network. The authors in [DFVH09] suggest that an in-depth analysis of the network outage, throughput, and achievable transmission rate can give insights into the maximum supported reporting rate and the corresponding performance. For centralised network topologies, a maximum achievable transmission rate exists, depending on the amount of deployed nodes; beyond this maximum, interference makes the achievable transmission rate decrease. For mesh topologies, the transmission strategy depends on the traffic profile, *e.g.*, limited activity nodes (long-range transmissions can be used in order to save energy and avoid multiple relays) or high activity

nodes (as performance decreases exponentially with the number of hops, the shortest possible hop strategy should be used, coming at the cost of numerous relaying nodes). The network coordination function has to deal with the burst traffic caused by temporally and spatially unsynchronised sensor nodes, but cannot be loaded due to the low power consumption and computation constrain requirements. As the BAN network is supposed to provide connectivity just for short range distances (on-body, in-body, and short off-body), remote applications (*i.e.*, alarm and monitoring) require integration of the BAN network with other existing mobile networks, like GSM or UMTS. In this case, the network layer should be aware that the overall delay is a common factor for both BAN and external networks, which might be critical for intolerant delay applications. Moreover, the interoperability in very difficult radio environments requires the smart deployment of sensors on the body and the establishment of alternative links. Note that sensor deployment and the number of antennas on the body depend on the application BER requirements (*i.e.*, alternative links can help improving BER).

At the data-link layer, energy can be saved by intelligent and power-aware Medium Access Control (MAC) protocols, which have to be adapted to the different applications requirements [GGSV09]. Several MAC protocols address fixed or variable sleep radio cycles, *i.e.*, maintaining nodes in sleep mode whenever packet transmission or reception is not expected. However, a large latency is a critical problem with this approach. Furthermore, MAC protocols built on the idea of opportune packet transmission are also a possibility for BANs [PrHa11]. Under this approach, optimal signal strength nodes are scheduled to transmit, as the chance of their correct reception is higher, this can be done through the selection of best paths by prediction over movement patterns and current power level of nodes.

A true cross layer protocol design is desired for BANs, achieved by actively exploiting the dependence between the different protocol layers in order to obtain performance gains. Instead of reaching particular optimisations for each layer (treated independently), a holistic solution can be found, thus, optimising interactions between layers. The authors in [CaRR04] and [XDSB09] outline the need for this approach to address known problems of mobility, packet losses and delay, or to optimise power consumption. An example application of the cross layer approach is the CICADA protocol [LBMB07].

The physical layer is of singular interest, since BANs experience challenging propagation characteristics, specifically related with the proximity of the human body. A careful characterisation of the radio wave propagation channel is required, as existing models and common antenna designs do not fit BANs. This work deals with the some of the problems addressed by the radio channel.

BANs can be built using different kinds of existing radio technologies, such as IEEE 802.11

[HDSZ10] or 802.15 families (*e.g.*, Bluetooth [Blue10], Ultra Wide Band (UWB) [KGTP10], Zigbee [Whee07]), each including different modulations, data rates, transmission power or power consumptions. However, the properties of on-body links may lead to spectrum inefficiency when using these systems, mainly because radio energy is directed away from the human body when the antenna is placed close to the skin. The Industrial, Scientific and Medical (ISM) band at 2.4 GHz is conventionally suitable for this application [HaHa06], but, as this band is being used for WLANs, interferences may occur. The frequency might be chosen according to the application, *e.g.*, it is very promising to use millimetre waves for streaming applications, which demand very high data rates. In these cases, the radio link can provide a high bandwidth, under the drawback that millimetre waves are strongly attenuated by obstacles, like human body tissues. In the meantime, a specific standard for BANs was developed, *i.e.*, the IEEE 802.15.6 [IEEE12]. According to it, compliant devices shall support at least one of the following frequency bands: 0.4 GHz, 0.8 GHz, 0.9 GHz, and 2.4 GHz.

1.2 Motivation and Objectives

Most of the open challenges for the design and study of on-body communications regard the propagation channel, and a key challenge is to account for the influence of the user on the radio channel. The peculiar characteristics of BANs demand for explicit solutions to enable the reliability of on-body communications, especially for applications demanding low BERs. The differences to traditional wireless sensor networks are tightly related to the performance of an antenna near body tissues, given an extensive range of conditions: the influence of human tissues, the dynamics of the human body, the short distances of propagation, the link geometry variability, as well as the arbitrary orientation of antennas, among others.

Mobility has also to be accounted for, as some nodes in a BAN might move relative to each other. Because of body movements (even when standing or sitting), a wearable antenna is constantly changing its direction of maximum radiation, which leads to significant changes in radio link performance. Those variations are especially severe when antennas are mounted on the upper limbs (arms and hands), and become extreme while playing sports or similar activities. Likewise, the neighbouring environment can introduce significant variations in the wireless signal, and should be accounted for.

This Thesis is essentially motivated by the challenges above mentioned, and intends to characterise the on-body channels, developing strategies for effective on-body communications using Multiple-Input-Multiple Output (MIMO) systems. Summarising, the general objectives of

the Thesis are:

- To analyse the influence of the body on the system performance;
- To account for the variability of the on-body channel (including mobility);
- To account for the impact of the operation environment;
- To analyse the use of MIMO;
- To develop strategies for optimum antenna selection.

A statistical approach to the problem of antenna-user interaction in BANs has not been considered by former studies. In [Sibi08], the idea of taking into account the effect of antennas in a general radio link in a statistically way is introduced. The authors in [MSRN11] present the statistical properties of the antenna/head interactions, resulting in the extraction of a statistical distribution to represent the impedance matching and the total efficiency of the disturbed antennas. One of the objectives of this Thesis is to extend this concept for the BAN antennas behaviour in the vicinity of the body. Different antenna-body separation distances should be considered, with the purpose of obtaining a statistical model for the on-body antenna. Such analysis is required, as antenna performance depends strongly on the distance, location, and type of body tissues. The presence of the body leads to changes in the antenna radiation pattern, shift of the resonance frequency, changes in input impedance, and also reduction of antenna efficiency.

To achieve this objective the problem began to be investigated with well-known theoretical models, considering simple body shapes (*e.g.*, a circular cylinder). This study addresses the antenna-body interaction via theoretical models, with basic radiation sources, to understand the impact of the body on the fields' distribution. Real antennas were considered, using full wave simulations, and/or, measurements.

Afterwards, several on-body links with different propagation conditions (*e.g.*, Line-Of-Sight (LOS) / Non Line of Sight (NLOS)) were evaluated. The proposed model started with a static user, in a simple free space environment. Later, the evolution to more complex environments was conducted, as well as the inclusion of the users' mobility.

Different radio channel parameters, like the channel gain, or capacity, were analysed. The final purpose was to use appropriate metrics for the selection of the optimum antenna placements in a BAN, when using MIMO.

Figure 1.2 illustrates the workflow of this Thesis, highlighting the main phases and outputs of the work.

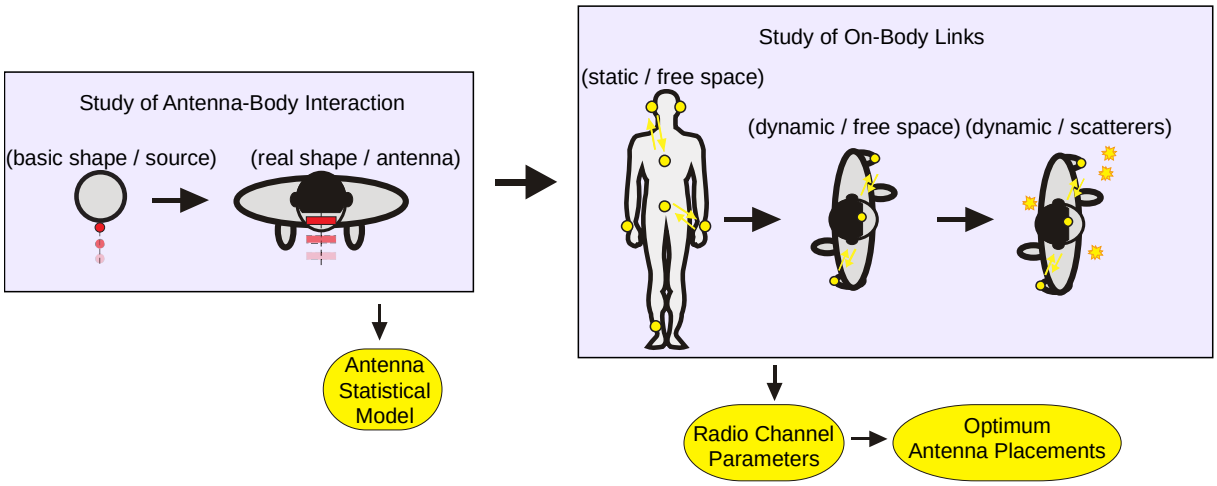

Figure 1.2. Thesis general workflow.

1.3 Novelty

This Thesis is the result of five years of investigation, during which the worldwide research on the area of BANs has experienced major developments. For instance, the IEEE 802.15.6 standard on Wireless Body Area Networks [IEEE12] was published during the final stage of the Thesis. Additionally, recent developments in voxel models made possible the commercialisation of a few posable voxel models, allowing user mobility in full wave simulations [ViFa12].

In spite of these advancements, the Thesis aims at providing a contribution to the evolution on the state of art on channel modelling for BANs, proposing some new methods, or improving existing ones.

Novelty is claimed to the statistical approach to model the interaction between antenna-body in BANs, which was introduced through the development of this work. To the author's knowledge, there are no comparable approaches to this concept for BANs in the literature. The concept of statistical model of antenna can be included in radio channel simulators for BANs. Although the calculated statistical radiation patterns are antenna dependent, the method can be applied for others, and it is generally usable.

The study of body dynamic in BANs via full wave simulations is still in an early stage. The introduction of user's mobility using real motion capture models was previously achieved by [GHBN11] or [AIKT11]. A similar methodology is used in this work for the *CST* simulator, but with improvements to the existing solutions. For instance, a realistic body shape is considered, and an original method to export the antenna placements during the movement is developed. The proposed method can be extended to other full wave simulators, antenna types, or

mobility scenarios. Moreover, the study presented in this Thesis covers other parameters than the usual path loss, like the correlation or the power imbalance between on-body branches. In the last stage of this work, recent research advances allow the use of posable voxel models in the *SEMCAD X* simulation platform ([ViFa12], [SEMC12]). However, such a tool is still not available for *CST*.

To the author's knowledge, the existing studies based on full wave simulations of the dynamic BAN, consider the body in a free space environment. Novelty is claimed to the proposed technique to analyse the body moving in a scattering scenario. The proposed solution combines the results of full wave simulations to generate the on-body component, with results from a geometrically based statistical channel model to generate the multipath components.

As seen before, the reliability of on-body communications is a major requirement for many applications. Accordingly, alternative strategies to the traditional Single-Input-Single-Output (SISO) links are required, making use of different nodes to create a virtual MIMO system. The use of MIMO/cooperative techniques for BANs is still a topic of debate in the literature, to which this Thesis contributes. Strategies for the selection of the best on-body placements based on different metrics, with examples for a 2×2 MIMO system, are given.

1.4 Research Strategy and Impact

The work developed in this Thesis was done within GROW [GROW12], in close collaboration with the colleagues Carlos Lopes and Michał Maćkowiak, who developed M.Sc. and Ph.D. theses, respectively, in complimentary topics on BANs. This straight collaboration resulted in the publication of some joint papers, as detailed below.

Furthermore, this Thesis was conducted within some European research frameworks, such as the 7*th* Framework Programme (FP7) and the Co-Operation in the field of Scientific and Technical research (COST), namely ICT-NEWCOM++ "Network of Excellence in Wireless Communications" [NEWC10], COST 2100 "Pervasive Mobile & Ambient Wireless Communications" [COST10] and COST IC1004 "Cooperative Radio Communications for Green Smart Environments" [COST12]. These projects enabled an international involvement with several researchers from academia and R&D institutes. This experience allowed a stimulating sharing of knowledge, and, most of all, enabled an important overview on what is being done worldwide in the topic of BANs.

Most of the work presented in this Thesis was already disseminated in several papers that were

published or submitted to various conferences, journals or book chapters:

- Book Chapters:

  Oliveira,C., Mackowiak,M. and Correia,L.M., "Statistical Characterisation of Antennas in BANs", in Guillaume de la Roche, Andres Alayon-Glazunov and Ben Allen (eds.), *LTE Advanced and Beyond Wireless Networks: Channel Modelling and Propagation*, John Wiley & Sons, Chichester, UK, 2012.

  Oliveira,C. and Correia,L.M., contribution to "Body Communications", in Roberto Verdone and Alberto Zanella (eds.), *Pervasive Mobile & Ambient Wireless Communications*, Springer, London, UK, 2012.

- International Journals:

  Mackowiak,M., Oliveira,C. and Correia,L.M., "Radiation Pattern of Wearable Antennas: A Statistical Analysis of the Influence of the Human Body", *Springer Int. Journal of Wireless Information Networks*, Vol. 19, No. 3, Sep. 2012, pp. 109-218.

  Oliveira,C. and Correia,L.M., "MIMO Capacity for On-Body Communications in Indoor Environment", *EURASIP Journal on Wireless Communications and Networking*, Apr. 2013 (submitted).

- International Conferences:

  Oliveira,C., Mackowiak,M. and Correia,L.M., "Modelling On- and Off-Body Channels in Body Area Networks", invited to *IMOC 2013 – Int. Microwave and Optoelectronics Conf.*, Rio de Janeiro, Brazil, August 2013.

  Oliveira,C. and Correia,L.M., "Signal Correlation and Power Imbalance in Dynamic On-Body Communications", in *Proc. of VTC 2013 Spring – IEEE 77th Vehicular Technology Conf.*, Dresden, Germany, June 2013.

  Oliveira,C. and Correia,L.M., "Perspectives for the use of MIMO in Dynamic Body Area Networks", in *Proc. of EuCAP'2013 – 7th European Conf. on Antennas and Propagation*, Gothenburg, Sweden, Apr. 2013.

  Oliveira,C., Mackowiak,M. and Correia,L.M., "A Comparison of Phantom Models for On-Body Communications", in *Proc. of PIMRC'2012 - 23rd IEEE Symp. on Personal, Indoor, Mobile and Radio Communications*, Sydney, Australia, Sep. 2012.

  Oliveira,C., Mackowiak,M. and Correia,L.M., "Correlation Analysis in On-Body Communications", in *Proc. of EuCAP'2012 – 6th European Conf. on Antennas and Propagation*, Prague, Czech Republic, Mar. 2012.

Mackowiak,M., Oliveira,C. and Correia,L.M., "Signal Correlation Between Wearable Antennas in Body Area Networks in Multipath Environment", in *Proc. of EuCAP'2012 – 6th European Conf. on Antennas and Propagation*, Prague, Czech Republic, Mar. 2012.

Oliveira,C., Lopes,C., Mackowiak,M. and Correia,L.M., "Characterisation of On-Body Communications at 2.45 GHz", in *Proc. of BodyNets'11 – 6th Intl. Conf. on Body Area Networks*, Beijing, China, Nov. 2011.

Mackowiak,M., Oliveira,C. and Correia,L.M., "A Statistical Analysis of the Influence of the Human Body on the Radiation Pattern of Wearable Antennas", in *Proc. of PIMRC 2011 - IEEE Intl. Symp. on Personal, Indoor and Mobile Radio Communications*, Toronto, Canada, Sep. 2011.

Oliveira,C., Mackowiak,M. and Correia,L.M., "Challenges for Body Area Networks Concerning Radio Aspects", in *Proc. of European Wireless 2011 – 17th European Wireless Conf.*, Wien, Austria, Apr. 2011.

Oliveira,C. and Correia,L.M., "A Statistical Model to Characterize User Influence in Body Area Networks", in *Proc. of IEEE VTC Fall*, Ottawa, Canada, Sep. 2010.

Oliveira,C., Pedrosa,L. and Rocha,R.M., "Characterizing On-Body Wireless Sensor Networks", in *Proc. of NTMS 2008 - Wireless Sensor Networks Workshop*, Tanger, Morocco, Nov. 2008.

1.5 Outline of the Contents

This Thesis attempts to present the information in a pleasant way for the reader, starting with background information on the topic dealt with; then, as it progresses, more specific information is given, until the activities and the outputs of the work are provided.

Chapter 1 gives a general overview of the Thesis. The scope and a brief state of the art are brought up in Section 1.1. Then, the work motivation and main targets are identified in Section 1.2. Section 1.3 highlights the original contributions given by this work. The strategy of investigation is described in Section 1.4, stressing the published work. Section 1.5 concludes the chapter, providing the Thesis structure.

Chapter 2 presents basic concepts on MIMO radio channels, providing a basis for the rest of the work. Section 2.1 introduces the most important concepts and parameters regarding radio

channel modelling. Section 2.2 describes the main aspects of MIMO systems, specifying the MIMO capacity for a 2×2 configuration. Section 2.3 discusses the impact of the channel on system capacity.

Chapter 3 contains the state of the art on channel modelling for BANs. Section 3.1 introduces the techniques for the description of the human body, while Section 3.2 overviews the antenna design for BANs. Section 3.3 describes the on-body propagation mechanisms, and Section 3.4 provides a literature review on on-body channel modelling. Section 3.5 discusses on the use of channel diversity/cooperative techniques for BANs.

Chapter 4 presents the proposed models used to analyse the interaction between antennas and the body. In Section 4.1, the concept of antenna-body interaction is introduced, claiming a statistical approach for modelling antennas' behaviour in the vicinity of the body. Section 4.2 details the analytical models firstly used for the general understanding of the behaviour of a plane wave, and of a simple radiation source, near the body. Section 4.3 reviews the main features of the numerical full wave simulation tool *CST Microwave Studio*, used to analyse the antenna-body interaction with a real patch antenna.

Chapter 5 describes the different studies performed to characterise the on-body channel. Section 5.1 introduces the concept. Section 5.2 introduces a preliminary study to analyse on-body communications for a static user in free space, its implementation including measurements and simulations. In Section 5.3, the mobility of the user is included in the analysis of the free space on-body channels. A new technique using motion capture software introduces the body dynamics in full wave simulations. In Section 5.4, a complex environment with random scatterers is then added to the study. A novel method, based on full wave simulations and on results from a geometrically based statistical channel model, is introduced.

Chapter 6 describes the reference scenarios, metrics and assumptions used throughout the Thesis. Section 6.1 introduces general metrics related to radiation patterns and statistical distributions. In Section 6.2, a set of general assumptions used through the work is presented. Section 6.3 and Section 6.4 describe the settings considered for the analytical and numerical studies, respectively. Section 6.5 summarises the measurement conditions of the studies performed.

Chapter 7 contains the main findings of the statistical analysis for modelling antennas' behaviour near the human body. Section 7.1 provides general conclusions on the impact of the body in the propagation of a plane wave, namely on the electromagnetic fields distribution. Section 7.2 gives the statistics of the radiation pattern of an elementary source placed at different distances to the user. Section 7.3 provides results from the analysis of a patch antenna

behaviour near the body, obtained through simulations. This section includes results from the assessment of *CST* meshing parameters, and from the comparison between homogeneous and voxel phantoms. Results from a measurement campaign are also provided.

Chapter 8 analyses the results obtained for the modelling of on-body channels. In Section 8.1, results from measurements and simulations with a static user in free space are presented. The main parameters addressed here are the channel gains, power imbalance and correlation. In Section 8.2, similar results are provided for a user moving in free space, and optimum 1×2 on-body placements are suggested. Section 8.3 provides capacity results for the body moving in a complex propagation environment, together with the optimum 2×2 MIMO antenna placements.

Chapter 9 concludes the Thesis, providing an overview of the problems addressed, summarising the strategies followed to solve them, highlighting the major results, and providing suggestions for future research. Section 9.1 summarises the work done, while Section 9.2 highlights the main findings. Section 9.3 proposes topics for future investigation.

A set of annexes is also included, with further information for some of the chapters. Annex A contains the dielectric properties considered for selected human tissues, namely the fitting parameters of the 4-Cole-Cole expression. Annex B contains the collection of results obtained for the elementary source, namely the radiation patterns at different body-source distances and their statistics. Annex C contains the collection of results obtained for the patch antenna, namely the radiation patterns obtained at different distances from various body parts, as well as their statistics. Annex D contains the classification of on-body links for the different transmitter placements.

Chapter 2

MIMO Radio Channels

This chapter presents basic concepts on MIMO radio channels, providing a basis for the rest of the work. Section 2.1 introduces the most important concepts and parameters regarding radio channel modelling. Section 2.2 describes the main aspects of MIMO systems, specifying the MIMO capacity for a 2×2 configuration. Section 2.3 discusses the impact of the channel on system capacity.

2.1 Radio Channel Modelling

The study of the properties of the radio wave propagation channel and the understanding of the physical phenomena involved in it are a key issue in any communications system, being the framework for an optimal system design. In this section, the most important issues regarding channel modelling are introduced, being used afterwards in BANs characterisation.

The problem of channel modelling ought to start with a good description of the propagation environment. In a wireless environment, a signal radiated by the TX antenna reaches the RX station through different paths, which should be completely identified whenever possible. Along these paths, different propagation mechanisms may occur between the signal and various objects. Possible mechanisms are specular reflections on large and plane surfaces, diffuse scattering from small surfaces exhibiting small irregularities, diffraction caused by shadowing of obstacles, or transmission through dense materials. Note that the concept of small or large is with respect to the wavelength.

This work is focused on the radio propagation channel, limited to signal filtering at RX, dismissing coding, decoding, modulation and demodulation. The RX can be described by its sensitivity, time resolution, and system maximum delay. The RX signal is the result of the processing, where rays are grouped and cumulated according to the time resolution, those exceeding the receiver maximum delay being dropped.

The identification of the different propagation mechanisms allows the development of propagation prediction models. In general, these models can be divided into three categories:

- *Deterministic models* intend to reproduce the actual physical propagation for a given environment, being based on suitable formulations of the propagation phenomena and on a deterministic description of the propagation scenario. Ray tracing and techniques solving full electromagnetic equations are the two main approaches for these models. These models are very accurate, but not very flexible.
- *Statistical and empirical models* attempt to reproduce, either directly or by statistical means, certain characteristics observed from measurements of the radio channel. These models are very flexible and have the advantage to take all factors (known and unknown) into account, but they are not too accurate.
- *Hybrid models* combine the properties of the two previously mentioned approaches, leading to an accuracy-complexity compromise.

In a multipath environment, the propagation of waves is done mainly by scattering from different surfaces and by diffraction over them. Various incoming waves arrive from different directions, with different time delays, being vectorially combined at the RX, resulting in constructive or destructive interferences between them. The total signal is the sum of the incoming waves, and can be expressed as a function of its amplitude A and phase ϕ.

The short term variations around the local mean value caused by multipath are commonly termed as *fast fading*. In narrowband systems, the fast fading must be distinguished between LOS and NLOS, being more severe in NLOS situations. In the case of NLOS, where the component waves at the RX are of equal (or approximately equal) amplitude, the fast fading can be modelled through a Rayleigh Distribution. When there is a dominant LOS path, or a dominant specular component, A is best described by a Rice Distribution, fewer deep fades are expected, and the specular component will be a major feature of the spectrum. In the literature, the Rician Distribution is often described in terms of a parameter K, which represents the ratio of the power in the dominant signal to that in the multipath components.

The longer term variations in the mean amplitude of an RX signal, usually caused by movement over distances large enough to produce gross variations in the geometry of the link, are termed *slow fading*. In mobile radio channels, as these variations are caused by changing visibility or obstruction of multipath components (*e.g.*, shadow of hills, trees, buildings, walls, furniture), the slow fading may also be termed *shadowing*. Although there are no complete physical models for slow fading, measurements indicate that the mean path loss is Lognormal Distributed.

One of the most important radio channel parameters is the *path loss*, L_p, whose prediction is a very important stage in radio planning. Path loss is defined as [Moli05]:

$$L_{p\,[\mathrm{dB}]} = P_{t\,[\mathrm{dBm}]} + G_{t[\mathrm{dBi}]} - P_{r\,[\mathrm{dBm}]} + G_{r[\mathrm{dBi}]} \tag{2.1}$$

where

- P_t is the transmitted power;
- G_t is the antenna gain of the TX;
- P_r is the received power;
- G_r is the antenna gain of the RX.

The term *channel gain* is many times used, being defined as the symmetric of L_p.

The power available at a receiving antenna in free space propagation, when there is only one clear LOS propagation path between the TX and the RX, is [Moli05]:

$$P_r = P_t G_t G_r \left(\frac{\lambda}{4\pi}\right)^2 \frac{1}{d^2} \tag{2.2}$$

where

- λ is the wavelength;
- d is the distance between TX and RX.

In this case, L_p is given by:

$$L_{p\,[\mathrm{dB}]} = L_{p0\,[\mathrm{dB}]} = \text{-}67.56 + 20\log\left(f_{[\mathrm{MHz}]}\right) + 20\log\left(d_{[\mathrm{cm}]}\right) \tag{2.3}$$

where

- L_{p0} is the free space path loss;
- f is the frequency.

If the usual average power decay model with distance (2.4) is considered, in free space, one has a path loss exponent $\alpha = 2$.

$$L_{p_{[\mathrm{dB}]}} = L_{p_{d0}\,[\mathrm{dB}]} + 10\alpha\log\left(d_{[\mathrm{cm}]}\right) + \Delta L_{p\,[\mathrm{dB}]} \tag{2.4}$$

where

- $L_{p_{d0\,[\mathrm{dB}]}} = L_{p_0\,[\mathrm{dB}]} - 10\alpha\log(d_{0\,[\mathrm{cm}]})$ (2.5)
  is the path loss at a reference distance d;
- ΔL_p is the signal fluctuation around the mean (fading).

Another important channel modelling parameter is the Channel Impulse Response (CIR). Wideband channel modelling is usually based in the time- or space-variant CIR, which shows several distinct components - corresponding to different propagation paths – at certain delay times usually related to Multipath Components (MPCs). As the radio channel is time dispersive, for a pulse $\delta(t)$ being transmitted, the impulse response of the channel, $h(t)$, is [Moli05]:

$$h(t) = \sum_{n=1}^{N_{mc}} h_n \delta(t - \tau_n) \tag{2.6}$$

where

- h_n is the amplitude of the n-th MPC;
- τ_n is the delay of the n-th MPC;
- N_{mc} is the number of MPCs.

It is common to evaluate the CIR through the Power Delay Profile (PDP), which represents

the average power of the channel distributed over the various paths in the multipath propagation, as a function of the delay with respect to the first arrival path. From the average PDP, important time dispersion parameters can be extracted, like the mean or the Root Mean Square (RMS) delay spread.

2.2 MIMO Systems

The theoretical investigations carried out by [FoGa98] and [Tela99] on MIMO systems have gained increased visibility over the last years. Since that time, research on MIMO has intensified and several applications are being developed, *e.g.*, UMTS with MIMO enhancements in Release 7, WLAN IEEE 802.11n.

MIMO consists of using multiple antenna elements at both link ends, offering increased transmission throughput via spatial multiplexing, as presented in Figure 2.1. The transmitter and/or the receiver consist of arrays made of several closely-spaced antennas, respecting the basic condition that the number of receiving antennas, N_R, is at least as large as the number of transmitting ones, N_T. The original data stream is multiplexed into several parallel streams, each one sent from one transmit antenna element. At the RX side, these data streams are "seen" as a combined weighted summation. These combinations will be linearly independent if the channel has a strong random behaviour, allowing the RX to separate data streams by using appropriate signal processing.

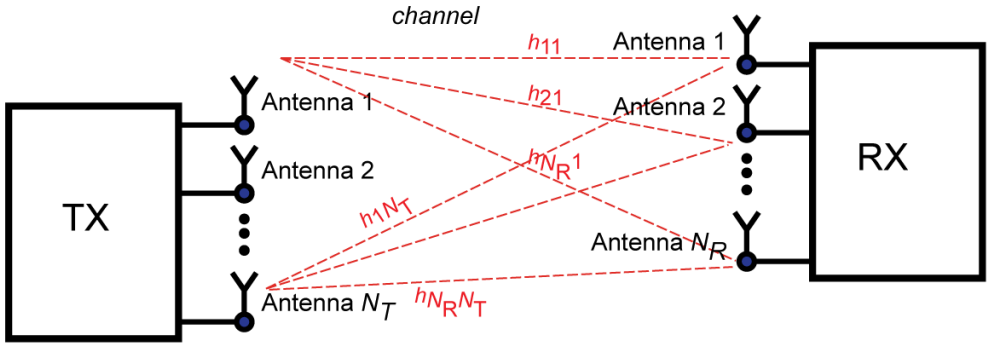

Figure 2.1. Block diagram of a MIMO system (adapted from [Moli05]).

At the transmission side, the data stream is sent from N_T antennas through a wireless propagation channel, which is assumed to be quasi-static and frequency-flat or narrowband (*i.e.*, the bandwidth is taken to be narrow enough that the channel can be treated as flat over frequency). One denotes the relation between the input and the output of this system as [FoGa98]:

$$\mathbf{y} = \mathbf{H_c}\mathbf{x} + \mathbf{n} \tag{2.7}$$

where

- $\mathbf{x} = [x_1, x_2, \dots, x_{N_T}]$ (2.8)

  is the transmitted signal vector from the N_T antennas;
- $\mathbf{y} = [y_1, y_2, \dots, y_{N_R}]$ (2.9)

  is the received signal vector at the N_R antennas;
- $\mathbf{H_c} = \begin{bmatrix} h_{11} & h_{12} & \cdots & h_{1N_T} \\ h_{21} & h_{22} & \cdots & h_{2N_T} \\ \vdots & \vdots & \cdots & \vdots \\ h_{N_R1} & h_{N_R2} & \cdots & h_{N_RN_T} \end{bmatrix}$ (2.10)

  is the $N_T \times N_R$ matrix of the channel, whose entries h_{kj} are transfer functions from the j-th transmit antenna to the k-th receive antenna, and $\boldsymbol{n}$ is the noise vector.

According to information theory, the capacity of a SISO radio channel, C_{SISO}, is given by Shannon's rule [Proa01] defined in (2.11). In the SISO situation, capacity increases logarithmically with the Signal to Noise Ratio (SNR), so that increasing transmitting power is an ineffective way of increasing capacity.

$$C_{\text{SISO [bps/Hz]}} = \log_2(1 + \rho_N |\mathbf{H_c}|^2) \tag{2.11}$$

where

- ρ_N is the SNR at the receiver;

For the frequency flat case, the transfer function $\mathbf{H}$ is just a scalar number.

When using a MIMO system, the spatial multiplexing capability is exploited. One has multiple parallel channels between the TX and the RX, which operate simultaneously on the same frequency band and at the same time, thus, the capacity of a channel is given by the sum of the capacities of the sub-channels [Moli05]. The theoretical capacity of a MIMO system, C_{MIMO}, has been derived by [FoGa98] as

$$C_{\text{MIMO[bps/Hz]}} = \log_2\left[det(\mathbf{I}_{N_R} + \frac{\overline{\rho_N}}{N_T}\mathbf{H_c}\mathbf{H_c}^H)\right] \tag{2.12}$$

where

- $\mathbf{I}_{N_R}$ is the $N_R \times N_R$ identity matrix;
- $\overline{\rho_N}$ is the mean SNR per reception branch.

From (2.12), it is possible to derive the upper and lower bounds of capacity in a MIMO system. The upper bound of channel capacity, defined as (2.13), corresponds to the case where channels are uncorrelated and signals propagate without path loss ($\mathbf{H_c}$ is the identity matrix).

$$C_{\mathrm{MIMO}_{|\rho=0\ [\mathrm{bps/Hz}]}} = N_{min}\log_2(1+\frac{\overline{\rho_N}}{N_T}) \tag{2.13}$$

where $N_{min} = \min\{N_T, N_R\}$.

The lower bound of MIMO capacity occurs when sub-channels are totally correlated, being defined as:

$$C_{\mathrm{MIMO}_{|\rho=1[\mathrm{bps/Hz}]}} = \log_2(1+N_{min}\frac{\overline{\rho_N}}{N_T}) \tag{2.14}$$

For the particular case of a 2×2 MIMO system, $N_T = N_R = 2$, and the $\mathbf{H_c}$ matrix is given by:

$$\mathbf{H_c} = h_{11}\begin{bmatrix}1 & c_1\\ c_2 & c_3\end{bmatrix} \tag{2.15}$$

where the coefficients $c_{\{1,2,3\}}$ represent the linear relation among the $\mathbf{H_c}$ entries and h_{11}.

Assuming an equal power distribution, the SNR is given by ρ_N, and the following general expression can be derived:

$$C_{\mathrm{MIMO[bps/Hz]}} = \log_2\left\{\left[1+\frac{2\rho_N(1+{c_1}^2)}{1+{c_1}^2+{c_2}^2+{c_3}^2}\right]\left[1+\frac{2\rho_N({c_2}^2+{c_3}^2)}{1+{c_1}^2+{c_2}^2+{c_3}^2}\right] - \left[\frac{2\rho_N(c_2+c_1c_3)}{1+{c_1}^2+{c_2}^2+{c_3}^2}\right]^2\right\} \tag{2.16}$$

2.3 Impact of the Channel

The general model adopted for MIMO systems must be adapted to the particularities of BAN channels. Issues like channel fading, multipath, channel correlations, or LOS versus non-LOS (NLOS) situations are of extreme importance for channel modelling, and cannot be neglected.

Based on (2.16), it is possible to analyse the trend of channel capacity with ρ_N for selected cases, like the ones illustrated in Figure 2.2. This analysis enables to understand the impact of the channel in MIMO capacity.

Expression (2.16) can also be applied to particular cases, like when $h_{12} = h_{21}$. Figure 2.3 displays the values of channel capacity for this particular case, as a function of ρ_N. It is possible to observe the upper and lower boundaries, corresponding to the top and bottom right squares in Figure 2.3, respectively.

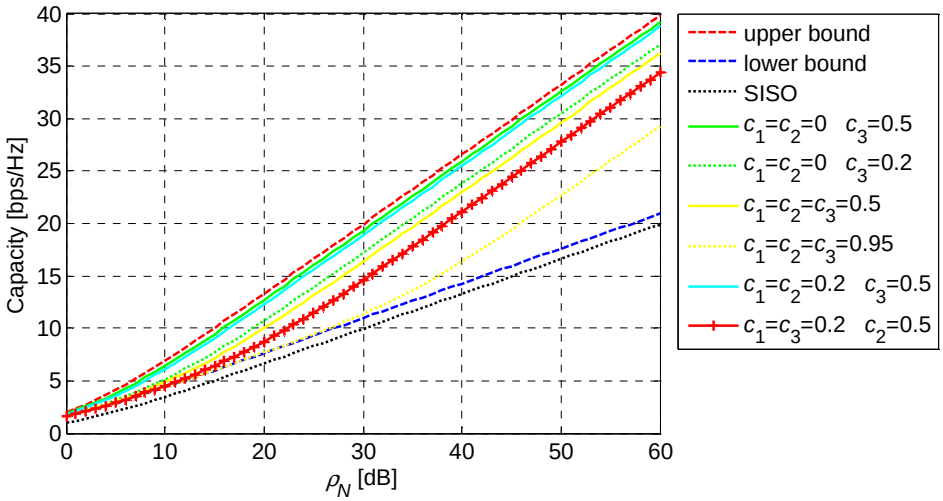

Figure 2.2. Trend of capacity with ρ_N in a 2×2 MIMO system.

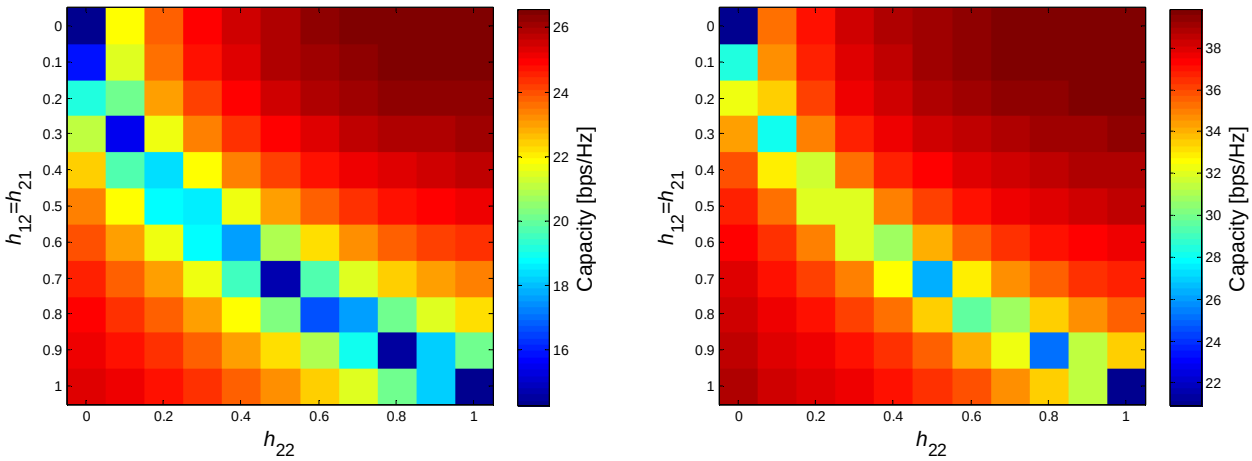

(a) ρ_N= 40 dB (b) ρ_N= 60 dB

Figure 2.3. Channel capacity for given ρ_N in a 2×2 MIMO system.

The lower and upper limits of capacity for a 2×2 MIMO system are given by:

- *Upper bound* (top right square in Figure 2.3): $h_{12} = h_{21} = 0$ and $h_{22} = h_{11}$

$$C_{\text{upper[bps/Hz]}} = 2\log_2\{1 + \rho_N\} \tag{2.17}$$

- *Lower bound* (bottom right square in Figure 2.3): $h_{11} = h_{12} = h_{21} = h_{22}$

$$C_{\text{lower[bps/Hz]}} = \log_2\{1 + 2\rho_N\} \tag{2.18}$$

For the particular case of uncorrelated channels, h_{12}=h_{21}=0, (2.19) states the MIMO capacity as a function of the linear relation between the branches ($h_{22} = c_3 h_{11}$):

$$C_{\mathrm{MIMO[bps/Hz]}} = \log_2 \left\{ 1 + 2\rho_N + \left(\frac{2\rho_N c_3}{1 + {c_3}^2} \right)^2 \right\} \tag{2.19}$$

Figure 2.4 displays the trend of the channel capacity with c_3 for different ρ_N values. The channel capacity is naturally higher for greater SNR and lower imbalances between the branches, and decreases with the higher imbalance up to a certain value. For high values of imbalance, the capacity tends to the lower bound of (2.18).

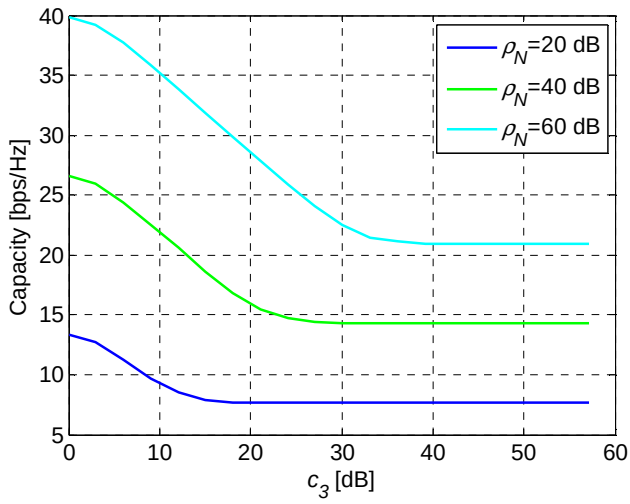

Figure 2.4. Trend of capacity with the imbalance between main branches.

Figure 2.5 illustrates the trend of channel capacity with ρ_N for selected cases, depending on the imbalance between the branches.

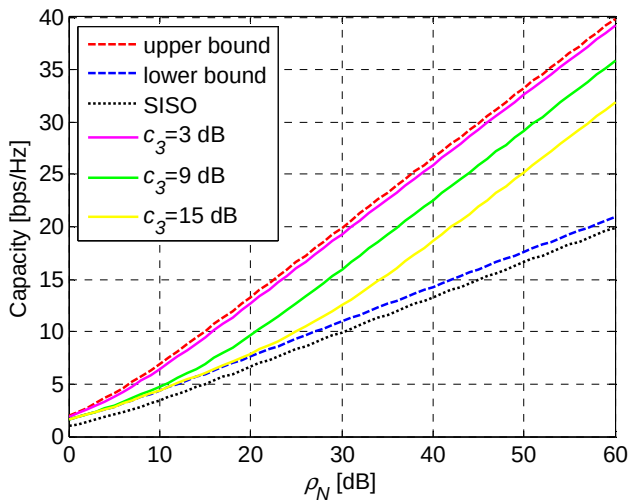

Figure 2.5. Channel capacity for selected cases in a 2×2 MIMO system.

The existence of channel fading between wireless links implies that the entries h_{kj} in the channel transfer matrix become random variables. In the case of sufficient distance between antenna elements and existence of heavy multipath, it is assumed that MIMO channels are

Rayleigh fading, independent and identically distributed. By having independent fading (no channel correlation), there is a high probability that the channel matrix is full rank and the eigenvalues are fairly similar to each other, consequently capacity increases linearly with the number of antenna elements. Thus, the existence of heavy multipath, which is usually considered a drawback, becomes a major advantage in MIMO systems.

While uncorrelated channels result in a high MIMO capacity, the correlation of the signals at different antenna elements can significantly reduce the capacity of a MIMO system. [FoGa98] refers that the elements of the field transmission matrix become strongly correlated as the spacing between antennas drops below $\lambda/4$, assuming that the significant rays are widely distributed in angle at the antenna array (90° or more). Also, for narrow angular spreads ($\leq 30^{o}$) the correlation between elements becomes strong at even one λ antenna spacing.

[Moli05] supports that for $\lambda/2$ spaced antennas, a uniform angular power spectrum leads approximately to a de-correlation of incident signals, and a smaller angular spread of the channel increases correlation. It is also stated that, for MIMO systems, one has to consider correlation both at the RX and TX. The authors assume that the correlation at the TX is independent of the one at the RX. However, [OeCl07] alerts that, in small spaced scenarios, the correlations at one end depend on the antenna considered at the other end of the link, so this model may not be valid. Analytical computation of capacity is much more complicated in the case of correlated channels.

The author in [Loyk01], supported by the use of an exponential correlation matrix model, concludes that the effect of channel correlation is the same as a decrease in the SNR, under some realistic conditions. For example, a factor of correlation of 0.7 is similar to a 3 dB decrease in SNR.

It is often common in BAN scenarios to have both LOS and NLOS situations. For LOS SISO links, the fading statistics become Ricean instead of Rayleigh. [Moli05] notes that capacity in LOS MIMO is much lower than for a NLOS channel, but only when assuming equal SNR. One should note that the offered SNR is often better in the LOS case, than in the NLOS one. Thus, for a power-limited scenario with realistic channels, the LOS case often offers the highest capacity, despite of the theoretical calculations. It is also noted that, if there is a strong plane wave in LOS, a larger spread is verified; for a spherical wave in LOS, a full rank matrix may be obtained if antenna elements are spaced appropriately.

Chapter 3

Body Area Networks

This chapter contains the state of the art on channel modelling for BANs. Section 3.1 introduces the techniques for the description of the human body, while Section 3.2 overviews the antenna design for BANs. Section 3.3 describes the on-body propagation mechanisms, and Section 3.4 provides a literature review on on-body channel modelling. Section 3.5 discusses on the use of channel diversity/cooperative techniques for BANs.

3.1 Body Description

A comprehension of the electromagnetic properties of the human body is mandatory for the study of on-body communication systems, as it will be the central medium through which the communication in BANs takes place. Each tissue has assigned unique dielectric properties at different frequencies, which have been examined by several researchers. However, this is not a straightforward task, as it is difficult to make measurements on live tissues. Most of these studies gather excised animal tissue (mostly ovine), human autopsy or *in vivo* materials.

Two basic quantities characterise the dielectric properties of biological material [Haba02]:

- Electric Conductivity, σ: describes energy dissipation, relating the conduction currents to the electric field (E);
- Relative Permittivity, ε_r: describes energy storage, relating the displacement of currents to the E field.

In [Gabr96], a comprehensive study to obtain the body tissue complex permittivity, ε, is presented for various tissues and frequencies ranging from 10 Hz to 100 GHz. The model used to obtain the dielectric data across this frequency range is a summation of four expressions, where each one is a Cole-Cole term related to a dispersion region m, resulting in the 4-Cole-Cole equation shown in (3.1). A summary of the fitting parameters is presented in Annex A [IFAP12].

$$\varepsilon_{[F/m]}=\varepsilon_{\infty[F/m]}+\sum_{m=1}^{4}\frac{\Delta\varepsilon_{m\,[F/m]}}{1+(j\omega_{[rad/s]}\,\tau_{m[s]})^{(1-\alpha_m)}}+\frac{\sigma_{i\,[S/m]}}{j\omega_{[rad/s]}\varepsilon_{0\,[F/m]}} \tag{3.1}$$

where

- ε_∞ is the permittivity of a given tissue in the THz frequency range ($\omega\tau_m \gg 1$);
- $\Delta\varepsilon_m=\varepsilon_s-\varepsilon_\infty$ (3.2)
- ε_s is the permittivity of a given tissue at field frequencies where $\omega\tau_m \ll 1$;
- $\omega = 2\pi f$ (3.3)
  is the angular frequency;
- τ_m is the relaxation time of each dispersion region;
- α_m is the distribution parameter (measures the broadening of dispersion within each region);
- σ_i is the static ionic conductivity;
- ε_0 is the permittivity of free space.

The permittivity of biological tissues depends on their type, water content, temperature and frequency. Moreover, tissue properties also fluctuate throughout the life time, because of the variations in water content of tissues [PeRG01]. Figure 3.1 and Figure 3.2 display the graphical variation of relative permittivity and conductivity, respectively, over the 10 Hz to 100 GHz frequency range. These graphs show that relative permittivity and conductivity of body tissues change considerably with frequency; however, in the range from 100 MHz to 1 GHz, variations are relatively small. Typically, the relative permittivity displays extremely high values at low frequencies, falling off in more or less distinct steps as the frequency is increased.

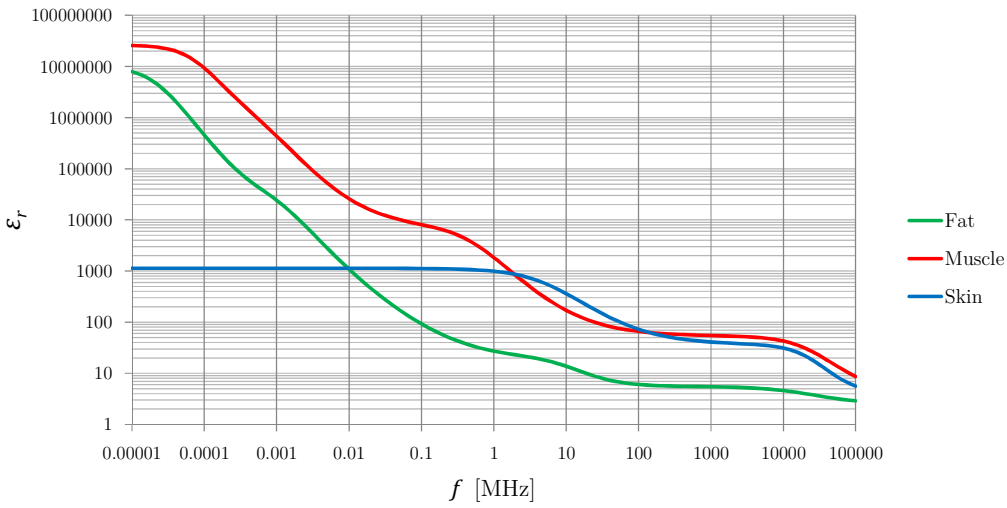

Figure 3.1. Relative permittivity of fat, muscle and skin tissues.

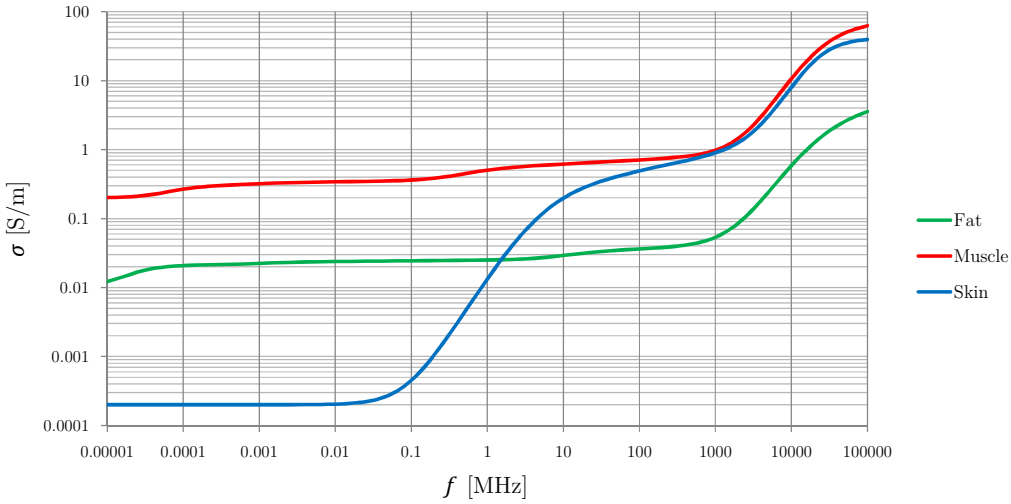

Figure 3.2. Conductivity of fat, muscle and skin tissues.

The permittivity and frequency may also determine how far the electromagnetic waves penetrate into the body. Figure 3.3 illustrates the behaviour of penetration depth over a wide range of frequencies. [Gabr96] concluded that variations are considerable in the range of 100 MHz to 1 GHz, decreasing as frequency increases. In general, penetration depth for

radiofrequencies is small, and propagation is around the surface of the body.

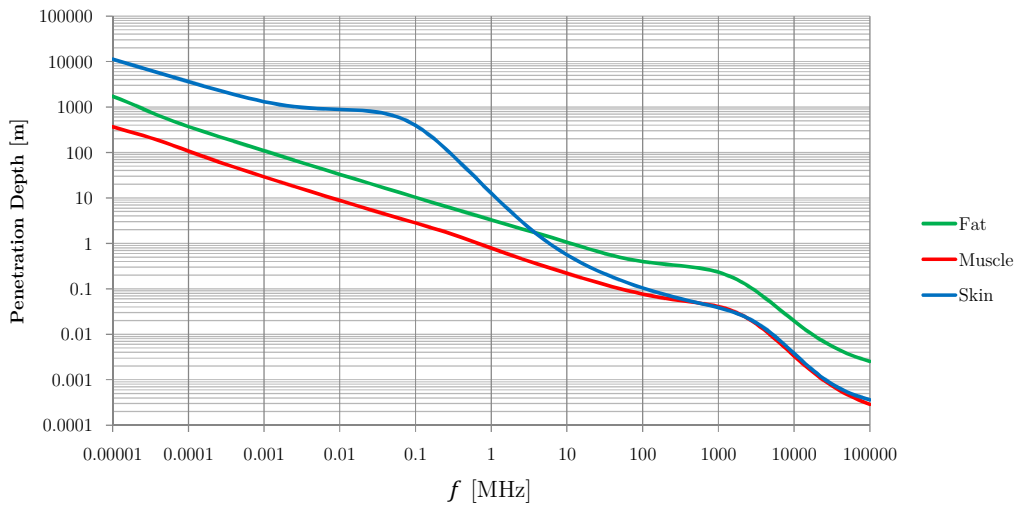

Figure 3.3. Penetration depth for fat, muscle and skin tissues.

To explore the interaction between the electromagnetic fields and the human body, it is necessary to have good models for the latter. This task can be accomplished by using either physical phantoms, made from solid, liquid, or gel materials, or numerical phantoms, created through computational simulations. Phantoms are not a novel issue, as they have been extensively used in the studies on the effects of electromagnetic fields on human health, as well as in safety and performance tests for mobile phones, *e.g.* [IOSU04].

A physical phantom is a physical model of the human body, simulating the characteristics of the biological tissues in a defined range of frequencies. When measuring antennas close to the human body, head, abdomen, torso, or whole-body, physical phantoms are usually used.

Liquid phantoms are the oldest physical phantoms, very easy to produce, usually made of a fiberglass material with low relative permittivity and conductivity, filled in by a homogenous fluid having the same electrical characteristics as the tissues in the human body. Gel phantoms are made of a coagulant capable of self-shaping, being suitable for simulating both high- or low-water content materials, and able to adjust its electrical properties over a wide frequency range. Invariably, gel phantom materials degrade over time, due to the loss of water or the growth of fungi. Solid physical phantoms are other type, being made of materials capable of maintain their mechanical and dielectric properties over time, accurately representing the inhomogeneous structure of the human body, although requiring expensive manufacturing.

Some examples of physical phantoms may be observed in Figure 3.4. An agar-based solid phantom is shown in Figure 3.4a, based on the human torso of a Japanese male, being able to simulate dielectric constant of high-water content tissues from 0.8 to 2.4 GHz, and from 3.8 to 5.8 GHz [IOSU04]. Figure 3.4b shows an example of a human-head dry phantom, commonly

used in measurements of the Specific Absorption Rate (SAR).

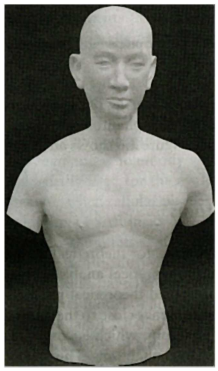

(a) Human Torso (extracted from [IOSU04]).

(b) Human Head (extracted from [HaHa06]).

Figure 3.4. Human Physical Phantoms

Numerical phantoms are 2D or 3D models of the human body embedded in numerical electromagnetic codes, and usually being composed of many pixels (2D models) or voxels (3D models). Those elements are constituted by a given well defined tissue, having assigned unique dielectric properties at each frequency of interest, consisting of a pair of values: one for the relative permittivity and the other for the conductivity. Recent developments in medical imaging technologies have supported the design of precise head and whole-body voxel models, for male, female, child, or even pregnant women and foetus. Figure 3.5 shows the SAM model [SEMC12] corresponding to the 90*th*-percentile dimensions of an adult male head based on an anthropomorphic study of US Army personnel. Figure 3.6 shows the Virtual Population static whole-body voxel models for adults and children, [ViFa12].

Figure 3.5. Numerical Head Model (extracted from [SEMC12]).

Phantoms are important tools for accurate prediction of radio propagation inside and around the body, thus, supplying an efficient design of on-body communication systems. They are used in many commercial numerical simulators, like *SEMCAD X* [SEMC12], *CST* [CSTe12] or *XFDTD®* [XFDT12]. These simulators employ common numerical techniques, such as the Uniform Geometrical Theory of Diffraction (UTD) [Path82], Ray-Tracing (RT) techniques [Glas89], the Method of Moments (MoM) [Sadi00], the Finite Element Method (FEM) [Sadi00], the Finite-Difference Time-Domain (FDTD) method [Sadi00], or the Finite Integration

Technique (FIT) [Weil77]. While *XFDTD®* uses the FDTD method and *CST* uses the FIT method, *SEMCAD* uses a combination of both.

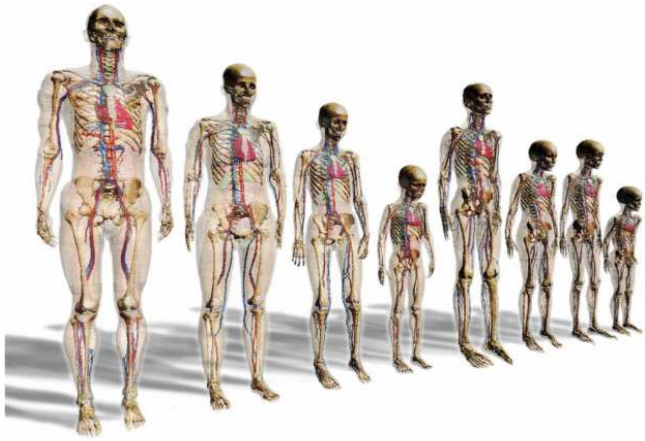

Figure 3.6. Virtual Family Models (extracted from [ViFa12]).

Most of the times, combinations or modified versions of these techniques are required to fulfil specific difficulties of communications in and over the body. For example, [HaRa98] proposes the locally distorted, non-orthogonal FDTD method to take the rounded shapes of the body into account; other solutions, proposed in [ZhHP05], are the application of dispersive FDTD or sub-band FDTD methods to accurately include material information in simulations.

It is important to mention that, during the timeframe of this Thesis, the majority of the voxel models were available in the static standing posture. The existing solutions enabling the model mobility were private property of a limited number of companies or universities. The authors in [GHBN11] and [AIKT11] were pioneers on the study of the dynamic on-body communication channel via simulations combined with motion capture body models. However, recent developments made possible the development of a few posable voxel models. For instance, the posture of the limbs of the Virtual Population can be adjusted by an animation tool available in the *SEMCAD* X simulation platform ([ViFa12], [SEMC12]).

3.2 Antennas

The particular propagation characteristics of BANs, mainly the proximity and the movement of the human body, demand for a careful and challenging design of on-body antennas.

Many publications have been written on the effects of antennas operating in close proximity to the human body (*e.g.*, on the absorption of electromagnetic energy emitted by mobile phones [SaRK04], [RoLa12]). This is not a straightforward task, as an accurate modelling requires the

study of an extensive range of conditions. The performance of an antenna located near dielectric materials has been comprehensively studied in the literature, under different approaches and for different applications. Some examples are given in what follows.

In [Kago90], the performance of directional and omni-directional antennas in the presence of a dielectric cylinder is compared through numerical models. It is shown that the input impedance of the directional antenna is almost constant, even when the distance to the cylinder is as close as 0.05λ. Moreover, changes in the radiation pattern are quite small, with peaks appearing in the opposite direction of the cylinder.

The authors in [QiMo06] study the influence of a lossy cylinder at [2, 25] mm to a printed UWB antenna, through a commercial simulator (*HFSS* [*HFSS10*]). A better performance is verified at closer distances to the cylinder, due to a partial attenuation of the incident wave by the cylinder, leading to attenuated reflected waves, thus, lower reflection coefficients over the impedance bandwidth. In some angular regions of the radiation pattern, there is a deviation from the omni-directional properties. Some authors agree that the destructive effects of body proximity increase as antenna-body separation decreases. [Burb92] foresees a 4 dB gain reduction when the antenna is placed on a shirt pocket, instead of on a jacket.

In [CoSc07b], 2.45 GHz FDTD simulations of a low-profile patch antenna, at 1 mm distance from a lossy medium, give a body-worn efficiency of more than 60%. The antenna radiates symmetrically around the azimuth plane when it is tissue-mounted, thus, optimising coupling between body-worn devices. It is concluded that this antenna may replace vertical wire monopoles in BANs.

In [AlHD07], the performance of conventional and planar antenna structures is analysed, in terms of radiation patterns, gain, efficiency and return loss. The *CST* simulator [CSTe12] is used to vary parameters like human body lossy tissues, antenna-body separation and location of the antenna on the body. Losses caused by the human body are verified, in particular in backward radiation, and increased directivity is noted in some angles, due to the body curvature. Authors argue that antenna gain and efficiency are reduced on left side of the body, compared to the right side. For instance, for a printed dipole, differences on gain between both sides can reach 1.7 dB. The further the antenna is from the body, the higher the gain is, as the reflected power increases and less energy is absorbed.

In [ScEB99], a study with a loop antenna at increased distances to the body ([1, 4] cm), at 418 MHz, concluded that as the separation distance increases, the forward pattern gain advantage reduces; in the reverse direction the mean gain rises, but nulls are still present.

Some authors had compared the performance of antenna at different frequencies, as human

body dielectric properties change with the frequency. The study carried out in [ScEv01], compares results at 418 and 916.5 MHz, showing a 7 dB increase of body losses at the higher frequency. Those results are consistent with the higher losses in biological tissues at 916.5 MHz. In the microwave region, the increased energy absorption suggests a greater influence of the human body on the performance of nearby antennas. However, the authors of [CrEv97] conclude that antenna performance can be surprisingly good at 2.45 GHz, especially when antenna-body separation is $\lambda/8$ or more. Radiation patterns show that gain is severely reduced in backward direction, on average by more than 15 dB.

[ToHA93] studied the effects of the presence of a person on portable antennas. It was found that the presence of the human body leads to a drop on the resonance frequency, to severe changes in the radiation pattern, cross-polarisation, and reduction of antenna efficiency (45% power lost). The main propagation mechanism is diffraction around and scattering from the head (note that this study was for a hand-held portable phone close to the human head). These changes affect the maximum channel capacity and minimum power consumption.

Regarding the movement of the user, parallel alignment between the RX and the TX antennas is sporadic. One would expect that the two antennas are most of the time in some degree of mutual cross-polarisation. Also, the antenna positions over the body determine the propagation mode. If the belt-to-wrist path is in some cases a free space one, when the arm is behind the body, one has a shadowed path with diffraction around the body. For free-space links, an antenna with maximum radiation away from the body is needed. In all cases, radiation into the body should be minimised. Also, it is important to take into account that, in the case of communications off the body, the characterisation of the far-field radiation pattern is appropriated. For most of the on-body communications, a characterisation of the near-field radiation pattern is more suitable.

For the reasons stated above, it is rather difficult to specify ideal antenna characteristics; however, two mandatory requirements in BAN's antennas design are identified in [HaHa06]:

- being insensitive to the proximity to the body, *i.e.*, attain input impedance match independently of the position of the body (adaptive matching);
- achieve optimum radiation patterns for minimising link losses.

The main criteria for on-body communication modules are the support of high data rates, the small size and the lightweight, and the consumption of minimum power. The first two criteria suggest the use of high frequencies, but the third one implies highly efficient links, which is not a characteristic of high frequencies, related to severe propagation losses. For both narrowband and UWB cases, the near field coupling to the body modifies antenna currents, hence, the matching, and often induces energy absorption. The dominant effect in narrowband cases is the

shift of the resonant frequency (mismatch), while UWB antennas can couple strongly with the body, resulting in important energy losses [ReTa12]. Accordingly, desensitisation techniques are demanded for UWB antennas, like the field screening with a floating ground plane or a ferrite sheet, or the use of absorbing materials [TCAB10].

Some works specifically addressing on-body communications are arising, *e.g.* [KeFC09]. In [HHNA07], it is stated that the quarter-wavelength monopole is a suitable antenna for many on-body links, due to its omnidirectional characteristics and the vertical polarisation to the body surface, however, being too large for a practical implementation. So, a reduced-height monopole, top-loaded, is proposed, leading to similar performance and having acceptable dimensions. Possible types of antennas for body centric communications are low-profile monopoles, planar disc monopole antenna (UWB applications), slot antenna (omnidirectional) and directional slot antenna [HaHa06].

The concept of wearable antennas takes form within the BANs sphere, leaping to the body worn antennas embedded in the so called "smart clothe", with extended applications: entertainment, sports outfits, emergency workers outfits, military, medical, or spatial applications. Textile materials as fleece, upholstery fabric, vellux, synthetic felt, or cordura, are very interesting microstrip substrates as they can be easily integrated into clothes or even onto biomaterials. Their very low dielectric constant reduces surface wave losses and improves impedance bandwidth. In the literature, one can find various studies on the effects of substrate materials on wearable antennas performance, [InSm02], [SaHu03]. Important design features of a wearable antenna include the selection of textile material, selection of material conductivity, study of antenna performance, ground plane optimisation, performance enhancement (taking into account bend surfaces), and performance near the human body.

Additionally, the design of antennas for BAN applications (wearable or not) must pay a special attention to the electromagnetic levels absorbed by the human body, as they are in close proximity to it. SAR levels absorbed by the human body should not exceed the basic restrictions specified in safety regulations [ICNI98], and antenna design should take this factor into account, namely when specifying radiation patterns. Note that extensive research has been done in this area with the deployment of mobile phones.

3.3 Propagation Mechanisms

To characterise the on-body channel it is important to identify the propagation mechanisms

that take place in each link. This may be an unfeasible task due to the numerous changes in the geometry and properties of the links, related with the natural and random body kinetics. Figure 3.7 shows probable antenna locations and different communication links.

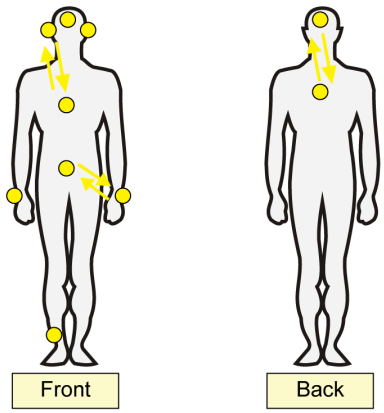

Figure 3.7. Possible antenna locations on a BAN (adapted from [HHNA07]).

[HHNA07] suggests a categorisation of on-body propagation links, according to the parts of the body at which the TX and RX antennas are attached (*e.g.*, trunk-to-trunk, trunk-to-head, trunk-to-limb). Characteristics of the propagation channels are expected to differ according to the link-geometry variability. For example, a trunk-to-trunk link is expected to be more stable than a trunk-to-limb one. Also, a link between two points on the body may be formed by radio waves passing through the tissue, or travelling around the body surface if there is no direct LOS path available.

Most of the work found in literature regarding channel modelling for BANs starts with a simplistic approach, which assumes the inexistence of significant scatterers in the vicinity of the human body. Under this approach, the body can be considered as being isolated in space. In theory, the different propagation mechanisms that could take place in this case are:

- *Direct transmission from the TX to the RX antennas*: In LOS conditions, the transmission will be done in free space, while for NLOS links, waves are transmitted through the body. The wavelength and propagation speed of electromagnetic waves will depend on the material parameters of the propagation medium.
- *Surface waves*: Since the human body consists of several layers of different tissues, surface waves are one possible propagation mechanism. These waves travel along the boundary between two different media and along curvatures.
- *Creeping or surface-diffracted waves*: If the direct path between the transmitter and the receiver is obstructed by an obstacle, electromagnetic waves can travel, at the speed of the light, into the shadow zone behind the obstacle. Shadowing is a very often situation in BANs, not only because of the obstruction of the LOS by the different parts of the

human body, but also because of mechanisms like antenna misalignment or pattern distortion.

- *Reflections and absorption*: Reflections may occur, being caused by the different parts of the body or by phenomena like the natural swinging of the arms or the legs. Absorption is another mechanism that can take place in a BAN link, which will be mainly dependent on the tissues involved in the communication.

When the body is inserted into a multipath environment, it is quite difficult to separate the different propagation mechanisms that can take place. Local scattering can be a source of variability of the channel due to the small propagation distances involved, as the changes in the surrounding environment can be as significant to the channel characteristics as the changes in the channel path length. Specifically, the reflectivity of walls (and objects in the environment) as well as the density of clutter and environments size can be important.

For LOS situations, the main propagation mechanisms are free space propagation and reflections from the different scatterers that compose the external environment. In [FRDD06], it is shown that the received energy due to MPC is significantly smaller than the energy components near the body, thus, it can be ignored.

For NLOS situations, reflections from MPCs should dominate over creeping waves' paths and "help" to increase connectivity. For example, the results obtained in [IEEE08] show that the path loss caused by the presence of the human body often reaches 25 dB in the anechoic chamber, while in a hospital room, where there are reflections from the walls and so on, the path loss due to the human body is less than 10 dB. Anyway, some MPC coming from walls or similar may be of the same order of magnitude than creeping waves [RDMH04].

An usual approach to deal with complex non-stationary wireless channels is to describe them over a small area, where the statistics are approximately stationary (small-scale). Variations in the small-scale statistics over large areas are then investigated separately. For BANs, statistical variations occur not only in terms of geographical areas, but also over strong changes in body posture, antenna alignment, and so on. Even when standing or sitting, the human body is subject to many small movements. In normal activities, movement is significant, becoming extreme during the playing of sports or similar activities. The movement of the parts of the body to which antennas are attached is the main source of variability, being especially severe to the channel when antennas are mounted on the upper members (arms and hands). Also, dramatic changes in the geometry of the local environment are expected to occur. In [HHNA07], propagation measurements show that the variability in path loss due to different antenna placement and due to posture changes can be as much as 50 dB. Due to the fact that

there are several communication paths highly variable with body posture, the authors suggest a combination of channel models, based on the classification of body postures.

For this reason, small-scale statistics in BANs context are due to small changes in location of the on-body device or body positions, in a given short period of time, being also termed as shadowing. Large-scale statistics refer to a large displacement of the body over a geographical area (motion), and also to major changes in the body posture. However, some authors, like [Taka08], state that it may be unfeasible to distinguish between shadowing and multipath fading in a rich multipath environment. Anyway, [FDWB07] suggests that separately analysing the small- and large-scale statistics provide a fairly complete description of the channel for many situations of practical interest and can often lead to simple, physically motivated modelling forms that are more useful for evaluating systems in practice.

3.4 Channel Modelling

When modelling the propagation channel, it is important to study parameters such as path loss, channel impulse response, and associated statistical information, RMS delay spread and power delay profile. [HaHa06] warns to the fact that numerical simulation tools, FDTD in particular, are very useful to obtain parameters such as average path loss or power delay profile, but they may not be suited for precise statistical information on these parameters. On the other hand, it is suggested that properly designed measurement campaigns can provide accurate parameters of this complex propagation channel, including realistic radio environments, various antenna designs, and user dynamics.

Several attempts to model path loss in BANs are found in literature. The main concern here is that the antenna–body interaction is an integral part of the channel, so that it is unrealistic to separate them. Moreover, further differences are found on the models used in traditional wireless communication systems, such as the influence of the user, the short distances between TX and RX antennas, as well as arbitrary orientation of antennas.

In practice, it is of general consensus that the main propagation mechanism dominating LOS links in BANs is free space transmission. Most of the LOS links follow the free space curve already expressed in (2.3), but are generally below it [HHNA07]. For example, [HHNA07] reports that the LOS measurement points, obtained at 2.45 GHz for a BAN with 14 sensors both in front and back of a body - with a 10 mm separation between the antenna and the body - follow the free space curve, being below it with a mean difference of -5.1 dB. The standard

deviation of the difference between the measured LOS values and those given by this model was 4.2 dB.

[Taka08] has derived a model for L_p similar to the free space one, supported by measurements of different LOS links at [400, 450] MHz, [608, 614] MHz, [950, 956] MHz, [2.4, 2.5] GHz and [3.1, 3.5] GHz, with a 15 mm separation between body surface and antenna:

$$L_{p[\mathrm{dB}]} = -129.4+46.5\log\left(f_{[\mathrm{MHz}]}\right)+27.6\left(d_{[\mathrm{cm}]}\right) \tag{3.4}$$

where

- 15 cm $< d <$ 100 cm;
- 400 MHz $< f <$ 2500 MHz.

As a general law, for LOS links, the average L_p could be modelled by the usual power decay law referred in (2.4). Some approaches following this law, with $\Delta L_p = 0$, were found in literature, being summarised in Table 3.1. The parameters for this model are generally obtained from measurements. Note that these parameters correspond to propagation on different parts of the body, and also to different antenna-body separations.

Table 3.1. Parameters for power decay law in LOS (free space).

Propagation	**Antenna-Body Separation [mm]**	$L_{p_{d_0}}$ **[dB]**	α	f **[GHz]**	**Reference**
Front of the body	10	5.33	2.0	2.45	[HHNA07]
Around the torso	0	-1.90	5.8	[3, 6]	[FRDD06]
	5	-10.60	5.9		
	10	-14.20	6.0		
Front of the body	0	26.50	3.1	[3, 6]	[FDRD05b]
	5	19.50	3.1		
Front of the body	0	16.00	3.3	[3, 6]	[ZASW03]

It is interesting to note that, in the GHz range, the path loss exponent near the body ($\alpha = 6$) is much higher than the free space one ($\alpha = 2$). This result is consistent with former gigahertz studies around the human torso, where α is estimated between 5 and 7.4 [FDRD05a], [FDRD05b], [LVMM04]. Lower exponents, with α between 2 and 3 are reported when propagation is along the front rather than around the torso. Also, [RJVM07] observed that this exponent is almost the same along the front and along the arm.

Other interesting observation is that $L_{p_{d_0}}$ is affected by the antenna-body separation. This

occurs because of the strong interactions between the antenna and the body, which affect antenna radiation pattern and impedance mismatch. As shown in Table 3.1, higher path losses are measured when the antenna is closer to the body.

Contrary to Table 3.1, some authors consider the shadowing effect, where the received power is different from the mean value for a given distance. The shadowing reflects the path loss variation around the mean, resulting not only from obstruction of LOS by some part of the human body due to natural movements, but also from antenna misalignment, pattern distortion or impedance mismatching

[Taka08] argues that the shadowing mechanism can be modelled by a Log-Normal Distribution. Also, in [IEEE09], from the IEEE P802.15 Working Group for Wireless Personal Area Networks, the authors consider that shadowing is a normally distributed variable with zero mean. Following this trend, [IEEE09] derives a path loss model, based on measurements covering the frequency bands of 400 MHz, 600 MHz, 0.9 GHz, 2.4 GHz and [3.1, 10.6] GHz, with a 15 mm separation between body surface and antenna, [IEEE08]. ΔL_p is assumed to be a normally distributed variable, with zero mean. The parameters for the model, obtained at different frequencies in anechoic chamber measurements, are given in Table 3.2.

Table 3.2. Path loss parameters, with 15 mm body-antenna separation (adapted from [IEEE09]).

f [GHz]	0.4	0.6	0.9	2.4	[3.1, 10.6]
α	2.26	1.72	2.88	2.93	3.41
$L_{p_{d_0}}$ [dB]	14.75	18.81	5.30	12.50	2.96
ΔL_p [dB]	5.60	6.96	11.70	6.89	4.85

Some authors have enhanced path loss models that include, for example, the natural arm swinging. [FDRD05b] has measured the influence of arms motion on path loss, considering a simple model on which arms are moved to the front or side of the body in increments of 10º. It was shown that, while arms motion to the side do not impact on communication when both TX and RX are on the front of the body, the same is not verified when the arms are moving in the front of the body. Specifically, reflections from the arms can be seen when they are positioned in [40º, 70º] in front of the body, arriving later as the arms are moved towards the torso. Also, arms can significantly influence the received energy if they are moved such that the LOS path between the TX and RX is shadowed. From the results for stationary and swinging arms, authors have concluded that the Lognormal and Nakagami Distributions are plausible to describe the received energy fluctuation due to arm motion.

For LOS situations in multipath scenarios, the standard decay law defined in (2.4) can be used with the proper parameters. Table 3.3 presents some examples, based on measurements from

[ZASW03] and [IEEE09].

Table 3.3. Parameters for power decay law in LOS (multipath environment).

Propagation	**Antenna-Body Separation [mm]**	$L_{p_{d_0}}$ **[dB]**	α	f **[GHz]**	**Reference**
Front of the body	0	21.80	2.70	3 - 6	[ZASW03]
Front of the body	15	37.60	0.30	0.4	[IEEE09]
		16.25	1.67	0.6	
		20.88	1.55	0.9	
		42.70	0.66	2.4	
		22.58	1.92	[3.1, 10.6]	

It is interesting to note that, compared to anechoic chamber, lower decay exponents are obtained in multipath environments. This is due to the reflecting nature of these scenarios, in contrast with anechoic chamber situations, where higher exponents are found due to their non-reflecting nature.

It is also of interest to study path loss under NLOS conditions, which is an often common situation in BANs, as sensors may be located in parts without visibility between themselves, *e.g.*, the TX in the heart and the RX in the back. NLOS can also happen because of shadowing due to movement of body parts, or because of mechanisms like antenna misalignment or pattern distortion. It has been shown by different authors that creeping waves are the dominant propagation mechanism while in NLOS.

For example, in [ZMAW06], an ear to ear UWB link was studied. After discarding the hypothesis of direct transmission through the head, of propagation of surface waves or of reflections and absorption through the head, the authors concluded that diffraction around the head is the dominant mechanism. This conclusion is not only supported by the fact that the other propagations mechanisms were discarded, but also because path delays correspond to the distances on the head surface, and furthermore, both measurements and calculations show attenuations of same order of magnitude. In Figure 3.8, one can observe the simulation results from this work, with the TX antenna located in the left ear and the RX in the right one. It can be observed that, although a portion of the transmitted power radiates into the head, waves are severely attenuated and the field is diffracted around the head.

The creeping wave propagation mechanism is not only valid for transmission around the head, but also for transmission around the torso. In Figure 3.9, the simulated E field around a body slice in the GHz range, obtained by [FDRD05a], can be observed. One can see that very little

energy is inside of the body, instead, the wave is diffracting around the torso rather than passing through it.

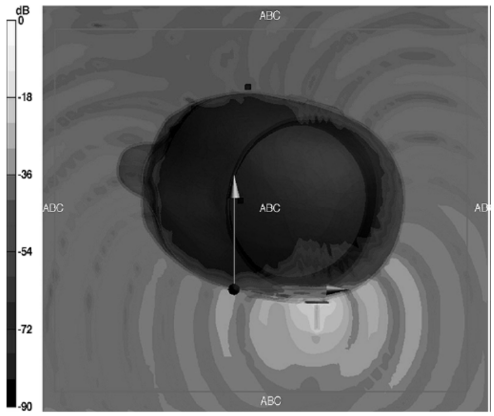

Figure 3.8. Field strength for a head phantom (extracted from [ZMAW06]).

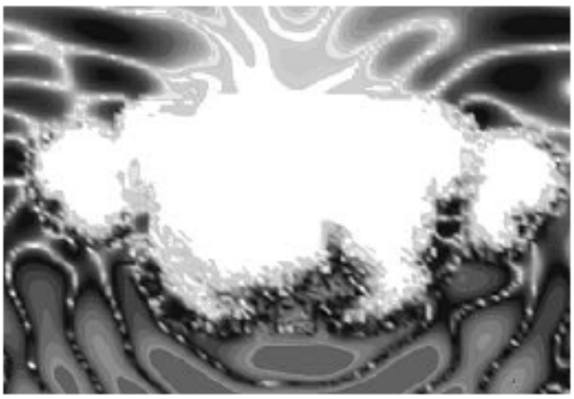

Figure 3.9. Field strength around a body slice (extracted from [FDRD05a]).

The distance variation of creeping waves is fairly complex, depends on a number of parameters, and is different on the free space sections of the propagation path and on the sections conformal to the body [HHNA07]. Although it is unfeasible to trace and model all propagation paths around the human body, NLOS points appear to experience an exponential attenuation of the type:

$$L_p(d)_{[\mathrm{dB}]} = L_{p_{d_{0\,[\mathrm{dB}]}}} + \alpha_{[\mathrm{dB/cm}]} d_{[\mathrm{cm}]} + \Delta L_{p[\mathrm{dB}]} \tag{3.5}$$

Table 3.4 indicates the values of these parameters, obtained by some authors through measurements of NLOS paths, with $\Delta L_p = 0$.

From the analysis of NLOS propagation mechanisms, [TTHI08] notes that the dielectric separation between the antenna and the body improves the link, decreasing L_p - similar to what happens in LOS links - and leading to higher decay rates.

For the case of a body in free space, most of the authors propose a dual slope model for NLOS propagation around the body, whose parameters generally come from linear regression of

measurements. The physical interpretation of this model has to do with two creeping waves that travel around the body in opposite directions. For instance, the authors in [HHNA07] investigated the variation of the signal strength around a human torso. It was found that it attenuates exponentially with the distance, confirming the creeping wave character of propagation. The decay factor depends on the loss in dielectric, with higher attenuations for higher frequencies. Two curves for channel gain were obtained, with a crossover point between them being approximately diagonally opposite to the TX antenna.

Table 3.4. Parameters for power decay law in NLOS.

Antenna-Body Separation [mm]	$L_{p_{d_0}}$ **[dB]**	$\boldsymbol{\alpha}$ **[dB/cm]**	$\boldsymbol{f}$ **[GHz]**	**Reference**
10	35	0.360	2.45	[HHNA07]
0	88	1.667	[3, 11]	[TTHI08]
12	60	2.225		

[HHNA07] has also studied the variability of path loss around the chest due to breathing, as it causes the chest cavity to expand and contract, thus, changing the interference between the two opposite travelling creeping waves. Signal variations of about 14 dB were observed, in consistence with measurements in some static positions.

In [LiDO08], a refined propagation model is proposed for the frequency band of 2.45 GHz, being based on a human body model, with natural arm swinging. This model considers three propagation paths: one reflected by the left arm, another reflected by the right arm, and a third one around body trunk. The model distinguishes between LOS and NLOS scenarios. In LOS, the reflected propagation paths are viewed as free space propagation, multiplied by the reflection coefficient of the arms. For NLOS, the propagation paths are combined by the tangent free space propagation path from the arm centre to the ellipse, and the creeping wave from the tangent point to the destination.

The exponential loss and the dual slope-exponential loss models for NLOS situations do not incorporate the influence of the surrounding environment. In the draft document [IEEE09], a refined path loss model for large-scale fading is proposed for propagation around the body, in the 0.9 GHz and 2.45 GHz bands, for a 5 mm body-antenna separation, according to the experiments from [FDWB07]. It is a combined exponential-linear saturation model, representing the exponential decay with distance (expected because of diffraction around a cylindrical body), followed by a flat saturation point due to energy received from multipath reflections off nearby scatterers. For distances smaller than 30 cm, energy is diffracted around the body. For distances greater than 30 cm - corresponding to propagation to the opposite side of the body - path loss flattens due to energy received from nearby scatterers.

For the small-scale fading statistics, the same authors propose a Ricean Distribution with a K factor that decreases as path loss increases. When the TX and RX are on opposite sides of the body, where multipath reflections from the surrounding environment are dominant, it approaches the Rayleigh Distribution. Also, both the mean and standard deviation increase with antenna separation, as more energy is concentrated on the reflected MPCs.

Studies like [HaHa06] show that there is a significant multipath on the body at 2.45 GHz, in an anechoic chamber. For example, simulation results from a signal transmitted in the front of the body and received in the back show that signals arrival at three different times, corresponding to reflected waves in different parts of the body. Extended measurements showed that the strong signals were arriving from the shoulders, the waist and from between the legs, whose path delays associated to their physical lengths correspond well with the timings noted in the received signal. In [RDMH04], the authors analysed the propagation delays around the torso, considering that, in the interference region, the two creeping waves propagating around the body are temporally irresolvable at the RX, thus a single path model is used to estimate the RMS delay spread. The delay for a creeping wave to travel from the sternum to the spine is simulated to be about 1.8 ns, close to the delay in free space for a dielectric coated cylinder.

Because of multipath reflections - caused from both reflections from the body and the external environment - the channel response of a BAN may look like a series of pulses. [HHNA07] states, however, that it may be difficult to determine time delays of on-body propagation paths: they can be estimated from the dimensions of the body, or by simulations. [RDMH04] notes that, if a body is placed in an indoor environment (*e.g.*, a medium sized room), some reflected rays would arrive at the RX together with the creeping wave. The given example of a ray, transmitted at the chest, and arriving at an RX in the spine at the same time than a reflected ray by a wall located at a few meters, suggests that in the estimation of the delay spread of an indoor BAN, the creeping wave must be seen as an extra path in the CIR. As the creeping wave arrives to the RX sooner than the first MPC, adding the creeping wave path to the CIR of a typical indoor channel results in an increase of the RMS delay spread from 37 to 57 ns.

In [IEEE08], the measured channel transfer functions obtained for the 0.4 GHz, 0.6 GHz, 0.9 GHz, 2.4 GHz and UWB frequencies show that all bands, except the UWB one, have flat responses. This means that these bands only require a path loss model, while the UWB one – which shows highly frequency selective channels - requires not only a path loss model, but also a power delay profile one.

Based on UWB measurements, [ZMAW06] derived an approximation of the average PDP for an ear to ear link, and calculated values for the mean excess delay and delay spread. The

obtained average PDP for all measurements shows two ranges with different linear decays. The first range - where most of the energy is concentrated and PDP is decaying relatively steeply - corresponds to transmission around the head. In the second range, 4 ns after, the linear decay gets flatter, probably because of the reflections from the body or from imperfections of the anechoic chamber absorption material. The mean excess delay and the delay spread, averaged over all measurements, are 2.1 ns and 1.5 ns, respectively.

On the other hand, the authors in [FRDD06] propose a dual slope model for propagation around the body, where the first group of clusters decays slowly than a second one. This model is based on the average trend across all performed measurements. When considering individual PDPs, multipath components appear to decay exponentially within each cluster.

Simulation results in [RDMH04] show that the delay for a creeping wave travelling from the sternum to the spine is about 1.8 ns. This means that, if a body is placed in an indoor environment, some reflected rays would arrive at the receiver together with the creeping wave. Thus, in the estimation of the delay spread of an indoor BAN, the creeping wave should be seen as an extra path in the impulse response of the channel.

The time-variant multi-link BAN channel has been well studied by measurements, [ATTK12], [VQLO12], [LDOD11]. The authors in [ATTK12] measured the temporal fluctuations of on-body propagation between six antenna positions during motion. The correlation coefficients, averaged among all movements, were found to be lower than 0.3. In [VQLO12], a channel model for a dynamic multi sensor BAN is derived from an extensive measurement campaign. Besides other parameters, the correlations between the different links were analysed, and were shown to be high, especially for the placements on the limbs. The authors in [LDOD11] observed that the dynamic local body scattering dominates the temporal and spatial properties of the on-body channels. The shadowing correlation is relatively higher when the user is static than when he/she is moving.

The study of body dynamic in BANs via full wave simulations is still in an early stage. The introduction of user's mobility using real motion capture models was previously achieved by [GHBN11] or [AIKT11]. These works use very simple body models, and the analysis of results is restrained to the path gain for selected on-body channels. Still, the authors in [GHBN11] prove that this approach, combining animation software with full wave simulations, allows characterising the long term channel fading.

3.5 Channel Diversity / Cooperative Techniques

The use of cooperative techniques in BANs is a natural strategy to save power, increase the connection reliability, and overcome the effects of deep fading [ReTa12], [DERM11]. Virtual MIMO or Multi-Sensor MIMO (MS-MIMO) is one of the options, using clusters of nodes, on the TX or/and RX sides, then combining multiple independent paths to behave like multi-antennas systems.

It is well known that MIMO performance highly depends on the correlation between the contributing channels, and on their power distribution (SNR). The use of multiple antennas is a good solution to increase the capacity of a network, although in BANs the small space in between antennas increases the correlation among the sub-channels, especially for LOS branches. The better performance will be obtained by statistically independent channels with equal average power. Generally, the difference in SNR should be below 10 dB and the correlation below 0.7 [VaAn87].

The use of MIMO in BANs has been studied essentially through measurements, held at anechoic chamber, office, or lab environments, *e.g.*, [GKHH12], [KhUH11], [KHNA10], [KhHa10]. Measurements overcome the problem of intensive computation demands required by simulations, but have some other drawbacks, as the reliability, prohibitive resource requirements or repeatability. This last issue is addressed in [KHGN08], where small, but acceptable, errors were found for most cases.

The authors in [KYNH07] analyse the performance of space and pattern diversity techniques. A higher correlation is found in an anechoic chamber or larger office than in lab environments, naturally resulting from the small number of scatterers. Correlation is very high for static and LOS channels, suggesting that dynamic channels are more suitable for diversity. The authors strengthen that the relationship between diversity gain and the correlation coefficient is not straightforward, as power imbalance has also a great impact.

In fact, the authors in [ChTa08] support that the MIMO channel capacity is mainly determined by the power imbalance between sub-channels, as for short range communications the power difference among elements in spatial arrays is significant. When the spacing between antennas is increased, some sub-channels have so low received power that they do not contribute to the MIMO channel capacity, even if they are uncorrelated. The same authors found that MIMO capacity is slightly dependent on the environment, due to the dominant body effect (for UWB systems).

The authors in [KhUH11] studied the correlation and power imbalance among three on-body

channels, and analysed the performance of different diversity configurations (1×2, 2×1, 2×2), for a moving user in a scattering indoor environment (at 2.45 GHz). Despite of the high imbalances obtained, significant gains are achieved with 2×2 MIMO for belt-head and belt-wrist channels. A capacity penalty, compared to the Rayleigh channel, is observed in belt-head and belt-chest channels by the authors in [GKHH12], due to the strong LOS component.

From the measurements performed in [CCSc09] it is concluded that, at 2.45 GHz, the local environment is a major contributor to the fading observed in dynamic on-body channels. For static measurements, the correlation between on-body sensors is generally strong, in contrast with the dynamic scenario, where no significant correlation is found. When the user is moving in large environments (*e.g.*, open office and hallway), correlation approached zero. Similar conclusions are taken at 868 MHz [CoSc07a], where the cross-correlation values are measured for NLOS on-body receiving antennas mounted on the upper torso, with an external TX, in indoor environments. Correlation values when the human is mobile do not exceed 0.6, being equal to zero in some branches (*e.g.*, left abdomen and right arm or left arm and back right).

In [KhHa10] and [KHNA10], the correlation in a 2×2 MIMO system is measured, when random movements are performed in an indoor environment. Small values are found, except for the belt-chest channel, for which correlation is moderate. The body movement and the relative TX/RX movements significantly decorrelate the channels. Despite the correlation between the sub-channels, a significant capacity increase due to use of MIMO was still observed. The average capacity increase is near to the 2 bps/Hz with every 3 dB increase of SNR for the belt-head and belt-wrist channels, for which the correlation is relatively low.

The author in [Wang08] analyses the influence of shadowing standard deviation, shadowing correlation and branch power imbalance on the MIMO channel capacity, by both numerical and experimental studies. The shadowing standard deviation determines the distribution of the channel power, and consequently it is dominant to the channel capacity. Antenna diversity gains for body shadowing mitigation can be achieved when the shadowing correlation between the antennas is low. Therefore, the shadowing correlation affects the outage capacity significantly. The same author studies the performance of UWB-MIMO systems in BANs, showing the dependency upon the spatial correlation properties among transmission links. The spatial correlation properties of MIMO radio channels in such scenarios are also expected to be time variant because of the user movements.

Cooperative mechanisms, like the ones used in wireless sensor networks, are possible for BAN communications: relay channel, multi-hop and virtual MIMO, as illustrated in Figure 3.10.

The relay channel can be applied when communication has to be established between body

front and back, [GGSV09], using the relay node to retransmit the message to destination. The relay channel consists of using a relay (or more) to retransmit the message of a source to a destination. Cooperation is performed at the physical layer, so that no routing is used.

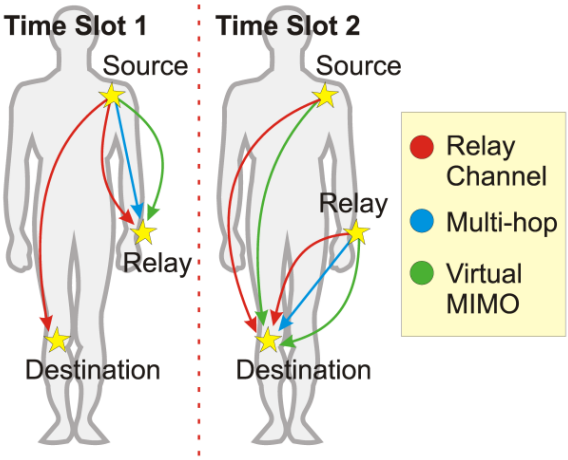

Figure 3.10. Cooperation Mechanisms in BANs.

The multi-hop technique transforms the star topology into a mesh network of on-body sensors. In spite of the robustness of this method, [GGSV09] argues that this approach is not appropriate for the case of BANs, as it corresponds to a serial transmission and all paths support the same path-loss.

Still, [WADB07] proposes a multi-hop protocol for BANs, with a self-organised structure made of clusters, that can facilitate finding a multi-hop path between source and destination, reducing the load of the network by performing data aggregation, and reducing energy consumption by turning off redundant nodes.

Virtual MIMO or MS-MIMO consists of using clusters of nodes, on the TX or/and RX sides, to behave like multi-antennas systems. Also, MIMO applied to BANs can increase the connection reliability and overcome the effects of deep fading by combining multiple independent fading paths. In off-body and body-body communications, MIMO can be applied in order to reject interference from nearby BANs. This method offers the highest theoretical capacity, however, the practical deployment can be constrained by the need for fine synchronisation and complex distributed coding methods.

Another approach is the combination of MS-MIMO systems with UWB transmissions, which is expected to minimise transmit power requirement and to increase battery lifetime of the body-worn sensors, [ROHD10].

Chapter 4

Models for Antenna-Body Interaction

This chapter presents the proposed models used to analyse the interaction between antennas and the body. In Section 4.1, the concept of antenna-body interaction is introduced, claiming a statistical approach for modelling antennas' behaviour in the vicinity of the body. Section 4.2 details the analytical models firstly used for the general understanding of the behaviour of a plane wave, and of a simple radiation source, near the body. Section 4.3 reviews the main features of the numerical full wave simulation tool *CST Microwave Studio*, used to analyse the antenna-body interaction with a real patch antenna.

4.1 Concept

The concept of a statistical model for the on-body antenna is claimed, as the presence of the user leads to modifications of the antenna performance, for instance, on the radiation pattern, the resonance frequency or the input impedance, as well as on its efficiency. The antenna performance strongly depends on the distance to the body, as well as on the placement. Thus, a statistical description of the on-body antenna is required, based on a practical scenario of a BAN, where the distance to the body can vary in time. For instance, the average variations of radiation patterns in given directions are one of the possible outcomes from this concept.

Figure 4.1 illustrates the idea of the statistical antenna model, identifying the different inputs (antenna model, body/part of the body, antenna-body distance distribution). From the set of radiation patterns obtained at the different distances of the antenna to the body, the outputs of the model are the statistics of the on-body antenna model:

- Average radiation pattern;
- Standard deviation of the radiation pattern.

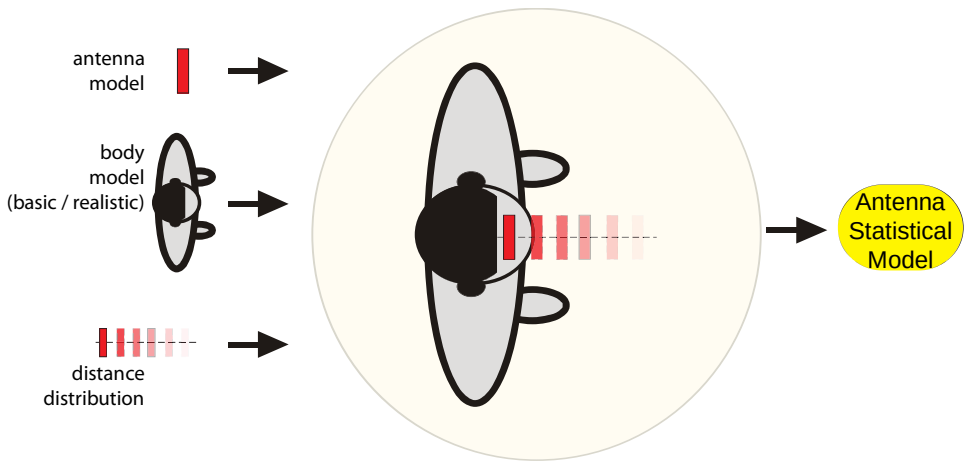

Figure 4.1. Modelling of antenna-body interaction.

The calculation of the antenna statistics is performed according to the distribution of the distance to the body. The distribution should be defined according to the needs of each particular scenario. For instance, uniformly distributed distance samples can be assumed if one wants to observe the trend in a given range, while other distributions can be defined by the features of the antenna location on the clothes, being concentrated on a central value (*e.g.*, "locally" Rayleigh).

The concept of the statistical on-body antenna can be applied to a full body model, or just to an explicit body part (*e.g.*, head, arm). The idea is that the statistical model describes the ranges of changes locally.

The concept of antenna statistical modelling can be included in radio channel simulators for BANs, the average and the standard deviation of radiation patterns being used to calculate multipath components. Although the calculated statistical radiation patterns are antenna dependent, the method can be applied for others, and it is generally usable.

The implementation of this concept for modelling the antenna-body interaction is firstly realised by using very simple and well known theoretical wave propagation models, like the plane wave and the elementary source analytical models. Herein, a basic 2D shape (circular cylinder) is used to model different parts of the body. As analytical models are confined to very basic geometries, the method is also applied in a full wave simulator, considering a realistic antenna (patch), radiating near a voxel model (or parts of it, *e.g*, head/arm/leg).

Table 4.1 summarises the implementation of the antenna-body interaction model, for each model the different inputs and outputs being identified, as well as the simulation tool.

Table 4.1. Implementation of the antenna-body interaction model.

Model	**Simulation Tool**	**Inputs**	**Outputs**
Plane Wave	*Matlab*	Frequency; Body model: dielectric cylinder; Wave polarisation: TE/TM; Square area of observation.	Electromagnetic fields distribution: average, standard deviation, range.
Elementary Source	*Matlab*	Frequency; Body model: dielectric cylinder; Source polarisation; Source/Body distance distribution.	Radiation patterns at different distance samples. Statistics of the patterns: average, standard deviation, range. Evaluation parameters.
Numerical Model	*CST*	Body model: voxel; Patch antenna; Antenna-body distance distribution.	Radiation patterns at different distance samples. Statistics of the patterns: average, standard deviation, range. Evaluation parameters.

A measurement campaign was also conducted to complement the study, as it deals with the whole complex on-body channel, naturally including the user dynamics.

4.2 Analytical Models

4.2.1 Plane Wave

The incidence of a plane wave on an infinitely long homogenous dielectric circular cylinder is a classic problem of electromagnetism, whose solution was given many years ago, [Wait59]. Figure 4.2 shows the geometry of the problem, in a cylindrical coordinate system (ρ,φ,z). A plane wave, coming from the x direction, with the E field polarised in the y one (TE incidence), is normally incident on a dielectric circular cylinder of radius a. The complex permittivity is ε for the outside medium (air), and ε_1 for inside of the cylinder. The permeability in both regions is equal to that of free space, so that $\mu_1 = \mu = \mu_0$.

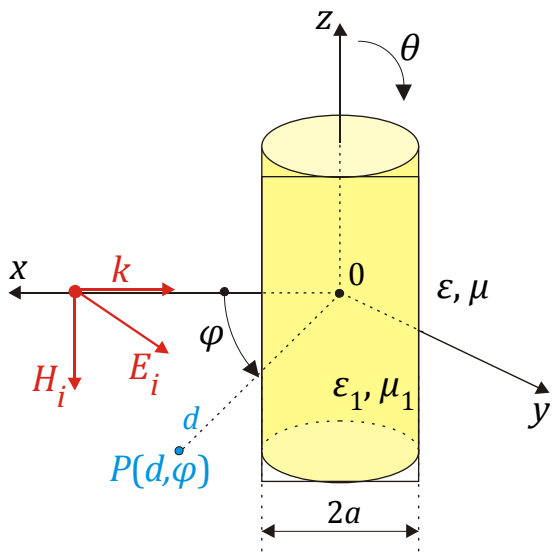

Figure 4.2. Geometry for a normal plane wave incidence on the cylinder.

Using the canonical forms given by [Wait59], the total magnetic (H_t) or electric fields (E_t), for the TE and TM modes, respectively, are calculated on an observation point $P(d, \varphi, 0)$, in the region external to the cylinder. For a TM incident wave, with amplitude A, the field solution outside the cylinder is given by:

$$E_t(A, \varepsilon, \mu, \varepsilon_1, \mu_1, a, d, \varphi, f) = E^i(A, \varepsilon, \mu, d, \varphi, f) + E^s(A, a, \varepsilon_1, \mu_1, d, \varphi, f)$$

$$= A \sum_{n=-\infty}^{+\infty} j^n J_n(kd) F_n(\varphi) + \sum_{n=-\infty}^{+\infty} a_n^s H_n^{(2)}(kd) F_n(\varphi) \qquad (4.1)$$

where

- E^i and E^s are the incident and the scattered fields, respectively;
- j is the imaginary unit;
- J_n and $H_n{}^{(2)}$ are n-th order Bessel and 2nd kind Hankel functions, respectively;

- $F_n(\varphi) = e^{-jn\varphi}$ (4.2)
- $a_n^s = -A\left[\dfrac{\frac{N^2 J_n'(u)}{KuJ_n(u)} - \frac{J_n'(v)}{vJ_n(v)}}{\frac{N^2 J_n'(u)}{KuJ_n(u)} - \frac{H_n^{(2)\prime}(v)}{vH_n^{(2)}(v)}}\right]\dfrac{J_n(v)}{H_n^{(2)}(v)}$ (4.3)
- $u = k_1 a$ (4.4)
- $v = ka$ (4.5)
- $k = \sqrt{\varepsilon_0\mu_0}\omega$ (4.6)
- $k_1 = \sqrt{\varepsilon_{1r}}k$ (4.7)
- $\varepsilon_{1r} = \varepsilon_1/\varepsilon_0$ (4.8)
- $N^2 = k_1^2/k^2$ (4.9)
- $K = \mu_1/\mu$ (4.10)
- $J_n{}'$ and $H_n{}^{(2)\prime}$ are the first derivates of J_n and $H_n{}^{(2)}$.

4.2.2 Elementary Source

A general understanding of the behaviour of a simple radiation source near the body can be obtained through very simple propagation models, considering different source orientations.

Considering the communication scenario between two on-body sensors, for example, the TX antenna is placed on the arm, while the receiving one is on the torso, the radiated signal may be approximated by the wave generated by an elementary electric source (*i.e.*, a Hertz dipole) located near a dielectric circular cylinder. This problem requires a non-trivial solution involving extensive integral computations; however, a much simpler method to obtain the radiation pattern in such conditions has been proposed in [Lytl71], and can be used for this scenario.

The author uses the principle of reciprocity [Week64] in conjunction with the scattering of a plane wave from a dielectric circular cylinder at oblique incidence to determine the radiation pattern for the elementary electric source for three orthogonal directions u_ρ, u_φ and u_z, in a cylindrical coordinate system, Figure 4.3.

For BAN communications, one can consider a further simplification, by confining the problem to the horizontal plane ($\theta = 90^{\circ}$). It is assumed that the TX is located in the x-y plane, positioned at $P(d,0,0)$, external to the cylinder ($d > a$). The observation point is positioned at $P(d,\varphi,0)$. The solutions for the different orientations of the elementary source are given by:

- u_ρ orientation:

$$\begin{cases} E_\theta = 0 & (4.11) \\ E_\varphi(A,\varepsilon,\mu,\varepsilon_1,\mu_1,a,d,\varphi,f) = \displaystyle\sum_{n=-\infty}^{+\infty}\left[-\left(\frac{\varepsilon}{\mu}\right)^{\frac{1}{2}}\frac{nj^n}{\omega\varepsilon d}J_n(kd) - \frac{n\bar{a}_n^s}{\omega\varepsilon d}H_n^{(2)}(kd)\right]F_n(\varphi) & (4.12) \end{cases}$$

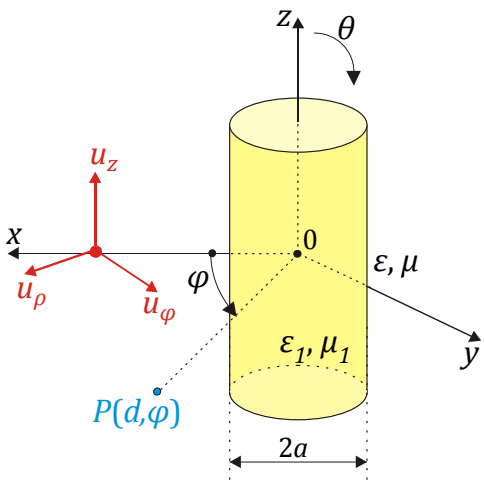

Figure 4.3. Geometry for an elementary source near a dielectric circular cylinder.

- u_φ orientation:

$$\begin{cases} E_\theta = 0 & (4.13) \\ E_\varphi(A,\varepsilon,\mu,\varepsilon_1,\mu_1,a,d,\varphi,f) = \sum_{n=-\infty}^{+\infty}\left[\left(\frac{\varepsilon}{\mu}\right)^{\frac{1}{2}}\frac{jk}{\omega\varepsilon}j^n J'_n(kd) + \frac{jk}{\omega\varepsilon}\bar{a}_n^s H_n^{(2)\prime}(kd)\right]F_n(\varphi) & (4.14) \end{cases}$$

- u_z orientation:

$$\begin{cases} E_\theta(A,\varepsilon,\mu,\varepsilon_1,\mu_1,a,d,\varphi,f) = \sum_{n=-\infty}^{+\infty} j^n J_n(kd)F_n(\varphi) + \sum_{n=-\infty}^{+\infty} a_n^s H_n^{(2)}(kd)F_n(\varphi) & (4.15) \\ E_\varphi = 0 & (4.16) \end{cases}$$

where

- $F_n(\varphi) = e^{-jn\varphi}$ (4.17)
- $\bar{a}_n^s = \left(\frac{\varepsilon_0}{\mu_0}\right)^{1/2}\frac{J'_n(v)}{J_n(v)}a_n^s$ (4.18)

4.3 Numerical Model

CST Microwave Studio is the numerical simulation tool chosen for the implementation of the on-body antenna statistical model. *CST* satisfies the main requirements, like the import of human voxel models, the use of realistic antenna, or the calculation of 3D radiation patterns, s-parameters and time signals. Besides, there was already previous experience in this tool, and a license was available at IST.

CST is a Windows based commercial software for accurate simulation of high frequency problems, using FIT [Weil77]. FIT is a numerical method that performs a spatial discretisation, in the time or frequency domains, of the integral form of Maxwell's equations, instead of the usual differential one.

The integral form of Maxwell's equations is reminded below [Sadi00]:

$$\oint_{\partial A} \mathbf{E}.d\mathbf{s} = -\oint_{A} \frac{\partial \mathbf{B}}{\partial t} \cdot d\mathbf{A} \tag{4.19}$$

$$\oint_{\partial A} \mathbf{H}.d\mathbf{s} = \int_{A} \left(\frac{\partial \mathbf{D}}{\partial t} + \mathbf{J}\right) \cdot d\mathbf{A} \tag{4.20}$$

$$\oint_{\partial V} \mathbf{D} \cdot d\mathbf{A} = \int_{V} \rho_e \, dV \tag{4.21}$$

$$\oint_{\partial V} \mathbf{B} \cdot d\mathbf{A} = 0 \tag{4.22}$$

where

- $\mathbf{E}$ is the electric field vector;
- $\mathbf{s}$ is an infinitesimal vector element of the closed contour ∂A;
- $\mathbf{B}$ is the magnetic induction field vector;
- $\mathbf{A}$ is a surface vector bounded by the closed contour ∂A;
- $\mathbf{H}$ is the magnetic field vector;
- $\mathbf{D}$ is the electric displacement field;
- $\mathbf{J}$ is the current density vector;
- V is the volume of integration;
- ρ_e is the electric charge volume density.

FIT solves these equations numerically, according to the scheme of Figure 4.4. Initially, a finite calculation domain is defined, enclosing the space region of interest. After that, this domain is split into orthogonal grid cells (hexahedral shape is used), creating a suitable mesh system. Maxwell's equation are discretised and solved in each cell. For the complete discretisation of Maxwell's equations in each single cell facet, two dual grid systems are required, the primary grid $\mathbf{G}$ and the secondary dual one $\widetilde{\mathbf{G}}$. The primary grid contains the electric grid voltages $\mathbf{e}$ and the magnetic facet fluxes $\mathbf{b}$, while the secondary dual one allocates the dielectric facet fluxes $\mathbf{d}$ and the magnetic grid voltages $\mathbf{h}$.

The discretisation of Maxwell's equations is performed as follows. In Faraday's law, (4.19), the closed integral on the equation's left hand side can be rewritten as the sum of four electric grid voltages, while the time derivative of the magnetic flux defined on the enclosed primary cell facet represents the equation's right hand side. The repetition of this procedure for all cell facets introduces the topological matrix $\mathbf{C}$, as the discrete equivalent of the analytical curl

operator.

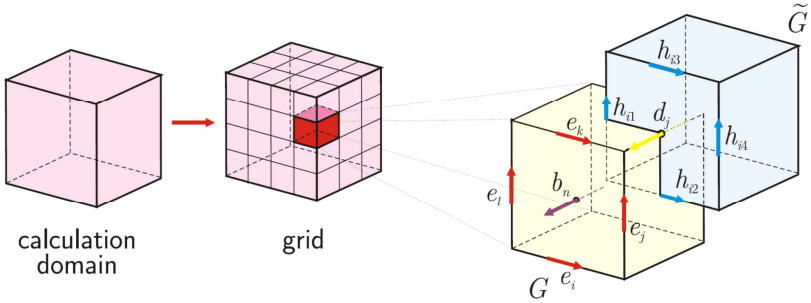

Figure 4.4. FIT spatial discretisation scheme (adapted from [CSTe12]).

The second discrete differential operator is the divergence one, (4.22), which describes the non-existence of magnetic charges within a cell volume. The evaluation of the surface integral yields a sum of six magnetic facet fluxes with different orientations, that when expanded to the whole cell complex creates the discrete divergence matrix $\mathbf{S}$. This matrix depends only on the grid topology, just as the discrete curl-matrix $\mathbf{C}$.

By analogy, the discretisation of Ampére's law, (4.20), is performed by summing up the magnetic grid voltages in order to obtain the displacement current and the conductive current through the considered cell facet. Finally, Gauss' law can be discretised for the dual grid cells, resulting in matrix equations featuring the topological grid operators $\tilde{\mathbf{C}}$ for the dual discrete curl and $\tilde{\mathbf{S}}$ for the dual discrete divergence.

For the cell complex pair $\{\mathbf{G}, \tilde{\mathbf{G}}\}$, the complete set of discretised matrix *Maxwell's Grid Equations* (MGE) is given by:

$$\mathbf{Ce} = -\frac{d}{dt}\mathbf{b} \tag{4.23}$$

$$\tilde{\mathbf{C}}\mathbf{h} = -\frac{d}{dt}\mathbf{d} + \mathbf{j_c} \tag{4.24}$$

$$\tilde{\mathbf{S}}\mathbf{d} = \mathbf{q} \tag{4.25}$$

$$\mathbf{Sb} = 0 \tag{4.26}$$

where

- $\mathbf{j_c}$ is the current density flux matrix;
- $\mathbf{q}$ is the electric charges matrix.

The matrix equations for the electromagnetic integral quantities obtained by FIT ensure a positive stability and convergence behaviour in the numerical implementation, as the intrinsic properties of Maxwell's equations with respect to charge and energy conservation are kept.

To complete the solution of the electromagnetic field problem on the discrete grid space, the

material relations in matrix form are required:

$$\mathbf{D} = \varepsilon \mathbf{E} \qquad \mathbf{d} = \mathbf{M}_{\varepsilon}\mathbf{e} \tag{4.27}$$

$$\mathbf{B} = \mu \mathbf{H} \quad \Rightarrow \quad \mathbf{b} = \mathbf{M}_{\mu}\mathbf{h} \tag{4.28}$$

$$\mathbf{J} = \sigma_c \mathbf{E} + \mathbf{J}_S \qquad \mathbf{j_c} = \mathbf{M}_{\sigma_c}\mathbf{e} + \mathbf{j}_S \tag{4.29}$$

where

- $\mathbf{M}_{\varepsilon}$ is the permittivity matrix;
- $\mathbf{M}_{\mu}$ is the permeability matrix;
- $\mathbf{J}$ is the current density;
- $\mathbf{J}_s$ is the surface current density;
- $\mathbf{M}_{\sigma_c}$ is the conductivities matrix;
- $\mathbf{j}_s$ is the surface current density flux matrix.

It is worth noting that this last point introduces the numerical inaccuracy in the FIT method, as when defining the relations between voltages and fluxes, the integral values have to be approximated within the grid edges and cell areas. Thus, the resulting coefficients will depend on the averaged material parameters, as well as on the spatial resolution of the grid. Moreover, the mesh grid can add dispersion to the model, which gets worse when the differences between two neighbouring mesh step sizes become larger. The smallest dispersion will occur in an equidistant mesh. To avoid these effects, the mesh generator may be forced to insert additional mesh lines that decrease the differences of mesh lengths.

The accuracy of the results is dependent on the way the structure is discretised, being improved for very fine mesh grids, when the mesh size gets so small that the discrete lengths become differentials. However, the finer the mesh is, the larger the number of mesh cells will be. With this, there will be a larger number of unknowns to be solved, extending the need of memory and simulation time. The *CST* mesh generator determines the important features of the structure under analysis and automatically creates the mesh grid, representing the structure and the fields equally well. However, some parameters can be controlled by the user, as the *Lines per Wavelength* (LW) or the *Mesh Line Ratio Limit* (RL), Figure 4.5.

The LW parameter is defined by N_{LW}, according to (4.30), and sets the minimum number of mesh lines in each coordinate direction that are used within a wavelength (wavelength for the highest frequency set for the simulation). This parameter sets the spatial sampling rate for the signals inside the structure, having a strong influence on the quality of the results and on the calculation time. Increasing LW leads to a higher accuracy, but also increases the total

simulation time. *CST* supplier suggests the default value of 10, for a good compromise between calculation time and accuracy, meaning that a plane wave propagating along one of the coordinate axes is sampled at least 10 times. The reduction of the wavelength when propagating through dielectric materials is taken into account here.

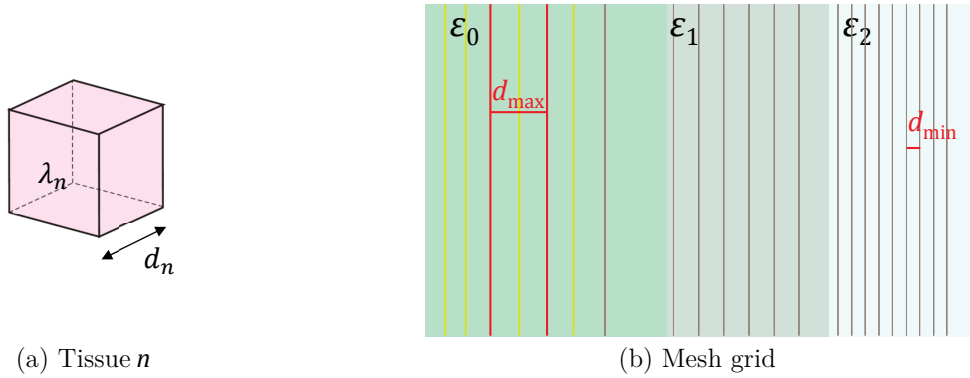

(a) Tissue n (b) Mesh grid

Figure 4.5. Mesh generation procedure in one direction.

$$N_{\mathrm{LW}} = \frac{\lambda_n}{\max(d_n)} \tag{4.30}$$

where

- $\lambda_n = \frac{\lambda_0}{\sqrt{\varepsilon_n}}$ (4.31)

  is the wavelength inside tissue n;
- d_n is the distance between mesh lines inside tissue n.

Not only the absolute number of mesh cells used is relevant, but also the distance between two mesh lines, which is decisive to define the mesh setting. The RL parameter sets the ratio limit between the highest and the smallest distances between mesh lines, as defined by N_{RL} in (4.32), forcing the algorithm not to overcome an absolute ratio. This way, the expression for N_{LW} is only valid if N_{RL} allows defining a meshing as detailed as required for the tissue; thus, unacceptable calculation times derived from very close mesh lines in high accuracy simulations are avoided. The RL setting strongly influences simulations, as the smallest distance existing in a mesh directly impacts on the width of the time steps usable in the simulation. The smaller the smallest distance, the smaller the time step and the longer it takes to simulate. The default value of 10 is very often a good compromise to start with.

$$N_{\mathrm{RL}} = \frac{d_{\max}}{d_{\min}} \tag{4.32}$$

where

- d_{max} is the highest distance between mesh lines;
- d_{min} is the smallest distance between mesh lines.

The simulation time is not only dependent on the number of unknowns, but also on the properties of the solver. Three solver types are available at *CST*: transient, frequency domain and eigenmode. From these, only the transient and the frequency domain solvers are used in this work.

The *transient solver* allows the simulation of the problem in a wide frequency range, in a single computation run, providing the s-parameters in the desired frequency range and the electromagnetic field patterns at various frequencies. The fields are calculated step by step, through time, according to the "Leap Frog" updating scheme, Figure 4.6.

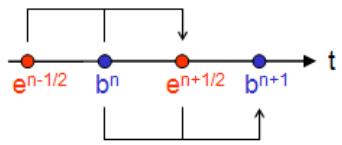

Figure 4.6. "Leap Frog" scheme of *CST* Transient Solver (adapted from [CSTe12]).

For the loss-free case, if one substitutes the time derivatives in the MGE by central differences, it yields to the following electric voltages and magnetic fluxes:

$$\mathbf{e}^{n+1/2} = \mathbf{e}^{n-1/2} + \Delta t \mathbf{M}_{\varepsilon}^{-1}\left[\tilde{\mathbf{C}}\mathbf{M}_{\mu}^{-1}\mathbf{b}^{n} + \mathbf{j}_{S}^{n}\right] \tag{4.33}$$

$$\mathbf{b}^{n+1} = \mathbf{b}^{n} - \Delta t \mathbf{C}\mathbf{e}^{n+1/2} \tag{4.34}$$

where

- $\mathbf{e}^{n+1/2}$ is $\mathbf{e}$ at instant $t = (n + 1/2)\Delta t$;
- $\mathbf{e}^{n-1/2}$ is $\mathbf{e}$ at instant $t = (n - 1/2)\Delta t$;
- Δt is the time step;
- $\mathbf{b}^{n}$ is $\mathbf{b}$ at instant $t = n\Delta t$;
- $\mathbf{j}_{S}^{n}$ is $\mathbf{j}_{S}$ at instant $t = n\Delta t$;
- $\mathbf{b}^{n+1}$ is $\mathbf{b}$ at instant $t = (n + 1)\Delta t$.

For instance, the magnetic flux at $t = (n + 1)\Delta t$ is computed both from the magnetic flux at the previous time step $t = n\Delta t$ and from the electric voltage at half a time step before, at $t = (n + 1/2)\Delta t$.

The "Leap Frog" scheme remains stable if the step width for the integration does not overcome a maximum usable time step, which is directly related to the minimum mesh step width used in the discretisation of the structure. The denser the chosen grid, the smaller the usable time step width. Hence, a high mesh resolution of a small detail inside a given structure probably sets the global time step, and therefore the total simulation time.

The *frequency domain* solver solves the problem for a single frequency at a time, or for a

number of adaptively chosen frequency samples in the course of a frequency sweep. This solver is based on MGE in the time harmonic case ($\partial/\partial t \rightarrow j\omega$), where fields are described as:

$$\mathbf{E}(t) = \Re\{\mathbf{E}(\omega)e^{j\omega t}\} \tag{4.35}$$

For loss-free problems this leads to the following second-order relation:

$$(curl\mu^{-1}curl - \omega^2\varepsilon)\mathbf{E} = -j\omega\mathbf{J} \qquad \Rightarrow \qquad (\tilde{\mathbf{C}}\mathrm{M}_{\mu^{-1}}\mathbf{C} - \omega^2\mathbf{M}_{\varepsilon})\mathbf{e} = -j\omega\mathbf{j} \tag{4.36}$$

For each frequency sample, the linear equation system is solved by an iterative (*e.g.*, conjugate gradient) or sparse direct solver. The solution comprises the field distribution as well as the **s**-parameters at the given frequency. The frequency domain solver converges slower with smaller mesh step sizes than with greater ones.

For any of the solvers, a geometrical model of the problem under study should be created together with the appropriate power sources (ports) and boundary conditions. The solver can only be started if at least one port is defined. In case of multiple ports, these ports may be stimulated differently: all ports stimulated sequentially, only one single port stimulated, some selected ports stimulated sequentially, or with some selected (or all) ports stimulated simultaneously.

Chapter 5

On-Body Channel Characterisation

This chapter describes the different studies performed to characterise the on-body channel. Section 5.1 introduces the concept. Section 5.2 introduces a preliminary study to analyse on-body communications for a static user in free space, its implementation including measurements and simulations. In Section 5.3, the mobility of the user is included in the analysis of the free space on-body channels. A new technique using motion capture software introduces the body dynamics in full wave simulations. In Section 5.4, a complex environment with random scatterers is then added to the study. A novel method, based on full wave simulations and on results from a geometrically based statistical channel model, is introduced. The 2×2 MIMO capacity for a body moving in a scattering environment is calculated and optimum antenna placements are suggested.

5.1 Concept

The on-body channel characterisation study intends to evaluate several on-body links, identifying classes with different propagation conditions (*e.g.*, LOS/NLOS/symmetry). The proposed modelling approach starts to analyse a static BAN, in a simple free space environment, to understand the relations between the on-body branches in the absence of multipath components. Different classes of on-body links are identified and characterised. Then, the mobility of the user is introduced, with the reproduction of common actions, as walk or run. The behaviour of channel parameters according to the movement is characterised, as well as on-body classes. Finally, a complex environment is considered, with a random distribution of scatterers according to the scenario (*e.g.*, office, street). For this multipath scenario, one considers the implementation of MIMO. Different radio channel parameters, like the channel gain, or capacity, are the outputs of this study. The final purpose is to use appropriate metrics for the selection of optimum antenna placements in a BAN, when using MIMO.

Figure 5.1 summarises the workflow of the study for the on-body channel characterisation, identifying the different stages. The outputs of the study are:

- Statistics of channel gain / power imbalance / correlation / capacity (average and standard deviation;
- Characterisation of classes of on-body links;
- Metrics for the selection of the optimum antenna placements.

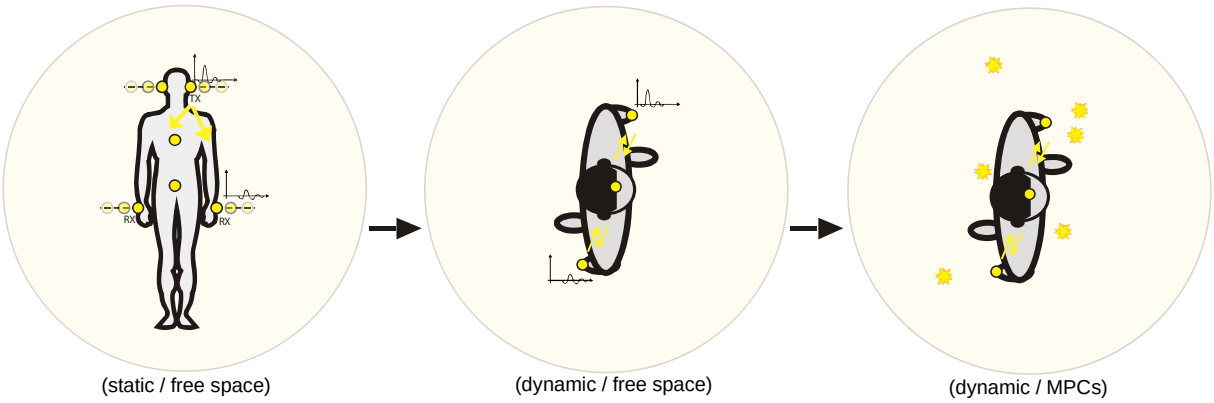

Figure 5.1. Characterisation of the on-body channel.

Table 5.1 summarises the implementation of the antenna-body interaction model, for each study the different inputs and outputs being identified.

A measurement campaign was also conducted to complement the study, as it deals with the whole complex on-body channel, including user's dynamics.

Table 5.1. Implementation of the on-body channel characterisation.

Study	Implementation	Inputs	Outputs
Static User in Free Space	Measurements	Body posture; Antenna placements; Antenna-body distance.	Return Loss Channel gain
	CST	Antenna placements; Antenna-body distance distribution.	Correlation Channel gain Power imbalance
Dynamic User In Free Space	*CST*	Antenna placements; Antenna-body fixed distance.	Correlation Channel gain Power imbalance
Dynamic User in Scattering Environment	*CST*, *Matlab*	Antenna placements; Antenna-body fixed distance; Environment.	Channel gain MIMO capacity

5.2 Static User in Free Space

The study described in this section analyses the on-body channels for a static user in free space. The idea is to understand the relations between the branches when no other reflectors than the body itself are present. For a given BAN configuration, one antenna is set as TX, and the others are RXs. The distance of the antennas to the body is changed according to a given distribution, as illustrated in Figure 5.2.

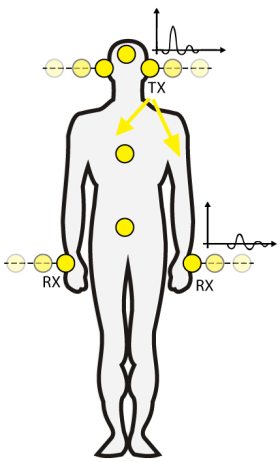

Figure 5.2. Static user in free space.

In a first stage, a measurement campaign was set-up for a static subject in an anechoic

chamber, holding four on-body antennas, and assuming different poses: standing, sitting and military posture. Three on-body links were recreated with the four antennas. The s-parameters are analysed in this study, namely the input reflection loss, s_{11}, and the transmission parameter, s_{12}. The analysis of s_{11} is important for the link budget, to quantify the reflection or mismatch losses caused by the presence of the body, while s_{12} quantifies the received power.

In a second stage, numerical simulations were set-up, as schematised in Figure 5.3. A static voxel model, in standing posture, carrying nine on-body antennas, was inserted in free space. At each simulation, one antenna is set as the TX and the remaining ones are the RXs. The distance of the different antennas to the body was set according to a specific scenario and distribution. The analysed parameters are the spatial correlation and the power imbalance between the on-body links.

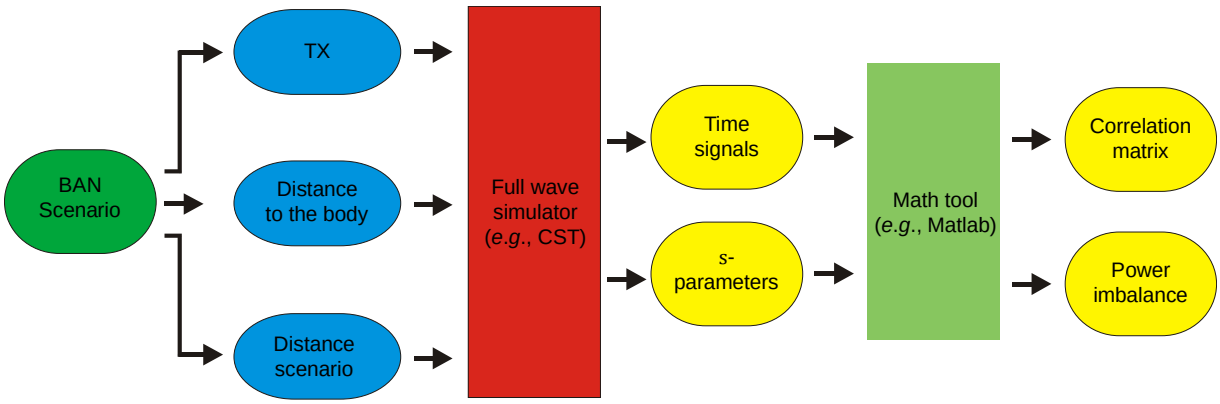

Figure 5.3. Routines for analysis of the static user.

Simulations were run for the nine possible TX locations, each one generating 28 possible correlation pairs. 20 distance samples were considered in each of the distance scenarios. The total time required for the simulations presented in this study was about one week. Each set of simulations for a given distance took about 2 hours, Table 5.2.

Table 5.2. Static User Simulation Time.

Task	Duration
CST scenario set-up	= 8 hours
CST simulation (Intel Xeon E5620 2×Quad-Core @2.4 GHz 32 GB RAM)	20 distance samples × 3 scenarios × 2 hours = 120 hours
CST export of results and data processing (time signals, s-parameters, 3D far fields)	= 4 hours
	= 132 hours (~6 days)

For every TX placement, it is possibly to classify the pairs of RXs. A pair of RX can be fitted into a specific class according to its relative position to the TX, and to the orientation between RXs. The following classes can be identified:

- SYM – RXs are symmetric to the TX;
- LOS – RXs have LOS between them;
- QLOS (*quasi*-LOS) – RXs can be shaded by the body, sometimes being in LOS and other times in NLOS;
- NLOS – RXs have no LOS between them.

For instance, if the TX is on the belt, the wrist antennas belong to class SYM. But, if TX is on the right ear, then the wrist antennas pair is classified as QLOS. It should be stated that the clear identification of these categories is not trivial, as sometimes two nodes can be in NLOS, but still having some symmetry. The mapping of correlation pairs to the different classes was done for each TX position (*e.g.*, in Figure 5.4 for TX on belt). The classification for each TX placement is shown in Annex D.

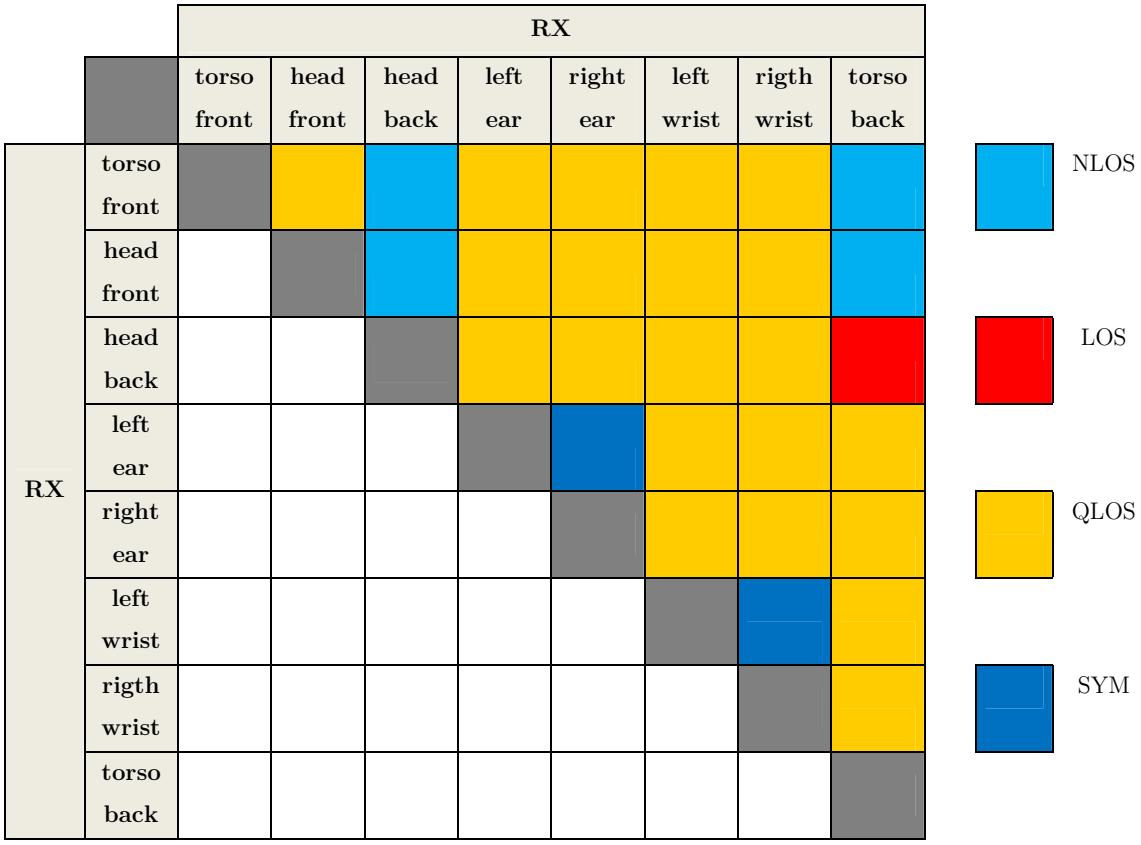

Figure 5.4. Mapping of RX pairs/classes for TX on belt.

The correlation between the signals received in antennas k and l, $\rho_{kj,lj}$, when antenna j is transmitting, is computed from the envelope of the time signals s_{kj} and s_{lj}. To calculate $\rho_{kj,lj}$, the signals are initially aligned (shifted) in time, through the cross-correlation function [Orfa96], so that the maximum value is obtained (as a worst case perspective):

$$\left(s_{kj} * s_{lj}\right)(\tau) \stackrel{\text{def}}{=} \int_{-\infty}^{\infty} s_{kj}(t)\, s_{kj}(\tau + t) dt \tag{5.1}$$

then, $\rho_{kj,lj}$ is computed by:

$$\rho_{kj,lj} = max\{\left(s_{kj} * s_{lj}\right)(\tau)\} \tag{5.2}$$

Taking into account the results of all possible TX placements, the global statistics of correlation with distance, are given by the mean value $\bar{\rho}$ and the standard deviation σ_{ρ}.

The power received at each RX is gathered from s_{21} at 2.45 GHz, and the power imbalance between RX antennas k and l, when antenna j is transmitting, $\Delta P_{kj,lj}$, is given by:

$$\Delta P_{kj,lj\,[\mathrm{dB}]} = |s_{kj}|_{[\mathrm{dB}]} - |s_{lj}|_{[\mathrm{dB}]} \tag{5.3}$$

5.3 Dynamic User in Free Space

The study described in this section is an improved version of the previous one, where the body is no longer static, and the mobility of the user is considered. This analysis allows to understand how the relations between the branches change according to the movement of the body. The parameters analysed in this investigation are the spatial correlation and the power imbalance between on-body links.

For this study, a similar methodology to the works in [GHBN11] and [AIKT11], to include the body dynamics in a full wave simulator, was used. However, an accurate body shape was considered here, and a new method to export the antenna placements along the movement was created. This approach was designed for simulations in *CST*, using homogeneous body models obtained from the *Poser* animation software, but the method is general and can be applied using similar tools. Figure 5.5 illustrates the concept developed to analyse the body dynamics.

The first step of the method starts with the animation tool (*e.g.*, *Poser*), with the selection of a 3D phantom. The location of the antennas on the body model is then identified by "guides", consisting on simple rectangles located at a given distance to the surface of the phantom (a 2 cm distance was used). These shapes are then "linked" to the body skeleton, and will move according to the movement of the phantom. For instance, moving and rotating one arm will move the attached rectangle accordingly.

The animation tool allows the user to apply realistic human motion movements to the 3D

phantom (*e.g.*, walk, run), so, a selected motion action is then applied to the phantom. Each point of time in the human motion is key framed to create a smooth animation, where each frame is a 3D object (a posture). In our approach, two typical human day-to-day activities are reproduced, walk and run, each one being a combination of 30 time frames, with 1/30 s duration each. Figure 5.6 illustrates some of the running frames.

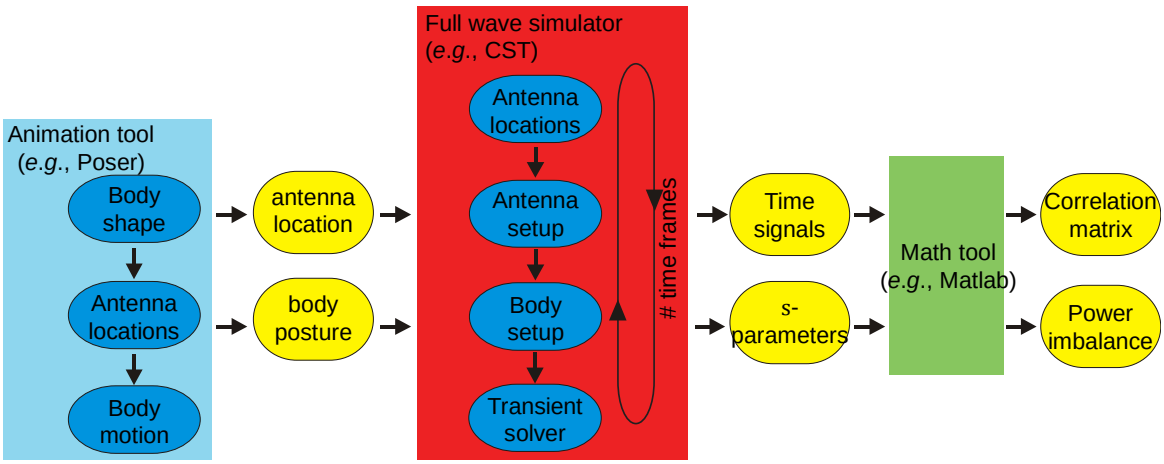

Figure 5.5. Routines for analysis of the dynamic user.

Figure 5.6. Running user reproduced in *Poser*.

For each time frame, two CAD format files (*e.g.*, .OBJ) are then exported from the animation tool: one containing the location of the antennas, and the other containing the 3D body model.

The next stage is to import the motion frames into the full wave simulator (*e.g*, *CST*), frame by frame, each frame corresponding to a project. For each frame, the file containing the rectangles location is imported into the simulator (but not being considered to the simulation), and the antenna (in our approach, a patch) is manually attached to each one of the rectangles. It is important to ensure that every antenna keeps its orientation in each time frame; otherwise this can be a source of error. Then, the file containing the body model is imported and filled with tissue properties obtained from the Cole-Cole model [IFAP12] (2/3 muscle was used). An example of the setup of a dynamic frame in *CST* is shown in Figure 5.7.

At this stage, it is important to state that the meshing generation in the full wave simulator can be a source of numerical error in these simulations. In *CST*, when several antennas are being used, not all of them are aligned with the meshing grid, which can cause numerical

inaccuracy in the simulations.

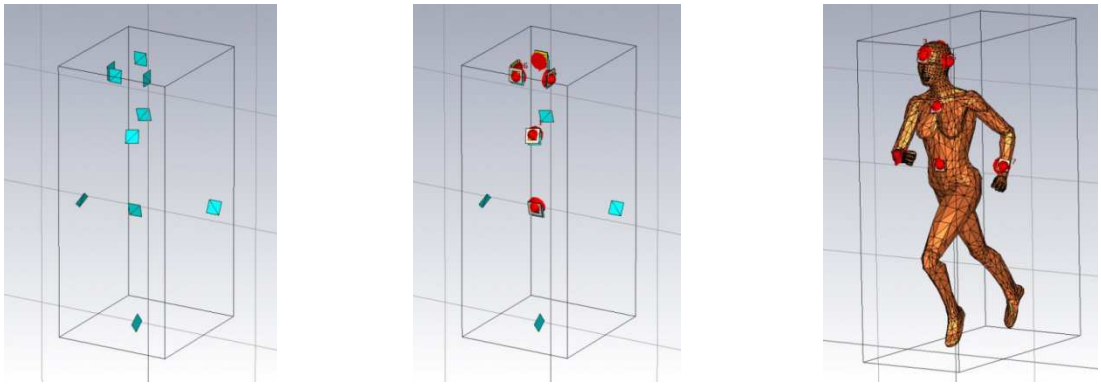

(a) Antenna Locations (b) Antenna Insertion I Body with antenna

Figure 5.7. Example of a dynamic frame set-up in *CST*.

The movement is studied in the full wave simulator in a discrete way, running the transient solver for each time frame (*i.e.*, running the different projects). For each frame, one antenna is set as the TX and the others as RXs. A Gaussian pulse is sent by the TX and the simulator stores the received signals, as well as the s-parameters. The procedure is applied for all the on-body antenna locations, in order to gather all possible TX-RX/RX-RX combinations.

The procedure described above is flexible enough to be extended to other phantoms, antennas, motion actions, or BAN configurations. However, the proposed solution is a time consuming and delicate process, especially due to the manual antenna addition in the full wave simulator.

This solution was implemented using only 15 from the 30 time frames generated in *Poser*. The total time required for the simulations presented in this study was about one month (excluding debugging overheads), Table 5.3.

Table 5.3. Body Dynamics Simulation Time.

Task	**Duration**
Poser scenario set-up and export of OBJ files	= 2 hours
CST import of .OBJ files and antenna setup	15 time frames × 2 scenarios × 2 hours = 60 hours
CST simulation (Intel Dual-4 Core @2.4 GHz 32 GB RAM)	15 time frames × 2 scenarios × 36 hours = 720 hours
CST export of results (channel impulse responses, s-parameters)	= 4 hours
	= 786 hours (~1 month)

5.4 Dynamic User in a Scattering Environment

This section describes the final step of the work developed in the Thesis, with the insertion of the dynamic user in a scattering environment. From this study, it was possible to calculate the capacity for a 2×2 MIMO BAN, and then select the optimum combinations of RXs/TXs.

The approach proposed here to model the on-body channel for a subject moving in a scattering environment consists of a combination of the results from full wave simulations (*e.g.*, *CST*), with the results from a geometrically based statistical channel model simulator adapted for BANs (GBSC_B) [MaCo12]. The concept is outlined in Figure 5.8, and the idea is that the signal at the RX results from the contribution of one on-body component (obtained from the full wave simulator) and of the several MPCs present in the environment (obtained from the GBSC_B model).

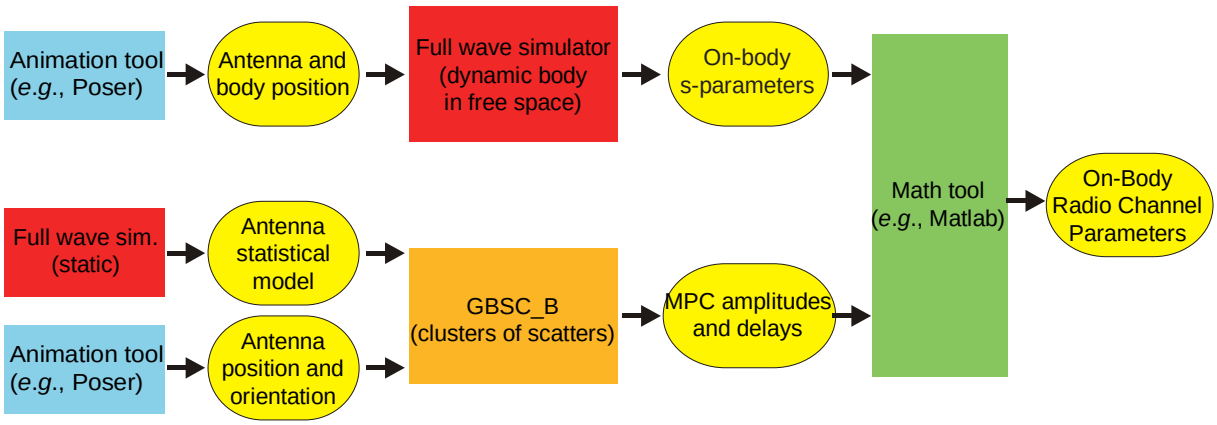

Figure 5.8. Analysis of the dynamic user in a scattering environment.

The GBSC_B model is an adaptation of the common GBSC models to BANs, where the TX and RX antennas are both on the body. These models are based on the concept that the multipath characteristics of a channel result of signal bounce (single and double) over numerous scatterers randomly generated and having a complex reflection coefficient. The deployment and the shape of clusters depend on the scenario. The output parameters are calculated according to the positions of TXs and RXs, and to the distribution of scatterers.

The inputs for the GBSC_B simulator are the statistical antenna patterns at different locations on the body (obtained from the method described in Section 5.2), and the geometrical description of the on-body antenna positions with the body dynamics (obtained from the animation tool). The outputs from the simulator are the amplitude, the phase and the time of arrival for each MPC, as:

$$h_{GBSC\_B}(t) = \sum_{n=1}^{N_{mc}} h_n \delta(t - \tau_n) \tag{5.4}$$

where

- h_n is the amplitude of the n-th MPC obtained from the GBSC_B simulator;
- τ_n is the delay of the n-th MPC obtained from the GBSC_B simulator.

In each GBSB_B simulation, the body is moving along the same path, during one walk cycle, with the desired behaviour (*i.e.*, walking or running). This movement is exactly the same as the one generated in the free space dynamic full wave simulations (described in the last section). The s-parameters obtained from the full wave simulations of the previous section are then used here, representing the on-body component. The information retrieved from the full wave simulator is the amplitude and the phase of the s-parameters.

The total impulse response, $h_T(t)$, *i.e.*, the signal obtained from the sum of the on-body component and of the MPCs, is obtained by:

$$h_T(t) = h_{kj}\delta(t - \tau_1) + \sum_{n=2}^{N_{mc}} h_n \delta(t - \tau_n) \tag{5.5}$$

where

- h_{kj} is the transmission parameter between the antennas k and j, obtained from *CST*.

To enable a statistical analysis, the propagation conditions in a particular type of environment (office or street) are changed through the generation of randomly disposed scatterers. So, N_s simulations are performed in the GBSB_B simulator, each one with a random distribution of scatterers. For a given time frame t_n (occurring for the same body posture and position in the cell), the variations in the output parameters come from the differences in the propagation environment. The total number of obtained CIRs for a dynamic scenario is:

$$N_{CIR} = N_p \times N_f \times N_s \tag{5.6}$$

where

- N_p is the number of antenna placements;
- N_f is the number of time frames.

Therefore, for the Run and Walk scenarios, the total number of performed simulations is 37 500 and 112 500, respectively. To obtain the CIRs for the more demanding scenario (*i.e.*, walk), 1 hour of simulations was required (and 3 hours more to obtain the parameters and their statistics) using a laptop with an Intel Core i5 @2.5 GHz 8 GB of RAM.

In what follows, the statistics are defined for the capacity; however, for the other output parameters, the definition is similar. The average MIMO capacity $\overline{C(t_n)}$ at each time frame t_n, and its standard deviation $\sigma_C(t_n)$ obtained over the N_s simulations are calculated by:

$$\overline{C(t_n)} = \frac{1}{N_s}\sum_{s=1}^{N_s} C(t_n, s) \tag{5.7}$$

$$\sigma_C(t_n) = \sqrt{\frac{1}{N_s}\sum_{s=1}^{N_s}\left[C(t_n, s) - \overline{C(t_n)}\right]^2} \tag{5.8}$$

Additionally, the statistics can be averaged in a required range of the time frames:

$$\Delta t_n = t_M - t_m \tag{5.9}$$

where

- t_m is the first time frame;
- t_M is the last time frame.

The average MIMO capacity $\bar{C}$, the standard deviation of the average $\sigma_{\bar{C}}$, and the average standard deviation $\overline{\sigma_C}$ are calculated by:

$$\bar{C}(\Delta t_n) = \frac{1}{\Delta t_n}\sum_{n=t_m}^{t_M} \overline{C(t_n)} \tag{5.10}$$

$$\sigma_{\bar{C}}(\Delta t_n) = \sqrt{\frac{1}{\Delta t}\sum_{n=t_m}^{t_M}\left[\overline{C(t_n)} - \bar{C}(\Delta t_n)\right]^2} \tag{5.11}$$

$$\overline{\sigma_C}(\Delta t_n) = \sqrt{\frac{1}{\Delta t_n}\sum_{n=t_m}^{t_M}\left[\sigma_C(t_n)\right]^2} \tag{5.12}$$

For convenience, two metrics to evaluate capacity are defined:

- C_{G}, the relative MIMO capacity gain defined in (5.13), as the relation between the capacity of the MIMO system to the "best" SISO capacity. The latter corresponds to the maximum throughput from the 4 SISO branches in the 2×2 system. This metric is evaluated at every time frame.

$$C_G(t_n) = \frac{C(t_n)}{\max\{C_{SISO}(tn)\}} \tag{5.13}$$

- $C_{G_{BAN}}$, the BAN MIMO capacity gain defined as (5.14). This metric evaluates the performance of a given 2×2 combination of TX/RX within a specific BAN system.

$$C_{G_{BAN}} = \frac{C - C_{lower}}{C_{upper} - C_{lower}} \tag{5.14}$$

The selection of the optimum placements is based on the values of the BAN MIMO capacity, the best placements corresponding to the systems with the highest values of $C_{G_{BAN}}$.

Chapter 6

Scenarios

This chapter describes the reference scenarios, metrics and assumptions used throughout the Thesis. Section 6.1 introduces general metrics related to radiation patterns and statistical distributions. In Section 6.2, a set of general assumptions used through the work is presented. Section 6.3 and Section 6.4 describe the settings considered for the analytical and numerical studies, respectively. Section 6.5 summarises the measurement conditions of the studies performed.

6.1 Definitions and Metrics

Various definitions and metrics are systematically used along this work, like the statistics and variations of electromagnetic fields, or different aspects regarding the radiation patterns. Their general definition is given in what follows.

The total radiation pattern of an antenna is described by the vector sum of the two orthogonally polarised radiated field components, *i.e.*, the co- and cross(x)-polarised components [Bala97]. The radiation pattern is usually given in terms of the generalised gain, $G(\theta, \varphi)$, although a description in terms of E field is also possible. The absolute gain of the antenna, G, can be measured through gain transfer techniques, using standard gain antennas (*e.g.*, horn antenna) [Bala97]:

$$G_{[\mathrm{dB}]} = G_{h\,[\mathrm{dB}]} + 10log(\frac{P_{test}}{P_h}) \tag{6.1}$$

where

- G_h is the absolute gain of the horn antenna;
- P_{test} and P_h are the received powers of the test and horn antennas, respectively.

In the practical scenario of a BAN, the distance of the antenna to the body can vary in time, which can be described statistically. By performing simulations or measurements of the antenna located with different distances to the body d_k (a discretisation of the distance is considered, in terms of index k), one obtains a set of radiation patterns $G(\theta_n, \varphi_m, d_k)$ (θ_n and φ_m being discrete values of the usual spherical coordinates). The distance sample d_k depends on the required distance to the body distribution, and on the total number of distance samples N_d (*i.e.*, the accuracy of the study). Note that the definitions given below are also valid for patterns given in terms of E. From the set of radiation patterns, it is possible to calculate the average one:

$$G_\mu(\theta_n, \varphi_m) = \frac{1}{N_d}\sum_{k=1}^{N_d} G(\theta_n, \varphi_m, d_k) \tag{6.2}$$

The standard deviation of the radiation pattern can be calculated from:

$$\sigma_G(\theta_n, \varphi_m) = \sqrt{\frac{1}{N_d}\sum_{k=1}^{N_d}[G(\theta_n, \varphi_m, d_k) - G_\mu(\theta_n, \varphi_m)]} \tag{6.3}$$

The average and the standard deviation of radiation patterns should be used in radio channel

simulators to calculate multipath components, therefore, being used as linear quantities. However, usually, results for antennas radiation patterns and gain are shown in a logarithmic scale, hence, the above mentioned entities are presented in dB. In this work, the following convention is used:

$$G_{\mu\pm\sigma}(\theta_n,\varphi_m)_{[\mathrm{dB}]} = 10log[G_\mu(\theta_n,\varphi_m) \pm \sigma_G(\theta_n,\varphi_m)] \tag{6.4}$$

$$\sigma_G(\theta_n,\varphi_m)_{[\mathrm{dB}]} = 10log[\sigma_G(\theta_n,\varphi_m)] \tag{6.5}$$

The minimum, G_{min}, and maximum, G_{max}, of the radiation pattern are calculated from the set of distance samples:

$$G_{min}(\theta_n,\varphi_m)_{[\mathrm{dB}]} = 10log[min_{d_k}\{G(\theta_n,\varphi_m,d_k)\}] \tag{6.6}$$

$$G_{max}(\theta_n,\varphi_m)_{[\mathrm{dB}]} = 10log[max_{d_k}\{G(\theta_n,\varphi_m,d_k)\}] \tag{6.7}$$

In order to evaluate the difference between a general radiation pattern G and a reference one G_{ref} (*e.g.*, the radiation pattern of isolated antenna), the partial pattern difference, calculated for a particular direction of radiation is given by parameter $\Delta G_{n,m}$:

$$\Delta G_{n,m} = \frac{\left|G(\theta_n,\varphi_m) - G_{ref}(\theta_n,\varphi_m)\right|}{G_{ref}(\theta_n,\varphi_m)} \tag{6.8}$$

Two parameters are additionally defined, *i.e.*, the Pattern Average Difference (PAD) given by (6.9) and the Pattern Weighted Difference (PWD) given by (6.10).

$$\overline{\Delta G} = \frac{1}{N_\varphi N_\theta}\sum_{n=1}^{N_\varphi}\sum_{m=1}^{N_\theta}\Delta G_{n,m} \tag{6.9}$$

$$\overline{\Delta G_w} = \frac{\sum_{n=1}^{N_\varphi}\sum_{m=1}^{N_\theta}\Delta G_{n,m}\, G_{ref}(\theta_n,\varphi_m)}{\sum_{n=1}^{N_\varphi}\sum_{m=1}^{N_\theta} G_{ref}(\theta_n,\varphi_m)} \tag{6.10}$$

where

- N_φ is the number of discrete azimuth angle samples;
- N_θ is the number of discrete elevation angle samples.

The difference between those two parameters is that $\overline{\Delta G}$ treats changes of the radiation pattern in all directions equally, whereas $\overline{\Delta G_w}$ weights these changes by the radiation pattern.

The normalisation factor $\bar{G}_{max}$ is the radiation pattern maximum average value:

$$\bar{G}_{max} = \max(\bar{G}(\theta)) \tag{6.11}$$

The relative difference between the radiation patterns taken at distances d and d_0 is given by the parameter ΔG^d, as:

$$\Delta G^d_{[\mathrm{dB}]} = \left|G_d(\theta) - G_{d_0}(\theta)\right| \tag{6.12}$$

Some statistical distributions that best fit the selected data are used, namely the Normal, the Exponential, the Rayleigh, the Beta, the Kumaraswamy, and the Truncated Normal Distributions. The goodness of fit is tested using the χ^2 or the R^2 tests [Orfa96]. For the χ^2 test, a value lower than the threshold for a 95% confidence interval ($\chi^2_{th95\%}$) means that the fitting is successful, otherwise it is not appropriate. The R^2 test value goes to 1 when optimum fitting is obtained.

The Probability Density Function (PDF) of the Beta Distribution [Abra65], for a random variable x distributed in the interval [0, 1], is:

$$p_B(x;\alpha_B,\beta_B) = \frac{x^{\alpha_B-1}(1-x)^{\beta_B-1}}{\mathrm{B}_{\alpha_B,\beta_B}} \tag{6.13}$$

The PDF of the Kumaraswamy Distribution [Kuma80] is:

$$p_K(x;\alpha_K,\beta_K) = \frac{\alpha_K\beta_K x^{\alpha_K-1}(1-x^{\alpha_k})^{\beta_k-1}}{\mathrm{K}_{\alpha_K,\beta_K}} \tag{6.14}$$

where

- α_B, β_B, α_K and β_K are shape parameters of the Beta and Kumaraswamy Distributions, respectively;
- $\mathrm{B}_{\alpha_B,\beta_B}$ and $\mathrm{K}_{\alpha_K,\beta_K}$ are normalisation constants for the Beta and Kumaraswamy Distributions, respectively, to ensure that the total probability integrates to unity.

The Truncated Normal Distribution corresponds to a normally distributed random variable, bounded in an interval $[a,b]$. For x normally distributed, with mean μ and variance σ^2, the PDF of the Truncated Normal Distribution [Robe95] is given by:

$$p_{TN}(x;\mu,\sigma,a,b) = \frac{\frac{1}{\sigma}\phi_N(\frac{x-\mu}{\sigma})}{\Phi_N\left(\frac{b-\mu}{\sigma}\right) - \Phi_N\left(\frac{a-\mu}{\sigma}\right)} \tag{6.15}$$

where

- $\phi_N(\ )$ is the PDF of the standard Normal Distribution [Abra65];
- $\Phi_N(\ )$ is the Cumulative Distribution Function (CDF) of the standard Normal

Distribution [Abra65];

- The mean μ_{TN} and variance σ_{TN} values of the Truncated Normal Distribution are given in [Robe95].

The Normal Distribution is the best fit for some data, $\overline{E^N}$ and σ_E^N being the maximum likelihood estimates for mean and standard deviation with a 95% confidence. An Exponential Distribution with rate parameter $1/\mu_{EE}$, is used to best fit other distributions. Also, a Rayleigh Distribution with mode m_R is the best fit for some other data. Some definitions are given here for the E field, but are naturally extended to other entities.

A measure of the variations of electromagnetic fields is given by the parameters ΔE and ΔH:

$$\Delta E = E_{max} - E_{min} \tag{6.16}$$

$$\Delta H = H_{max} - H_{min} \tag{6.17}$$

where

- E_{max} and E_{min} are the maximum and the minimum values of E field, respectively;
- H_{max} and H_{min} are the maximum and the minimum values of H field, respectively.

When assessing the numerical simulation tool, the changes of the output parameters for a meshing with N_c mesh cells relative to the case of the maximum number of mesh cells, $N_{c_{max}}$, are defined as exemplified in (6.18) for the resonant frequency f_r. The definition is valid for the radiation pattern G, the radiation efficiency η_{rad}, as well as for the s_{11} parameter.

$$\Delta f_r = \frac{\left|f_r(N_c) - f_r\left(N_{c_{max}}\right)\right|}{f_r\left(N_{c_{max}}\right)} \tag{6.18}$$

The average and respective standard deviations of the return loss parameter are given by $\mu_{s_{11}}$ and $\sigma_{s_{11}}$, respectively. The same assumption is taken for s_{12}, whose range is given by $\Delta_{s_{12}}$.

6.2 General Assumptions

The biological system of a body is an irregularly shaped dielectric medium, and the amount of scattered energy depends on the electromagnetic properties of the body and on its geometry, as well as on the frequency of the incident wave. Two frequencies are taken as examples for possible bands in BANs: 0.9 GHz in the cellular range, and 2.45 GHz in the Industrial, Scientific and Medical (ISM) one.

In order to identify the location of the antenna on the body, a practical segmentation of the body was schematised. The placements are described by the label *nn_m*, where *nn* defines the location: TO – torso, WA – waist, HE – head or AB – arm's bottom part; and *m* the side: B – back, F – front, L – left or R – right. For instance, HE_L refers to an antenna located on the left side of the head.

In order to measure shifts of the antenna orientation, a reference coordinate system is taken, in which the reference direction is the front of the body, and azimuth φ and co-elevation θ angles are calculated as presented in Figure 6.1, taking the usual spherical coordinate system. A BAN topology composed of wireless nodes distributed in locations that can correspond to a realistic usage scenario is also shown in Figure 6.1.

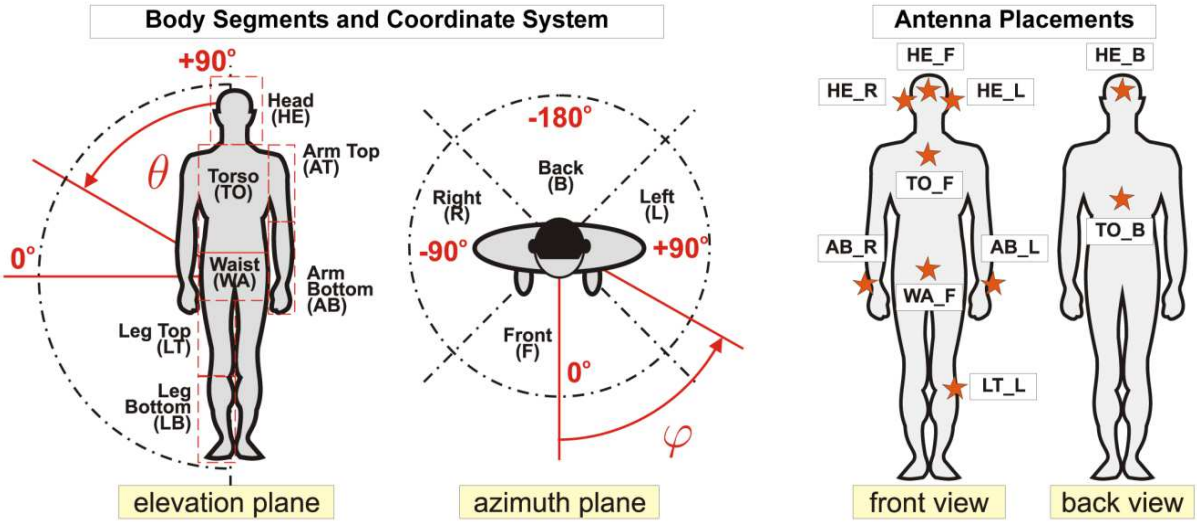

Figure 6.1. Human body segmentation.

Different body postures can be assumed (*e.g.*, standing (STD), sitting (SIT), military (MIL)), Figure 6.2. The arm poses in the standing and sitting postures characterise their movement at different snapshots: arms down (ADOWN), arms in front of the body (AFRONT), arms in back of the body (ABACK), arms up (AUP) and arms bend (ABEND). The military position represents a soldier carrying a firearm in two surveillance postures (STEP and KNEE).

The mobility scenarios can be classified as:

- Static;
- Pedestrian;
- Specific actions (*e.g.*, walk, run).

Three scenarios are analysed in this work, static, walk and run, which are the most typical human day-to-day activities. The mobility scenarios walk and run are examples of slow and fast movement, respectively. The walking and running speeds were set to 4.8 km/h and 14.4 km/h, respectively, according to [KnPN96].

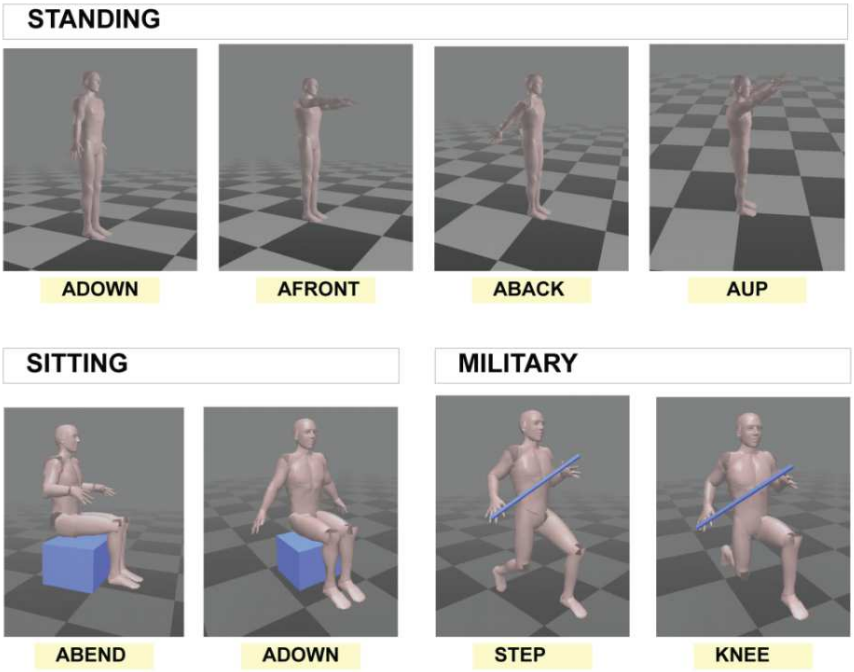

Figure 6.2. Body postures.

The environment where the BAN is operating can be classified as:

- Free space (theoretical scenario);
- Indoors;
- Outdoors;
- Specific (*e.g.*, hospital, bed, car, space, battlefield).

Besides free space, indoor office and outdoor micro-cell street scenarios are used in this work. The office environment includes a set of 6 clusters, of 3 scatterers each, with a Uniform Distribution inside a cuboid, Figure 6.3. The body is walking on a straight line, in the middle of the room (*i.e.*, $y = 2.5$ m), in range $x \in [2.5\text{-}\frac{v_{[m/s]}}{2}, 2.5\text{+}\frac{v_{[m/s]}}{2}]$ m. The street environment includes a set of 10 clusters, of 3 scatterers each, with a Uniform Distribution in the half space of an ellipsoid. The dimensions of the ellipsoid are as indicated in Figure 6.4. The body is moving (*i.e.*, walking or running) on a straight line with speed v, in the middle of the street (*i.e.*, y=10 m and in range $x \in [100\text{-}\frac{v_{[m/s]}}{2}, 100\text{+}\frac{v_{[m/s]}}{2}]$ m.

According to the application, the nodes in the BAN can cooperate in many different ways. Some most probable configurations can be identified, as, for instance, the 2×2 scheme consisting in two neighbouring data sensors sending information to the body central unit (sink), also composed by two nearby sensors, Figure 6.5.

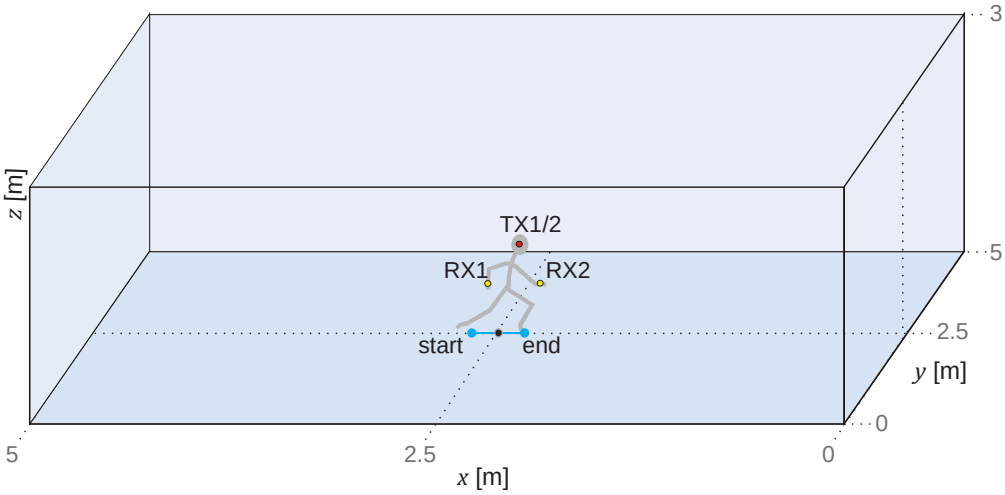

Figure 6.3. Office environment.

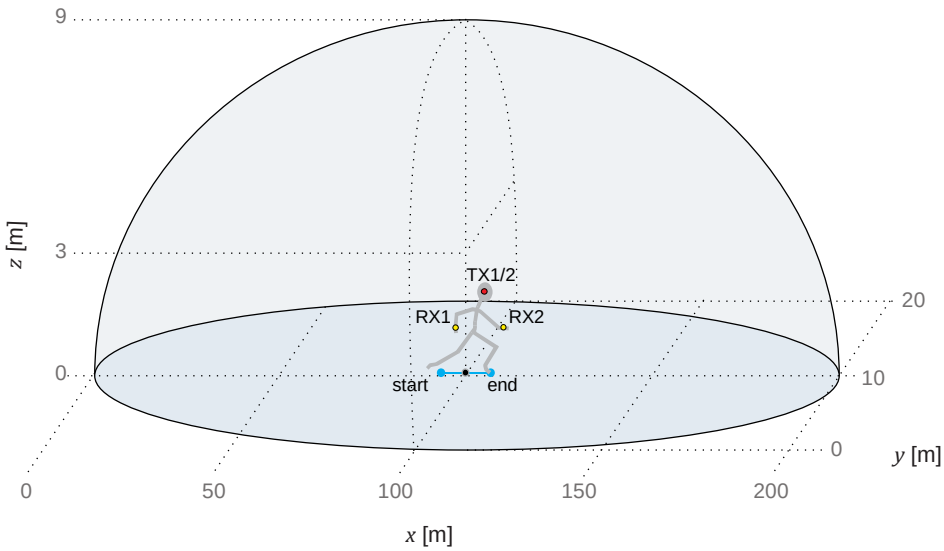

Figure 6.4. Micro-cell street environment.

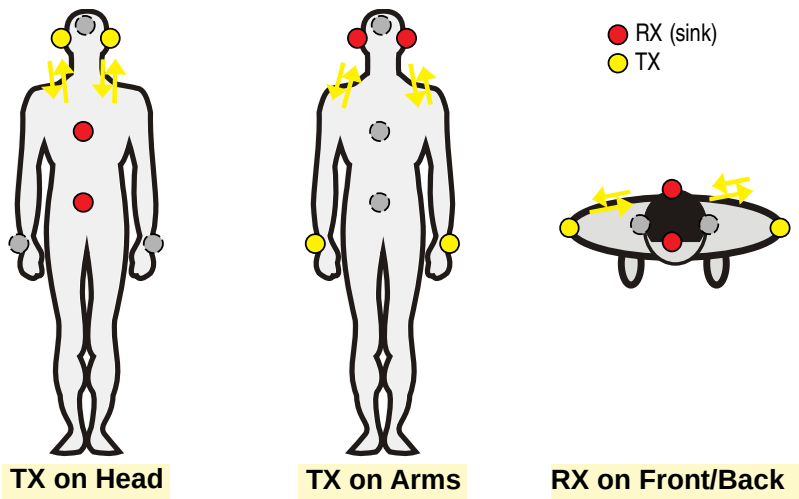

Figure 6.5. Possible 2×2 configurations.

Table 6.1 identifies some of the possible TX and RX placements for a 2×2 virtual MIMO scheme, with a brief description on the probable applications.

Table 6.1. Possible 2×2 configurations.

Sink		Data sensors		Description
RX1	**RX2**	**TX1**	**TX2**	
TO_F	WA_F	HE_F	HE_B	Sink in front of the body. Data sensors in the head, transmitting different information: vision, hearing, navigation, voice.
		HE_F	HE_L	
		HE_F	HE_R	
		HE_B	HE_L	
		HE_B	HE_R	
		HE_L	HE_R	
TO_F	TO_B	HE_F	HE_B	Sink in front and back. Data sensors in the head, transmitting different information: vision, hearing, navigation, voice.
		HE_F	HE_L	
		HE_F	HE_R	
		HE_B	HE_L	
		HE_B	HE_R	
		HE_L	HE_R	
TO_F	WA_F	AB_L	AB_R	Sink in different locations. Data sensors in the arms, transmitting different information: navigation, vital signs.
TO_F	HE_F			
TO_F	TO_B			
HE_F	HE_B			
HE_L	HE_R			

Note that the aspects of synchronisation between the on-body nodes in the virtual MIMO scheme are beyond the scope of this work. One assumes the optimistic scenario of perfect synchronism among the on-body sensors and the sink.

For the purpose of this work, the radio channel settings summarised in Table 6.2 are assumed. Note that the transmitted power and the noise floor are kept constant. Also, adjacent WLAN noise in the 2.45 GHz band is considered.

Table 6.2. Radio channel settings.

Carrier frequency [GHz]	2.45
Bandwidth [MHz]	1
Time resolution (RX filter) [μs]	1
Transmitted Power [dBm]	0
Noise floor [dBm]	-110 (adjacent WLAN noise is considered)

6.3 Analytical Models

While using analytical models, the body is usually defined as a geometrical shape, with homogeneous filling. Different parts can be modelled, with dimensions based on an average person [HeUl10], and a circular cylindrical shape can be assumed. Accordingly, the torso, arms and legs are modelled as homogeneous cylinders, with different filling properties. Their corresponding permittivity and conductivity are obtained from the 4-Cole-Cole model, based on

data compiled in [Gabr96]; Table 6.3 and Table 6.4 summarise the used characteristics.

Table 6.3. Characteristics of the human body.

	Tissue	**Radius, a [cm]**	a/λ	
			0.9 GHz	**2.45 GHz**
Torso	Fat	16	0.48	1.31
Leg	Muscle	11	0.33	0.90
Arm	Muscle	5	0.15	0.41

Table 6.4. Dielectric properties of materials.

	f = 0.9 GHz		f = 2.45 GHz	
	ρ [S/m]	ε_r	ρ [S/m]	ε_r
Fat	0.051	5.462	0.105	5.280
Muscle	0.943	55.032	1.739	52.729

For the statistical study on the variations of radiation patterns, different distance samples to the body were considered, assuming uniformly distributed intervals, with a 0.05 cm resolution. Table 6.5 presents both the absolute and the relative (to λ) values for those intervals.

Table 6.5. Distances used in simulations of elementary source model.

	Distance to the body [cm]	d/λ	
		f = 0.9 GHz	f = 2.45 GHz
Torso	]0, 20]	]0, 0.60]	]0, 1.63]
Leg	]0, 10]	]0, 0.30]	]0, 0.82]
Arm	]0, 5]	]0, 0.15]	]0, 0.41]

The electric field is obtained relative to the isotropic radiation of 1 V/m, in free space, in far field, hence, all values being normalised and presented in dB.

6.4 Numerical Model

The antenna selected as a case study for the numerical simulations is the patch from [CaMe06], illustrated in Figure 6.6, and with the technical parameters presented in Table 6.6.

This patch was selected for this study as it was designed in IST, and numerical and physical prototypes are available. Although it was not designed for on-body communication purposes, it can be easily integrated in clothes or equipment, due to its small dimensions and flat configuration, and it radiates out of the body. Note that the coax fed microstrip port of the real antenna was simplified to a discrete port.

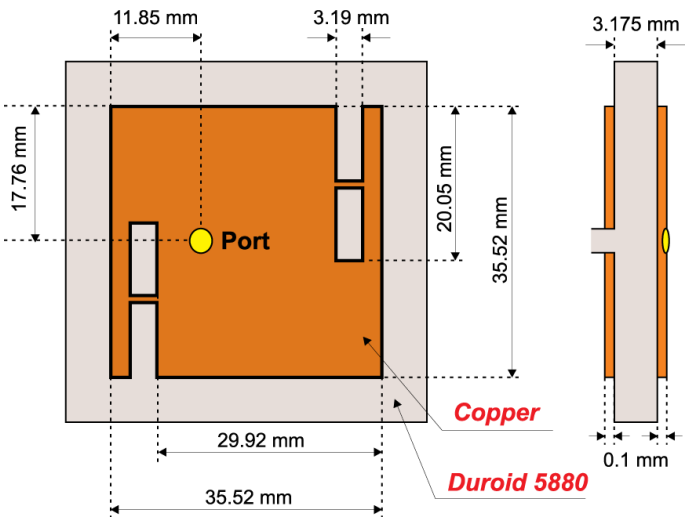

Figure 6.6. Patch antenna used in the Thesis (adapted from [CaMe06]).

Table 6.6. Technical specifications for the patch [CaMe06].

Gain	6.58 dBi
Total radiation efficiency	80.2%
Resonance frequency	2.44 GHz
Input return loss	-12.35 dB

A half-wavelength dipole is also used for comparison purposes, because, contrary to the patch antenna, it radiates towards the body, so a strong influence from it is expected.

The *CST* mesh settings are decisive for the accuracy and time of simulation, particularly the RL and LW parameters, which set the spatial sampling rate and the limit for the smallest distance between mesh lines, respectively. Five scenarios with different RL/LW combinations are defined to perform an assessment study that will elect the mesh settings for this work:

- RL10/LW14 (reference scenario): High accuracy and high resolution (large number of mesh cells). It is the most accurate scenario, thus, boasting the most demanding computation requirements.
- RL10/LW12: High accuracy and good resolution (large number of mesh cells).
- RL10/LW10: Default accuracy and default resolution (tolerable number of mesh cells)
- RL7/LW16: Moderate accuracy and high resolution (reduced number of mesh cells).
- RL7/LW10: Moderate accuracy and default resolution (small number of mesh cells).

For the numerical simulations, an adult female is taken as case study, and two phantom models are considered, Figure 6.7: homogeneous and heterogeneous. It was decided to use only one female, because very specific body parts are being studied and no large changes are expected between genders. To perform a more detailed study, one should consider not only both genders, but also different morphologies (fat, thin, tall, ...).

The homogeneous model of the female was obtained from the *Poser* library [Pose12], and it was

filled with 2/3 muscle tissue. Different poses are used with this model, corresponding to actions obtained from realistic motion capture (*e.g.*, walk or run).

(a) Homogeneous ([Pose12]) (b) Heterogeneous ([ViFa12])

Figure 6.7. Female body models.

The heterogeneous voxel model was selected from the Virtual Family [ViFa12], and it is the one that generates fewer mesh cells from the available voxel library. All routines are performed using the voxel in the standing pose, with both arms down, *i.e.*, considering no dynamics. To streamline and accelerate the simulation routines, single slices of the voxel are analysed in specific studies, instead of the full body.

In the practical scenario of a BAN, the distance of the antenna to the body can vary in time, which impacts on antennas performance and gives a closer perspective to what happens in real life. The distance ranges from the antenna attached to the skin to a maximum value constrained by the flexibility of the clothes (*e.g.*, antenna being a button in a jacket).

Two antenna-body distance distributions are considered: Uniform in range [0, 2λ] (*i.e.*, [0, 24.5] cm), and "locally" Rayleigh with a maximum probable distance of 2 cm. The Uniform Distribution analyses the possible range of changes of radiation pattern within the distance interval, limited by 2λ, which is the maximum distance of antenna to the body (*e.g.*, wearable antenna on a coat). The Rayleigh Distribution describes a realistic scenario, where the distribution parameters are defined by the features of the antenna location on the clothe: goes from 0 to a large value, and it is concentrated on a central distance. Numerical simulations were performed for 20 distance samples, calculated according to the corresponding distribution.

Moreover, the following distance scenarios are considered:

- Scenario *All*: All antennas are at the same distance from the body in the range [0, 2λ]. This scenario is unrealistic, but it enables the possible range of changes in a 2λ interval

(up to 24.5 cm to the body).

- Scenario *Arms*: The arm antennas (AB_L and AB_R) are at the same distance from the body in the range [0, $\lambda/2.5$] (up to 5 cm to the body). The other antennas are attached to the body, or at a distance of $\lambda/5$. This scenario includes an antenna attached to the skin, to a watch, or a shirt.
- Scenario *Torso*: The distance of the torso antenna (TO_F) to the body varies in the range [0, 2λ]. The other antennas are attached to the body, or at a distance of $\lambda/5$. This scenario includes an antenna attached to the skin, to a shirt, or a button in a jacket, for instance. The range of distances goes up to 25 cm.

Table 6.7 summarises the scenarios defined for the different studies performed with the numerical simulation tool.

Table 6.7. Scenarios for the different studies with the numerical simulation tool.

	Antenna	**Antenna placements**	**Distance to the body**	**Body model**
Meshing Assessment	Patch	HE_L	0 cm	Voxel (Head)
Radiation Pattern Statistics	Patch, Dipole	HE_L, TO_F, AB_L, LT_L	Uniform Distribution: [0, 24.5] cm Rayleigh Distribution: max. probable 2 cm	Voxel (Head, Torso, Arm, Leg)
Comparison Between Phantoms	Patch	HE_F	Uniform Distribution: [0, 24.5] cm Rayleigh Distribution: max. probable 2 cm	Voxel (Half body) Homogeneous (Full body)
Static User	Patch	TO_F, WA_F, HE_F, HE_B, HE_L, HE_R, AB_L, AB_R, TO_B	Uniform Distribution: [0, 24.5] cm Distance scenarios: All, Arms, Torso	Voxel (Half body)
Dynamic User	Patch	TO_F, WA_F, HE_F, HE_B, HE_L, HE_R, AB_L, AB_R, TO_B	2 cm	Homogeneous (Full body)

6.5 Measurements

The measurements were performed at IST-TUL premises, in the microwave and millimetre-

wave laboratories of IT Lisbon [ITLa13]. These labs are equipped for antenna measurements in an anechoic environment and in real application scenarios. All the measurements were done with three human testers, a female and two males. The antenna used in measurements was the 2.45 GHz patch. Two sets of measurements were conducted as indicated in Table 6.8.

Table 6.8. Measurement scenarios.

	Antenna	**Antenna Placements**	**Distance to the body**	**Body Posture**
Antenna-Body Interaction	Patch	TX: HE_L	{0, 2 , 4} cm	Standing (ADOWN)
On-Body Channel Modelling	Patch	TX: AB_L RX: HE_L, TO_F, LT_L	2 cm	Standing (ADOWN, AFRONT, ABACK, AUP) Sitting (ABEND, ADOWN) Military (STEP, KNEE)

For the study on the antenna-body interaction, a gain transfer technique was used with a standard gain antenna (horn), to measure the on-body radiation pattern of the patch antenna, in an anechoic chamber. The calibrated horn antenna, with parameters G_h=11.25 dBi and half power beam-width α_{3dB}= 48º, was located at about 4 m away from the patch, and set as RX. The patch, isolated or on-body (TO_F), was the TX, with 0 dBm of transmitted power. The measurement setup was as indicated on Figure 6.8.

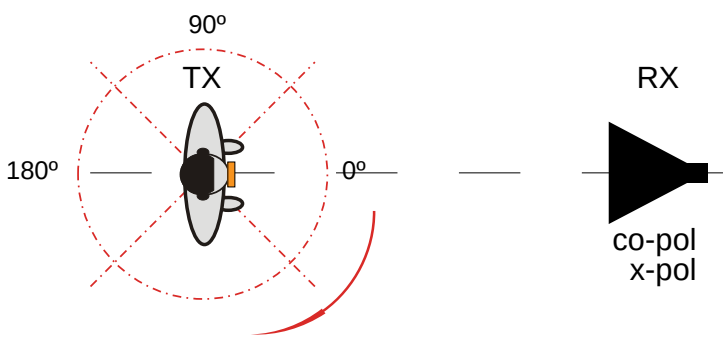

Figure 6.8. Measurement setup for antenna-body interaction.

The volunteers were placed on the automatic rotating positioner, keeping a constant speed of 2º/s in clockwise rotation. The system sequentially retrieves the received power, the phase and the rotation angle. The total azimuth radiation pattern is obtained from measurement of the co- and x-polarised patterns, achieved by positioning the horn antenna in the planes θ=0º and θ=90º.

The radiation pattern was initially measured for the isolated patch, and then for the patch on the body. In the latter, the patch was placed at {0, 2, 4} cm (*i.e.*, {0, 1/6λ, 1/3λ}), from the chest of the testers (location TO_F), Figure 6.9.

(a) TX side (Patch + Body). (b) General overview.

Figure 6.9. Measurement environment for the antenna-body interaction study.

For the on-body channel modelling study, the network topology was set as 1×1. Two patches were used, at 2 cm from the user. The TX was the patch located in the arm (AB_L). The RX was placed on the right ear (HE_R), on the torso (TO_F), or on the right leg (LB_R), recreating different on body links. Those links were measured for the standing, sitting and military postures, combined with different poses for the arms and the legs. Figure 6.10 presents an overview of the measurement environment devices and the human testers.

(a) Female (b) Male 1 (c) Male 2

Figure 6.10. Measurement environment.

The input signal at TX was set with a transmitting power of 0 dBm, within the [2.4, 2.5] GHz band, with a 250 kHz step. Both TX and RX antennas were connected to the two ports of a vector network analyser (Agilent E8361A), used to measure the s-parameter matrix, with a data acquisition rate of 100 samples per measurement.

A systematised matrix of connections was generated, identifying whether a given link has QLOS or NLOS, Table 6.9. The QLOS condition is applied whenever the antennas do not have any obstacle between them, but takes into account that they are not aligned with each other in the maximum gain direction.

Table 6.9. Matrix of connections (TX on AB_L).

		Head (HE_R)	Chest (TO_F)	Leg (LB_R)
Military	**MIL_STEP**	NLOS	QLOS	NLOS
	MIL_KNEE	NLOS	QLOS	NLOS
Standing	**STD_ADOWN**	NLOS	NLOS	NLOS
	STD_AFRONT	QLOS	QLOS	NLOS
	STD_AUP	QLOS	QLOS	NLOS
	STD_ABACK	NLOS	NLOS	QLOS
Sitting	**SIT_ADOWN**	NLOS	NLOS	NLOS
	SIT_ABEND	QLOS	QLOS	NLOS

The same postures were reproduced by human testers, but their anatomical differences create links with different lengths, Figure 6.11. These lengths correspond to the shortest path between the antennas, and were measured with a distance meter. Due to the short distances involved, the standard technique of using the phase shift to measure the length of the link was not used.

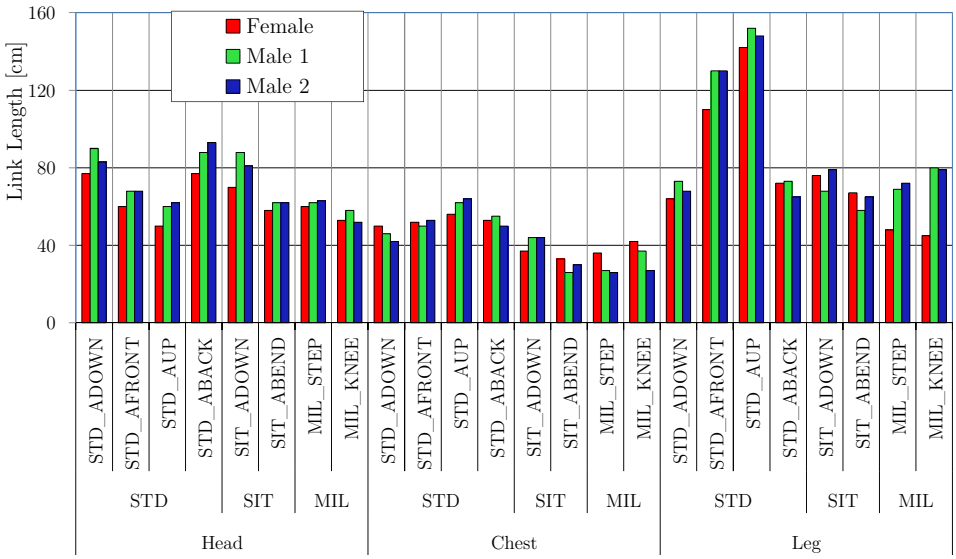

Figure 6.11. Length of on-body links.

Chapter 7

Analysis of Antenna-Body Interaction

This chapter contains the main findings of the statistical analysis for modelling antennas' behaviour near the human body. Section 7.1 provides general conclusions on the impact of the body in the propagation of a plane wave, namely on the electromagnetic fields distribution. Section 7.2 gives the statistics of the radiation pattern of an elementary source placed at different distances to the user. Section 7.3 provides results from the analysis of a patch antenna behaviour near the body, obtained through simulations. This section includes results from the assessment of *CST* meshing parameters, and from the comparison between homogeneous and voxel phantoms. Results from a measurement campaign are also provided.

7.1 Plane Wave

The analytical model described in Section 4.2.1, for the scattering of a plane wave near a dielectric cylinder, was implemented in *Matlab* [Matl12]. This model was applied in order to obtain the fields distribution around the body, calculated according to (4.1), and gather general conclusions on the impact of the body on the propagation of a plane wave, with TE and TM incidences. The torso, arms and legs were modelled as homogeneous circular cylinders, with different filling properties as described in Section 6.3, for 0.9 GHz and 2.45 GHz. Results are given normalised to incident fields, for both TM and TE modes.

In Figure 7.1 and Figure 7.2, one can see results for the total electric field (TM mode), at 0.9 GHz and 2.45 GHz, respectively, on a square of 1 m of distance from the centre of the cylinder. The same results are presented for TE mode in Figure 7.3 and Figure 7.4. Note that, at 0.9 GHz, the observation area corresponds to 3λ; while at 2.45 GHz, it corresponds to 8λ. The field values were not calculated inside the cylinder, which is represented by a black circle.

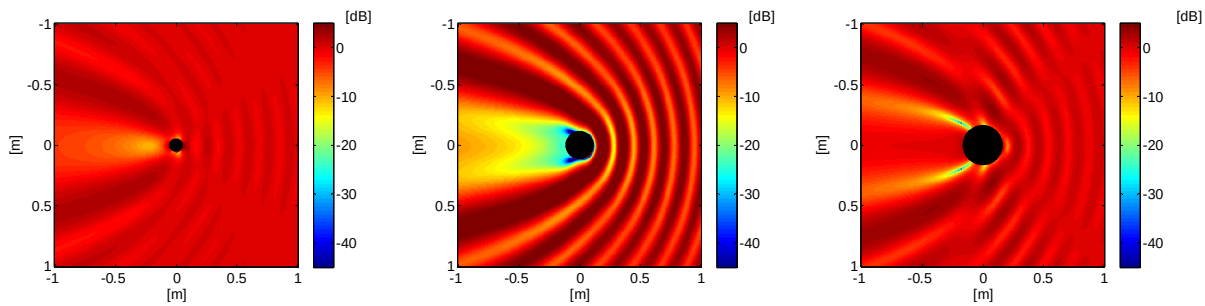

(a) arm (a/λ=0.15) (b) leg (a/λ=0.34) (c) torso (a/λ=0.47)

Figure 7.1. E field distribution at 0.9 GHz (TM Mode).

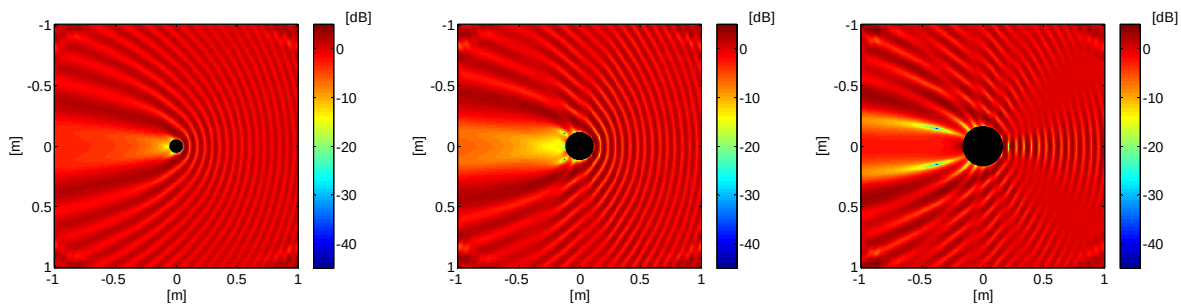

(a) arm (a/λ=0.40) (b) leg (a/λ=0.92) (c) torso (a/λ=1.28)

Figure 7.2. E field distribution at 2.45 GHz (TM Mode).

A general observation derived from these results is that the incoming plane wave is reflected when approaching the cylinder, with particular patterns of interference depending on the given

scenario, as expected. Moreover, this wave suffers a diffraction phenomenon around the cylinder. Higher or smaller shadow areas are observed, according to the dimensions of the body and composition of human tissues.

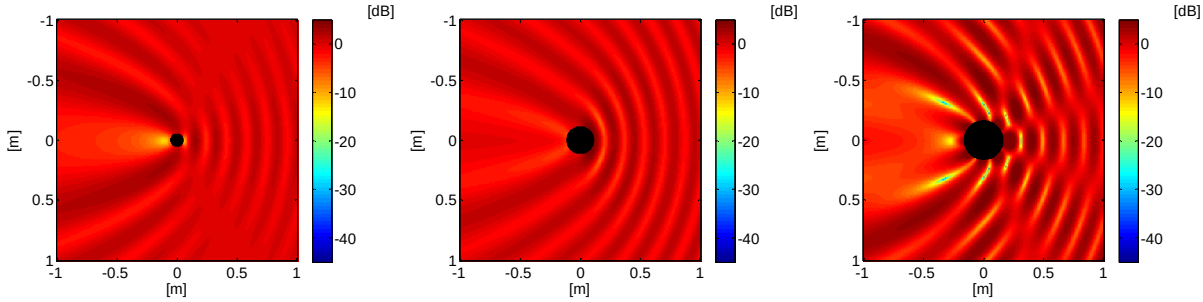

(a) arm (a/λ=0.15) (b) leg (a/λ=0.34) (c) torso (a/λ=0.47)

Figure 7.3. H field distribution at 0.9 GHz (TE Mode).

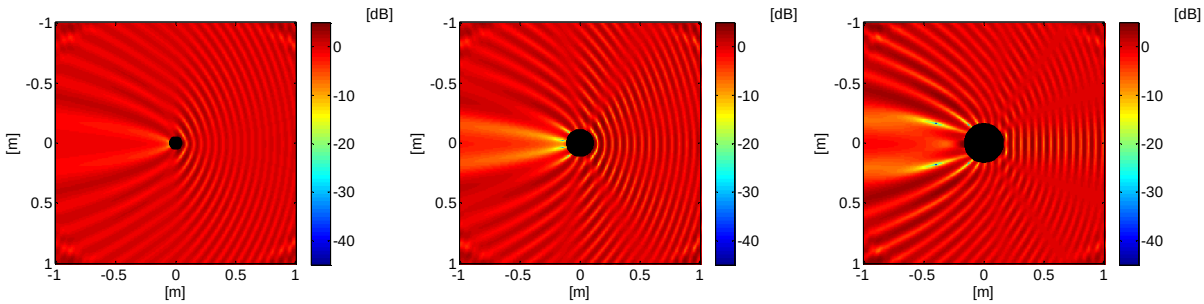

(a) arm (a/λ=0.40) (b) leg (a/λ=0.92) (c) torso (a/λ=1.28)

Figure 7.4. H field distribution at 2.45 GHz (TE Mode).

The results for the arm and the leg, which are both muscle filled, can be compared, allowing one to obtain conclusions on the impact of the dimensions of the body. The radius of the arm is smaller than the leg's one, being lower than 0.5λ at both frequencies, thus, a small impact on the propagation of the plane wave is expected. This is confirmed by the harder pattern of reflections, with well-defined shadow areas, for the leg, compared to the arm. At 2.45 GHz, leg dimensions are comparable to the wavelength.

Concerning the torso, which has larger dimensions and a lower permittivity, a clear pattern of reflections is observed, being also visible that field values in the deep shadow area are not so attenuated as in the leg, most likely because of diffraction, and also due to the higher penetration depth of fat compared to muscle. When comparing the results at different frequencies, it is also possible to analyse the impact of the wavelength. The larger wavelength at 0.9 GHz is clearly observed on the behaviour of the incoming wave. The diffraction around the cylinder is a good explanation for the narrow shadow area at 2.45 GHz, as the radius of cylinder is of the same order of magnitude of λ.

Although with slight differences, a similar behaviour is found for the total magnetic and

electric fields of the TE and TM modes, respectively.

A summary of the spatial statistics of E and H over the area of observation (a square of 2 m side) is presented in Table 7.1 and Table 7.2, for TM and TE modes respectively. Note that the values are normalised. This analysis enables to characterise the distribution of the fields, and to quantify the impact of the different body parts and frequencies. In both tables, the maximum likelihood estimates for the parameters of a Normal Distribution (assumed as a first approximation for the field values), at 95% confidence, are presented. A simple indication of field variations is also presented, by means of ΔE and ΔH, for TM and TE modes, respectively, defined by (6.16) and (6.17). It is important to keep in mind that this statistical analysis allows a general overview, being somehow sensitive to the numerical accuracy of calculations. Some approximations were done, namely on the number of terms of calculations, which were reduced to a few tens of terms.

Table 7.1. Statistical analysis: TM Mode.

	f = 0.9 GHz			f = 2.45 GHz		
	$\overline{E^N}$ [dB]	σ_E^N [dB]	ΔE [dB]	$\overline{E^N}$ [dB]	σ_E^N [dB]	ΔE [dB]
Arm	< 0.1	0.5	15.7	-0.1	1.6	35.1
Leg	-1	5.5	84.2	0.1	1.8	42.0
Torso	-0.1	1.8	43.5	-0.2	1.7	51.4

Table 7.2. Statistical analysis: TE Mode.

	f = 0.9 GHz			f = 2.45 GHz		
	$\overline{H^N}$ [dB]	σ_H^N [dB]	ΔH [dB]	$\overline{H^N}$ [dB]	σ_H^N [dB]	ΔH [dB]
Arm	< 0.1	1.1	35.7	-0.2	1	16.6
Leg	-0.2	1.3	29.3	-0.2	1.8	38.9
Torso	-0.5	2.9	47.7	-0.1	1.9	48.2

In general, the field distribution presents a similar behaviour for both frequencies, with small mean values (< 1 dB). This result shows that the plane wave does not suffer a major attenuation when approaching the body. Anyway, the standard deviations (up to 5.5 dB for muscle) and, especially the field variations with several orders of magnitude (up to 84 dB), are considerable when compared to the mean values. From the visual inspection of the field distribution, it is clear that these disturbances occur in the area immediately surrounding the body.

The statistical analysis does not evidence main differences according to the frequency of the plane wave. For the same frequencies and materials, it is possible to analyse the impact of different sized body parts on the field behaviour. Lower fluctuations (values of the standard deviation lower than 1.6 dB) are observed for the arm, which is the smallest body part, as its dimensions are smaller than λ. However, this statement also depends on the relative size (to λ)

of the area under observation. For instance, in the TM mode, for the arm at 2.45 GHz ($a/\lambda = 0.3$), fluctuations over the mean value round 1.6 dB, but fluctuations around 5.5 dB are found for the leg at 0.9 GHz ($a/\lambda = 0.3$).

High values of ΔE and ΔH were obtained for all the cases, ranging from 16 dB to 84 dB. These values are significantly higher than the standard deviation ones over the observation area, which is explained by the existence of deep shadow areas focused on small points near the body.

Concerning TE and TM modes, and as seen visually from the field distribution, a common trend in the fields behaviour is found, with similar mean values for all the cases. The field variations in the TE mode are smoother compared to the TM case, but it is important to state that this might be a result of the numerical accuracy of the simulations.

The results for the plane wave propagation confirm the well-known phenomenon of reflection and refraction when it approaches the body. Harder patterns of reflections are verified for larger body parts (compared to the wavelength), and narrower shadow areas become visible for tissues with larger penetration depths.

7.2 Elementary Source

The analytical model described in Section 4.2.2 to obtain the far-field of a elementary source (Hertz dipole) near a dielectric cylinder was implemented in *Matlab* [Matl12]. The idea is to extract statistics of the user's influence in the performance of the source, when placed at different distances to the body. These distances range from the antenna attached to the skin to it being attached to clothes. Expressions (4.12), (4.14) and (4.15) were applied to obtain the radiation patterns for the u_ρ, u_φ and u_z orientations, respectively, on the x-y plane of Figure 4.3. Note that each pattern is normalised by its maximum. Two frequency bands are considered in this study, 0.9 GHz and 2.45 GHz.

An overview of the main outcome and different statistics are given in what follows. The analysis focuses on the comparison of patterns for the three orientations of the source, and at different body-source distances, modelling of field distributions, and average field fluctuations. The full set of results is left for Annex B.

Figure 7.5 and Figure 7.6 show the average radiation patterns for the different body parts, in terms of electric field, $\overline{E(\theta)}$, obtained at 0.9 GHz and 2.45 GHz, respectively.

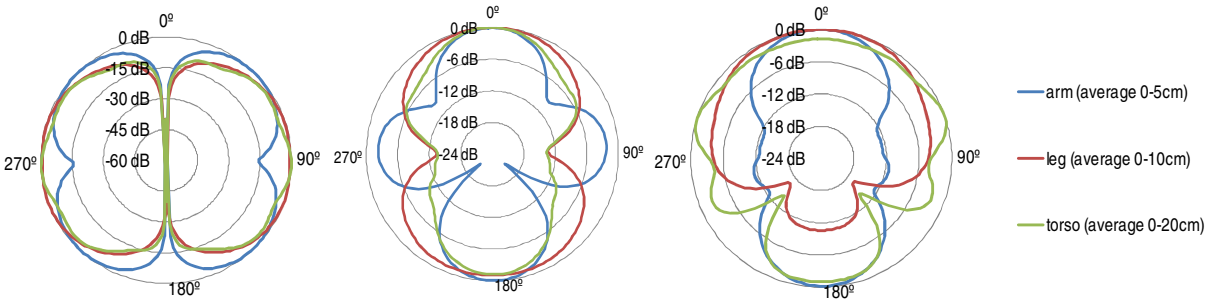

(a) u_ρ (b) u_φ (c) u_z

Figure 7.5. Average radiation patterns (0.9 GHz).

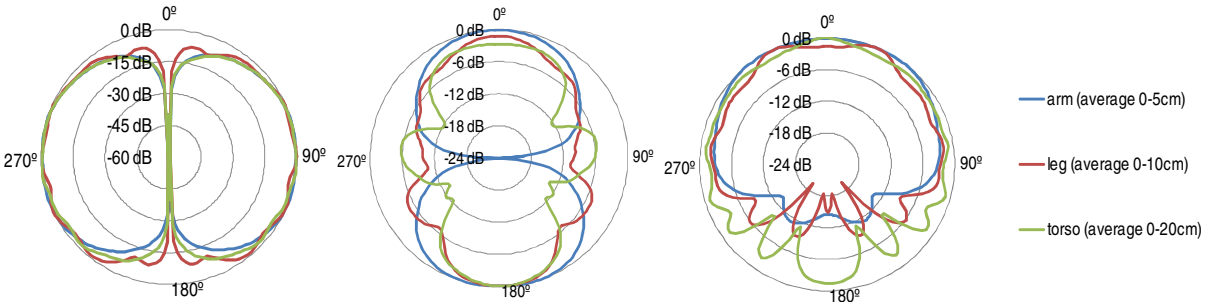

(a) u_ρ (b) u_φ (c) u_z

Figure 7.6. Average radiation patterns (2.45 GHz).

A general comment is that radiation patterns are symmetric with respect to the x axis, as expected. For the perpendicular polarisation (u_ρ), it is observed that the cylinder has a minor impact on the radiation pattern, as the source does not radiate on its own direction. For the u_φ and u_z polarisations, the influence of the body is clearly observed, particularly with a narrower pattern being obtained and with the "absorption" of backward radiation by the body. This influence evidently depends on body dimensions, tissue's composition, distance to the source, and frequency. For the u_φ orientation, a narrower and modified pattern is visible, while for the u_z one, the predominant effect is the attenuation of backward radiation. This phenomenon is particularly visible at 2.45 GHz (*e.g.*, attenuation up to 20 dB in case of leg at 2.45 GHz).

Figure 7.7 shows the radiation patterns for the leg scenario, for different values of d. One can observe the modified patterns, resulting from reflections on the cylinder. These reflections can be constructive or destructive, depending on the distance of the source to the body.

Table 7.3 shows the average ($\overline{\Delta E^d}$) and the maximum ($\overline{\Delta E^d_{max}}$) differences between the field obtained at distance d and at a reference distance $d_0 = 0.05$ cm. The averaging is performed for all the considered angles.

For the u_ρ orientation, no major differences in the shape of the patterns between 0.9 and 2.45 GHz are found at the different body-source distances. However, some fluctuations in the patterns are found at 2.45 GHz, probably resulting from numerical inaccuracy. For the u_φ

orientation, at 0.9 GHz, the average difference between patterns can be of 10 dB (*e.g.*, for the arm); at 2.45 GHz, narrower patterns are observed with lower differences (*e.g.*, up to 4 dB for the arm). For the u_z orientation, higher gains are found for increased distances to the body. On average, larger variations with distance are found for 2.45 GHz (*e.g.*, up to 19 dB for the arm).

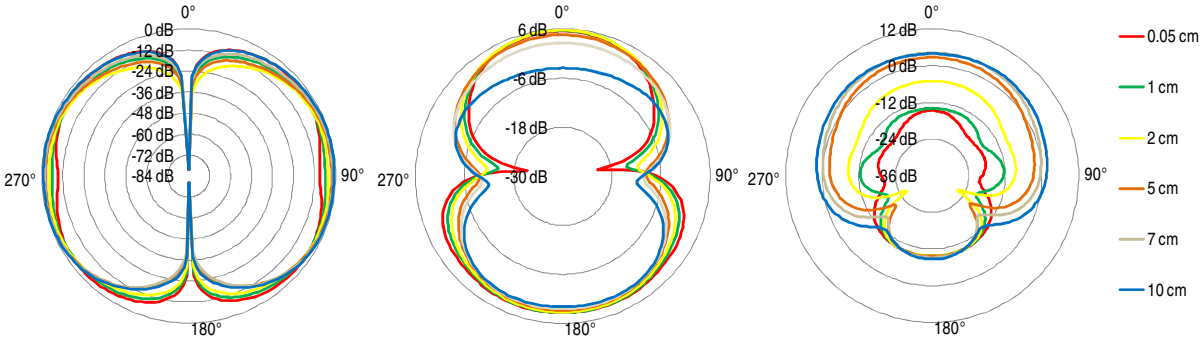

(a) u_ρ (b) u_φ (c) u_z

Figure 7.7. Radiation patterns for leg for different d (0.9 GHz).

Table 7.3. Statistical overview for different d: u_z orientation.

	d [cm]	0.9 GHz		2.45 GHz	
		$\overline{\Delta E^d}$[dB]	$\overline{\Delta E^d_{max}}$ [dB]	$\overline{\Delta E^d}$[dB]	$\overline{\Delta E^d_{max}}$ [dB]
arm	**1**	3.4	13.2	13.7	41.5
	2	5.7	17.6	16.6	46.7
	3	7.4	24.3	18.2	48.9
	4	7.4	22.7	18.9	49.5
	5	7.0	22.5	18.7	48.8
leg	**1**	2.5	7.0	5.0	20.3
	2	7.2	12.6	7.3	24.8
	5	11.7	20.0	8.8	25.7
	7	12.8	22.0	8.4	25.8
	10	13.8	22.9	9.3	26.9
torso	**5**	5.0	17.5	7.1	22.5
	10	6.2	24.3	6.6	22.9
	15	6.9	28.1	7.1	22.0
	20	6.9	30.6	7.5	20.7

A comprehensive statistical study on the variations of radiation patterns was carried out for all scenarios. The average patterns and corresponding standard deviations are one of the main outcomes of this study. Figure 7.8 to Figure 7.10 show the results for a vertical polarised elementary source near the leg, in the uniformly distributed interval]0, 10] cm. Note that those values have been calculated in linear units and then expressed in logarithmic scale. Moreover, for each scenario, the radiation patterns are normalised to their maximum.

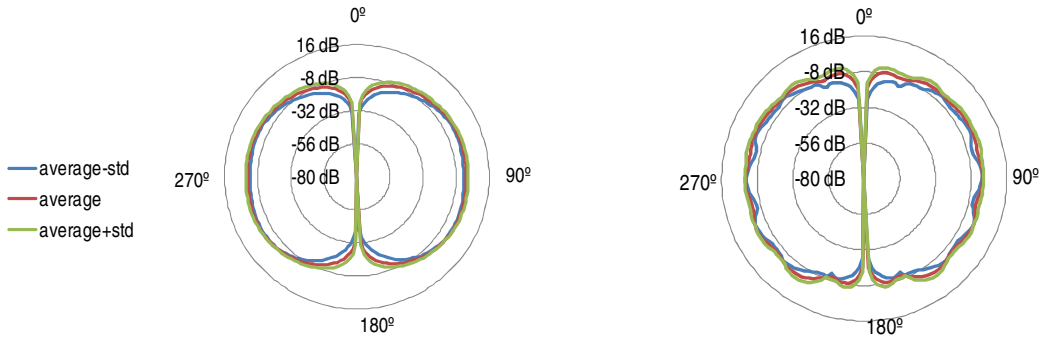

(a) f = 0.9 GHz (b) f = 2.45 GHz

Figure 7.8. Average radiation patterns for leg: u_ρ orientation.

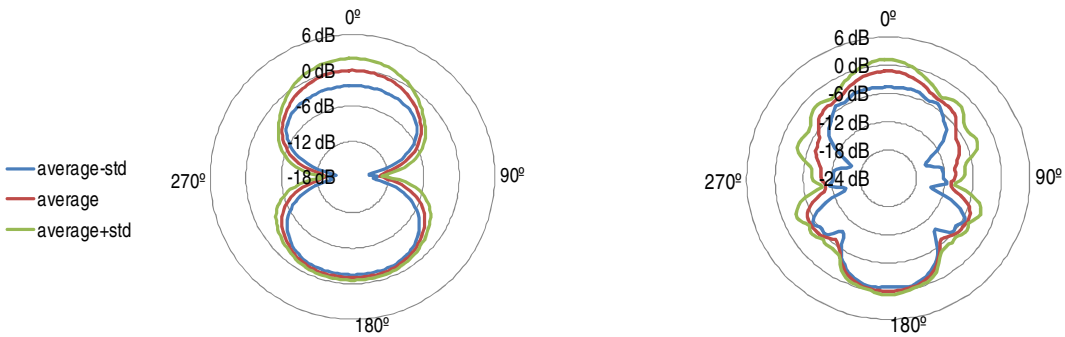

(a) f = 0.9 GHz (b) f = 2.45 GHz

Figure 7.9. Average radiation patterns for leg: u_φ orientation.

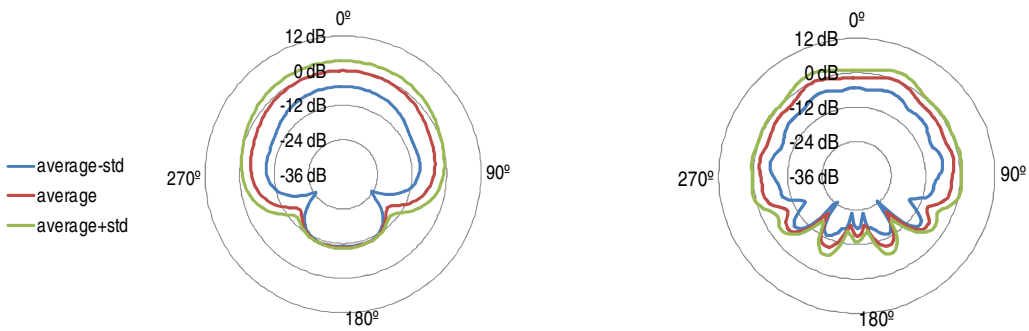

(a) f = 0.9 GHz (b) f = 2.45 GHz

Figure 7.10. Average radiation patterns for leg: u_z orientation.

The average patterns for u_ρ orientation are similar for the different body elements; some attenuation in backward lobe is verified for the torso, probably resulting from its larger dimensions and higher penetration depth of fat tissue. With an u_φ orientation, the average patterns experience an increase of directivity and some attenuation on body's direction. The average patterns for u_z orientation show a clear suppression of backward radiation, especially at 2.45 GHz, suggesting absorption by the body tissues. The fluctuations of the average radiation pattern depend on the angle of observation (φ). The maximum fluctuation is obtained for $\varphi = 180^{\circ}$, that is, the backward direction.

For the leg and the torso, the large observation distances were divided in smaller intervals, the average pattern being then computed for each new distance interval. This work was done for the leg, results being presented from Figure 7.11 to Figure 7.13; the same analysis is shown in Annex B for the torso.

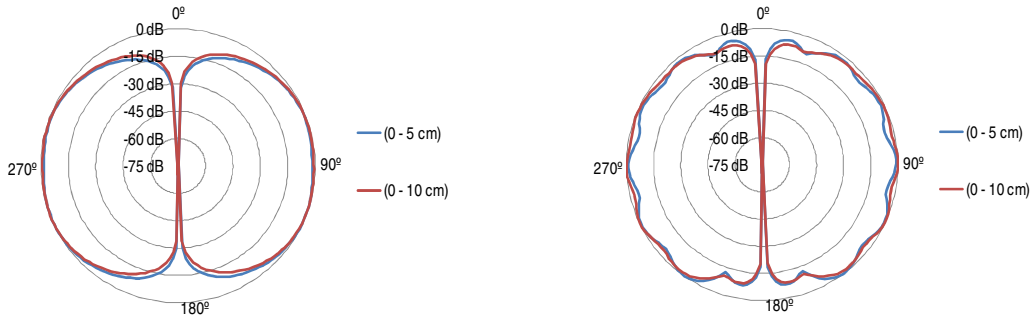

(a) $f = 0.9$ GHz (b) $f = 2.45$ GHz

Figure 7.11. Average radiation patterns at different distances: u_ρ orientation (leg).

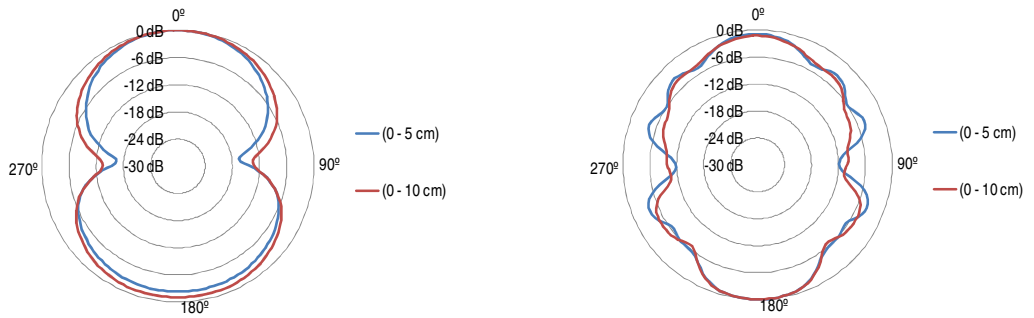

(a) $f = 0.9$ GHz (b) $f = 2.45$ GHz

Figure 7.12. Average radiation patterns at different distances: u_φ orientation (leg).

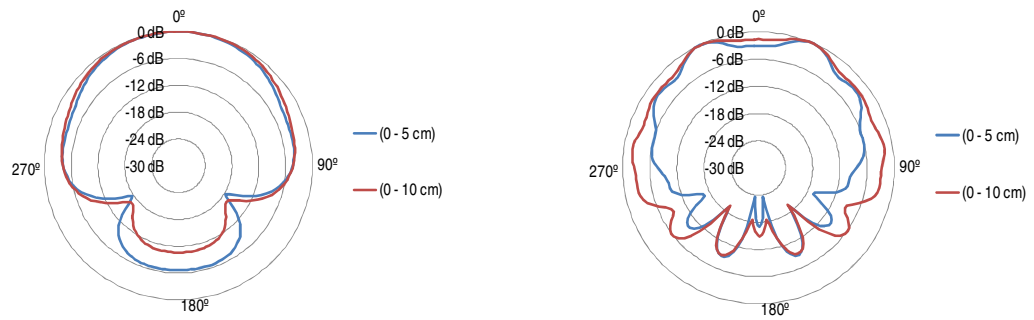

(a) $f = 0.9$ GHz (b) $f = 2.45$ GHz

Figure 7.13. Average radiation patterns at different distances: u_z orientation (leg).

A general trend is that the shape of the radiation patterns remains almost constant for the different average intervals; the more apparent modification is observed in gain values. For both body parts, the noticeable changes occur for the u_z orientation, some changes being also visible in u_φ orientation. As expected, the torso patterns experience higher alterations for the shorter interval distances (*e.g.*, one gets a 25 dB variation at 5 cm and 14 dB at 20 cm). Similar conclusions were gathered for 0.9 and 2.45 GHz, with small fluctuations at 2.45 GHz.

As a complement to the statistics given above, the PDFs of the envelope of the obtained E field are shown from Figure 7.14 to Figure 7.16, for given values of φ. Note that, for the u_ρ orientation, only the 90º orientation is analysed, as the 270º orientation is symmetric to 90º, and 0º/180º are directions of nulls. A simple visual inspection shows an exponential decay in most of the histograms, therefore, a fitting to the Exponential Distribution with (inverse) rate parameter μ_{EE} is plotted together with the results from the χ^2 test.

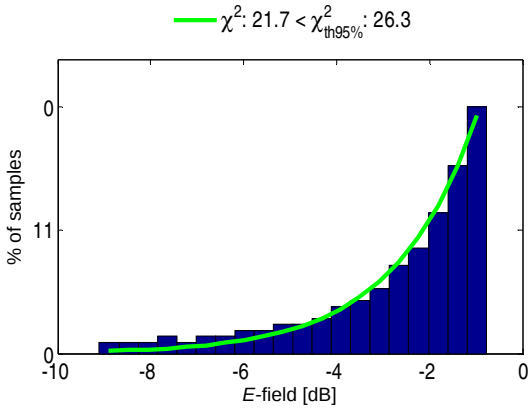

(a) $f = 0.9$ GHz

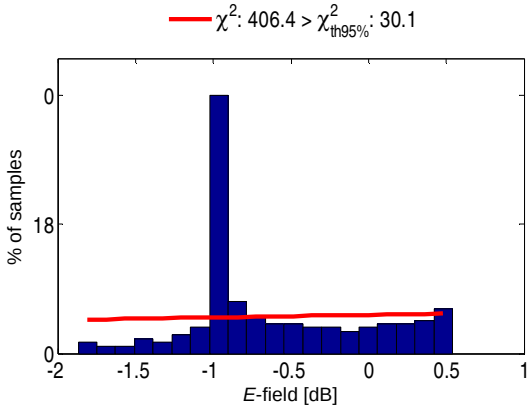

(b) $f = 2.45$ GHz

Figure 7.14. Histogram plots for leg: u_ρ orientation.

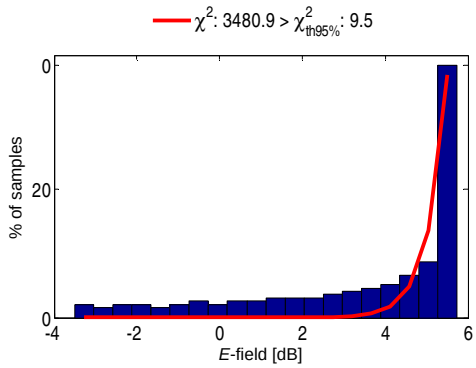

(a) $\varphi = 0^o$

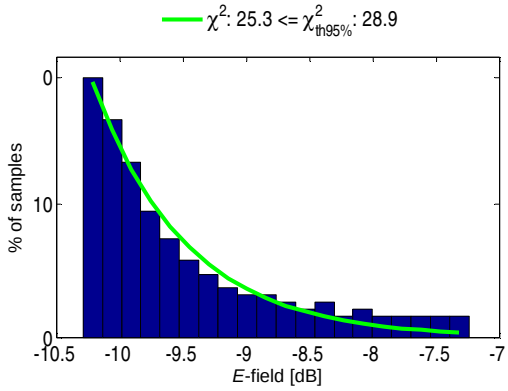

(b) $\varphi = 90^o$

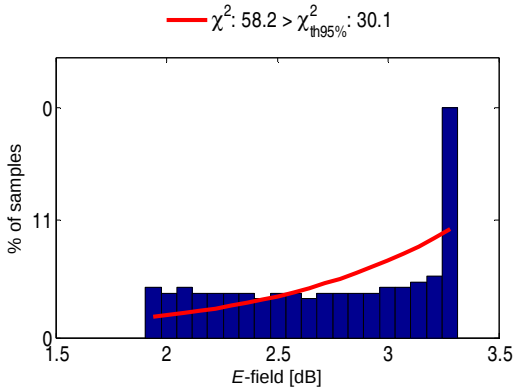

(c) $\varphi = 180^o$

Figure 7.15. Histogram plots for leg: u_φ orientation (0.9 GHz).

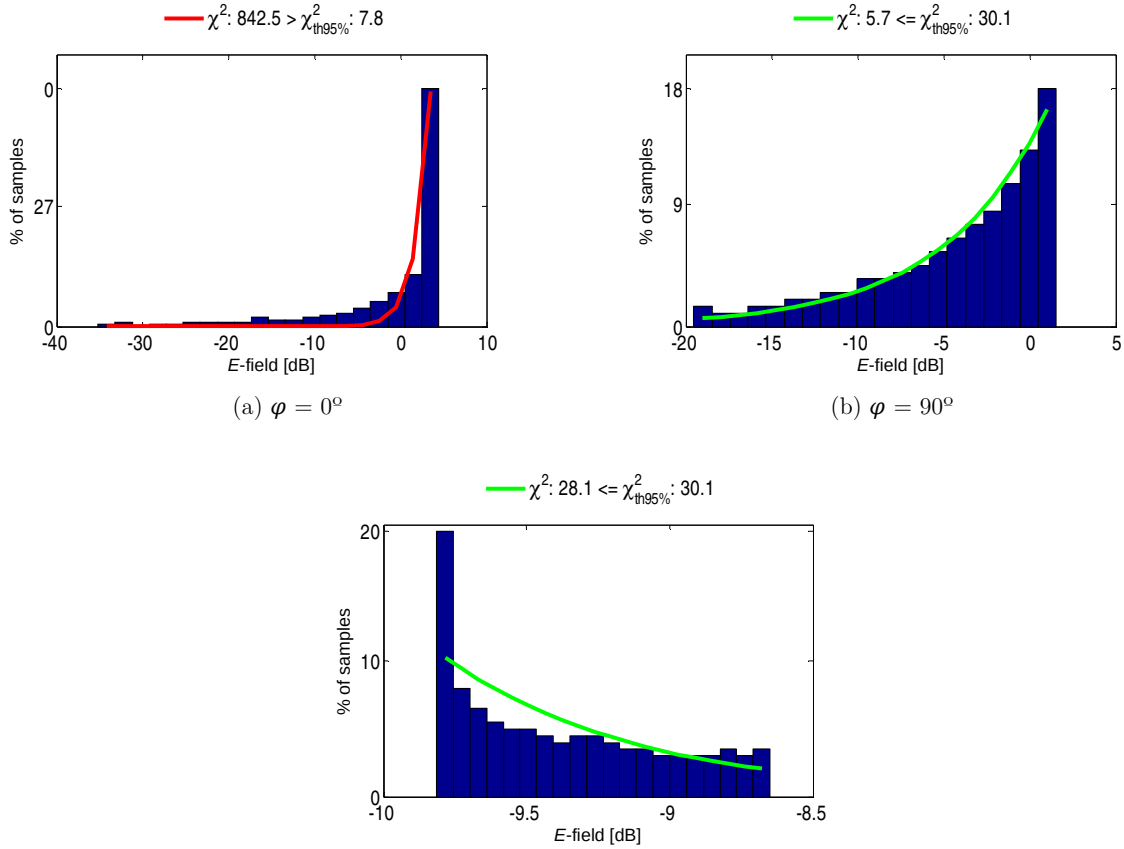

(a) $\varphi = 0^{o}$ (b) $\varphi = 90^{o}$

(c) $\varphi = 180^{o}$

Figure 7.16. Histogram plots for leg: u_z orientation (0.9 GHz).

It is assumed that the fitting to the Exponential Distribution is successful if the result of the test is lower than the threshold for a 95% confidence interval ($\chi^2_{th95\%}$); otherwise, it is not appropriate. An overview of these results is presented from Table 7.4 to Table 7.6.

Table 7.4. Statistical overview: u_ρ orientation.

	φ	0.9 GHz				2.45 GHz			
		μ_{EE}	$\chi 2$ test	$\chi^2_{th95\%}$	Exp. Dist. Validity	μ_{EE}	$\chi 2$ test	$\chi^2_{th95\%}$	Exp. Dist. Validity
arm	90°	0.03	10.32	22.36	yes	0.05	3.08	27.59	yes
leg		0.01	21.69	26.30	yes	0.10	406.38	30.14	no
torso		0.01	1743.98	21.03	no	0.05	149.91	30.14	no

For the u_ρ orientation, similar distributions are found in the majority of the scenarios, following an exponential decay. A higher dispersion of values is verified at 0.9 GHz. For the u_φ orientation, the $0^{o}/90^{o}/180^{o}$ orientations are analysed. The distribution of fields for the observed directions follows an exponential decay. Small dispersions are found whenever there is some suppression of back radiation. Higher dispersion of values is found for directions of nulls;

higher variations are found at 0º. For the u_z orientation, the 0º/90º/180º directions are analysed. In most of the cases, the histograms also experience exponential decays. A small dispersion of values is verified at 180º for the cases where there is suppression of backward radiation. Higher fluctuations are found at 0º. Large fluctuations of the field are found, *e.g.*, 11.6 dB and 2.3 dB at $\varphi = 0º$ and $\varphi = 180º$, respectively.

Table 7.5. Statistical overview: u_φ orientation.

	φ	0.9 GHz				2.45 GHz			
		μ_{EE}	χ^2 test	$\chi^2_{th95\%}$	Exp. Dist. Validity	μ_{EE}	χ^2 test	$\chi^2_{th95\%}$	Exp. Dist. Validity
arm	0º	0.03	3.29	30.14	yes	4.96	660.83	12.59	no
	90º	0.05	7.03	30.14	yes	0.02	61.66	30.14	no
	180º	0.06	0.75	30.14	yes	1.06	26.51	30.14	yes
leg	0º	2781.50	3480.86	9.49	no	0.17	325.17	19.68	no
	90º	33874.01	25.69	28.87	yes	0.02	499.34	30.14	no
	180º	2.96	58.21	30.14	no	0.00	238.45	15.51	no
torso	0º	0.06	567.17	21.03	no	0.06	58.55	30.14	no
	90º	0.20	6.02	30.14	yes	0.04	8.63	30.14	yes
	180º	0.02	7.84	30.14	yes	0.27	54.44	30.14	no

Table 7.6. Statistical overview: u_z orientation.

	φ	0.9 GHz				2.45 GHz			
		μ_{EE}	$\chi 2$ test	$\chi^2_{th95\%}$	Exp. Dist. Validity	μ_{EE}	$\chi 2$ test	$\chi^2_{th95\%}$	Exp. Dist. Validity
arm	0º	0.16	0.90	30.14	yes	0.11	113.08	11.07	no
	90º	0.20	7.19	30.14	yes	0.09	12.29	23.68	yes
	180º	0.12	0.90	30.14	yes	253476.50	14.31	25.00	yes
leg	0º	0.08	842.50	7.81	no	0.10	68.14	30.14	no
	90º	0.04	5.71	30.14	yes	0.42	3616.04	9.49	no
	180º	77089.74	28.13	30.14	yes	0.90	296.50	30.14	no
torso	0º	0.04	108.30	30.14	no	0.04	274.32	23.68	no
	90º	0.03	281.44	30.14	no	0.04	194.59	30.14	no
	180º	0.00	1523.14	18.31	no	0.05	326.12	27.59	no

From the PDFs analysis, it is concluded that the fitting to the Exponential Distribution is appropriated in the directions of strong lobes, with small fluctuations from the average (small values of standard deviation). But, whenever there are secondary lobes, or a higher dispersion of values, fitting is inefficient.

Another outcome is the fluctuation of the standard deviation according to the angle of

observation; an example is presented in Figure 7.17, for the u_z orientation.

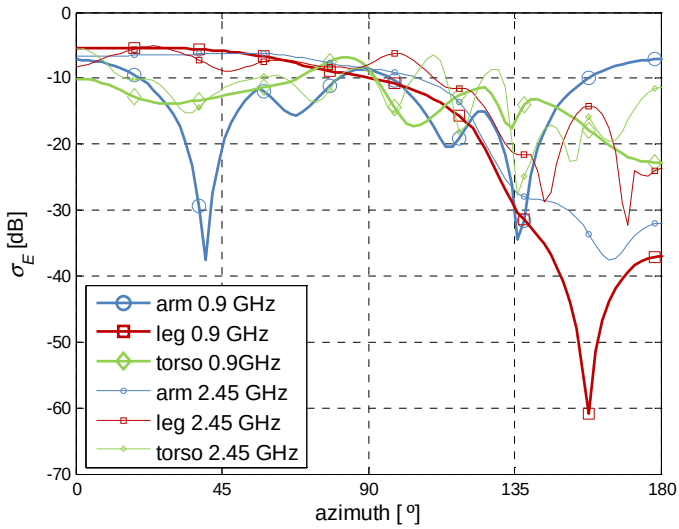

Figure 7.17. Fluctuations of σ_E: u_z orientation.

A general comment is that σ_E depends on the angle of observation, whatever the orientation of the source. The general trend is that σ_E decreases from $\varphi = 0^{\circ}$ to $\varphi = 180^{\circ}$, in range $\sigma_E \in$ [-60, -5] dB. Exception is verified for the 0.9 GHz arm scenario; this case experiences the highest variation of σ_E at $\varphi = 180^{\circ}$. The behaviour of σ_E does not show a clear correlation of the results with the frequency, although higher variations are generally experienced at 2.45 GHz.

Results from this study confirm that the larger body segments have a stronger impact on the field produced by an elementary source (Hertz dipole) – with different polarisations, and at different distances from the body –, especially when the antenna is closer to the body. An Exponential Distribution of the fields with distance in the directions of strong lobes (forward direction of the body) is observed. These lobes present small fluctuations from the average (standard deviation lower than 5 dB), while great fluctuations (up 24 dB) are found for other directions (backwards).

7.3 Patch Antenna

7.3.1 Meshing Assessment

The statistical concept described in Section 4.1 to model the antenna-body interaction was implemented in *CST* with a patch near a voxel model. A performance assessment was initially

done for some features of *CST*, based on the meshing scenarios defined in Section 6.4, in order to elect the mesh settings that conduct to a most favourable trade-off between numerical accuracy and simulation time.

The numerical accuracy of *CST* is tight linked with the error sources of every discretisation method, either because the simulation model is in disagreement with the reality, or because the numerical simulation is subject to errors itself.

The assessment is based on the outputs, in terms of:

- Memory;
- Simulation time;
- Impact on radiation pattern and s-parameters accuracy.

Note that the simulation time is a decisive criterion for defining the "optimal" configuration. The outputs in terms of memory and simulation time merely provide an indication value, as the conditions of computation were not the same over all the simulations (*e.g.*, number of threads, allocated memory, temporary files or internal temperature). For this assessment, a regular laptop, with an Intel Core 2 Duo, @ 2.40 GHz, 3 GB RAM was used.

The selection of the frequency band for the numerical simulations takes into account the *CST* limitations in terms of material parameters, not only because not all the human tissues are considered in the voxel model, but also because the values of material parameters are defined for a single frequency (not for the entire band of interest). The frequency dependency of the material values, Figure 7.18, has been analysed, being observed that the relative permittivity does not change significantly from 0 to 3 GHz, but the conductivity of most of the tissues has considerable changes.

A narrowband analysis (*e.g.*, [2.4, 2.6] GHz) has the disadvantage of reaching unfeasible computation times, while a wideband one performs faster due to the shorter excitation signal. However, the upper frequency should be chosen carefully, not being too large, as the number of mesh cells rapidly increases with it. Having these constraints in mind, the frequency band of [0.3, 2.6] GHz was chosen for the performance assessment.

Table 7.7 summarises the general properties – in terms of number of mesh cells, memory and time of simulation – of the test scenarios chosen for the performance assessment study, which exploit different combinations of the RL and LW parameters.

The decrease of RL and LW parameters, *i.e.*, the decrease of accuracy, leads to a significant reduced number of mesh cells, required memory, and simulation time. While the simulation time is decisive, but does not present a physical problem, the memory is the bottleneck for the available resources; a huge number of mesh cells requires inexistent memory resources. A

reduction of 13 times on the number of mesh cells is verified from the most accurate scenario (RL10/LW14) to the poorer one (RL7/LW10 case), resulting in incomparable memory requirements (2.8 GB *vs.* 0.4 GB) and computation times (34 min *vs.* 2 min). A quick analysis of these results suggests that the RL7/LW10 configuration looks an interesting alternative to the reference scenario. Nevertheless, it is essential to test its performance in terms of radiation patterns and s-parameters.

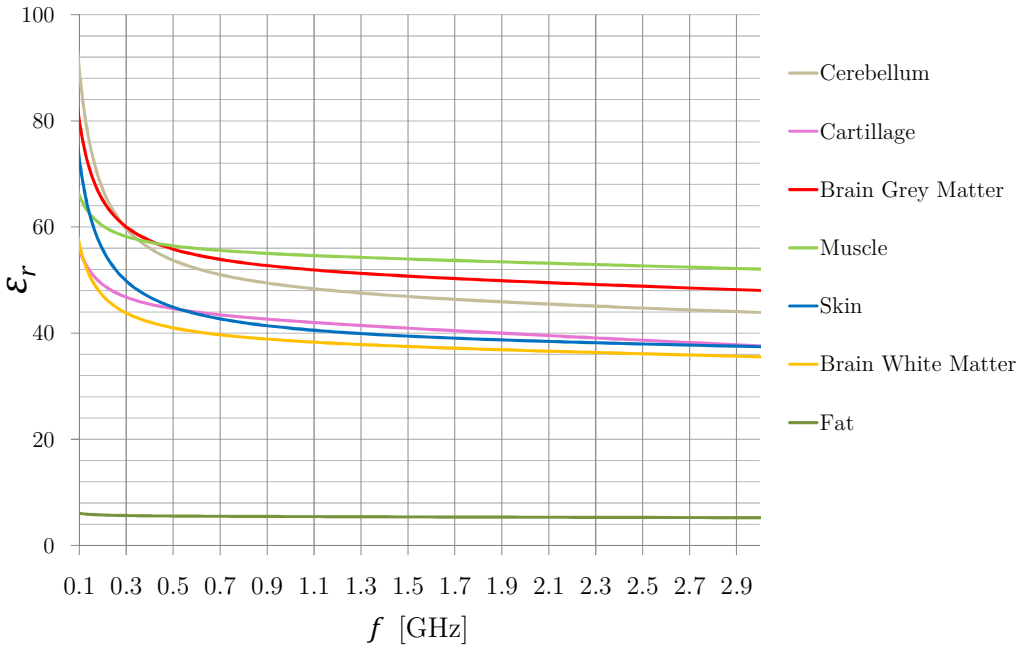

(a) Permittivity

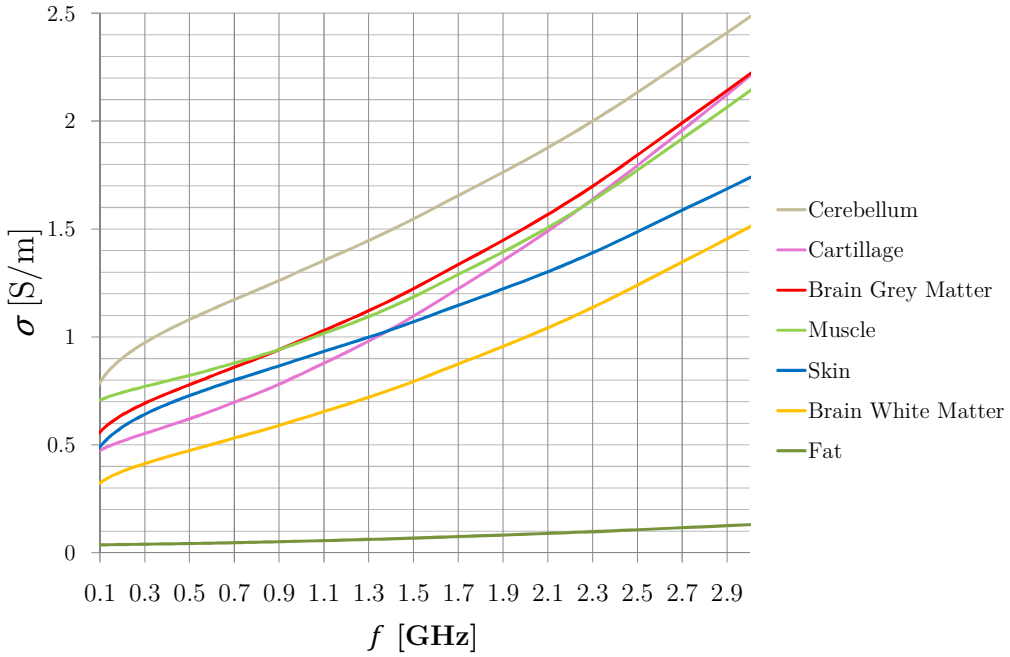

(b) Conductivity

Figure 7.18. Frequency dependence of head tissues.

Table 7.7. Complexity of selected meshing scenarios, at [0.3 – 2.6] GHz.

RL	**10**			**7**	
LW	**14**	**12**	**10**	**16**	**10**
mesh cells [10^6]	8.8	5.7	3.5	2.4	0.7
memory [GB]	2.8	2.0	1.3	0.9	0.4
simulation time [min]	34	22	11	10	2

Figure 7.19 displays the radiation patterns of the patch antenna isolated in free space and then near the human head (RL10/LW14 reference scenario). Note that the patch was located at HE_L, attached to the body. The most visible effects of the presence of the body are a partial attenuation of the back side of radiation, and a general reduction of gain values. A decrease of 1.19 dB in gain is verified, meaning a loss of 24% of power.

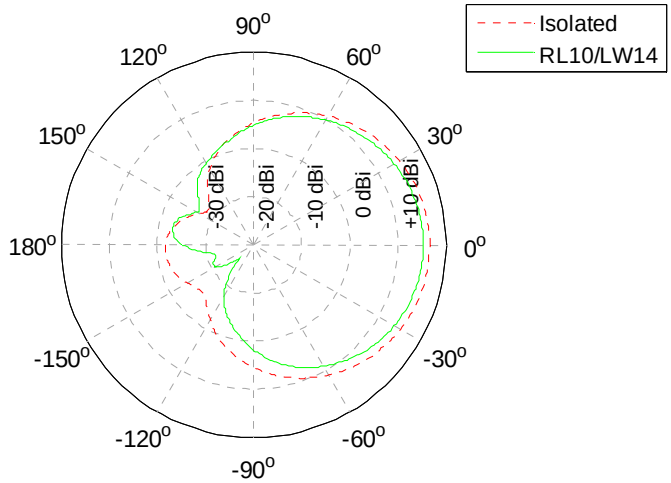

Figure 7.19. Patterns for free space and for HE_L (RL10/LW14).

Figure 7.20 displays the radiation patterns of the patch antenna in the same conditions near the human head, but for the different mesh configurations. A quick visual inspection shows the minor discrepancies between the plots, the main differences being in the backside of radiation, thus, meaning that the overall influence of meshing in the radiation pattern is not significant.

Table 7.8 quantifies the average (in all directions) and weighted (in direction of main lobe) differences between the radiation pattern of the reference scenario and the test ones. Also, the differences in gain in the direction of maximum radiation and radiation efficiency (η_{rad}) are presented. As expected, the decrease of accuracy leads to higher differences in the radiation patterns (average errors up to 12%), but the low values of weighted error (in the direction of main lobe) show that these discrepancies are not important, as they do not occur in the direction of interest (main lobe). This is confirmed by the differences in gain in the direction of maximum radiation that are insignificant (< 0.1 dB), except for the RL7/LW10 configuration, ΔG = 0.61 dB, due to its poorer accuracy.

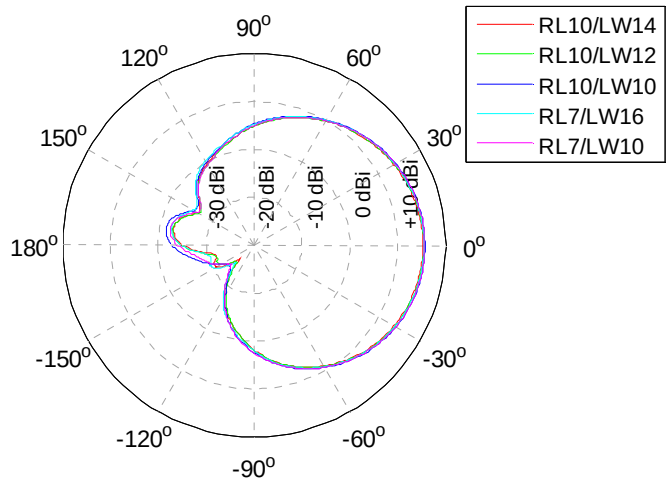

Figure 7.20. Patterns for different mesh configurations (HE_L).

Table 7.8. Radiation patterns error (compared to RL10/LW14).

RL	**10**		**7**	
LW	**12**	**10**	**16**	**10**
$\overline{\Delta G}$ [%]	2.38	5.43	3.67	12.79
$\overline{\Delta G_w}$[%]	0.99	1.77	1.98	10.67
η_{rad} [dB]	-1.97	-1.86	-1.86	-1.85
$\Delta\eta_{rad}$ [dB]	-0.04	0.07	0.07	0.08
G [dBi]	5.37	5.47	5.34	6.00
ΔG [dB]	-0.02	0.08	-0.05	0.61

Regarding the accuracy of s-parameters, Figure 7.21 displays the input return loss (s_{11}) plots for the different meshing configurations, while Table 7.9 compares their performance with the reference scenario.

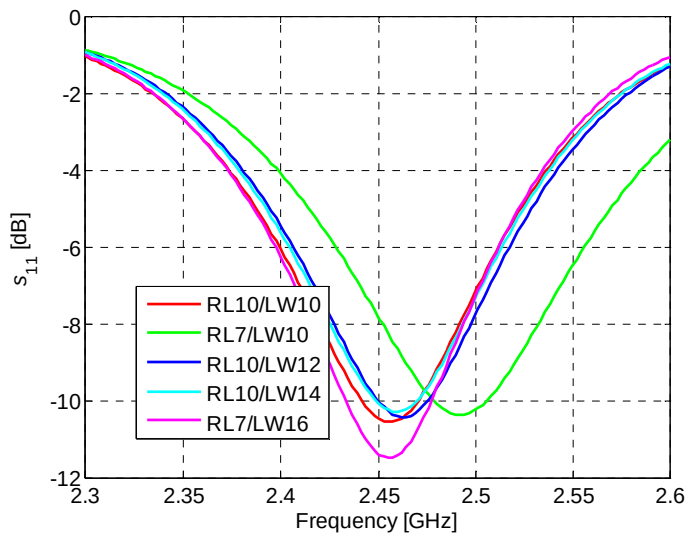

Figure 7.21. s_{11} curves for different mesh configurations ([0.3 – 2.6] GHz).

Table 7.9. Return loss performance (compared to RL10/LW14).

RL	**10**			**7**	
LW	**14**	**12**	**10**	**16**	**10**
s_{11} [dB]	-10.30	-10.43	-10.56	-11.49	-10.36
Δs_{11} [dB]	-	-0.13	-0.26	-1.19	-0.06
f_r [GHz]	2.46	2.46	2.46	2.46	2.49
$\Delta f_r/f_r$ [%]	-	0.08	0.20	0.20	1.30

In the reference scenario, the presence of the head model shifts the resonant frequency of the patch from 2.45 GHz to 2.46 GHz; moreover, s_{11} increases 2.05 dB, meaning that the power reflected at the resonance frequency has increased by 60.4%, compared to the isolated antenna. The results for different mesh configurations show minor changes for any of the scenarios, both in terms of shifts in resonant frequency or in s_{11}. Only the RL7/LW10 scenario presents a significant shift on the resonant frequency, which is no more than 32 MHz, although its s_{11} value is in agreement with the reference scenario. The RL7/LW16 configuration presents a pronounced return loss curve, compared to the other scenarios, with an irrelevant increase of 1 dB in s_{11}.

Figure 7.22 presents a graphical overview of the performance assessment study, outlining the main results for each mesh configuration. Based on the different results under study, it is concluded that the accuracy of the candidate configuration RL7/LW10 is poor compared to the others, not only in terms of radiation pattern, but also in terms of return loss behaviour (shift in frequency).

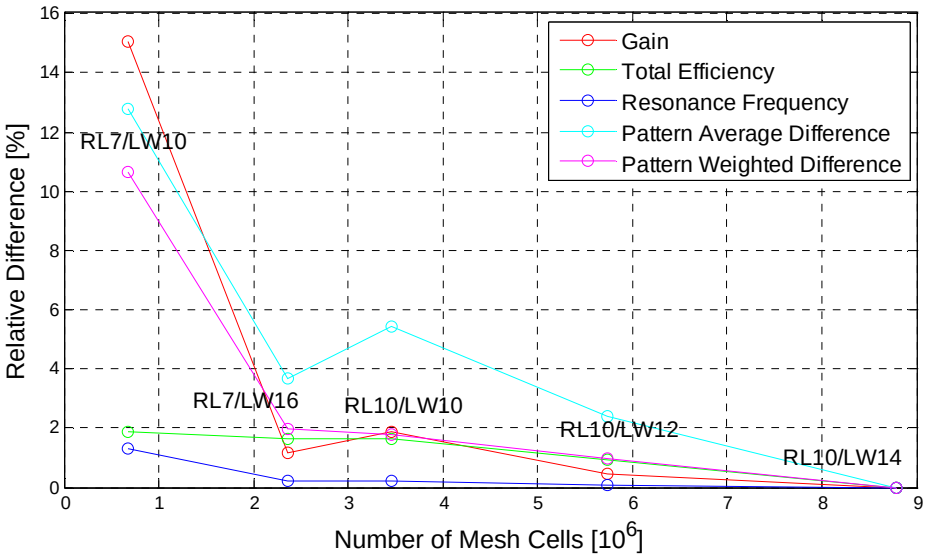

Figure 7.22. Overview of the performance assessment.

Accordingly to the latter, one has chosen the "optimal" configuration of RL7/LW16, whose combined performance in terms of memory requirements (0.34 GB *vs.* 1.43 GB of the reference

scenario), time of simulation (5 times faster than the reference) and accuracy (< 2% of relative error compared to the reference scenario) satisfies completely the requirements of the work. Moreover, the required number of mesh cells of this scenario falls into an acceptable value for regular processors.

7.3.2 Radiation Pattern Statistics

As mentioned before, the statistical concept described in Section 4.1 to model the antenna-body interaction was implemented in *CST* with a patch antenna near a voxel model. A dipole was also analysed for comparison, because, contrary to the patch, it radiates towards the body, so a strong influence from it is expected.

To speed up simulations, the voxel was sliced into four parts confined to placements in the HE_L, TO_F, AB_L and LT_L. Two antenna-body distance distributions were analysed: Uniform in range [0, 2λ], and "locally" Rayleigh with a maximum probable distance of 2 cm. All the details on the considered scenarios for this study are given in Section 6.4.

Simulation results are composed of 3D radiation patterns; however, they are only presented in the azimuth plane, since somehow similar results are obtained for others. By performing simulations of the patch located at different distances to the body, one obtains a set of radiation patterns. From this set of radiation patterns, it is possible to calculate statistics on the on-body antenna model (average and standard deviation). Also, in order to evaluate the antennas performance in different scenarios, different metrics for comparison of radiation patterns are analysed as defined in Section 6.1.

The radiation patterns for the antennas at different distances to the chest (TO_F), as well as in free space, are presented in Figure 7.23 as a case study.

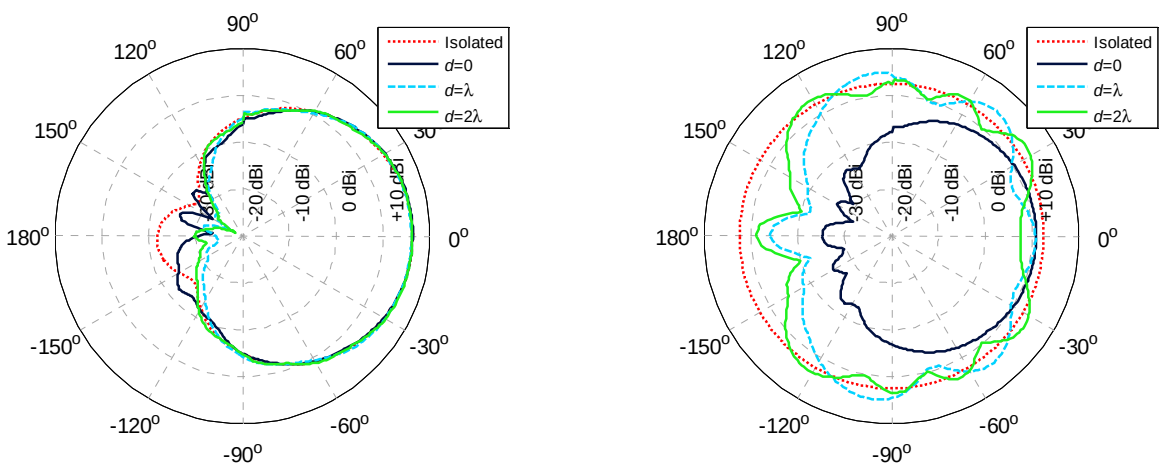

(a) Patch (b) Dipole

Figure 7.23. Antenna radiation pattern for various distances from the chest.

The highest variations are observed in the direction of the body and in the side lobes, for both patch and dipole. The gain with the patch on the body is less than the one for the isolated antenna, for any of the distances. For the patch antenna attached to the body (*i.e.*, d=0), the gain in the backward direction is higher than for the other distances.

In order to better investigate the changes in the radiation pattern when the antenna is moving closer to the body, $\overline{\Delta G_w}$ was calculated relative to the isolated antenna, for all scenarios for the Uniform Distribution, Figure 7.24.

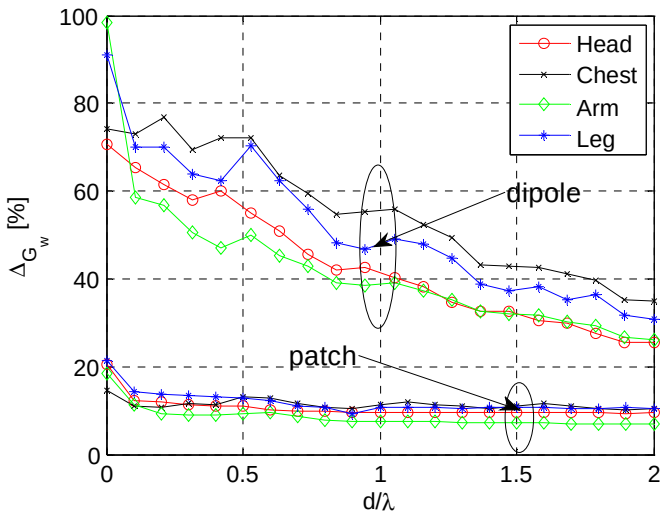

Figure 7.24. PWD for all body regions in range of [0, 2λ].

The changes of the radiation pattern are higher when the antenna is attached to the user, as the coupling with the body is the highest, resulting in a significant reduction of radiation efficiency, which affects the overall shape of the radiation pattern. In general, moving the antenna away from the body results in a smaller value for $\overline{\Delta G_w}$; however, this is not a monotonous trend, especially in the case of the patch on the chest. As observed in Figure 7.24, the decay with distance is valid for both antennas (patch and dipole), however, $\overline{\Delta G_w}$ reaches higher values for the dipole, which has no ground plane and is greatly disturbed by the body.

The statistics of the radiation pattern (*i.e.*, G_μ, $G_{\mu+\sigma}$, G_{min} and G_{max}) of the patch located near the chest, relative to the isolated antenna, are shown in Figure 7.25.

The plot is not symmetric due to the natural asymmetry of the body (and of the body voxel model – including organs), but there is a similar trend in ranges [0º, 180º] and [-180º, 0º]. The range of changes of the radiation pattern is the highest near the backward direction (*i.e.*, $\varphi = \pm 180^o$), being almost 15 dB. For azimuth angles in [-60º, 60º] and both distributions, the average radiation pattern is similar to the one of the isolated patch. Then, in range [60º, 130º], the average radiation pattern for the Rayleigh Distribution is below the Uniform one, and a maximum of 2 dB is found. When the azimuth is higher than 130º, the trend inverts, Rayleigh

being above Uniform, and a maximum difference of 2 dB is obtained for 166º. A similar trend is found for symmetric angles, although with higher fluctuations. On average, the radiation pattern of the patch located near the chest is always lower than the isolated one.

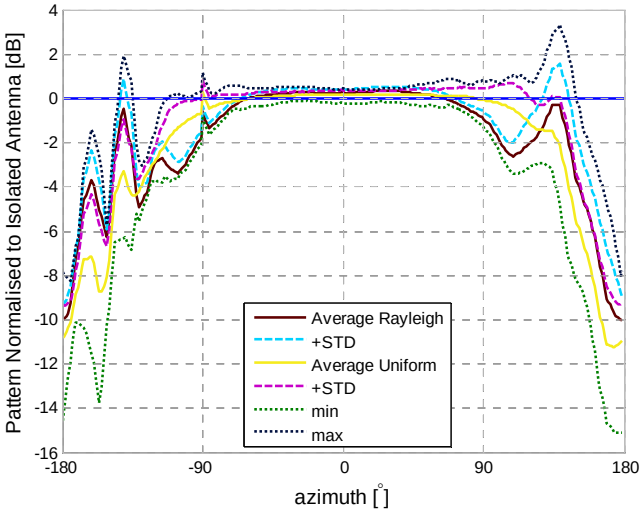

Figure 7.25. Statistics of the radiation pattern of the patch near the chest.

Table 7.10 summarises the statistics of the patch radiation pattern (average radiation pattern G_μ and standard deviation σ_G) for all the studied body segments, and for selected angles.

Table 7.10. G_μ and σ_G for selected φ and for $\theta = 90^o$ (patch).

		φ	Head	Chest	Arm	Leg
G_μ [dBi]	Uniform	0º	6.2	6.5	6.2	6.1
		90º	-4.9	-5.5	-4.8	-5.0
		180º	-17.7	-22.8	-17.7	-21.4
	Rayleigh	0º	6.3	6.6	6.4	6.2
		90º	-5.6	-6.6	-6.1	-5.7
		180º	-19.2	-21.8	-16.6	-21.3
σ_G [dB]	Uniform	0º	-6.1	-6.7	-4.6	-4.9
		90º	-13.9	-13.6	-12.5	-13.1
		180º	-21.1	-26.1	-15.7	-24.3
	Rayleigh	0º	-5.7	-7.7	-5.1	-4.2
		90º	-16.5	-18.4	-13.4	-15.1
		180º	-22.0	-27.4	-15.3	-23.8

The average radiation pattern in the forward direction, *i.e.*, $\varphi = 0^o$, varies slightly among body regions in [6.1, 6.7] dBi. In the backward direction, *i.e.*, $\varphi = 180^o$, the lowest radiation is obtained for chest and leg, due to the large attenuation of the tissues. For all body regions, the highest σ_G is observed for the forward direction. For both distance distributions, for arm and leg, it is higher by 1 to 2 dB compared to other body regions. In the backward direction, independently of the distance distribution, and of the body region, σ_G is very small. The reason

is that, in the backward direction, the average radiation pattern takes very small values.

The comparison between average radiation patterns, for the Rayleigh Distribution, for all body regions, as well as the radiation pattern of the isolated patch, are presented in Figure 7.26.

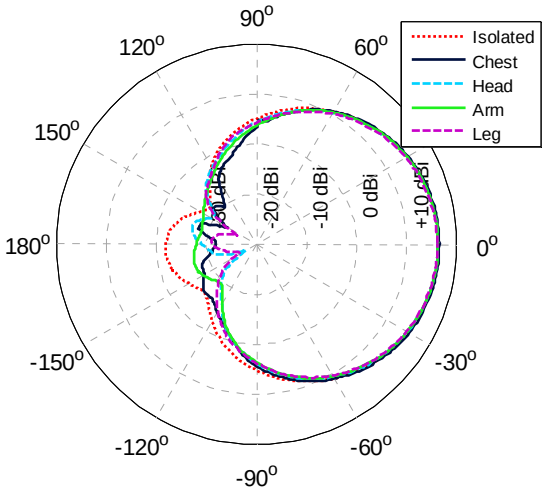

Figure 7.26. Average radiation patterns for the Rayleigh Distribution and various body regions (patch).

Averages $\overline{\Delta G}$ and $\overline{\Delta G_w}$, calculated relative to the isolated antenna, for all locations and both distributions, are gathered in Table 7.11, for the patch and the dipole. Note that $\overline{\Delta G}$ is not displayed for the dipole, as it takes high values resulting from the disturbance of the radiation pattern in the presence of the body: lobes of radiation are introduced by the body in former directions of nulls, thus, generating very high values when calculating $\overline{\Delta G}$.

Table 7.11. PAD and PWD compared to the isolated antenna.

			Head	**Chest**	**Arm**	**Leg**
patch	$\overline{\Delta G}$ [%]	**Uniform**	12.1	22.2	9.7	16.0
		Rayleigh	18.1	24.3	18.7	22.9
	$\overline{\Delta G_w}$ [%]	**Uniform**	4.8	9.8	4.1	6.3
		Rayleigh	6.9	11.0	7.4	9.3
dipole	$\overline{\Delta G_w}$ [%]	**Uniform**	20.2	32.0	19.5	24.4
		Rayleigh	54.6	66.6	47.9	61.2

Regarding the patch, for both distance distributions and all body regions, $\overline{\Delta G}$ is higher than $\overline{\Delta G_w}$. In the case of the Uniform Distribution, when the antenna is located at the maximum distance of 2λ (*i.e.*, around 24.5 cm), $\overline{\Delta G}$ and $\overline{\Delta G_w}$ are lower compared to the Rayleigh one. This is because the influence of the body is weaker when the antenna is moved away from it.

Regarding the dipole, the value of $\overline{\Delta G_w}$ is much higher in all the scenarios when compared to the patch (*e.g.*, up to 8 times higher in case of head and Rayleigh Distribution). As already stated, this comes from the fact that this basic antenna (with no ground plane) is greatly

disturbed by the presence of the body. The values for the Rayleigh Distribution are almost 2.5 times higher than for the Uniform one, due to the close proximity to the body. The body coupling effect is much stronger for the largest body part (chest).

These results clearly indicate that the selection of the wearable antenna is an important aspect for the performance of the system: well isolated antennas from the body will ensure stability. Concerning the view point of on-body communications, results show that the patch antenna ensures a much better performance than the dipole.

7.3.3 Comparison Between Homogeneous and Voxel Phantoms

This study compares the patch performance when the homogeneous or voxel models described in Section 6.4 are used. It includes simulations of the patch antenna in front of the head (HE_F) of two female phantoms: a full-body homogeneous model (coming from *Poser* [Pose12] and filled with 2/3 muscle tissue), and a truncated voxel (from Virtual Family [ViFa12]). As illustrated in Figure 7.27, both phantoms are in the standing posture in this study.

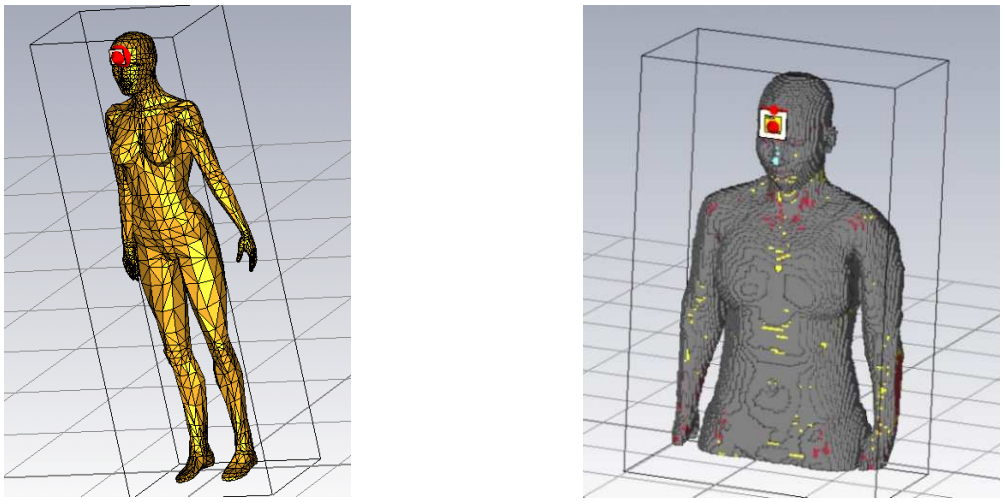

(a) Homogeneous (b) Voxel

Figure 7.27. Phantom models.

Uniform and Rayleigh Distributions of the antenna to the body are considered, as described in Section 6.4. The outputs given from this study are:

- The solver statistics;
- The antenna parameters;
- The radiation patterns and their comparison.

Note that simulation results are composed of 3D patterns, however, in here only the azimuth and elevations planes are shown, for the sake of brevity.

Regarding the solver statistics, the homogeneous model generated about 1.5 million meshcells,

with a total simulation time of about 4 min for each antenna/body separation distance. The voxel model generated about 20 million meshcells, and took 5 times longer computations.

Table 7.12 gives the average results for the on-body antenna parameters obtained from both models, considering a Rayleigh Distribution of the antenna-body separation distance.

Table 7.12. Average on-body antenna parameters (Rayleigh Distribution).

	Homogeneous	**Voxel**
Gain [dBi]	7.2	6.7
$\boldsymbol{f_r}$ **[GHz]**	2.44	2.49
$\boldsymbol{S_{11}}$ **[dB]**	-12.49	-9.98

When the patch is near the homogeneous model, the reflection coefficient is lower than for the voxel one, resulting in a better performance of the antenna. Also, the pattern in this case is narrower (gain is 0.5 dB higher). These differences can be related to the reflections from the whole-body model, which are partially neglected in the truncated phantom.

In order to investigate the changes in the radiation pattern when the antenna is moving closer to the model, PWD was calculated relative to the isolated antenna, in a [0, 2λ] distance interval, Figure 7.28.

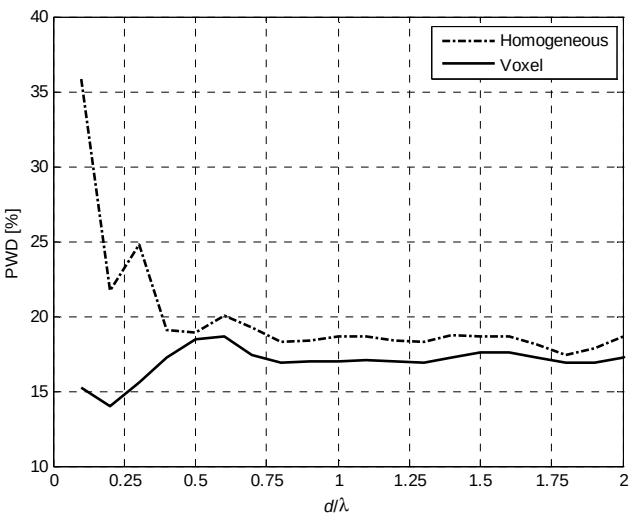

Figure 7.28. Trend of PWD with antenna-body separation distance.

The greatest differences to the pattern of the isolated antenna occur at the closer distances to the body (from 0 to 0.75λ), and PWD can range from 36% to 17% for the homogeneous model, or from 14% to 19% for the voxel. Above a 0.5λ distance, the trend is very similar for both phantoms, meaning that the patterns are not much different.

Figure 7.29 displays the average 3D radiation patterns for both phantoms (Rayleigh Distribution, which is the most realistic).

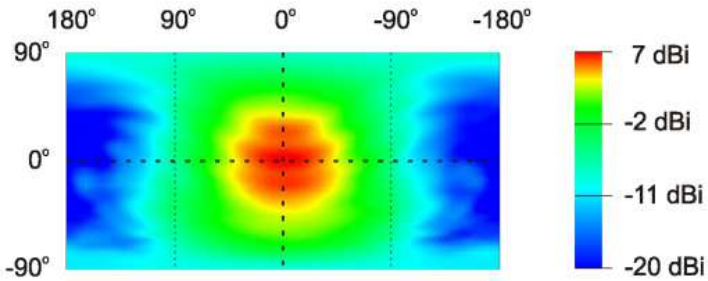

(a) Homogeneous

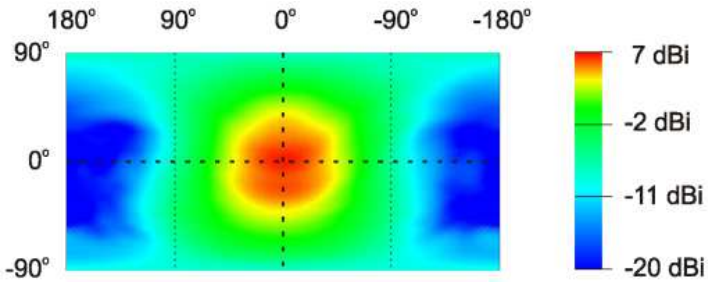

(b) Voxel

Figure 7.29. Average 3D patterns (Rayleigh Distribution).

The main visual differences in the shape of radiation patterns are on the back, with no significant impact for on-body communications. The narrower beam obtained with the homogeneous model is also observed, especially in the azimuth plane. The average weighted difference between the phantoms 3D patterns was calculated relative to the homogeneous model and results are 11% and 9%, for the Rayleigh and the Uniform Distributions, respectively. These results are negligible in the area of interest for on-body communications.

Based on the results from this study, it is concluded that homogeneous models also fulfil the on-body communications modelling requirements, with the great advantages of requiring lower hardware requirements, and being much more flexible in terms of postures, thus, being suitable to introduce dynamic scenarios in electromagnetic simulation software.

7.3.4 Measurement of Radiation Patterns

A measurement campaign was conducted in order to assess the impact of the phantom shape in BANs simulations. The measurement conditions are described in Section 6.5. Simulations and measurements of the patch antenna are compared in two conditions: in free space (*i.e.*, isolated antenna), and in the front of the torso (TO_F). The outputs of the study are:

- The antenna main parameters;
- The radiation patterns for different antenna-body separations;
- The statistics of the patterns over distance.

Table 7.13 displays the results for the antenna parameters obtained via measurements and

simulations. Results from measurements and simulations are quite similar, and in good agreement with the ones from literature. The discrepancies are mainly due to measurement and simulation inaccuracy.

Table 7.13. Antenna parameters (isolated).

	Measurements	**Simulations**
Gain [dBi]	6.4	6.6
f_r **[GHz]**	2.43	2.44
S_{11} **[dB]**	-14.95	-12.35

Figure 7.30 displays the azimuth radiation pattern for the isolated antenna, and at different distances from the body ({0, 2, 4} cm).

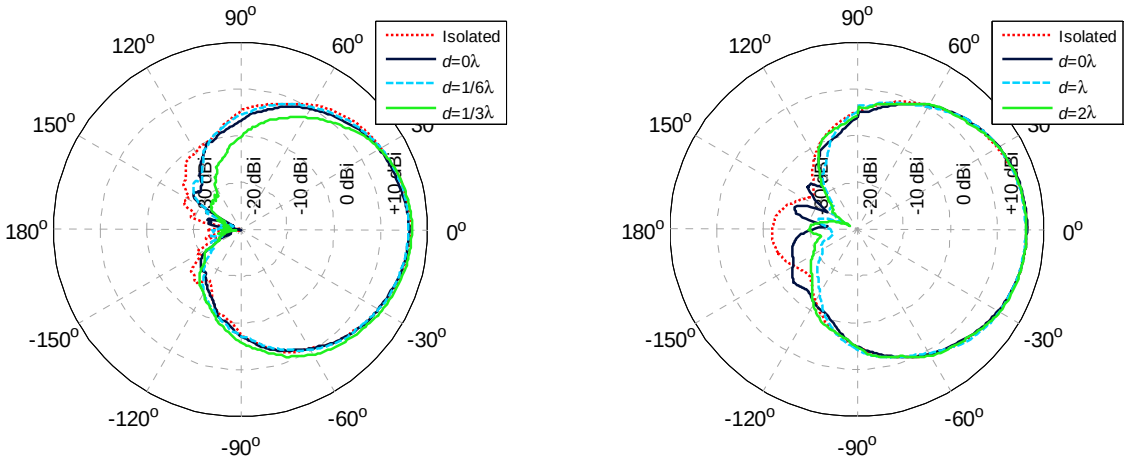

(a) Measurements (b) Simulations

Figure 7.30. Average radiation patterns for various distances.

A common comment to the measured patterns is that the backward lobe is suppressed by the supporting structure of the positioner. Still, both approaches (measurements and simulations) show that when the patch is on the body, the highest differences to the free space pattern are observed in the back and the sides. This is an immediate consequence of body coupling and reflections. Regarding the trend with distance, it is observed that the on-body pattern changes as the antenna is moved away from the body. In simulations, the on-body gain is always less than the free space one. In measurements, it is higher when the antenna is at the maximum distance to the body (d=4 cm).

The statistics of the radiation pattern (*i.e.*, G_μ, G_{min} and G_{max}) of the antenna located near the chest, relative to the isolated antenna, are shown in Figure 7.31.

Changes in the radiation pattern are higher near the chest, reaching almost 15 dB, which is in line with *CST* results. Again, the plot is not symmetric, due to the natural asymmetry of the

body. The average radiation pattern is similar to the one of the isolated antenna in the range [-30º, 30º]. In the range [-170º, 30º], the average radiation pattern of the patch on the body is always below the isolated antenna one, with a great decay on gain values for angles below -110º. Only in backwards, it is above the isolated patch pattern, with a maximum of 3 dB at -170º, these results being influenced by the support structure. An opposite effect is found in the symmetric range [30º, 180º].

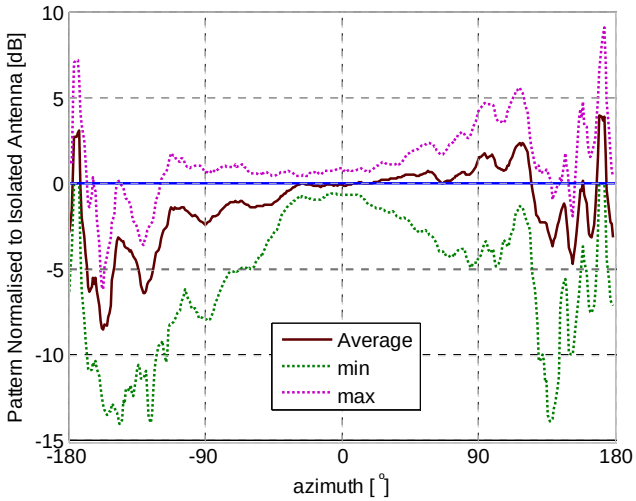

Figure 7.31. Statistics of the measured pattern of the path near the chest, relative to the isolated one.

Figure 7.32 presents the average patterns over distance obtained through *CST* and measurements, for the isolated antenna and for the antenna on the body. Table 7.14 summarises the statistics of the patterns. Note that, because of the few number of samples in measurements, the interval of variation is indicated, instead of giving the standard deviation.

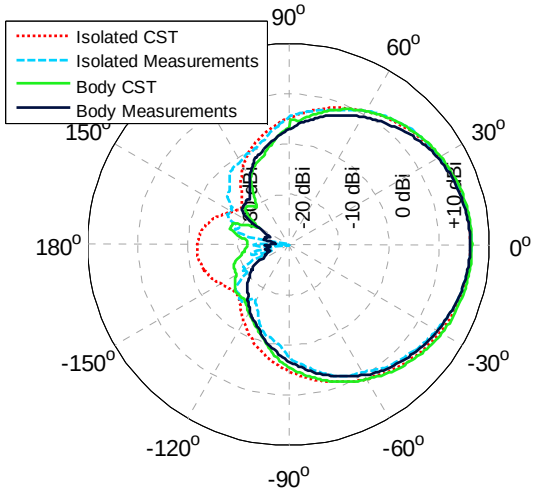

Figure 7.32. Comparison between measurements and *CST*.

The average on-body pattern is not symmetric, due to the natural asymmetry of the body. From the statistics, it is observed that the range of changes with distance in front of the patch

is much smaller than on the sides, or on the back. This trend is similar for both approaches. In the azimuth range [-90º, 90º], the area of interest for on-body communications, no large changes are observed between *CST* and measurements. In this range, an average difference of 0.6 dB is found between the free space patterns; for the antenna on the body, the average difference is 0.9 dB.

Table 7.14. Statistics of the azimuth pattern (on-body).

φ	Measurements		Simulations (Rayleigh)	
	G_μ[dBi]	Range [dBi]	G_μ[dBi]	σ_G [dB]
0º	6.3	[5.7, 7.3]	6.6	-7.7
90º	-7.1	[-12.7, -4.0]	-6.6	-18.4
180º	-26.0	[-30.0, -22.4]	-21.8	-27.4

Although measurements deal with the whole on-body channel, they are too resource- and time-consuming, compared to simulations. The good match between both approaches, with an average difference lower than 1 dB, suggests that the use of truncated models in *CST* is a valid approach to model BANs.

Chapter 8

Analysis of On-Body Channel

This chapter analyses the results obtained for the modelling of on-body channels. In Section 8.1, results from measurements and simulations with a static user in free space are presented. The main parameters addressed here are the channel gains, power imbalance and correlation. In Section 8.2, similar results are provided for a user moving in free space, and optimum 1×2 on-body placements are suggested. Section 8.3 provides capacity results for the body moving in a complex propagation environment, together with the optimum 2×2 MIMO antenna placements.

.

8.1 Static User in Free Space

8.1.1 Measurement of On-Body Links

A measurement campaign was conducted for a static subject in an anechoic chamber, holding four on-body antennas, and assuming different poses: standing, sitting and military posture. Three on-body links were recreated with the four antennas. The goal of the study is to investigate the impact of the body in the communication link. The measurement scenarios are described in Section 6.5. The analysis presented here is based on the measured s-parameters, namely, on the input reflection loss, s_{11}, and on the transmission, s_{12}.

The s_{11} parameter was measured for the different on-body links, its mean value was extracted and compared with the one obtained for the isolated patch, Figure 8.1.

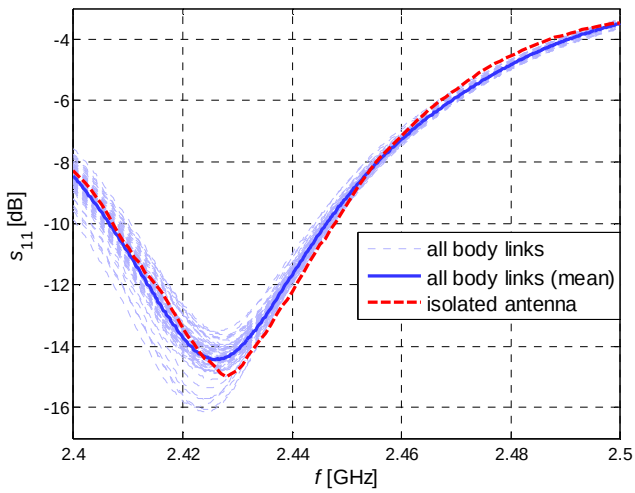

Figure 8.1. Input reflection coefficient (overview).

Results show that the input reflection coefficient is affected by the presence of the body. On average, the antenna performance on the body is 0.6 dB worse than in free space, which is reflected in a decrease of less than 1% on the antenna reflection efficiency. Additionally, there is a small detuning from free space resonance, which is less than 5 MHz, the practical implication being the increase of the standard deviation of s_{11}. At the frequency of interest for this work, 2.45 GHz, the curves for the different links are almost coincident, with s_{11}< - 8 dB, meaning that almost 85% of the input power is transmitted, which is in agreement with the specifications for short distance communications.

The comparison of the average return loss, $\mu_{s_{11}}$, and respective standard deviation, $\sigma_{s_{11}}$, for the

different poses (military, standing and sitting) is presented in Figure 8.2 and Figure 8.3. It is observed that the military and sitting poses present a slight worse performance compared to the standing posture (about 0.5 dB poorer). This effect might be a consequence of the arm rotation, causing antenna depolarisation, and of the influence of nearby objects (*e.g.*, the presence of the chair in the sitting position). Conversely, the standing posture presents a higher standard deviation of s_{11} curves, compared to the other postures, as observed in Figure 8.3, which also shows that the standard deviation of s_{11} is quite sensitive near the resonant frequency.

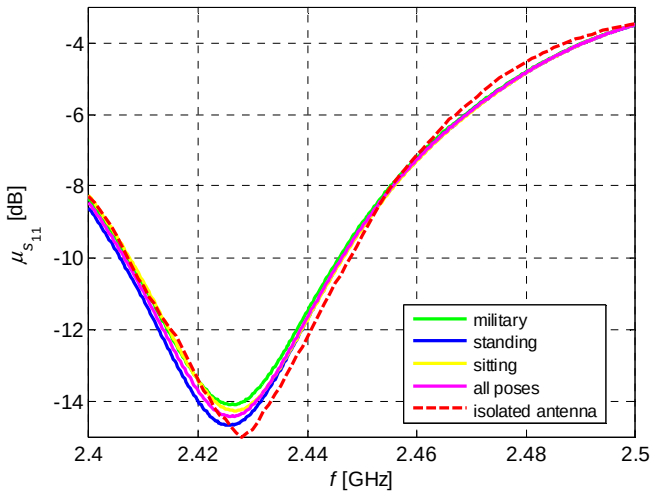

Figure 8.2. Input reflection coefficient (average curves).

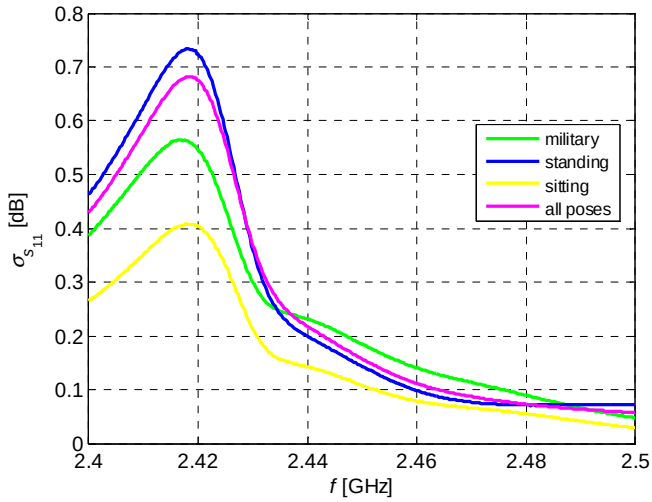

Figure 8.3. Input reflection coefficient (standard deviation curves).

The power received in each RX node was measured, Figure 8.4 displays s_{12} for each of the different postures, differentiating the different links. An overview of the main quantities is presented in Table 8.1, namely, the average $\mu_{s_{12}}$, its standard deviation $\sigma_{s_{12}}$ and the range $\Delta_{s_{12}}$. It is worthwhile mentioning that the number of samples in this study does not allow an

acceptable statistical confidence for some configurations, which sometimes motivates an analysis based on the range of changes of s_{12}.

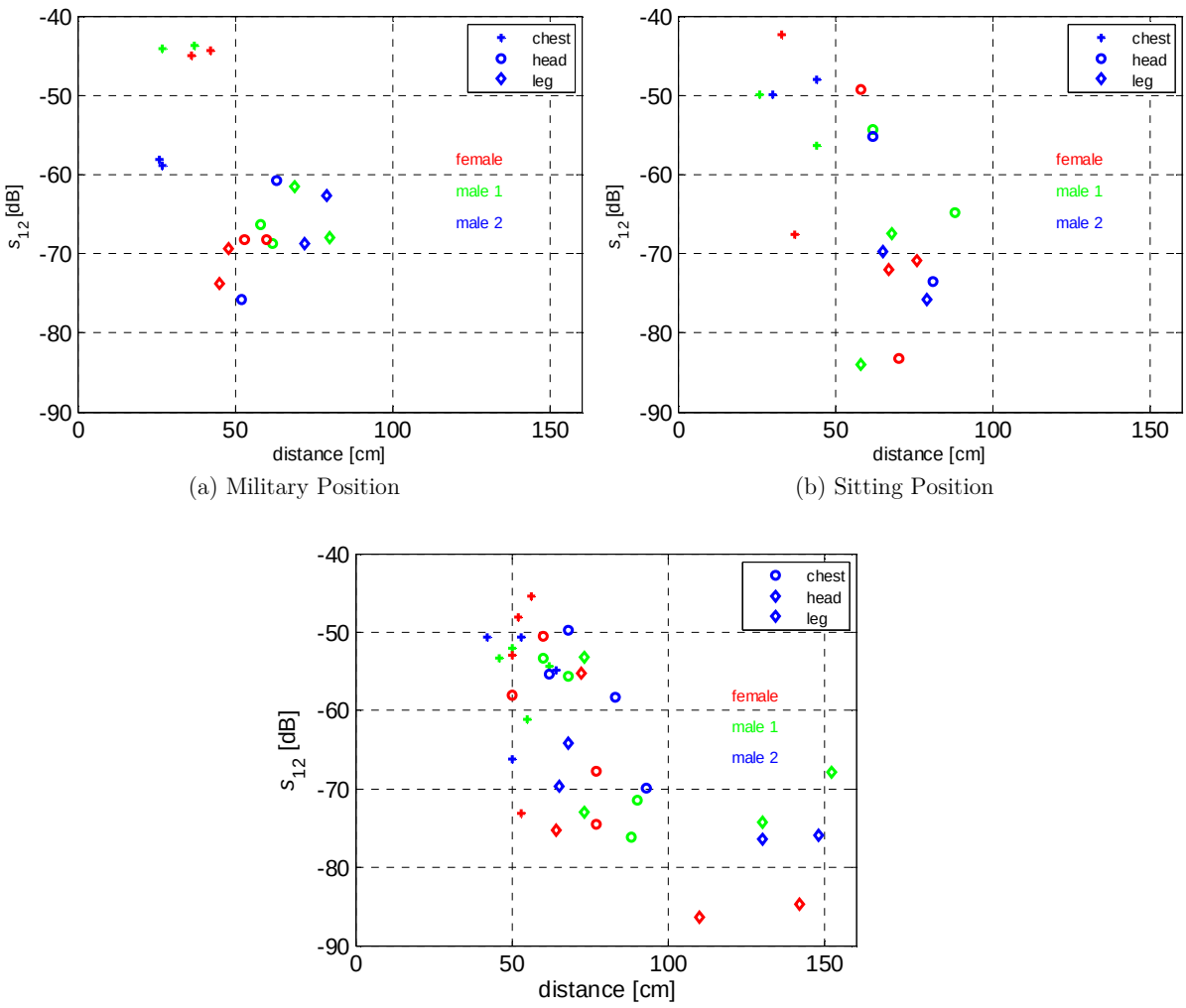

(a) Military Position

(b) Sitting Position

(c) Standing Position

Figure 8.4. Overview of s_{12} results.

Table 8.1. Overview of s_{12} results.

		Head (HE_R)	Chest (TO_F)	Leg (LB_R)
Military	$\mu_{s_{12}}$ [dB]	-68	-49	-67
	$\boldsymbol{\sigma}_{s_{12}}$ [dB]	5	7	5
	$\boldsymbol{\Delta}_{s_{12}}$ [dB]	15	15	12
Standing	$\mu_{s_{12}}$ [dB]	-62	-55	-71
	$\boldsymbol{\sigma}_{s_{12}}$ [dB]	10	8	10
	$\boldsymbol{\Delta}_{s_{12}}$ [dB]	26	28	26
Sitting	$\mu_{s_{12}}$ [dB]	-63	-52	-73
	$\boldsymbol{\sigma}_{s_{12}}$ [dB]	13	9	6
	$\boldsymbol{\Delta}_{s_{12}}$ [dB]	34	25	17

Results show that the received power in the chest link is higher than in the head or leg ones,

with values at least 18, 7 and 11 dB higher, for the military, standing and sitting postures, respectively. This observation, more than being related to the slight small links lengths, is associated to the visibility and stability between TX and RX antennas.

The plots of Figure 8.4 also show that there are different paths with similar lengths, but having tens of dB of difference. For the military posture, the dynamic range of both the head-arm and chest-arm links is as high as 15 dB. Flexing the knees produced an additional link variability of 7 dB for the chest-arm link. For the standing position, the dynamic range is even larger, for example, 33 dB for the leg-arm link. For the chest-arm link, it is also observed that the movement of the arm results in a standard deviation of 8 dB. Regarding the sitting posture, the higher dispersion of values at the same distance is for the arm to head link (34 dB). Alternating the arm position between bend and straight down results in a standard deviation of 7 dB for the chest-arm link.

The large range of variations results from a mixture of different factors, such as the dielectric properties of the human body and the body posture. The amount of energy absorbed by the human body depends on the position of the antenna and on the posture. Two individuals with exactly the same posture, having antennas in the same position, are likely to produce different results, mainly because of different body composition. However, the differences in received power can also be the result of hand rotation, hence, a channel can change from QLOS to NLOS very quickly, which results in increased path loss. An additional contributing factor is the polarisation mismatch between TX and RX antennas.

An analysis of the CDF of the received power, corresponding to the different body postures is plotted in Figure 8.5. This plot confirms that the received power values are higher for the standing pose than for the military or sitting postures; for 50% of the cases its received power is 5 dB higher than in the other poses. The set of data formed with all the samples from all body postures was tested against the Normal Distribution using the χ^2 test. The results presented in Table 8.2, show that, with 95% confidence, the hypothesis that data follows a Normal Distribution cannot be rejected, with 98% of probability of observing the given statistic. The parameters for this distribution are estimated as mean of -67 dB and standard deviation of 10 dB.

Considering the matrix of connections (Table 6.9), the CDF for links with different natures (NLOS and QLOS) is presented in Figure 8.6. These curves might be fitted by a Normal Distribution, at a confidence level of 95%, with probability equal to 96% and 95%, respectively for the NLOS and QLOS links. Parameters for this distribution were estimated as a mean of -73 dB and -57 dB, and standard deviation of 8 and 6 dB, respectively for the NLOS and QLOS links. These results show that the change of the link nature between QLOS and NLOS

originates a decay on the received power of more than 15 dB, which can determine whether a given link has connectivity or not.

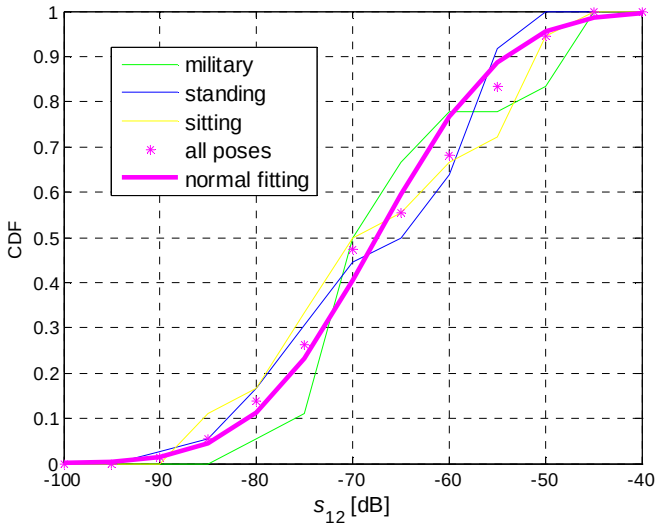

Figure 8.5. Overview of s_{12} results.

Table 8.2. Results from Normal fitting (χ^2 test).

			Confidence Level: 95%		Confidence Level: 99%	
	Probability [%]	χ^2 **test**	$\chi^2_{th95\%}$	**Normal Dist. Validity**	$\chi^2_{th95\%}$	**Normal Dis. Validity**
All Poses	98	0.0008	3.84	yes	6.63	yes
NLOS	96	0.0023	3.84	yes	6.63	yes
QLOS	95	0.0045	3.84	yes	6.63	yes

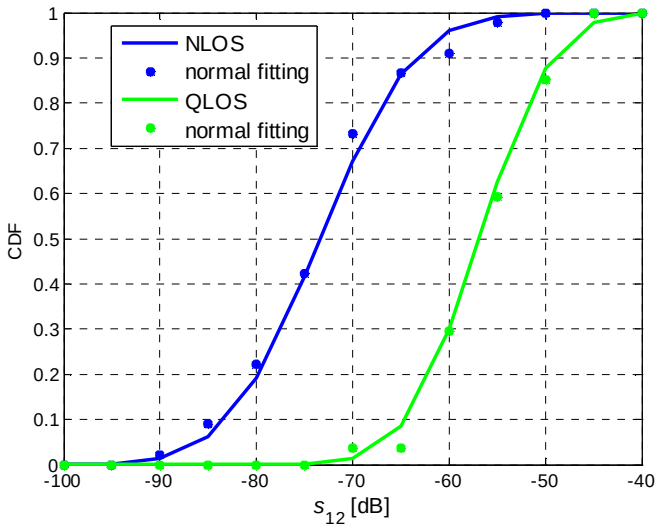

Figure 8.6. CDF of s_{12} for QLOS/NLOS links.

Figure 8.7 and Figure 8.8 show s_{12} as a function of the distance between the TX and the RX antennas, and also the range of variations within 3 cm long intervals, for the NLOS/QOS sets,

respectively. Fitting functions were set to characterise the power decay with distance for all measurements, also being displayed in Figure 8.7 and Figure 8.8, together with results from the goodness of fit R^2 test. Note that P_r is expressed in dBm.

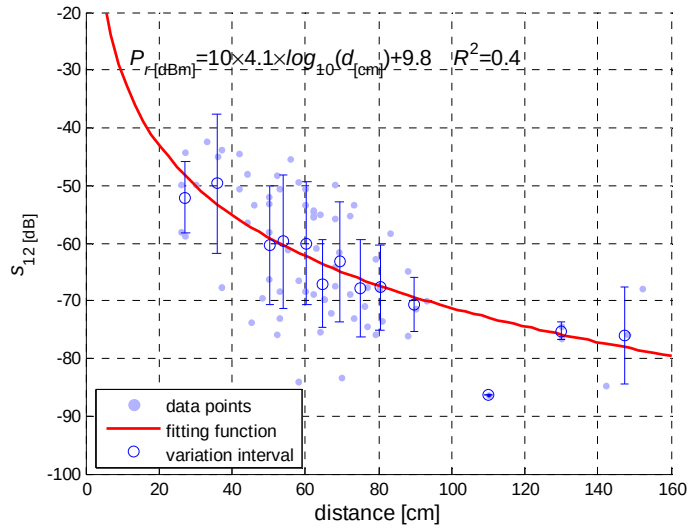

Figure 8.7. s_{12} decay with distance for all data points.

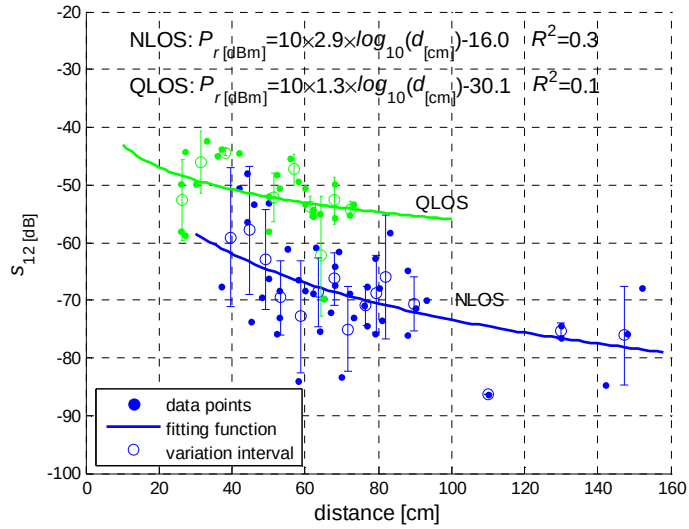

Figure 8.8. s_{12} decay with distance for NLOS/QLOS data points.

Table 8.3 summarises the analysis of s_{12}. The standard deviation of all the data set is about 8 dB, with a maximum deviation of about 12 dB, which corresponds to a NLOS link. On average, NLOS links present 3 dB more variations than QLOS ones. The large variations of the received power are a direct result of the stochastic nature of the channel, which gives additional support to the statistical modelling approach claimed in this Thesis.

A general poor correlation with the usual average power decay model was naturally observed (small R^2 values), due to the spread of values. A rather unexpected value for the path loss

exponent equal to 1.3 was obtained for the QLOS link, which is usually obtained in local guided propagation, like indoor corridor and outdoor street canyon environments. This is an interesting result that requires further investigation, as it may support the idea of a local guided propagation effect together with local (body) multipath and antenna coupling effects for short distance links, additional to potential effects of the radiation patterns.

Table 8.3. Analysis of s_{12} results.

	Δs_{12} [dB]	$\overline{\sigma_{s_{12}}}$ [dB]	α
All Poses	12	8	4.1
NLOS	12	7	2.9
QLOS	10	4	1.3

On-body measurements of static users in an anechoic chamber show a detuning of less than 5 MHz, and a 0.6 dB worst performance, compared to the isolated antenna. Channel gains can have a dynamic range of 33 dB for path links with the same length, as a consequence of antenna misalignment. This effect can turn a QLOS link into a NLOS one, increasing path loss up to 15 dB, which must be taken into account in link calculations for BANs.

8.1.2 Correlation of On-Body Links

This study is based on full wave simulations and analyses the correlation between the different on-body links for a static user in free space, carrying nine on-body antennas, as described in Section 5.2. At each simulation, one antenna is set as the TX and the remaining ones are the RXs. For every TX placement, the pairs of RXs are classified as SYM, LOS, QLOS or NLOS. The idea of the study is to understand the relations between the branches when no other reflectors than the body itself are present. The distance of the different antennas to the body was set for the scenarios All, Arms and Torso, as defined in Section 6.4.

The trend of the statistics of correlation with the distance for each class (SYM, LOS, QLOS and NLOS) is shown in Figure 8.9. These curves correspond to the average results from all possible TX placements.

The predictable result that, as antennas are moved away from the body, signals become more correlated is confirmed. This effect is more visible in the “All” scenario, especially for non-symmetric links (LOS, QLOS and NLOS). The standard deviation slightly decreases with antenna-body separation. For the “Arms” scenario (not shown), correlation values almost do not change with the distance to the body.

A detailed study on the evolution of correlation with distance can be done through a deep analysis of histogram plots, *e.g.*, Figure 8.10 for the “Torso” scenario. Note that the histograms

for the other scenarios are quite similar, hence, not being represented.

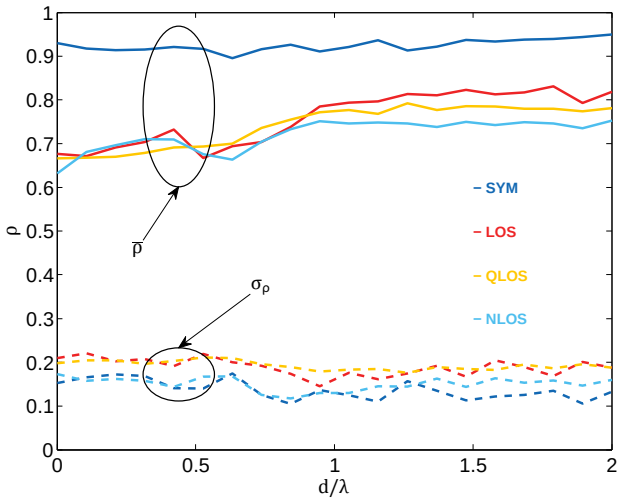

Figure 8.9. Trend of correlation statistics with distance: scenario "All".

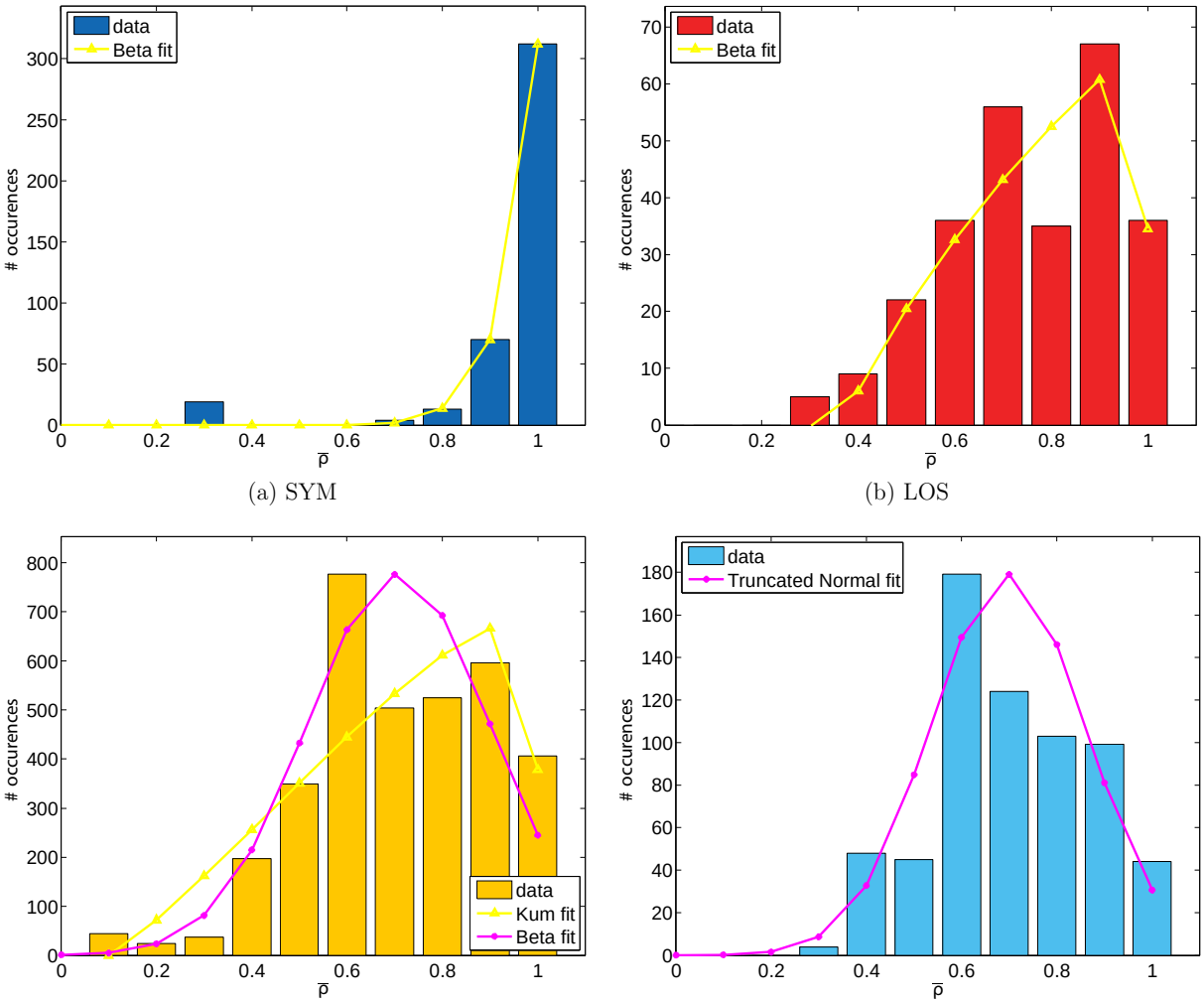

(a) SYM (b) LOS

(c) QLOS (d) NLOS

Figure 8.10. Global histograms of correlation with distance: scenario "Torso".

SYM links present the well distributed PDF, tending to the extreme value of 1, with the Beta

and Kumaraswamy Distributions fitting very well to this class (R^2=1). Concerning LOS links, the values of correlation are generally high, above 0.7, and the Beta and Kumaraswamy Distributions have also a good fitting, with R^2 values around 0.9. For QLOS links, the values of correlation have an average value around 0.7, and Beta and Kumaraswamy Distributions were tested together with the Truncated Normal one, better results being obtained for the Truncated Normal Distribution. Anyway, a visual inspection detects the presence of some local maxima, which suggests the fitting with a bimodal distribution. The NLOS class has also a mean value around 0.7, following a Truncated Normal like Distribution, although a bimodal approach could also be exploited. Table 8.4 presents the maximum likelihood estimates for the parameters of these distributions, at 95% confidence, together with the R^2 results.

Table 8.4. Fitting Parameters.

	Beta			**Kumaraswamy**			**Trunc. Normal**		
	α_B	β_B	R^2	α_K	β_K	R^2	μ_{TN}	σ_{TN}	R^2
SYM	9.4	1.0	1.00	9.5	1.0	1.00	-	-	-
LOS	1.9	1.0	0.94	1.9	1.1	0.91	-	-	-
QLOS	2.2	1.1	0.89	2.1	1.1	0.89	0.68	0.02	0.91
NLOS	-	-	-	-	-	-	0.69	0.02	0.91

Figure 8.11 shows the statistics for the different classes for the particular scenario of the TX on the belt. The pairs located on arms and ears, classified as SYM, present strong correlations with $\bar{\rho}$ close to the prohibitive value of 1. The QLOS and NLOS links also show high mean correlation values, around 0.8 and 0.7, respectively. For this TX placement, there is a single LOS link, corresponding to the pair TO_B&HE_B, which seems to be the best approach to use for spatial multiplexing, with a correlation value around 0.5.

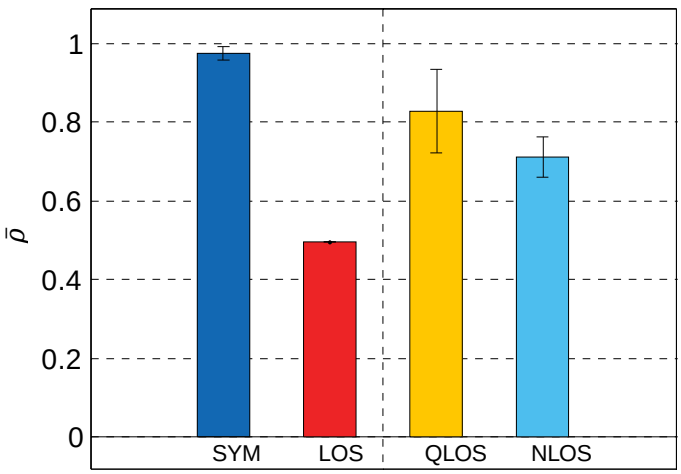

Figure 8.11. Correlation statistics for TX on WA_F: scenario "All".

Taking into account the results of all possible TX placements, an overview of the global statistics of correlation with distance, with the mean value and the standard deviation per

class, is presented in Table 8.5.

Table 8.5. Correlation Statistics.

	SYM		LOS		QLOS		NLOS	
	$\bar{\rho}$	σ_ρ	$\bar{\rho}$	σ_ρ	$\bar{\rho}$	σ_ρ	$\bar{\rho}$	σ_ρ
All	0.92	0.14	0.76	0.19	0.74	0.19	0.72	0.15
Torso	0.94	0.14	0.76	0.17	0.71	0.19	0.70	0.16
Arms	0.93	0.15	0.68	0.21	0.66	0.21	0.64	0.18

It is observed that, for all scenarios, the SYM nodes present the highest correlation values (0.9) and the smallest range of variations with distance to the body $\sigma_\rho < 0.15$, which is intuitive, due to the symmetry of the body. The mean correlation slightly decreases according to the sequence LOS – QLOS – NLOS links, with higher variations for the LOS/QLOS classes. LOS signals were expected to be highly correlated than QLOS or NLOS ones, but this statement is not so linear. For instance, if RXs are far away from the TXs, their signals are very poor, thus, resulting in small correlation.

Figure 8.12 presents the global mean correlation values (and standard deviations) when the TX is localised in different parts of the body: head, front, back and arms. It is seen that arms and back TX placements generate the smallest mean correlation values (around 0.7). The front and head groups show correlation values higher than 0.8, might limiting the advantages of spatial multiplexing. Note that these results are similar for the "Arms" and "Torso" scenarios. Anyway, these conclusions are somehow scenario dependent, as seen for the case study of TX on the belt.

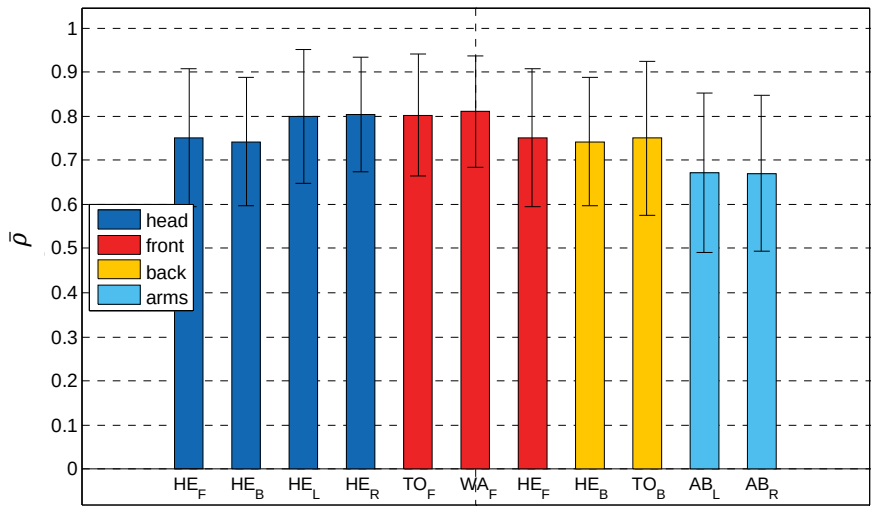

Figure 8.12. Correlation statistics for different TX placements: scenario "All".

The numerical simulations of the static user in free space enabled to study the spatial correlations among on-body channels, when no other reflectors than the body itself exist.

Different classes of links were defined and their correlations were statistically characterised. A symmetrical placement of the RXs relative to the TX is naturally not favourable for MIMO due to high correlation (values round 0.9). The mean correlation goes from 0.8 to 0.7, according to the sequence LOS – QLOS – NLOS. The values obtained for the static user in free space are high under the point of view of MIMO (correlation should be below 0.7), but they are expected to decrease with the body dynamics and the local environment.

8.1.3 Power Imbalance of On-Body Links

This study is based on full wave simulations and analyses the power imbalance between the different on-body links for a static user in free space, wearing nine on-body antennas, as described in Section 5.2. At each simulation, one antenna is set as the TX and the remaining ones are the RXs. For every TX placement, the pairs of RXs are classified as SYM, LOS, QLOS or NLOS. The goal of the study is to understand the power relations between the branches when no other reflectors than the body itself are present. The distance of the different antennas to the body was set for the scenario All, as defined in Section 6.4.

Figure 8.13 exemplifies the statistics (mean and standard deviation) of the channel gain for the different RXs, when the body is standing and the TX is on the belt (WA_F).

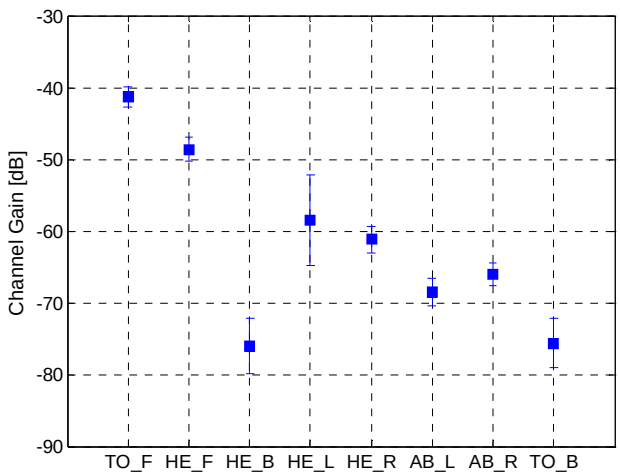

Figure 8.13. Statistics of the channel gain for static user (TX on WA_F).

As expected, the channel gains are higher when nodes are in LOS, or at a short distance, to the TX. For instance, TO_F and HE_F are both in LOS with the TX, but the gain is higher for TO_F due to the shorter distance to the TX. The nodes on the back (HE_B and TO_B) have the lowest channel gains, as they are in NLOS with the TX. The placements in symmetric positions to the TX, like in the arms, have the similar channel gains, as expected.

The trend of the channel gain with the distance of antennas to the body, when the TX is on

the belt (WA_F), is shown in Figure 8.14.

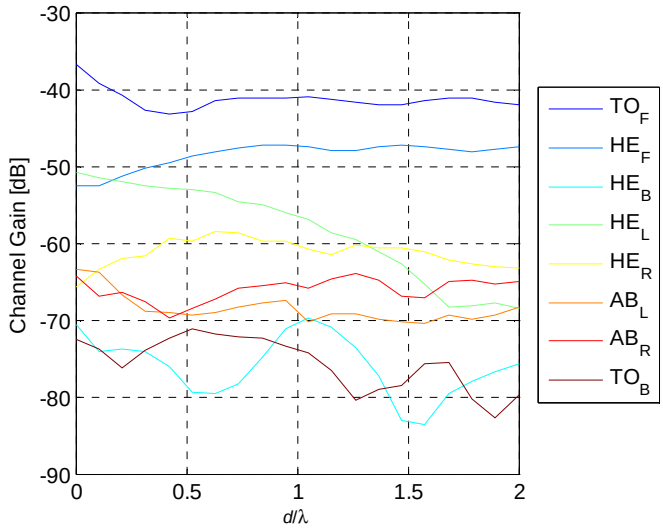

Figure 8.14. Trend of channel gain with distance to the body (TX on WA_F).

The channel gain for the placements in LOS with the TX experiences larger changes when the RXs are closer to the body (up to 0.5λ distance). The NLOS antennas (HE_B and TO_B) show several oscillations (around 10 dB) possibly resulting from reflections in the body, but the trend is to decay with d. The nodes on the arms show decay up to 0.5λ distance, but then the trend of their channel gain becomes constant. A pronounced decay (about 20 dB) is verified for the RXs on the ears, because as d increases, these antennas become far away from the TX.

The channel gains obtained from simulations can be compared with the ones from the on-body measurements, for the standing posture with arms down, Table 8.6. Note that in this case simulation results were averaged in $d \in [0, 2]$ cm.

Table 8.6. Comparison of simulation and measurement results (TX on AB_L).

	Head (HE_R)		**Chest (TO_F)**	
	Measurements	**Simulations**	**Measurements**	**Simulations**
$\mu_{s_{12}}$ [dB]	-62	-73	-55	-54
$\sigma_{s_{12}}$ [dB]	10	1	8	4

A good agreement between measurements and simulations is observed for the chest, while an 11 dB difference is found for the head. More than numerical/measurement inaccuracy, this difference could be the effect of dissimilar subject heights in the measurements.

The statistics (mean and standard deviation) of power imbalance among the RX pairs were calculated for all cases, an example being shown in Figure 8.15 for the particular TX placement on WA_F. Figure 8.16 presents the CDF plots of power imbalance obtained for the different TX placements.

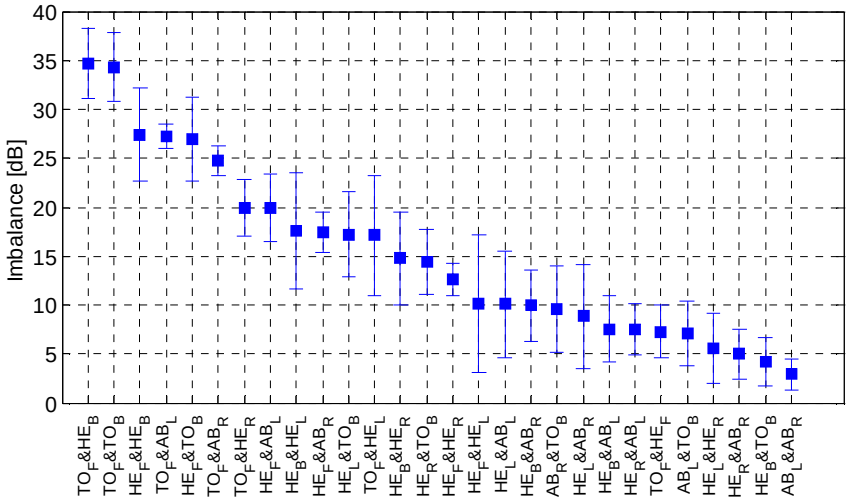

Figure 8.15. Statistics of power imbalance for the static user (TX on WA_F).

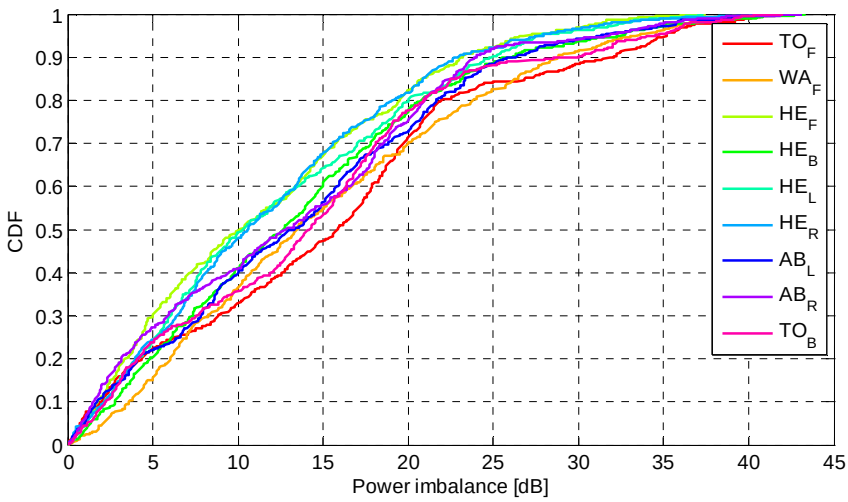

Figure 8.16. Statistics of power imbalance for the static user (TX on WA_F).

In this static scenario, a simple look at the imbalance statistics evidences the classes of links. NLOS links, like TO_F and TO_B experience high imbalances (around 35 dB), while LOS or SYM connections have imbalances lower than 5 dB. From the CDFs, it is possible to understand that the TX placements on the head generate balanced links (lower imbalances), *e.g.*, 50% of the links are below 10 dB which might enable MIMO gains. On the contrary, the nodes on front of the body, like TO_F and WA_F, promote stronger power imbalances between the branches.

From the summary of the statistics of power imbalance by class for the different TX placements, Figure 8.17, several conclusions can be taken. In general, the NLOS pairs have higher imbalances (up to 35 dB), with exception for the placements on the sides of the body, whose imbalance is less than 15 dB. Then, QLOS links show an imbalance value around 15 dB,

and almost no difference is verified between SYM and LOS placements (imbalance around 5 dB). It is important to note that, in fact, the values of imbalance in this study are overestimated because the body distance interval of [0, 24.5] cm is considered.

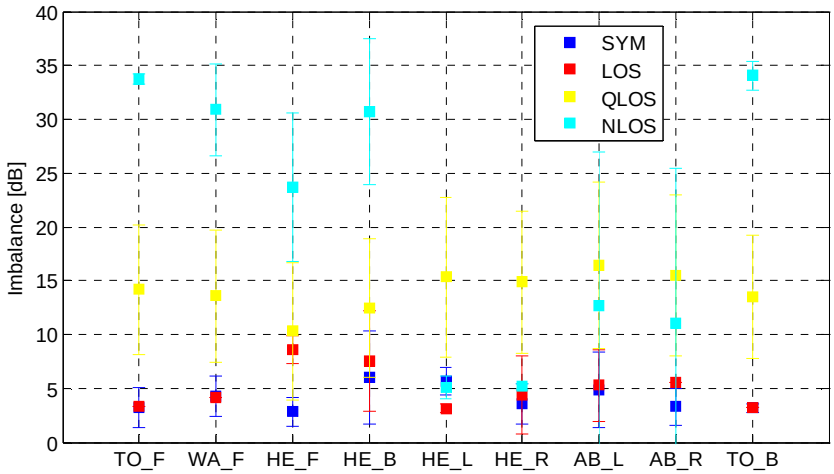

Figure 8.17. Statistics of power imbalance by class for the static user.

Taking the results of all possible TX placements into account, a summary of the global statistics of imbalance with distance, with the mean value and the standard deviation per class, is presented in Table 8.7.

Table 8.7. Imbalance statistics for the static user.

SYM		LOS		QLOS		NLOS	
$\overline{\Delta P}$ [dB]	$\sigma_{\Delta P}$ [dB]	$\overline{\Delta P}$ [dB]	$\sigma_{\Delta P}$ [dB]	$\overline{\Delta P}$ [dB]	$\sigma_{\Delta P}$ [dB]	$\overline{\Delta P}$ [dB]	$\sigma_{\Delta P}$ [dB]
4	2	5	1	14	7	21	6

It is observed that, for all scenarios, the SYM and LOS nodes present the lowest imbalance values (4 and 5 dB, respectively), together with the lowest deviations. The QLOS and NLOS links have prohibitive mean values of 14 and 21 dB, excessively high for the 10 dB threshold to benefit from MIMO.

The study of the power imbalance between on-body channels, for a static user in free space, clearly evidenced the classes of links. A symmetrical placement of the RXs relative to the TX, or a LOS link between two RXs, enable balanced channels (mean imbalance below 5 dB). Under the view point of MIMO, QLOS and NLOS branches should be avoided, as their imbalances are above the 10 dB threshold. Anyway, the values obtained in this study are overestimated because of the static nature of the scenario, the inexistence of scatterers, and also because of the large antenna-body distance interval considered.

8.2 Dynamic User in Free Space

8.2.1 Correlation of On-Body Links

The study described in this section is an improved version of the previous one, where the body is no longer static, and the mobility of the user is considered. This analysis allows to understand how the relations between the branches change according to the movement of the body, as described in Section 5.3. The parameter analysed in this section is the spatial correlation between on-body links.

The trend of correlation during a motion cycle (walk), when the TX is on the belt (WA_F), is shown in Figure 8.18, for selected pairs of antennas representative from the various classes.

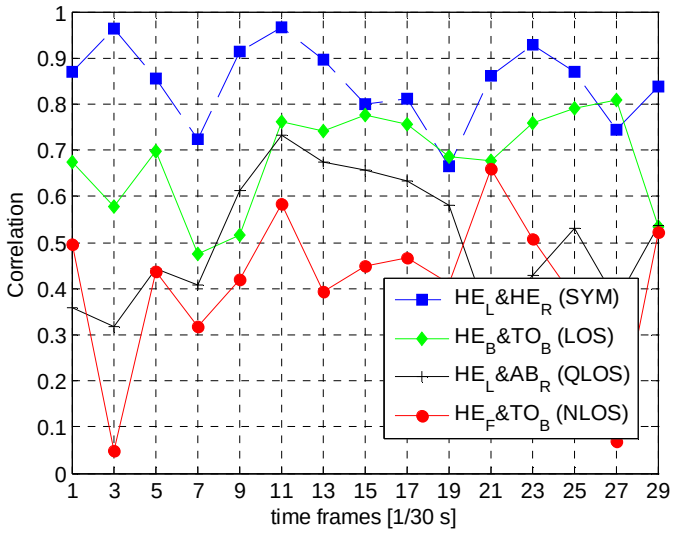

Figure 8.18. Correlation for selected pairs of antennas (TX on WA_F: walk).

Before going on with the analysis of results, it is important to notice that there are significant fluctuations in the results from frame to frame. This is not a major consequence of the body dynamics, but rather a result from the already mentioned limitations of the *CST* meshing. Nevertheless, this constraint does not invalidate the overall conclusions taken from this study.

The distinction between the classes is visible in the walk scenario, with the SYM and LOS classes presenting the higher correlation values. The NLOS class has the lowest correlation during the motion, with fluctuations resulting from signal reflections in the arms. The effect of the arm swing is visible in the QLOS curve, where correlation is higher between the 9th and the 19th frames, because the AB_R antenna is in front of the body and slightly rotated, putting the AB_R and the HE_L antennas in a symmetric position to the TX. In the running scenario (not shown), because the body is moving faster, the pairs classification is not so clear, especially for the QLOS, the LOS and the SYM cases.

Figure 8.19 compares the correlation statistics for all possible links with previous results for the standing body, when the TX is on the belt (WA_F).

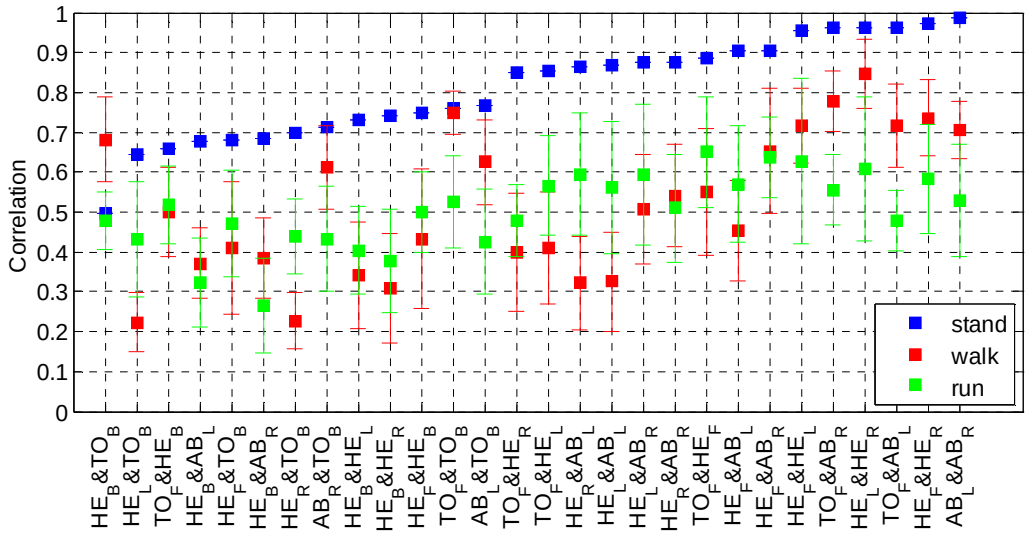

Figure 8.19. Statistics of correlation (TX on WA_F).

As expected, it is clear that the correlation is generally lower when the body is moving than when it is standing. This happens because signals decorrelate while the arms and the legs are moving, and the head and the trunk are rotating. The mean correlation is below 0.7 for most of the links, which is an important result for MIMO. In general, the standard deviation of correlation is higher when the body is running, than when it is walking.

The average correlation and the standard deviation during the motion were calculated for all combinations of TXs and RXs pairs. The CDFs of correlation for the different classes are displayed in Figure 8.20.

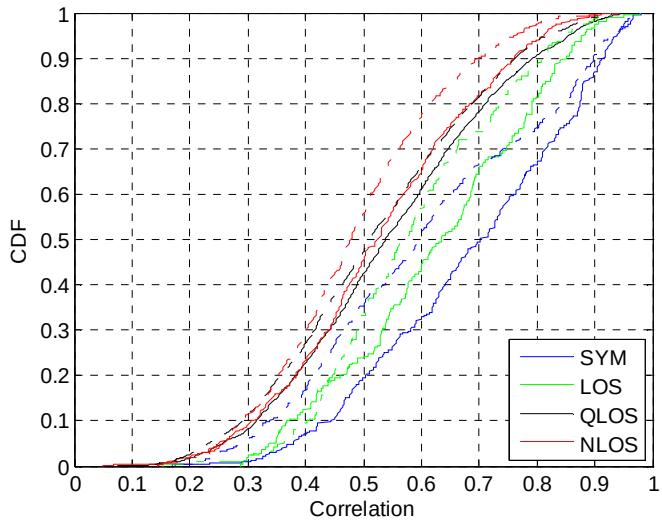

Figure 8.20. Comparison of correlation CDFs for walk (solid) and run (dashed).

The SYM class has a mean correlation of 0.6 for run, and 0.7 for walk. The LOS has a mean correlation of 0.55 for run, and 0.65 for walk. The QLOS has a mean correlation around 0.5 for run, and 0.54 for walk. The NLOS has a mean correlation of 0.48 for run, and 0.52 for walk.

Taking the correlation value of 0.7, it is clear that correlations are lower in the run scenario for most of the time: 90% of the run samples are below 0.7, against 80% for the walk. This is evidenced in the SYM curves, where only 50% of the samples are below 0.7 for the walk case, against 70% for the run. Also, the curves for the run case are more concentrated than in the walking one, showing a not so clear applicability of the classes scheme.

Based on the results of correlation for all combinations, it is possible to identify the less correlated channels, and, thus, the optimum antenna placements. Figure 8.21 and Figure 8.22 present the CDFs of correlation for each of the TXs.

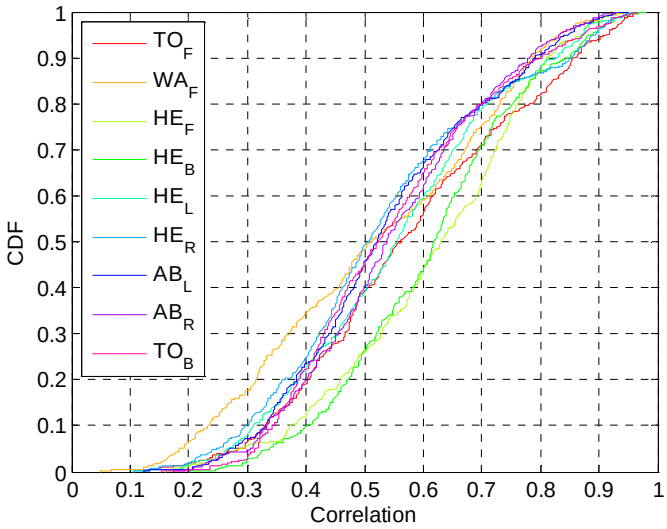

Figure 8.21. CDF of correlation for selected TX placements (walk).

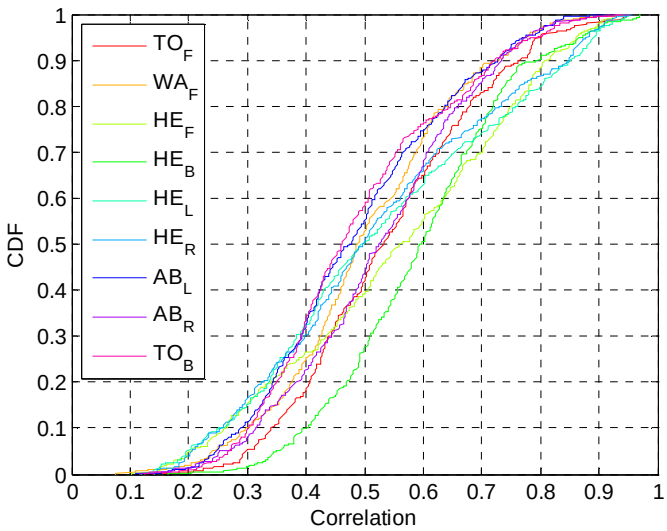

Figure 8.22. CDF of correlation for selected TX placements (run).

The CDFs are somehow different for the two types of mobility, but both show that the TXs with a higher number of links with correlation below 0.7 are the ones on the arms and TO_B. On the contrary, TXs on the head generate highly correlated branches. These results are in line with the ones obtained when the body is static.

Results from this study show that the correlation is naturally lower when the body is moving, being below 0.7 for 90% of the links while the user is running (against 80% for walk). This happens because the arms and legs are moving, the head and the trunk are rotating, and signals become decorrelated. The arms placements enable less correlated channels, being more favourable for MIMO.

8.2.2 Power Imbalance of On-Body Links

The study presented in this section is based on full wave simulations, and considers the mobility of the user, as described in Section 5.3. This analysis allows to understand how the relations between the branches change according to the movement of the body. The parameter analysed in this section is the power imbalance between on-body links.

MIMO performance in BANs can be constrained by the high power difference between the signals, especially for NLOS antennas. Figure 8.23 exemplifies the statistics (mean and standard deviation) of the path gain for the different RXs, when the body is moving and the TX is on WA_F. Previous results for the static user are also shown, for comparison.

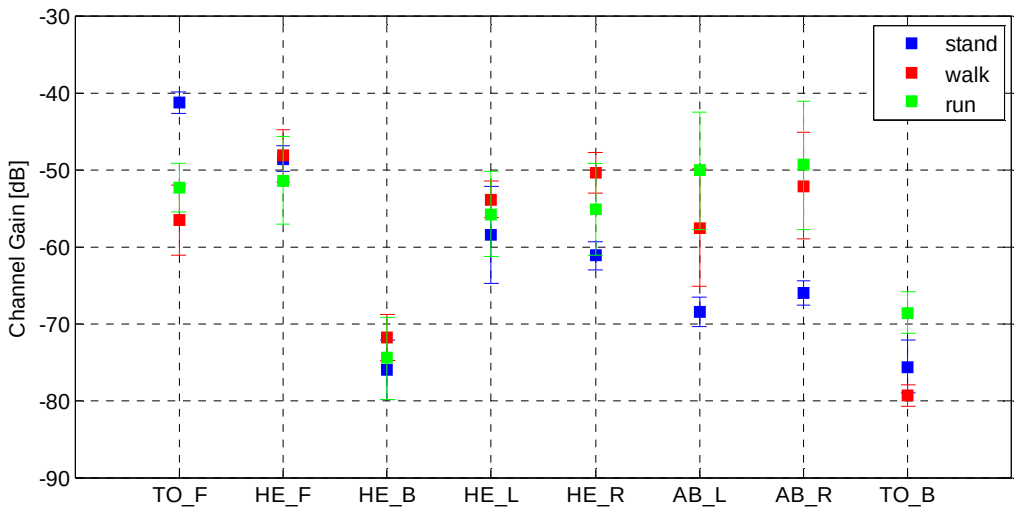

Figure 8.23. Statistics of the channel gain (TX on WA_F).

As in the static scenario, the channel gains are higher when nodes are in LOS, and lower for the NLOS nodes (*e.g.*, on the back). Yet, body dynamic seems to decrease the channel gain for LOS placements, and to increases their values for NLOS (at least, for run). This is expected

because of the reflections from the arm swing that also contribute to increase the power received in the arms. For walk, the distinction between the channel gains is more visible than for run, thus, power imbalances will be higher. When the body is running, the standard deviation of the channel gain increases (compared to walking).

The trend of power imbalance during a motion cycle, when the TX is on the belt (WA_F), is shown in Figure 8.24, for selected pairs of antennas representative from the various classes.

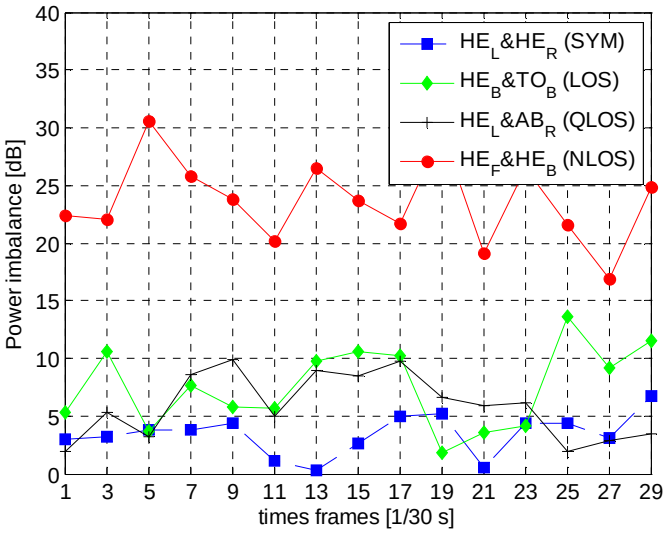

Figure 8.24. Power imbalance (TX on WA_F: walk).

The NLOS pair of branches (HE_F and HE-B), the one with lower correlation, presents the highest power imbalance during the motion, as expected. On the contrary, the SYM pair (HE_L and HE_R) has the lowest imbalance (< 5 dB). The QLOS pair presents more fluctuations due to the arm swing and head rotation while the user is running. For the LOS placements, the trunk and the head rotation during the movement also promote some fluctuations.

Taking into account the results of all possible TX placements, a summary of the global statistics of imbalance over time, with the mean value and the standard deviation per class, is presented in Table 8.8.

Table 8.8. Imbalance statistics for the dynamic user.

	SYM		LOS		QLOS		NLOS	
	$\overline{\Delta P}$ [dB]	$\sigma_{\Delta P}$ [dB]	$\overline{\Delta P}$ [dB]	$\sigma_{\Delta P}$ [dB]	$\overline{\Delta P}$ [dB]	$\sigma_{\Delta P}$ [dB]	$\overline{\Delta P}$ [dB]	$\sigma_{\Delta P}$ [dB]
Walk	7	4	9	3	12	5	15	4
Run	10	6	10	4	12	6	17	6

For the dynamic user, it is observed that the standard deviation of power imbalance generally increases, compared to the static scenario. SYM and LOS nodes still present the lowest imbalance values, below 10 dB, being somewhat higher when the user is running than when

walking. But, contrary to the static user, the distinction between the classes is not so visible. For instance, the QLOS has an average imbalance of 12 dB (for both walk and run), not much different from the SYM and LOS values. NLOS links have prohibitive mean values of 15 and 17 dB, for walk and run respectively, too high to benefit from MIMO. As expected, the movement of the user decreases the imbalance of NLOS branches, as the reflections on the dynamic limbs contribute to increase the power received in the NLOS RXs. The LOS RX placements seem to be the most promising for MIMO.

Similarly to what was done for correlation, the CDFs of power imbalance were obtained for the different TX placements. Figure 8.25 and Figure 8.26 present the CDFs for the TXs with the higher number of links with imbalance below 10 dB.

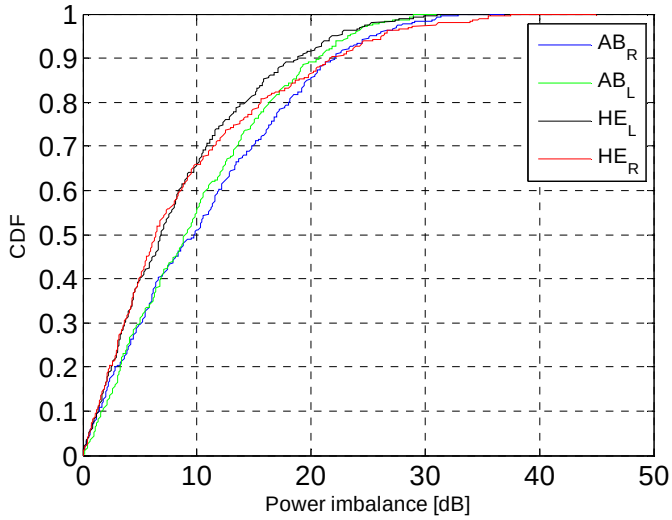

Figure 8.25. CDF of power imbalance for selected TX placements (walk).

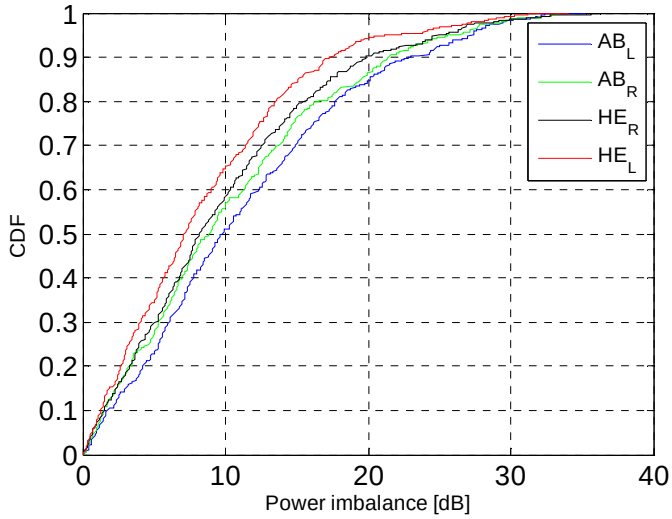

Figure 8.26. CDF of power imbalance for selected TX placements (run).

With respect to the 10 dB target for MIMO, the TX placements on the sides of the body, *i.e.*,

on head and arm left and right, promote the lowest and the less spread power imbalance between the branches. The TX locations that generate the higher imbalances are the ones on the back (not shown), due to their NLOS position to most of the nodes, and associated poorer signal levels. Similar conclusions were obtained for run and walk cases.

Results from this study show that the body dynamics generally increases the standard deviation of the power imbalance. NLOS branches become more balanced when the body is moving, than when it is static. The applicability of the classes' scheme fails in these dynamic scenarios. With respect to the 10 dB target for MIMO, the TX placements on the sides of the body, *i.e.*, on ears and arms, promote the lowest and the less spread power imbalance between the branches.

8.2.3 Optimum 1×2 Placements

The results from the previous sections show that a joint analysis of correlation and imbalance is required to select the best combinations of TXs and RXs to be used in a MIMO scheme. These best combinations should fall inside a target area to theoretically benefit from MIMO, *i.e.*, correlation and imbalance below 0.7 and 10 dB, respectively.

The mean values of correlation and power imbalance during a motion cycle were calculated for all combinations of TXs and RXs (in a 1×2 scheme). Figure 8.27 and Figure 8.28 display their mapping for the walk and run scenarios, respectively. The target area to benefit from MIMO is enclosed in the maps by the red lines. The histograms of correlation and power imbalance are also displayed, for a better interpretation and statistical characterisation of the results.

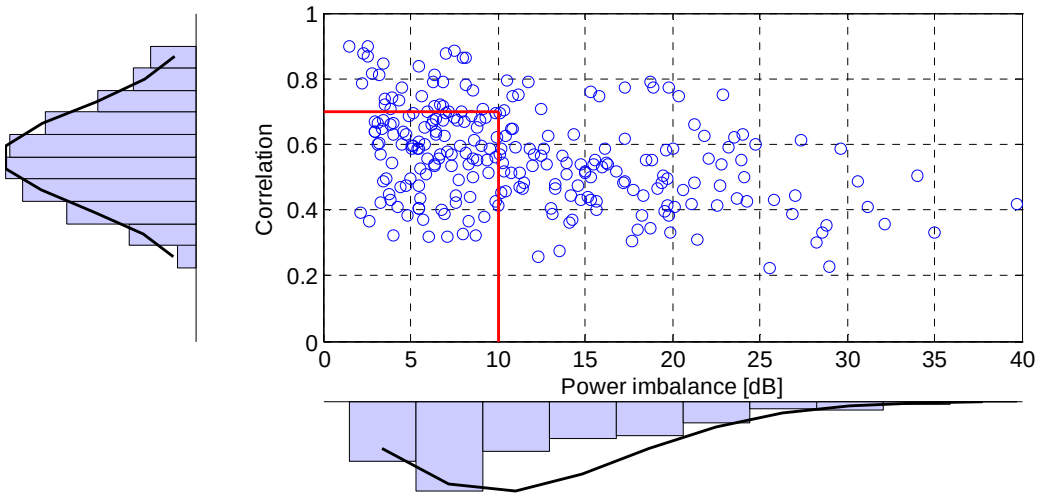

Figure 8.27. Map of correlation and power imbalance (walk).

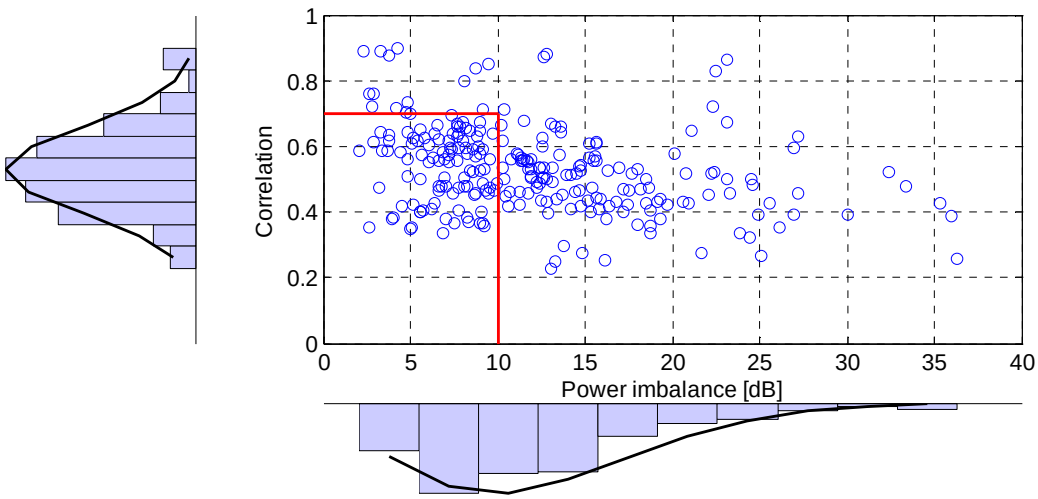

Figure 8.28. Map of correlation and power imbalance (run).

The maps are slight different according to the mobility scenario, with a larger spread of values being observed in walk. The major differences between walk and run are expected to come from the numerical accuracy of simulations. Anyway, the fast movements in the run scenario support the slight lower mean values for correlation and imbalance.

As seen from the histograms, the correlation ranges in [0.2, 0.9] for both scenarios, being Truncated Normally distributed, with a mean value around 0.6 for walk, and 0.5 for run. Power imbalance ranges in [2, 40] dB for walk, while for running it varies in [2, 36] dB. A mode value around 10 dB was found for both scenarios, and it can be fitted by a Rayleigh Distribution.

Table 8.9 presents the estimates for each parameter of the fitting curves, together with the R^2 goodness of fit test.

Table 8.9. Statistical 152haracterization of correlation and imbalance.

	Correlation (Trunc. Normal Distribution)			**Imbalance (Rayleigh)**	
	μ_{TN}	σ_{TN}	R^2	m_R [dB]	R^2
Walk	0.56	0.14	0.96	9.96	0.75
Run	0.53	0.13	0.95	9.85	0.92

The slow or fast mobility of the user has little impact on the mean values of correlation and power imbalance between on-body channels. However, the visual observation of the maps shows slight different distributions, evidencing less correlated signals for the fast movements.

Based on these maps, it is possible to identify the best combinations of RXs for each TX placement, *i.e.*, the ones that fall inside the target area. It is observed that 40% of the possible 1×2 links for the running action are inside the target area for MIMO, against 39% for walk.

The percentage of links, per TX, falling into the target area is given in Figure 8.29, from which it is possible to identify the antenna placements with better conditions to achieve performance gains.

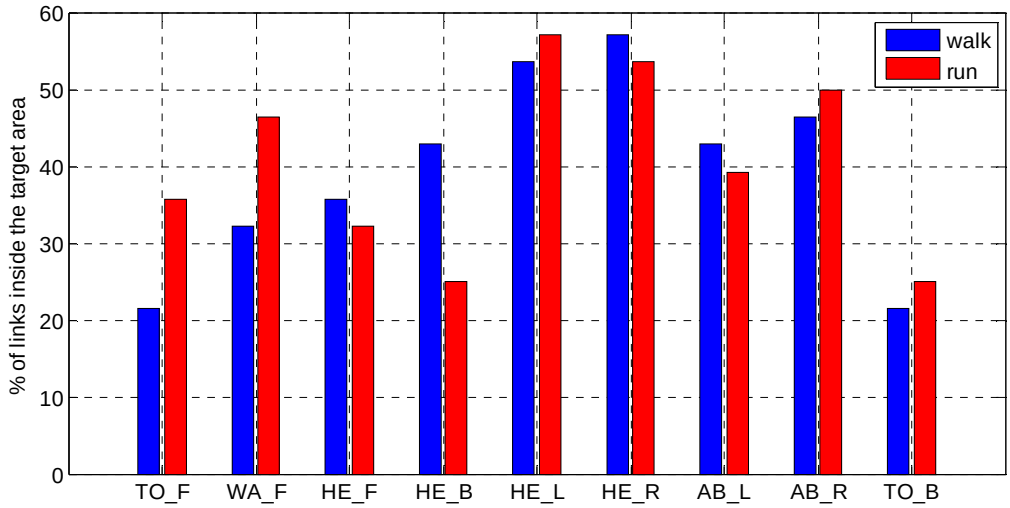

Figure 8.29. Analysis of the conditions of each TX.

Results from correlation and power imbalance support that the most favourable TX locations are on the ears (HE_L and HE_R), with about 55% of the links falling into the target area. Then, the arms are the second best placements, with [40, 50]% of the links inside the area. These results suggest that the TX placements on the sides of the body have better conditions to achieve improved performances. The worst placements for the TX include nodes on the back for both mobility scenarios, which is an intuitive result, as the weak signals in these nodes promote strong imbalances between branches.

Table 8.10 indicates the "best" combinations of RXs for each TX, sorted by the lowest imbalance. It is important to state that although, in theory, on-body nodes can cooperate in many different ways, one should look carefully at these results. The application viewpoint should be understood, and realistic and probable configurations have to be selected from the database of results.

Results show fair similarity between both mobility scenarios. Some TX placements, like those on TO_F and HE_L, have the same best pair of RXs for both scenarios. Generally, considering the optimum TX locations, results suggest that TXs should be combined with RXs in NLOS or QLOS conditions, to enable uncorrelated and balanced channels.

The use of MIMO addresses an increased complexity compared to the 1×2 scheme. The correlation and power imbalance are no longer given by a pair of values obtained from two branches, but need to take the four branches of the 2×2 MIMO system into account, being

analysed among the sub-channels. Accordingly, correlation and power imbalance are given by 4×4 matrices, that, due to symmetry, reduce to six significant coefficients.

Table 8.10. The "best" RX combinations for each TX (sorted by the lowest imbalance).

	Walk		**Run**	
TX	**RX1**	**RX2**	**RX1**	**RX2**
TO_F	WA_F HE_B WA_F	HE_B AB_R AB_L	WA_F WA_F WA_F	HE_B AB_L AB_R
WA_F	TO_F HE_F HE_L	HE_L AB_R AB_R	HE_L TO_F HE_F	HE_R HE_F HE_L
HE_F	WA_F HE_B WA_F	HE_R HE_R HE_L	WA_F HE_L HE_B	HE_B AB_L AB_L
HE_B	TO_F HE_F HE_F	HE_F HE_L AB_R	TO_F AB_L TO_F	AB_L AB_R AB_R
HE_L	HE_B HE_R WA_F	TO_B AB_L TO_B	HE_B HE_B HE_F	TO_B AB_L TO_B
HE_R	WA_F HE_F AB_R	HE_F TO_B TO_B	HE_B HE_F AB_R	TO_B TO_B TO_B
AB_L	TO_F WA_F HE_R	HE_F HE_L AB_R	WA_F TO_F HE_B	HE_F HE_F AB_R
AB_R	TO_F WA_F HE_F	HE_F HE_F TO_B	HE_B TO_F TO_F	AB_L HE_F WA_F
TO_B	TO_F HE_R HE_L	HE_F AB_R AB_R	TO_F TO_F WA_F	WA_F HE_F HE_F

A probable configuration of a 2×2 MIMO, consists of two neighbouring TX sensors sending information to a body central unit (sink), composed of two nearby RXs. Figure 8.30 represents a possible option when considering the best placements obtained from the results, *i.e.*, TXs on head. Considering the reciprocity of the channel, the RXs are placed on arms. This is a feasible configuration enabling two main uncorrelated and balanced branches between both TXs.

8.3 Dynamic User in a Scattering Environment

8.3.1 Influence of the environment

The environment in which the BAN is operating has a limited influence in the performance of

on-body communications, due to the short length of the links. This first analysis of the dynamic user in the scattering environment intends to observe the effect of the environment in the communications, namely on the channel gains. For this purpose, it is considered that the BAN is operating in two scenarios with dissimilar dimensions and scatters distribution: indoor (office) and outdoor (street), described in Section 6.2. The mobility scenario considered in this study is "walk". The channel gain is calculated as described in Section 5.4, and it is based on the assumption that the signal at the RX results from the contribution of one on-body component (obtained from the full wave simulator, *CST*) and of the several MPCs present in the environment (obtained from the GBSC_B model).

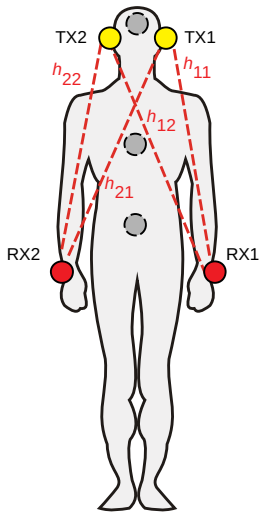

Figure 8.30. Possible MIMO configuration.

Figure 8.31 and Figure 8.32 show, for the office and the street environments, respectively, the channel gains resulting from the different contributors, namely: on-body component (*CST*), multipath components (MPC) and the total mean power (*CST*+MPC). The selected case study considers the transmitters on TO_F and TO_B, and the sink composed by nodes on HE_F and HE_B. Table 8.11 summarises the statistics of the channel gains (over time) from the different contributors.

In the office environment, the MPCs may actually contribute to the total received power. This is particularly true for NLOS nodes, where the MPCs "help" to improve the quality of the signal. For instance, the HE_F node is in NLOS with the TX on TO_B, and the MPCs clearly increase the channel gain from -71 dB to -59 dB. In case of HE_B, in LOS and at a short distance with the TX TO_B, the on-body component is dominant (-40 dB), and MPCs (-51 dB) have little impact on the total power (-39 dB). The mean value of the MPCs in the office environment ranges in [-59, -51] dB, with standard deviations up to 3 dB.

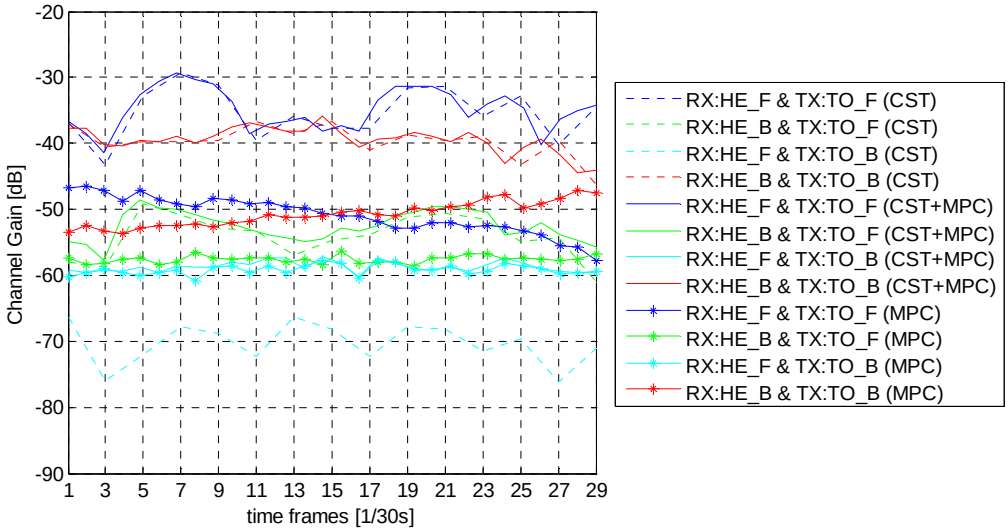

Figure 8.31. Channel gain at office environment (TXs: TO_F&TO_B / RXs: HE_F&HE_B).

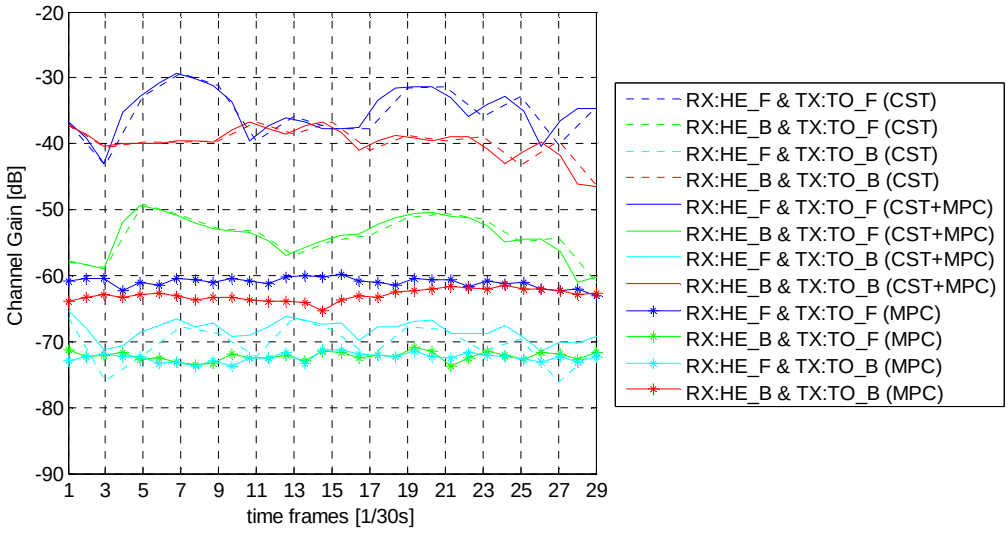

Figure 8.32. Channel gain at street environment (TXs: TO_F&TO_B / RXs: HE_F&HE_B).

Table 8.11. Statistics (over time) of the different components for the user in scattering environments.

			On-Body (*CST*)		**Environment (MPC)**		**Total (CST+MPCs)**	
	RX	**TX**	$\overline{h_{kl}}(\Delta t_n)$ [dB]	$\sigma_{\overline{h_{kl}}}(\Delta t_n)$ [dB]	$\overline{h_{GBSC\_B}}(\Delta t_n)$ [dB]	$\sigma_{\overline{h_{GBSC\_B}}}(\Delta t_n)$ [dB]	$\overline{h_T}(\Delta t_n)$ [dB]	$\sigma_{\overline{h_T}}(\Delta t_n)$ [dB]
Office	**HE_F**	**TO_F**	-35	4	-51	3	-35	3
	HE_B		-54	3	-57	1	-52	2
	HE_F	**TO_B**	-71	3	-59	1	-59	1
	HE_B		-40	2	-51	2	-39	2
Street	**HE_F**	**TO_F**	-35	4	-61	1	-35	3
	HE_B		-54	3	-72	1	-54	3
	HE_F	**TO_B**	-71	3	-72	1	-68	2
	HE_B		-40	2	-63	1	-40	2

On the contrary, the large dimensions of the street environment, compared to the short propagation distances in the BAN, make the MPCs weaker and with less variations, ranging in [-72, -61] dB with a standard deviation around 1 dB, and being unimportant to the on-body communications (at 2.45 GHz). The on-body component is dominant for most of the cases, even if it is weak, and then, the total power has negligible contributions from the MPCs. This is observed in the HE_F node, in NLOS with the TX on TO_B, that it is no longer "helped" by the MPCs, and the received power remains very low (-68 dB).

To highlight the impact of each environment, the case TX: TO_F and RXs: HE_F&HE_B, with the RXs respectively in LOS and NLOS with the TX, is analysed in more detail. Figure 8.33 and Figure 8.34 exemplify the statistics (average and standard deviation) of the channel gain over the $N_s = 50$ simulations with random distributed scatterers, for the office and street environments, respectively. Table 8.12 summarises these statistics.

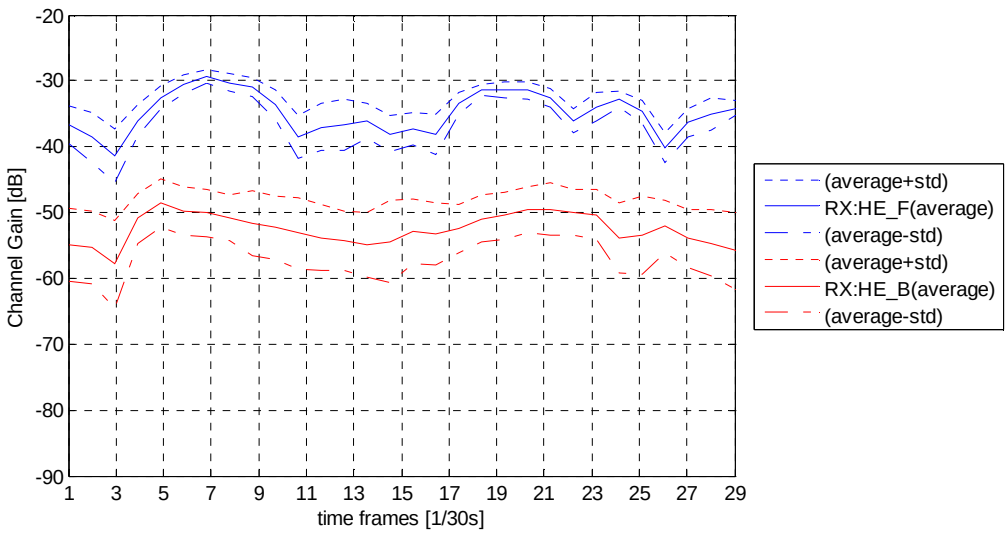

Figure 8.33. Statistics of channel gain at office (TX: TO_F / RXs: HE_F&HE_B).

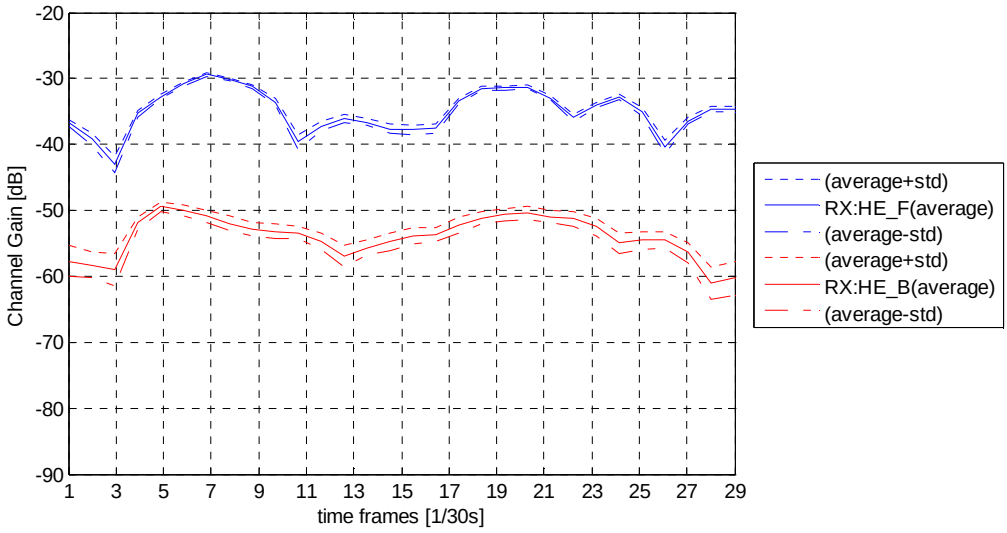

Figure 8.34. Statistics of channel gain at street (TX: TO_F / RXs: HE_F&HE_B).

Table 8.12. Statistics of channel gain for the user in scattering environments.

	RX	TX	$\overline{h_T}(\Delta t_n)$ [dB]	$\overline{\sigma_{h_T}}(\Delta t_n)$ [dB]
Office	**HE_F**	**TO_F**	-35	2
	HE_B		-52	5
Street	**HE_F**	**TO_F**	-35	0
	HE_B		-54	1

The stronger impact of the MPCs in the office environment is instantly noticeable by the higher mean values of standard deviation ranging in [2, 5] dB in office, against [0, 1] dB in street. This phenomenon is especially visible in the HE_B placement which is in NLOS with the TX.

Results from the comparison between the BAN performance in a street and inside an office showed that multipath at large environments is unimportant compared to the on-body component (at the studied frequency of 2.45 GHz). Based on these results, the capacity study in the next section is provided only for the office environment.

8.3.2 Capacity for an indoor environment

This section gives results for the MIMO capacity for the selected 2×2 configurations of on-body antennas represented in Figure 8.35, which were previously described in Table 6.1 from Section 6.2. These configurations represent probable scenarios for a 2×2 MIMO system in BANs, consisting in two nearby data sensors sending information to the body central unit (sink). These data sensors can be on the head or on the arms, while the sink is on the front (or front/back) of the body. The user is inserted in a scattered office environment, and the mobility scenario is "walk". The MIMO capacity statistics and metrics mentioned in this section were calculated as described in Section 5.4.

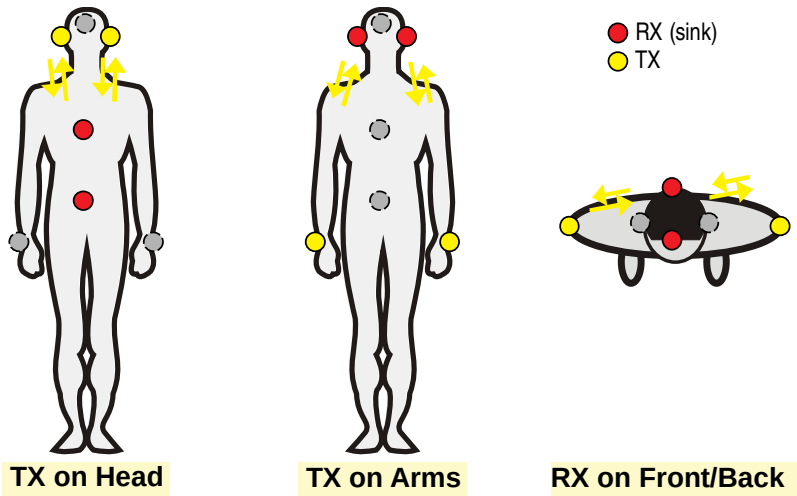

Figure 8.35. Selected 2×2 configurations.

The trend of the average capacity over time (over the $N_s = 50$ simulations) for the selected case studies is represented in Figure 8.36 and Figure 8.37 for the data sensors on the head and on the arms, respectively.

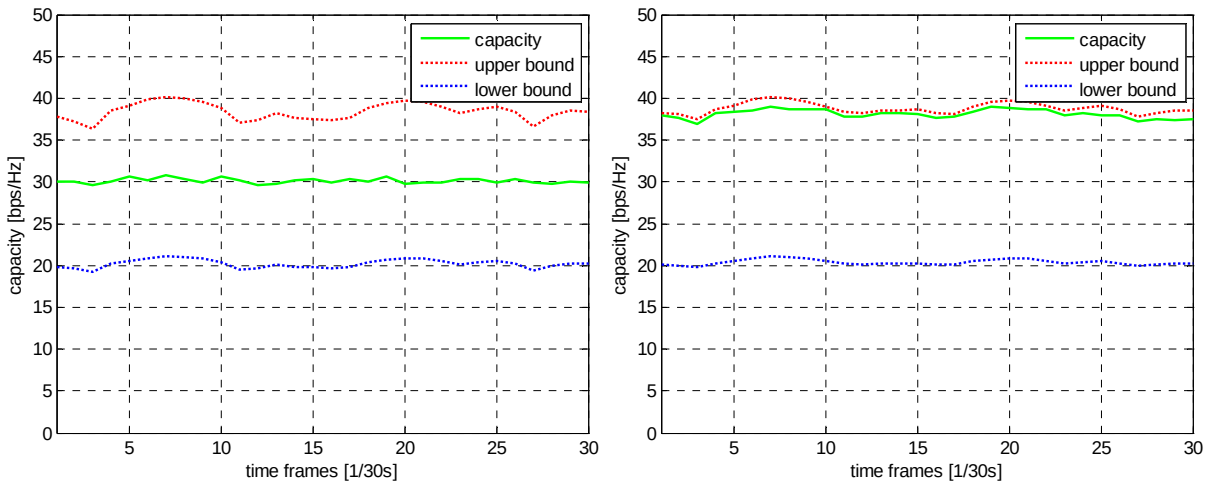

(a) Sink on front (RXs: TO_F&WA_F) (b) Sink on front/back (RXs: TO_F&TO_B)

Figure 8.36. Capacity trend (sensors on the head, TXs: HE_F&HE_B).

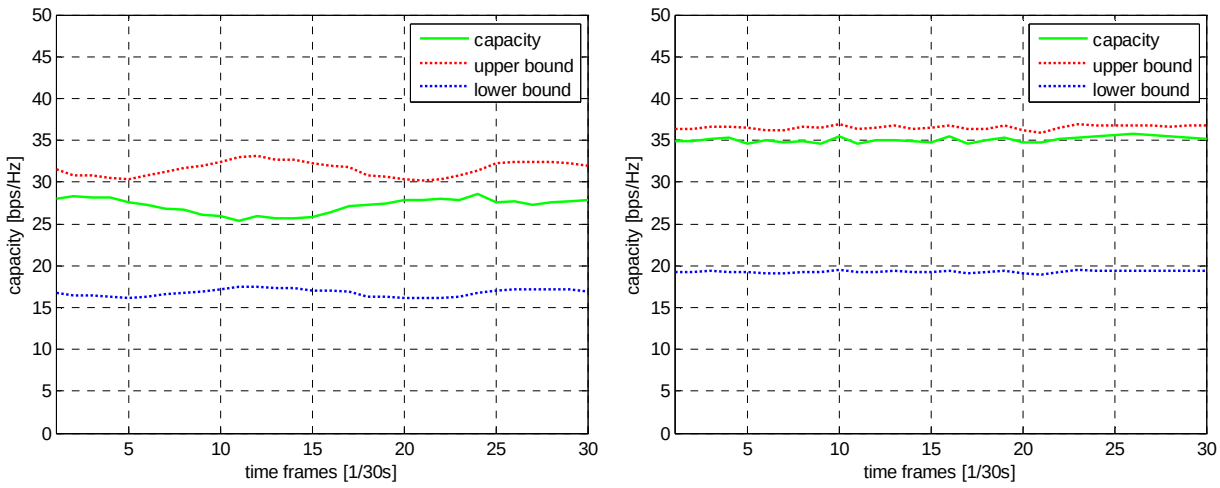

(a) Sink on front/back (RXs: TO_F & WA_F) (b) Sink on head (RXs: HE_L & HE_R)

Figure 8.37. Capacity trend (sensors on the arms, TXs: AB_L&AB_R).

For the case of the sensors on the front/back of the head, and the sink in front of the body, the signals between the different branches are balanced, but they are highly correlated due to the short distances and LOS between nodes. For this reason, in Figure 8.36a, the capacity is in-between the upper and the lower bounds. If the sink nodes are on the front and back of the body, then the signals are balanced and uncorrelated, and capacity almost reaches the upper bound, as seen in Figure 8.36b.

When the sensors are on the arms and the sink is on the front of the body, the signals are

balanced and uncorrelated by the arms movement, so the capacity is high as shown in Figure 8.37a. However, it is observed that if the sink is placed on the ears, then the branches become even more uncorrelated, and capacity approaches the upper bound (Figure 8.37b).

The selection of the optimum placements should be done according to the specific system under study. The metric $C_{G_{BAN}}$, the BAN MIMO capacity gain defined in (5.13), gives the indication of the gain of a specific configuration in relation to the capacity of a particular system. Figure 8.38 and Figure 8.39 show the trend of $C_{G_{BAN}}$ during the motion for selected case studies.

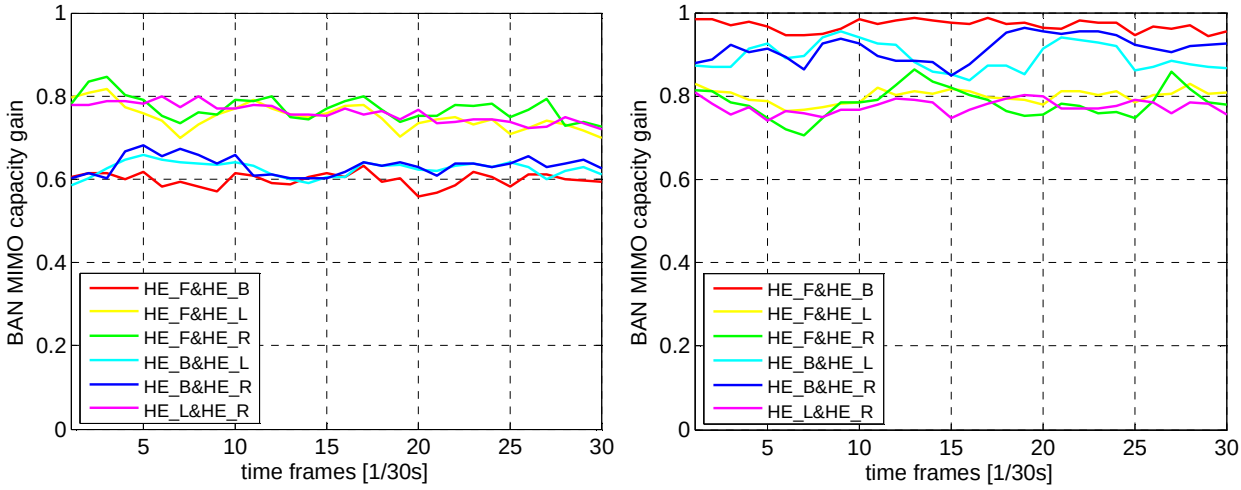

(a) Sink on front (RXs: TO_F & WA_F) (b) Sink on front/back (RXs: TO_F & TO_B)

Figure 8.38. BAN MIMO capacity gain trend (sensors on the head).

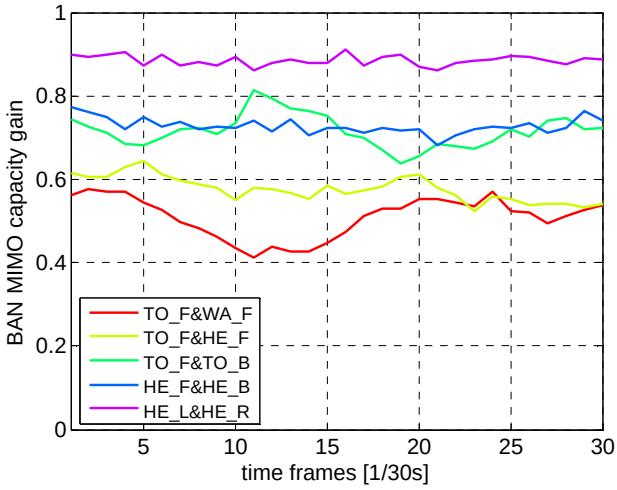

Figure 8.39. BAN MIMO capacity gain trend (sensors on the arms).

When the sensors are on the head, it is observed from Figure 8.38 that higher gains are obtained if the belt sink nodes are located in front and back (RXs: TO_F & TO_B), than when both sink nodes are on the front (RXs: TO_F & WA_F). This result is a consequence of the high correlation between nearby and LOS branches. When the sensors are on the arms,

Figure 8.39 shows that higher gains are obtained if the sink RXs are in the ears. Also, it is possible to observe the effect of arm swing in the trend of the capacity gain, meaning that capacity is not constant during the motion.

Figure 8.40 and Figure 8.41 show the statistics of the BAN capacity gain for the selected case studies. Table 8.13 summarises the general statistics of capacity over time for the selected cases, providing an overview of $C_{G_{BAN}}$, allow understanding which configurations achieve higher performances, and also of C_G, which enables to quantify the gain relative to the best SISO link.

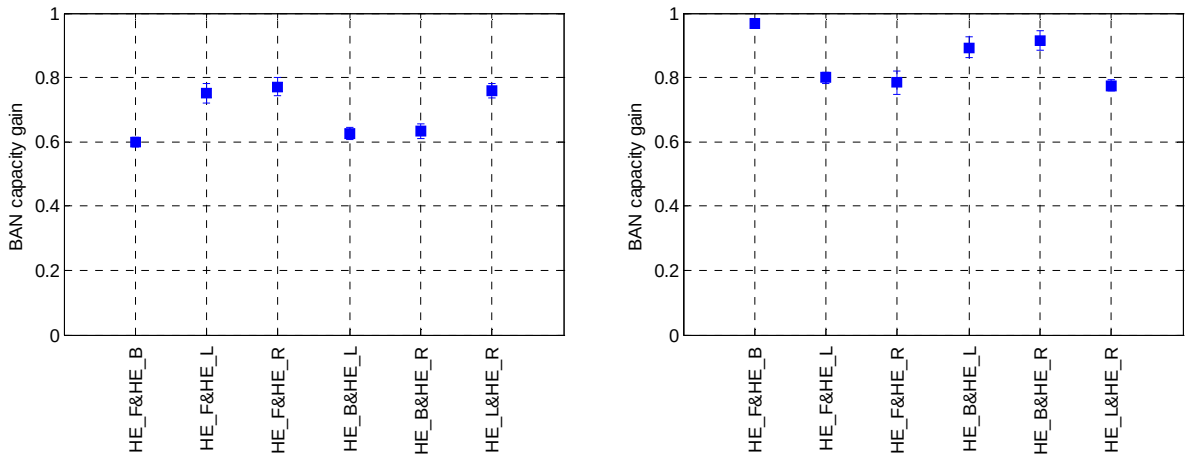

(a) Sink on front (RXs: TO_F & WA_F) (b) Sink on front/back (RXs: TO_F & TO_B)

Figure 8.40. BAN MIMO capacity gain statistics (sensors on the head).

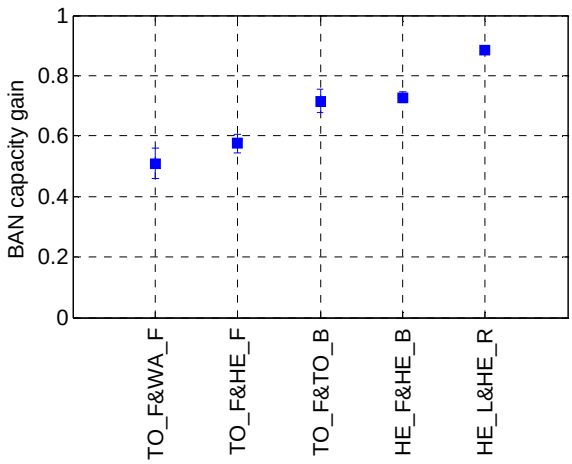

Figure 8.41. BAN MIMO capacity gain trend (sensors on the arms).

Figure 8.42 shows the optimum placements for the selected case studies. The combination enabling the best performance corresponds to the sensors on the head (TXS: HE_F & HE_B), and the sink nodes on front and back of the body (RXs: TO_F & TO_B). For this combination, $\overline{C_{G_{BAN}}}$ is very high (0.97), meaning that capacity approaches the upper bound,

and it has a relative gain to SISO of 1.97. The low values of the standard deviation metrics obtained for this configuration also show that it is stable, not fluctuating with the environment, neither with the body dynamics. For this sink configuration, the worst performance is obtained when the sensors are on HE_L&HE_R, where the symmetry is high, and branches are correlated.

Table 8.13. Statistics of capacity for selected 2×2 configurations.

Sink		Data sensors		$\overline{C_{G_{BAN}}}$	$\sigma_{\overline{C_{G_{BAN}}}}$	$\overline{\sigma_{C_{G_{BAN}}}}$	$\overline{C_G}$	$\sigma_{\overline{C_G}}$	$\overline{\sigma_{C_G}}$
RX1	RX2	TX1	TX2						
TO_F	WA_F	HE_F	HE_B	0.60	0.02	0.10	1.57	0.04	0.11
		HE_F	HE_L	0.75	0.03	0.10	1.72	0.04	0.12
		HE_F	HE_R	0.77	0.03	0.09	1.74	0.04	0.10
		HE_B	HE_L	0.62	0.02	0.09	1.73	0.03	0.12
		HE_B	HE_R	0.63	0.02	0.09	1.72	0.04	0.12
		HE_L	HE_R	0.76	0.02	0.11	1.81	0.03	0.11
TO_F	TO_B	HE_F	HE_B	0.97	0.01	0.04	1.97	0.02	0.04
		HE_F	HE_L	0.80	0.02	0.08	1.78	0.03	0.09
		HE_F	HE_R	0.78	0.04	0.07	1.76	0.05	0.08
		HE_B	HE_L	0.89	0.03	0.06	1.90	0.04	0.07
		HE_B	HE_R	0.91	0.03	0.06	1.92	0.03	0.06
		HE_L	HE_R	0.77	0.02	0.10	1.83	0.03	0.11
TO_F	WA_F	AB_L	AB_R	0.51	0.05	0.11	1.73	0.10	0.14
TO_F	HE_F			0.58	0.03	0.11	1.79	0.04	0.14
TO_F	TO_B			0.72	0.04	0.10	1.73	0.05	0.13
HE_F	HE_B			0.73	0.02	0.10	1.80	0.03	0.13
HE_L	HE_R			0.89	0.01	0.08	1.92	0.01	0.08

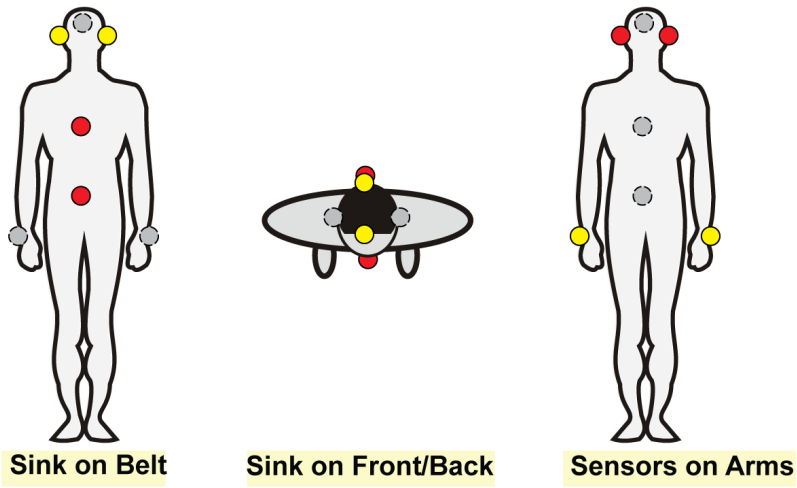

Figure 8.42. Optimum 2×2 placements.

When the sink is on the front of the body (RXs: TO_F & WA_F), the best placements include antennas on front and sides of the head (TXs: HE_L&HE_R, HE_F&HE_L/HE_R), with gains up to 1.81 (with respect to SISO). The worst performance pairs include placements on HE_B, as a result of the weak signal in this node, which provides a little contribution to the improvement of capacity.

If the sensors are on the arms, the best sink location is again on the ears (RX: HE_L&HE_R), with a relative SISO gain of 1.92, while the worst pair is on front of the body (RXs: TO_F&WA_F), with a relative SISO gain of 1.73, and the highest standard deviation. The arm swing causes the higher values of the standard deviation metrics, compared to the other case studies.

The performance of all the selected 2×2 case studies is enhanced, compared to the best SISO scenario, even for LOS branches. This conclusion is taken from the $\overline{C_G}$ values, ranging in [1.57, 1.97]. It is observed that the maximum capacity gains are achieved for symmetric configurations of the TXs and the RXs. This is the intuitive expected result, as it corresponds to the case where channels are less correlated and more balanced.

To sum up, the estimation of the MIMO capacity for a user walking in an indoor environment shows that the best performance is obtained when the sink nodes are on front and back of the body, and the sensors are on the head, with a relative capacity gain to SISO of 1.97. When the sensors are on the arms, the best sink placements are on the sides of the head, with a relative gain of 1.92.

Chapter 9

Conclusions

This chapter concludes the Thesis, providing an overview of the problems addressed, summarising the strategies followed to solve them, highlighting the major results, and providing suggestions for future research. Section 9.1 summarises the work done, while Section 9.2 highlights the main findings. Section 9.3 proposes topics for future investigation.

9.1 Summary

Body Area Networks (BANs) are at the heart of the next generation of wireless systems, linking personalisation and convergence, through a network of wearable sensors. A key challenge for on-body communications is the influence of the user's body on the radio channel. The peculiar characteristics of BANs, like the influence of human tissues, the dynamics of the human body, the short distances of propagation, the link geometry variability, as well as the arbitrary orientation of antennas, demand for explicit solutions that enable the reliability of on-body communications, especially for applications demanding low bit error rates (*e.g.*, healthcare and battlefield).

This Thesis is motivated by the challenges above mentioned, and aims to characterise the on-body radio channel, as well as developing strategies for effective communications using MIMO. The main objectives of the work are to analyse the influence of the user on system's performance, to account for the variability of the channel through user's mobility, to account for the impact of the operation environment, to analyse the use of MIMO in BANs, and to develop strategies for optimum antenna placements. The structure of this document reflects the progress of the Thesis and the research strategy, being organised as follows.

Chapter 1 provides a general overview of the Thesis, introducing the scope and the motivation, and then pointing out the objectives, and the original contributions given by this work. The plan of investigation highlights the integration of the Thesis into European research frameworks, such as FP7 and COST. Also, references to the main published work are provided, including journal and conference papers, as well as contributions for book chapters. The document structure is described in the end of the chapter.

Chapter 2 prompts the most important concepts and the main parameters regarding radio channel modelling. The focus of the chapter is on MIMO systems, the MIMO capacity estimation being particularised for a 2×2 configuration. The impact of the on-body radio channel on the MIMO capacity is discussed, covering aspects like channel fading, multipath or channel correlations.

In Chapter 3, the State of the Art on channel modelling for BANs is provided. The chapter starts with the description of the electromagnetic properties of the human body, introducing the numerical phantoms. A detailed description of the body dielectrics parameters is left for Annex A. Then, the various challenges for the wearable antennas design are discussed, in

special the proximity of the human body. The chapter goes through the on-body propagation mechanisms, like line of sight free space propagation, or surface and creeping waves. Proper BAN models for the most relevant radio channel parameters are reviewed, like for path loss, channel impulse response, or associated statistical information. An overview on the use of channel diversity/cooperative techniques for BANs, especially the use of MIMO, is also provided.

Chapter 4 describes the models applied for the characterisation of the interaction between the on-body antenna and the BAN user, under a statistical viewpoint. The statistical approach for modelling antennas' behaviour in the vicinity of the human body is firstly introduced. The proposed models to implement this approach are then described, starting from well-known theoretical wave propagation models, with basic radiation sources near a simple 2D homogeneously dielectric filled shape. A plane wave with TE and TM incidences at 0.9 and 2.45 GHz, as well as an elementary radiation source (*e.g.*, Hertz dipole) with different orientations at 2.45 GHz, are considered. The implementation is enhanced by a realistic 2.45 GHz patch antenna and a 3D voxel model of the body, realised through a full wave simulator (*CST Microwave Studio*), using the Finite Integration Technique.

Chapter 5 describes the three studies carried out to characterise the on-body channel at 2.45 GHz under different conditions. The first study considers a static user in free space, wearing nine on-body antennas, and analyses the relations among the on-body links in the absence of multipath components. This study is realised through measurements and numerical simulations. The complexity of the problem is then increased, and the subsequent study includes the mobility of the user, using motion capture software to perform dynamic numerical simulations. Both static and dynamic studies characterise the spatial correlation and the power imbalance among on-body branches. The third study makes use of the information provided by a geometrically based statistical channel model to include the operating scattering environment. The statistical modelling of antennas in BANs is separated into antennas in the vicinity of the body (including body dynamics) and propagation environment. The estimation of the MIMO capacity is described for this study.

Chapter 6 deals with the specific scenarios and parameters used in this Thesis. General metrics related to radiation patterns and statistical distributions are firstly provided. The conventions used throughout the Thesis are described, like the body segmentation, postures and coordinate systems, network topology, mobility and environment scenarios, as well as the radio channel settings. The particular parameters considered in the analytical and numerical studies are given, namely the body tissues and dimensions, selected radiation sources/antennas, and antenna-body distance distributions. The measurement circumstances for the different studies

performed are also provided.

Chapter 7 presents the main findings of the statistical analysis for modelling the antennas' behaviour near the human body. General conclusions resulting from the application of analytical models to basic body shapes and radiation sources are firstly taken. The impact of the body in the propagation of a plane wave is characterised, together with the statistics of the radiation pattern of an elementary source (dipole) when placed at different distances to the user. The full collection of results obtained for the elementary source is left for Annex B. Therefore, results are given for a realistic patch antenna and a 3D model of the body, implemented through the full wave simulator *CST*. A selection of appropriated meshing parameters for the simulator is performed, based on their computation requirements (memory and simulation time), as well as on the accuracy of results. The numerical simulation results, under a statistical viewpoint, of a patch antenna radiating at different distances to the user, are given. A comparison with a dipole radiating near the user is also performed. From the database of results, statistics on the on-body antenna model (average and standard deviation) are calculated. The full set of results is left for Annex C. The patch performance is also compared when different body models (homogeneous and voxel phantoms) are used. Results from a measurement campaign of the on-body radiation patterns are also provided, to assess the limitations of the simulated body models.

Chapter 8 reports the conclusions from the different studies carried out to model the on-body channel at 2.45 GHz. A static user in free space, wearing one transmitter and eight receivers, is firstly analysed through measurements and numerical simulations. The on-body links are classified based on the nodes placement and on the transmitter location. A summary of this classification is left for Annex D. Channel gains, power imbalance and correlation among on-body links are the main parameters addressed here. Then, similar results are provided when user's mobility is added to the model, and optimum 1×2 on-body placements are suggested. The situation of a user moving in a complex propagation environment (indoor and outdoor) is finally considered. The influence of the environment is analysed, and the MIMO capacity results are presented. Based on proper metrics, optimum 2×2 antenna placements are suggested.

This Chapter concludes the Thesis, providing an overview of the different problems addressed, with a summary of the strategies followed to solve them. The major achievements obtained throughout this work are highlighted, and suggestions for future research are also addressed.

9.2 Main Findings

This works starts by analysing the impact of the user on the on-body antenna performance. Two simple and well known analytical models, addressing basic sources radiating near a simple 2D body model (dielectric cylinder), are firstly implemented. Then, the problem is studied using accurate full wave simulations.

The results for the plane wave propagation near different sized body segments and tissues confirm the well-known phenomenon of reflection and refraction when the wave approaches the user. The extent of these phenomena naturally depends on the frequency, dimensions of the body, and tissues properties. A slight impact on propagation is verified, especially for small body segments, compared to the wavelength. Harder patterns of reflections are verified for larger body parts, and narrower shadow areas become visible for tissues with large penetration depths. A similar behaviour is found for both TE and TM plane wave incidences, the fields following a Normal Distribution. Parameters for this distribution are given for different body tissues and frequencies, showing higher mean and standard deviation values for muscle filled tissues (*e.g.*, for a TM wave incident on the leg, the field is Normally distributed, with mean of 1 dB and standard deviation of 5 dB).

The results for the field produced by an elementary source (Hertz dipole) – with different polarisations, and at different distances from the body – confirm that the larger body segments have a stronger impact on propagation, especially when the antenna is closer to the body. An Exponential Distribution of the fields with distance in the directions of strong lobes (forward direction of the body) is observed. These lobes present small fluctuations from the average (standard deviation lower than 5 dB), while great fluctuations (up 24 dB) are found for other directions (backwards).

The preliminary calculations with the basic theoretical models show that the body disturbs the antenna radiation pattern. This reinforces the pertinence of the proposed concept of an antenna statistical model, describing the changes in its overall performance (*e.g.*, radiation pattern, efficiency, and input impedance).

Before setting up the full wave simulations with *CST*, a performance assessment was done to elect the mesh settings that lead to a most favourable trade-off between numerical accuracy and time of simulation. For a reference case study, the "optimal" configuration of RL7/LW16 was selected, leading to relative error less than 2% compared to the most accurate settings.

Full wave simulations performed with *CST* enabled a collection of radiation patterns, at 2.45 GHz, at different distances from selected body segments (chest, head, arm and leg). From

this study, average on-body radiation patterns are provided, together with standard deviations. Results show that the body coupling effect is much stronger when the antenna is attached to the user, and the disturbances are stronger for the largest body part (chest). When a patch is near the chest, the change of the average radiation pattern can reach 24%, relative to the isolated antenna. The highest variations are observed in the direction of the body and in the side lobes, for both patch and dipole. Simulations with the dipole prove that this basic antenna (with no ground plane) is greatly disturbed by the presence of the user. Results clearly indicate that the selection of the wearable antenna is an important aspect for the performance of the system: well isolated antennas from the body will ensure stability.

The selection of the numerical phantom (homogeneous or voxel) is also discussed, based on a comparison of the solver statistics, the antenna parameters and the radiation patterns. A patch in front of the head, with different distribution distances to the user, was simulated with both body models. The homogeneous simulations are 5 times faster than the voxel ones. The average gain values differ in 0.5 dB, and the pattern weighted difference between phantoms is about 11%, without visible changes in the area of interest for on-body communications.

The on-body radiation pattern of the patch was measured, with the aim of assessing the simplifications introduced in the simulation models, like the use of truncated models. The scenario of the patch in front of the chest, changing its distance to the body, is replicated in measurements and simulations, and the statistics of the radiation pattern are compared. In the area of interest for on-body communications ($\varphi \in [-90^{o}, 90^{o}]$), an average difference between *CST* and measurements of 0.9 dB is found. The conclusion from this study is that the use of truncated models is a valid approach to model BANs.

Several studies were carried out to characterise the on-body channel under different conditions: static user in free space, dynamic user in free space and dynamic user in a scattered environment. The simplest case was analysed via measurements and full wave simulations, the others are analysed just through simulations.

On-body measurements of static users in an anechoic chamber show a detuning of less than 5 MHz, and a 0.6 dB worst performance, compared to the isolated antenna. Channel gains can have a dynamic range of 33 dB for path links with the same length. This is a consequence of antenna misalignment, which can turn a *quasi* Line-Of-Sight (QLOS) link into non LOS (NLOS), increasing path loss up to 15 dB. This effect must be taken into account in link calculations for BANs, as the connectivity should be assured. For the selected configuration, channel gains can be 5 dB lower for sitting than for standing, due to body shadowing.

The numerical simulations of the static user in free space enabled to study the spatial

correlations and power imbalances among on-body links. This study gives important information to understand the on-body channel when no other reflectors than the body itself exist. Correlation among on-body links depends on the orientation between the receivers, and also on their relative position to the transmitter. For the static user, different classes of links were defined and statistically characterized. A symmetrical placement of the receivers relative to the transmitter is naturally not favourable for MIMO due to high correlation (values round 0.9). The Beta and the Kumaraswamy probability Distributions are good fits to the SYM (symmetric) and LOS links, for NLOS links the Truncated Normal Distribution is the best fit, while for QLOS a bimodal probability distribution should be studied. In this static scenario, a simple look at the imbalance statistics evidences the classes of links. NLOS links, like front/back branches might experience imbalances around 35 dB, QLOS links show an imbalance value around 15 dB, while LOS or SYM connections have imbalances around than 5 dB. Transmitter placements on the head generate balanced lower imbalances (50% of the links are below 10 dB).

The study of correlation and power imbalance was extended to the case where the user is moving in free space, performing specific activities (walk or run). This was done using the *Poser* animation software, and a technique was developed to introduce the body dynamics in the full wave simulator. The movement is studied in a discrete way, running the transient solver for each time frame. The correlation is naturally lower when the body is moving, being below 0.7 for 90% of the links while the user is running (against 80% for walk). This happens because the arms and legs are moving, the head and the trunk are rotating, and signals become decorrelated. In general, correlation is Truncated Normally distributed, with a mean value around 0.5; while power imbalance has a mean value around 10 dB, and can be fitted by a Rayleigh Distribution. The NLOS links exhibit lower correlations, but present the higher power imbalances during the motion. With respect to the 10 dB target for MIMO, the transmitter placements on the sides of the body, *i.e.*, on head and arm left and right, promote the lowest and the less spread power imbalance between the branches.

The mapping between the mean values of correlation and power imbalance during a motion cycle was presented for all possible 1×2 combinations of transmitters and receivers. Based on this map, it was possible to identify the most favourable pair of receivers for each transmitter. That is, the ones falling into a target area having correlation and power imbalance below 0.7 and 10 dB, respectively. Transmitter locations on the ears were found to be the ones with a higher number of links falling into the target area (55%). To enable uncorrelated and balanced channels, these locations should be combined with receivers in NLOS or QLOS conditions.

The natural next step of the work was the study of mobility in a scattering environment, and

the subsequent calculation of the MIMO capacity. As expected, the immediate local environment (up to a few meters) contributes to the fading observed in on-body channels, decreasing their correlations and balancing power levels. A comparison between the BAN performance in a street and inside an office showed that multipath at large environments is unimportant compared to the on-body component (at this frequency of 2.45 GHz).

The MIMO capacity was estimated for selected 2×2 configurations and shows that the best performance is obtained when the sink nodes are on front and back of the body, and the sensors are on the head, with a relative capacity gain to SISO of 1.97. When the sensors are on the arms, the best sink placements are on the sides of the head, with a relative gain of 1.92.

9.3 Future Work

The work presented in this Thesis can naturally be improved and continued. Indeed, other scenarios can be considered, and the proposed solutions can be optimised. Topics and challenges to be investigated in a future work are suggested in what follows.

The statistical models for the antenna-user interaction, as well as the studies to characterise the on-body channel, will benefit from assessment with other types of antennas. Namely, with specific wearable antennas designed for on-body communications, where the impact of the body on the antenna performance is theoretically reduced.

The limitations on the available resources, like the inexistence of a posable voxel model for the full wave simulator, leaded to simplifications on the models used. It will be interesting to analyse the user's mobility with a voxel model, instead of the homogeneous phantom. For instance, with the posable voxel modes from *Poser* [Pose12], through the recently added animation tool for *SEMCAD* X [SEMC12].

The inexistence of a local MIMO testbed for on-body measurements limited the range of studies performed. The validation of the proposed approach to include the scattering environment with a well-designed measurement campaign will be of added value, although the reproducibility of the scenarios is hard to accomplish. This is especially difficult in what concerns the synchronism of the body dynamics among simulations and measurements.

Concerning the network topology, and the use of diversity / MIMO techniques to improve the reliability of the communication, more realistic antenna placements can be investigated. Pairs of antennas at the proposed locations can be considered, instead of a single antenna. Also, further strategies to enable virtual MIMO in BANs are foreseen.

Information on the radio channel characterisation needs further investigation, namely for parameters like the delay spread, or the second order statistics, among others.

The analysis of the exposure of the user to the electromagnetic fields generated by the on-body network, namely the calculation of the specific absorption ratio (SAR) levels is pertinent and must be taken into account in a real operating scenario.

Annex A

Properties of Human Tissues

This Annex contains the dielectric properties considered for selected human tissues, namely the fitting parameters of the 4-Cole-Cole expression.

The fitting parameters of the 4-Cole-Cole expression for selected tissues are given in Table A.1 (adapted from [IFAP12]).

Table A.1. 4-Cole-Cole fitting parameters for given tissues.

	ε_∞	$\Delta\varepsilon_1$	τ_1 [ps]	α_1	$\Delta\varepsilon_2$	τ_2 [ns]	α_2	$\Delta\varepsilon_3$ ($\times 10^5$)	τ_3 [ns]	α_3	$\Delta\varepsilon_4$ ($\times 10^7$)	$\tau 4$ [ms]	α_4	σ_i
Aorta	4.000	40.00	8.842	0.100	50	3.183	0.100	1.00	159.155	0.200	1.000	1.592	0.000	0.250
Bladder	2.500	16.00	8.842	0.100	400	159.155	0.100	1.00	159.155	0.200	1.000	15.915	0.000	0.200
Blood	4.000	56.00	8.377	0.100	5200	132.629	0.100	0.00	159.155	0.200	0.000	15.915	0.000	0.700
Bone (cancellous)	2.500	18.00	13.263	0.220	300	79.577	0.250	0.20	159.155	0.200	2.000	15.915	0.000	0.070
Bone (cortical)	2.500	10.00	13.263	0.200	180	79.577	0.200	0.05	159.155	0.200	0.010	15.915	0.000	0.020
Brain (gray matter)	4.000	45.00	7.958	0.100	400	15.915	0.150	2.00	106.103	0.220	4.500	5.305	0.000	0.020
Breast fat	2.500	3.00	17.680	0.100	15	63.66	0.100	0.50	454.700	0.100	2.000	13.260	0.000	0.010
Cartilage	4.000	38.00	13.263	0.150	2500	144.686	0.150	1.00	318.310	0.100	4.000	15.915	0.000	0.150
Cerebrum spinal fluid	4.000	65.00	7.958	0.100	40	1.592	0.000	0.00	159.155	0.000	0.000	15.915	0.000	2.000
Cornea	4.000	48.00	7.958	0.100	4000	159.155	0.050	1.00	15.915	0.200	4.000	15.915	0.000	0.400
Eye tissues (sclera)	4.000	50.00	7.958	0.100	4000	159.155	0.100	1.00	159.155	0.200	0.500	15.915	0.000	0.500
Fat (aver. Infiltrated)	2.500	9.00	7.958	0.200	35	15.915	0.100	0.33	159.155	0.050	1.000	15.915	0.010	0.035
Gall bladder bile	4.000	66.00	7.579	0.050	50	1.592	0.000	0.00	159.155	0.200	0.000	15.915	0.200	1.400
Heart	4.000	50.00	7.958	0.100	1200	159.155	0.050	4.50	72.343	0.220	2.500	4.547	0.000	0.050
Kidney	4.000	47.00	7.958	0.100	3500	198.944	0.220	2.50	79.577	0.220	3.000	4.547	0.000	0.050
Liver	4.000	39.00	8.842	0.100	6000	530.516	0.200	0.50	22.736	0.200	3.000	15.915	0.050	0.020
Lung (inflated)	2.500	18.00	7.958	0.100	500	63.662	0.100	2.50	159.155	0.200	4.000	7.958	0.000	0.030
Muscle	4.000	50.00	7.234	0.100	7000	353.678	0.100	12.00	318.310	0.100	2.500	2.274	0.000	0.200
Skin (dry)	4.000	32.00	7.234	0.000	1100	32.481	0.200	0.00	159.155	0.200	0.000	15.915	0.200	0.000
Skin (wet)	4.000	39.00	7.958	0.100	280	79.577	0.000	0.30	1.592	0.160	0.003	1.592	0.200	0.000
Small intestine	4.000	50.00	7.958	0.100	10000	159.155	0.100	5.00	159.155	0.200	4.000	15.915	0.000	0.500
Stomach	4.000	60.00	7.958	0.100	2000	79.577	0.100	1.00	159.155	0.200	4.000	15.915	0.000	0.500
Testis	4.000	55.00	7.958	0.100	5000	159.155	0.100	1.00	159.155	0.200	4.000	15.915	0.000	0.400
Tongue	4.000	50.00	7.958	0.100	4000	159.155	0.100	1.00	159.155	0.200	4.000	15.915	0.000	0.250

Annex B

Analysis for the Elementary Source

This Annex contains the collection of results obtained for the elementary source, namely the radiation patterns at different body-source distances and their statistics.

B.1 Patterns at Different Body-Source Distances

A database of radiation patterns was obtained for the source located at different distances from the body parts under study (arm, leg, torso), at 0.9 and 2.45 GHz. Some examples are given below, from Figure B.1 to Figure B.5.

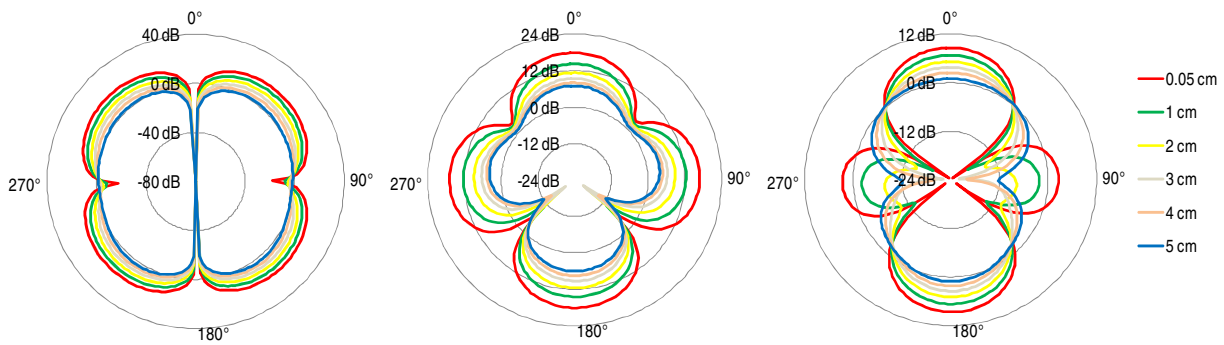

(a) u_ρ (b) u_φ (c) u_z

Figure B.1. Radiation patterns for arm for different d (0.9 GHz).

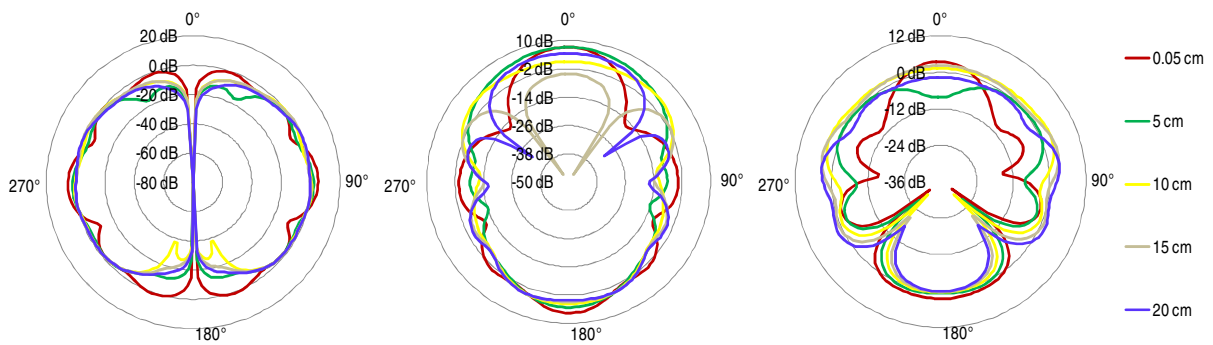

(a) u_ρ (b) u_φ (c) u_z

Figure B.2. Radiation patterns for torso for different d (0.9 GHz).

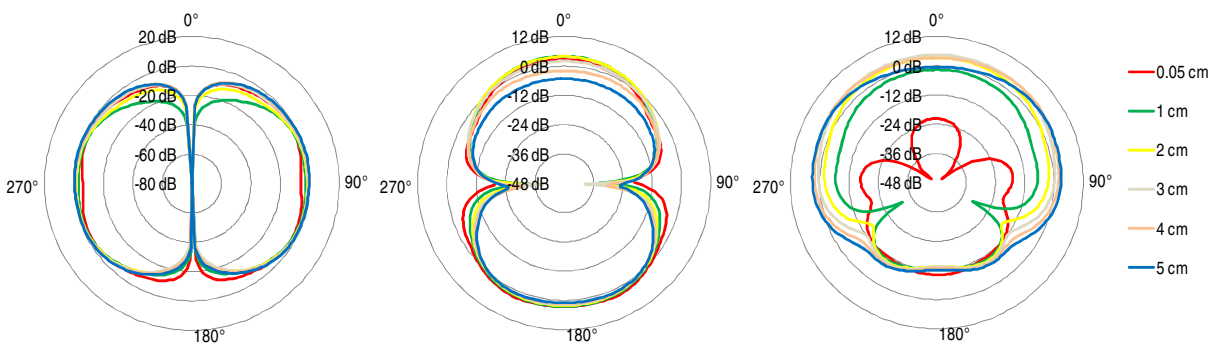

(a) u_ρ (b) u_φ (c) u_z

Figure B.3. Radiation patterns for arm for different d (2.45 GHz).

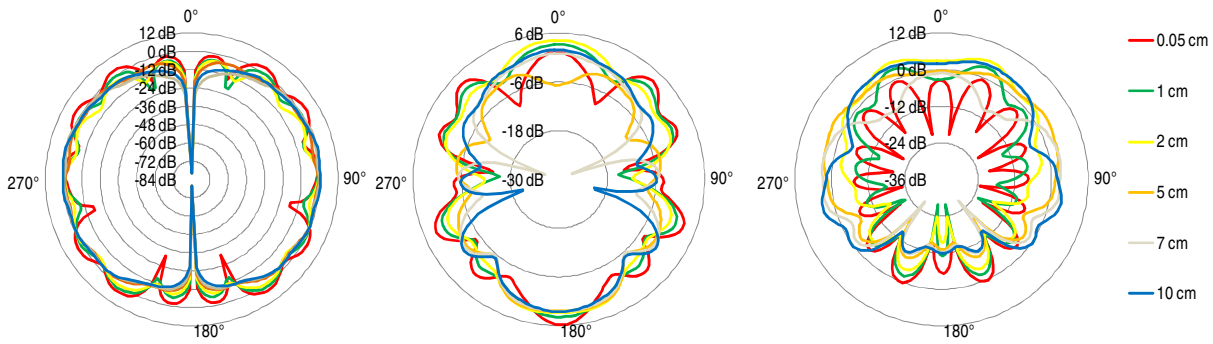

(a) u_ρ (b) u_φ (c) u_z

Figure B.4. Radiation patterns for leg for different d (2.45 GHz).

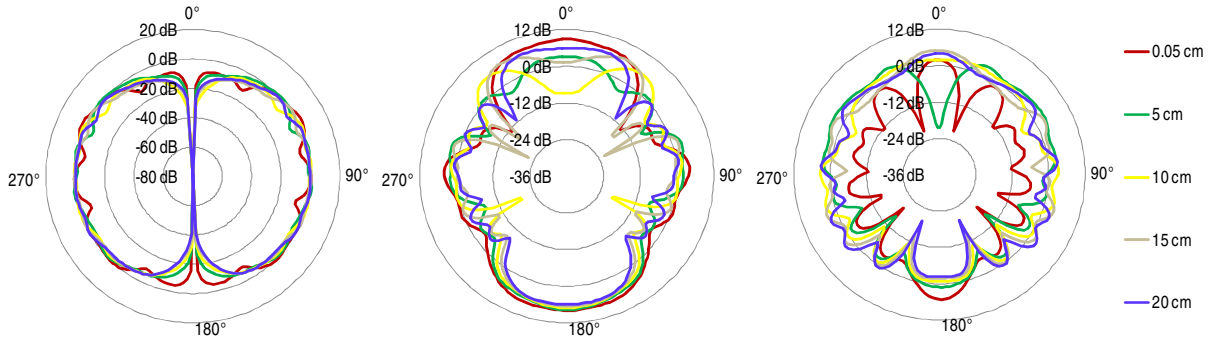

(a) u_ρ (b) u_φ (c) u_z

Figure B.5. Radiation patterns for torso for different d (2.45 GHz).

B.2 Statistical Overview for Different Body-Source Distances

Table B.1 and Table B.2 show the average ($\overline{\Delta E^d}$) and the maximum ($\overline{\Delta E^d_{max}}$) differences between the field obtained at distance d and at a reference distance $d_0 = 0.05$ cm, for the u_ρ and u_φ orientations, respectively. The averaging is performed for all the considered angles.

Table B.1. Statistical overview for different d: u_ρ orientation.

	d [cm]	0.9 GHz		2.45 GHz	
		$\overline{\Delta E^d}$ [dB]	$\overline{\Delta E^d_{max}}$ [dB]	$\overline{\Delta E^d}$ [dB]	$\overline{\Delta E^d_{max}}$ [dB]
arm	**1**	3.7	9.3	4.1	13.5
	2	7.0	12.6	3.1	10.9
	3	9.8	14.3	2.6	12.4
	4	12.3	15.4	2.8	10.1
	5	14.5	17.3	2.7	8.1
leg	**1**	2.1	4.4	3.0	15.7
	2	4.2	11.1	4.5	19.2
	5	5.0	12.7	5.0	21.1
	7	4.3	14.1	6.0	20.9
	10	3.7	10.6	5.9	20.6
torso	**5**	5.3	14.2	3.3	11.4
	10	6.5	38.3	4.4	16.8
	15	5.6	20.5	4.1	21.6
	20	5.9	17.7	4.1	25.4

Table B.2. Statistical overview for different d: u_φ orientation.

	d [cm]	0.9 GHz		2.45 GHz	
		$\overline{\Delta E^d}$ [dB]	$\overline{\Delta E^d_{max}}$ [dB]	$\overline{\Delta E^d}$ [dB]	$\overline{\Delta E^d_{max}}$ [dB]
arm	**1**	3.7	8.9	1.7	14.7
	2	6.7	20.2	2.2	17.9
	3	8.7	25.7	2.3	23.5
	4	9.9	21.7	3.0	17.3
	5	10.7	20.2	4.1	11.9
leg	**1**	0.9	7.6	2.3	9.3
	2	1.6	10.8	3.1	9.6
	5	2.7	14.6	4.5	10.3
	7	3.3	15.6	5.1	27.9
	10	4.8	16.0	4.5	22.1
torso	**5**	4.7	18.3	3.7	13.8
	10	5.3	18.5	4.9	19.2
	15	6.3	39.8	3.5	17.0
	20	4.2	18.2	3.8	13.1

B.3 Average Radiation Patterns

The average patterns and corresponding standard deviations for the arm and the torso are given from Figure B.6 to Figure B.11, for different orientations of the elementary source. Note that the values were calculated in linear units, and then expressed in logarithmic scale, and the radiation patterns are normalised to their maximum.

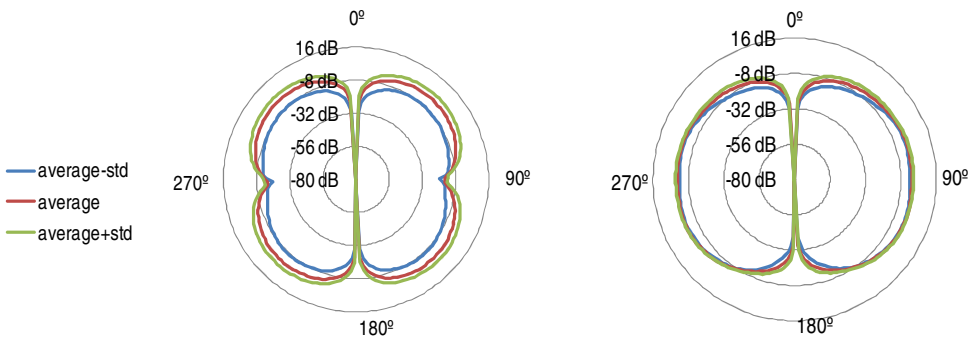

(a) $f = 0.9$ GHz (b) $f = 2.45$ GHz

Figure B.6. Average radiation patterns for arm: u_ρ orientation.

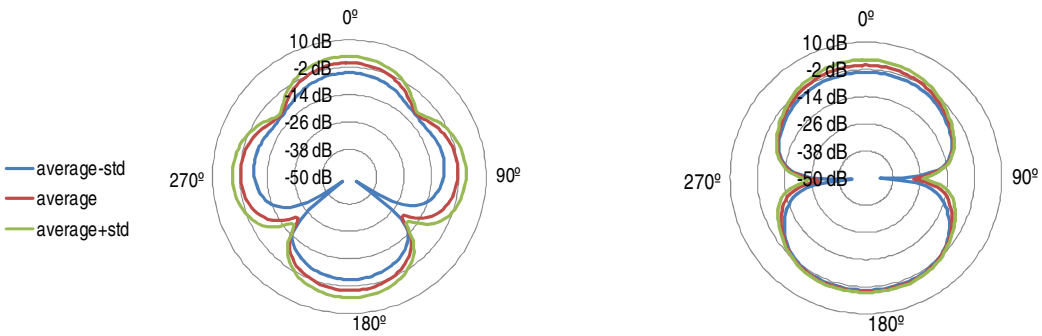

(a) $f = 0.9$ GHz (b) $f = 2.45$ GHz

Figure B.7. Average radiation patterns for arm: u_φ orientation.

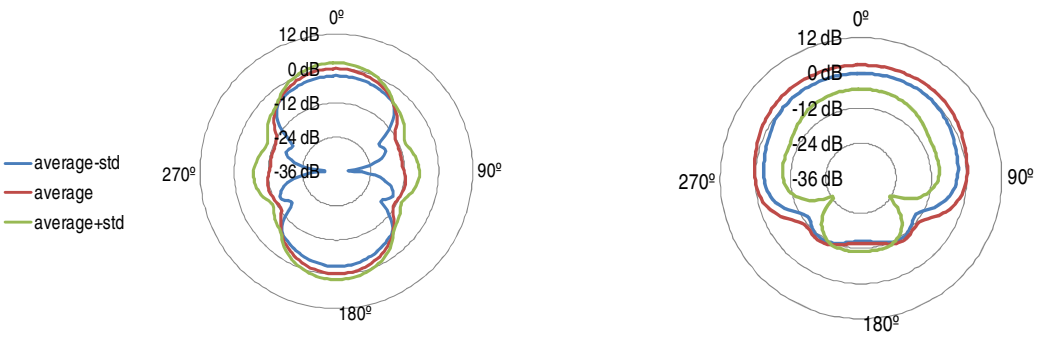

(a) $f = 0.9$ GHz (b) $f = 2.45$ GHz

Figure B.8. Average radiation patterns for arm: u_z orientation.

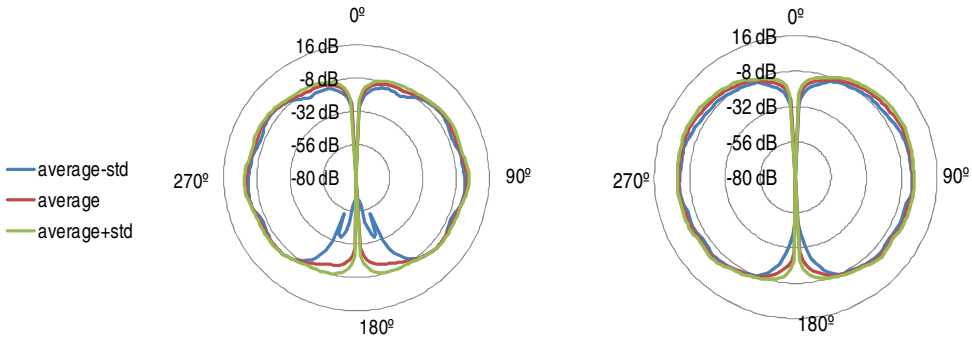

(a) $f = 0.9$ GHz (b) $f = 2.45$ GHz

Figure B.9. Average radiation patterns for torso: u_ρ orientation.

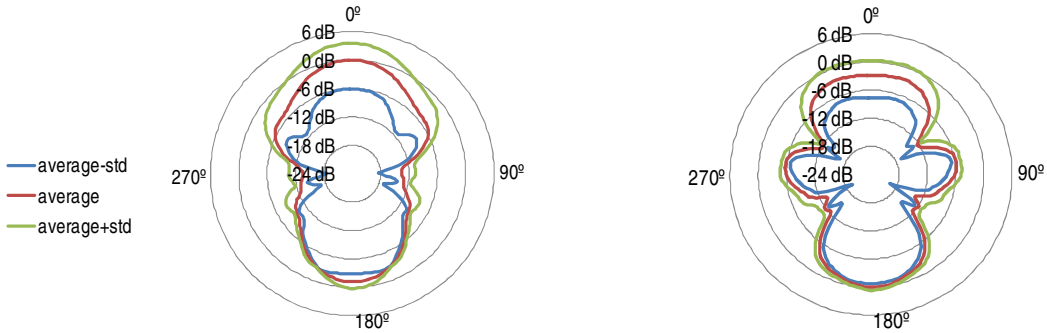

(a) $f = 0.9$ GHz (b) $f = 2.45$ GHz

Figure B.10. Average radiation patterns for torso: u_φ orientation.

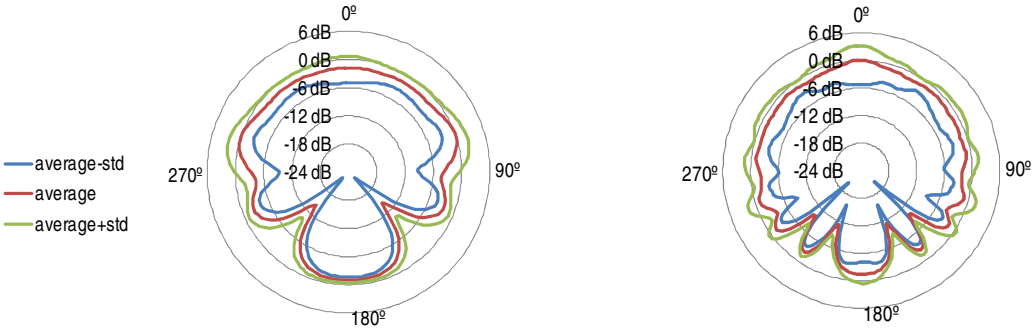

(a) $f = 0.9$ GHz (b) $f = 2.45$ GHz

Figure B.11. Average radiation patterns for torso: u_z orientation.

B.4 Average Radiation Patterns at Different Distances

For the leg and the torso, the large observation distances were divided in smaller intervals, the average pattern being then computed for each new distance interval. Results for torso are presented from Figure B.12 to Figure B.14.

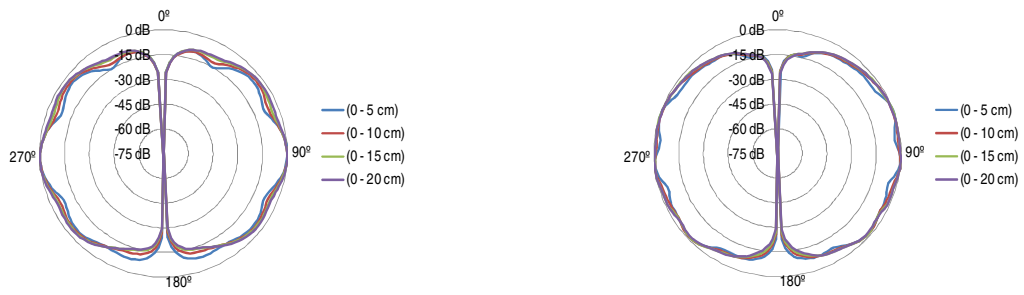

(a) $f = 0.9$ GHz (b) $f = 2.45$ GHz

Figure B.12. Average radiation patterns for torso taken at different distances: u_ρ orientation.

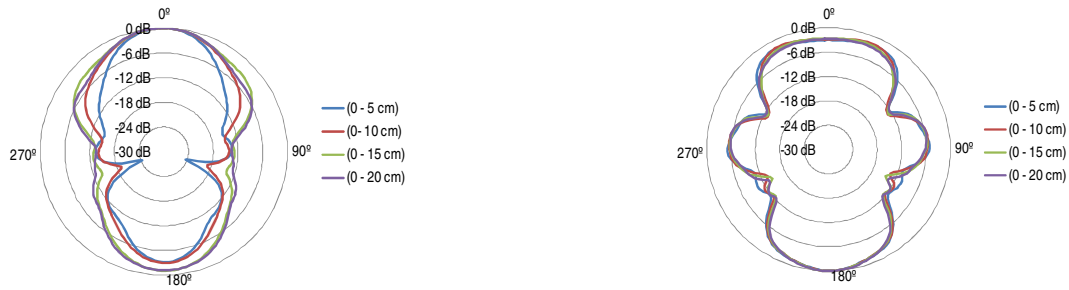

(a) $f = 0.9$ GHz (b) $f = 2.45$ GHz

Figure B.13. Average radiation patterns for torso taken at different distances: u_φ orientation.

(a) $f = 0.9$ GHz (b) $f = 2.45$ GHz

Figure B.14. Average radiation patterns for torso taken at different distances: u_z orientation.

B.5 *E field Histogram Plots*

The PDFs of the envelope of the obtained E field near the arm, the leg and the torso are shown from Figure B.15 to Figure B.26, for given values of φ. An exponential fitting function with mean $\overline{E^E}$ is plotted together with the results from the χ^2 test

.

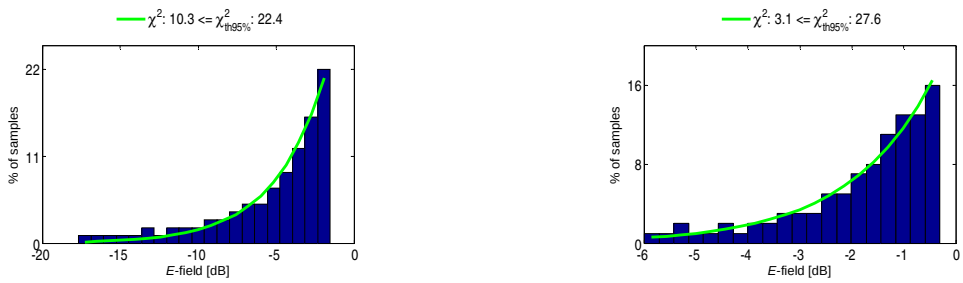

(a) $f = 0.9$ GHz (b) $f = 2.45$ GHz

Figure B.15. Histogram plots for arm: u_ρ orientation.

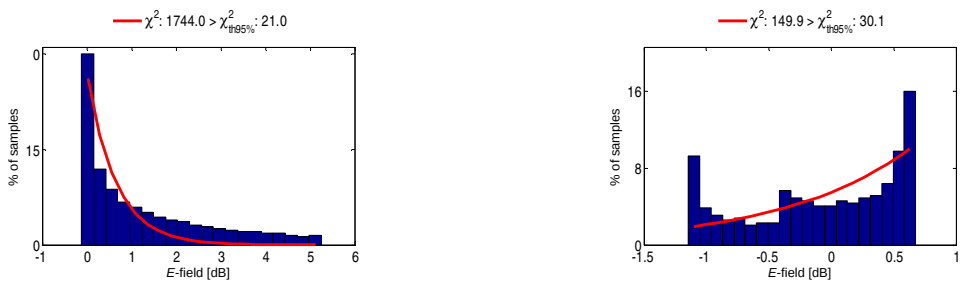

(a) $f = 0.9$ GHz (b) $f = 2.45$ GHz

Figure B.16. Histogram plots for torso: u_ρ orientation.

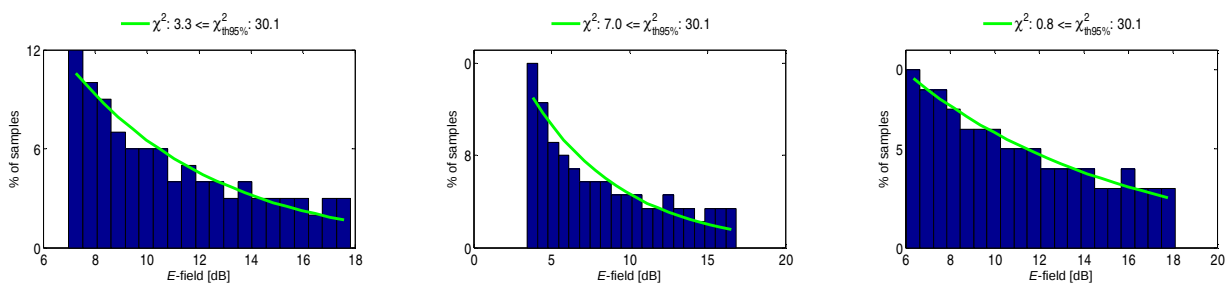

(a) $\varphi = 0^{\text{o}}$ (b) $\varphi = 90^{\text{o}}$ (c) $\varphi = 180^{\text{o}}$

Figure B.17. Histogram plots for arm: u_φ orientation (0.9 GHz).

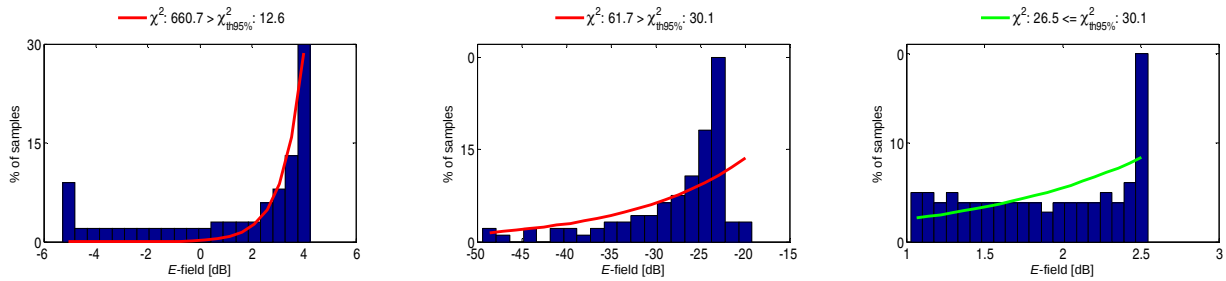

(a) $\varphi = 0^{o}$ (b) $\varphi = 90^{o}$ (c) $\varphi = 180^{o}$

Figure B.18. Histogram plots for arm: u_{φ} orientation (2.45 GHz).

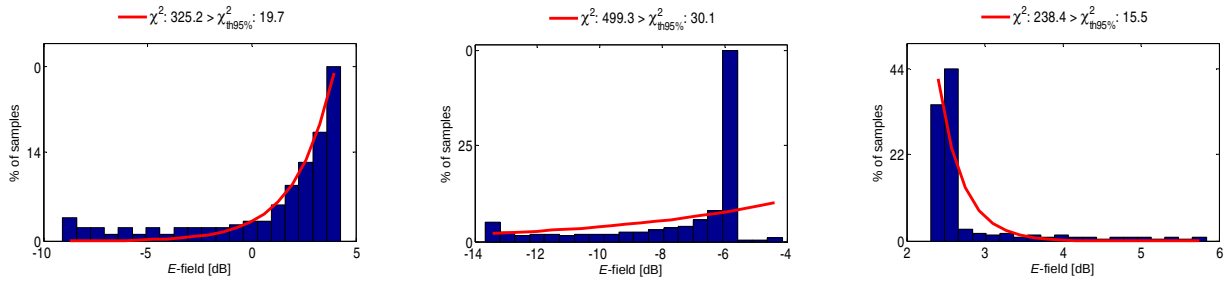

(a) $\varphi = 0^{o}$ (b) $\varphi = 90^{o}$ (c) $\varphi = 180^{o}$

Figure B.19. Histogram plots for leg: u_{φ} orientation (2.45 GHz).

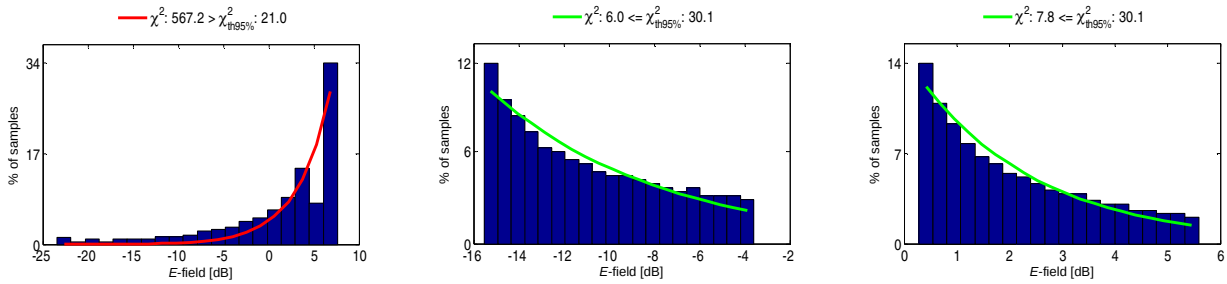

(a) $\varphi = 0^{o}$ (b) $\varphi = 90^{o}$ (c) $\varphi = 180^{o}$

Figure B.20. Histogram plots for torso: u_{φ} orientation (0.9 GHz).

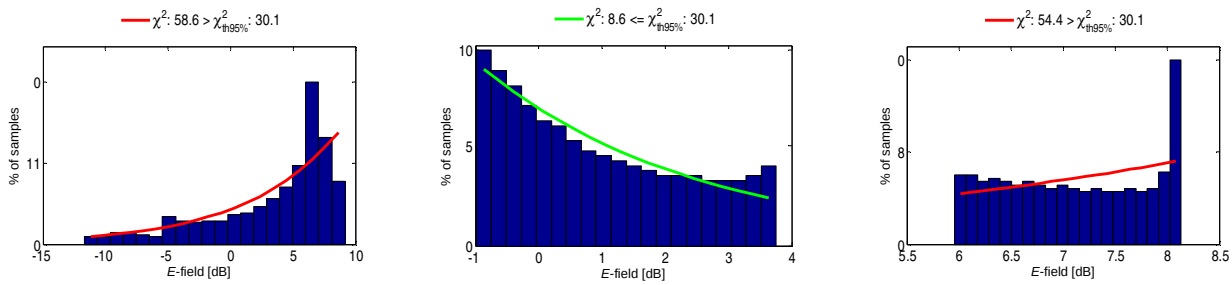

(a) $\varphi = 0^{o}$ (b) $\varphi = 90^{o}$ (c) $\varphi = 180^{o}$

Figure B.21. Histogram plots for torso: u_{φ} orientation (2.45 GHz).

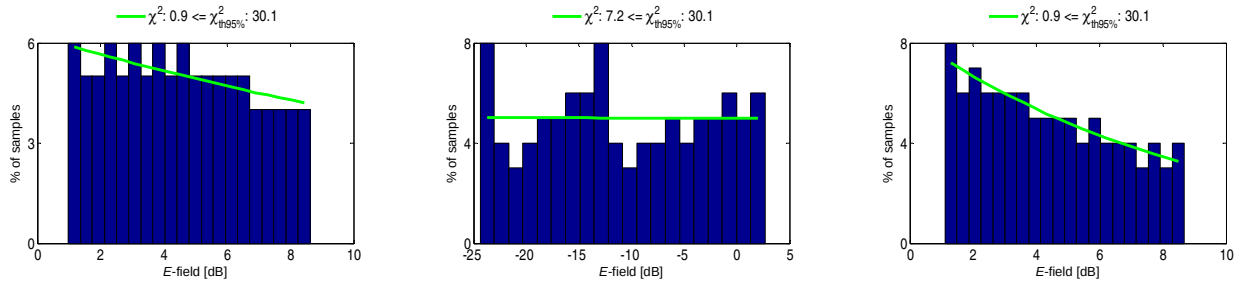

(a) $\varphi = 0^{\circ}$ (b) $\varphi = 90^{\circ}$ (c) $\varphi = 180^{\circ}$

Figure B.22. Histogram plots for arm: u_z orientation (0.9 GHz).

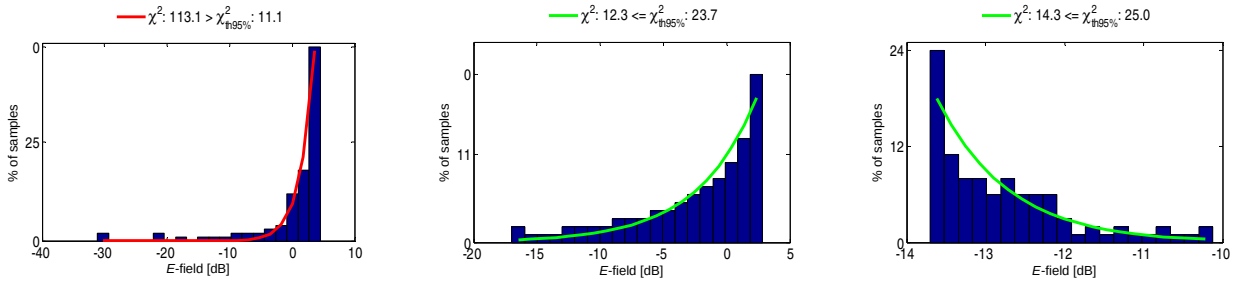

(a) $\varphi = 0^{\circ}$ (b) $\varphi = 90^{\circ}$ (c) $\varphi = 180^{\circ}$

Figure B.23. Histogram plots for arm: u_z orientation (2.45 GHz).

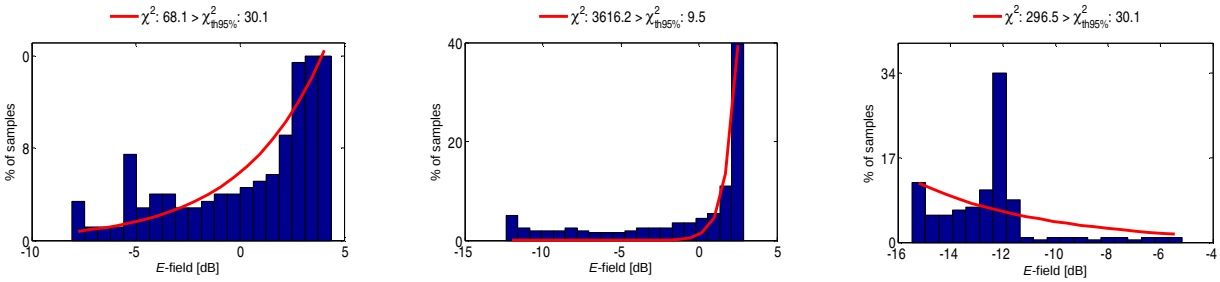

(a) $\varphi = 0^{\circ}$ (b) $\varphi = 90^{\circ}$ (c) $\varphi = 180^{\circ}$

Figure B.24. Histogram plots for leg: u_z orientation (2.45 GHz).

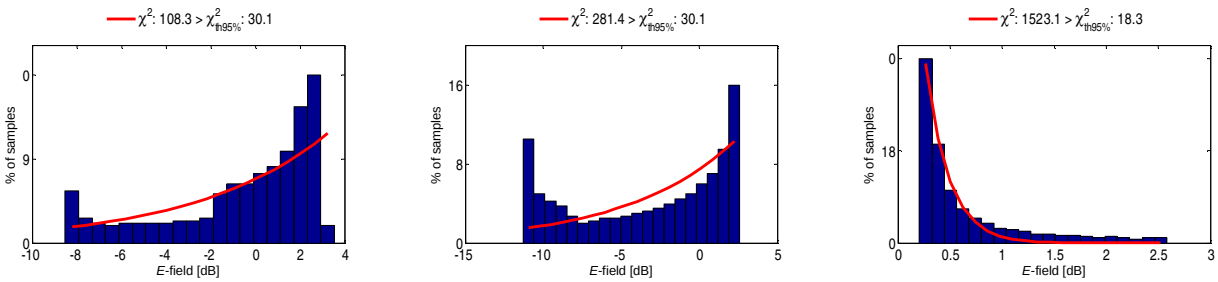

(a) $\varphi = 0^{\circ}$ (b) $\varphi = 90^{\circ}$ (c) $\varphi = 180^{\circ}$

Figure B.25. Histogram plots for torso: u_z orientation (0.9 GHz).

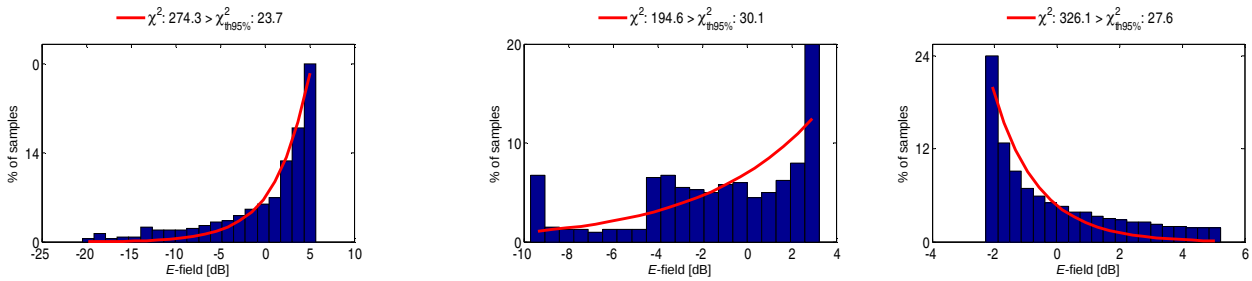

(a) $\varphi = 0^{\circ}$ (b) $\varphi = 90^{\circ}$ (c) $\varphi = 180^{\circ}$

Figure B.26. Histogram plots for torso: u_z orientation (2.45 GHz).

B.6 *Fluctuations of E field Standard Deviation*

The fluctuation of the standard deviation according to the angle of observation for the u_ρ and u_φ orientations of the source are presented in Figure B.27 and Figure B.28, respectively.

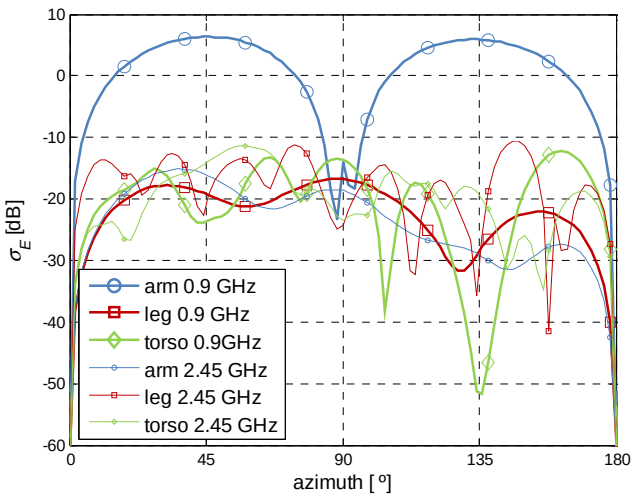

Figure B.27. Fluctuations of σ_E: u_ρ orientation.

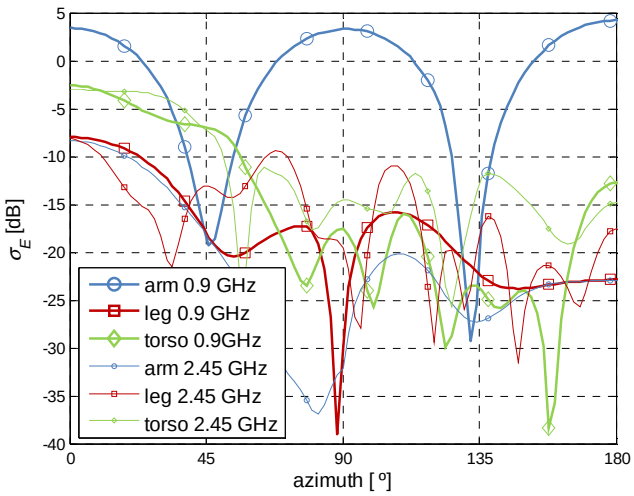

Figure B.28. Fluctuations of σ_E: u_φ orientation.

Annex C

Analysis for the Patch Antenna

This Annex contains the collection of results obtained for the patch antenna, namely the radiation patterns obtained at different distances from various body parts, as well as their statistics.

The radiation patterns for the antennas at different distances from the head (HE_F), the arm (AB_L), and the leg (LT_L), as well as in free space, are presented from Figure C.1 to Figure C.3. Likewise, the statistics of the radiation pattern (*i.e.*, G_{μ}, $G_{\mu+\sigma}$, G_{min} and G_{max}) of the patch located near these body parts, relative to the isolated antenna, are shown from Figure C.4 to Figure C.6.

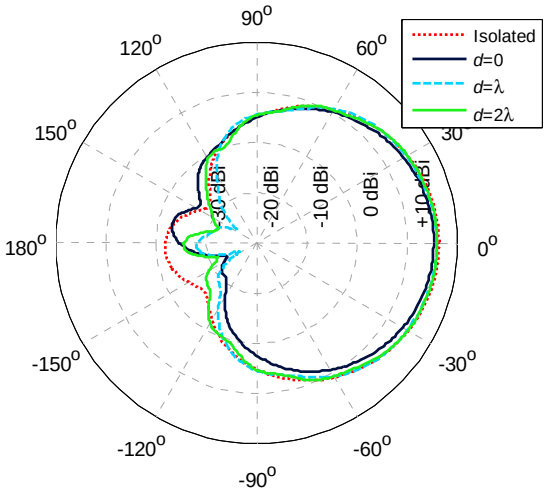

Figure C.1. Patch radiation patterns for various distances from the head.

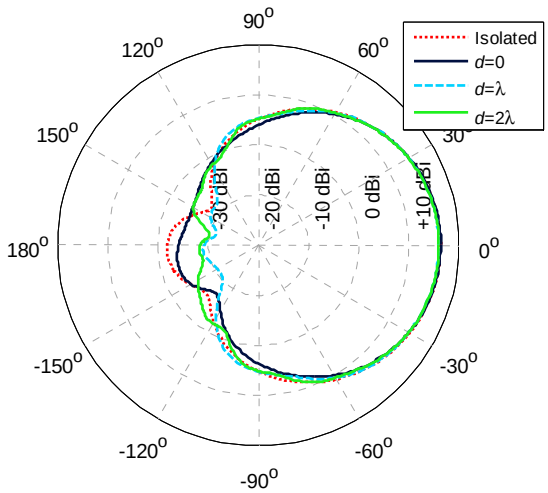

Figure C.2. Patch radiation patterns for various distances from the arm.

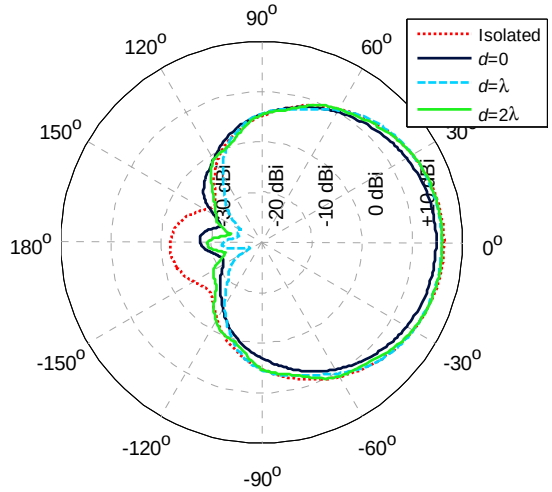

Figure C.3. Patch radiation patterns for various distances from the leg.

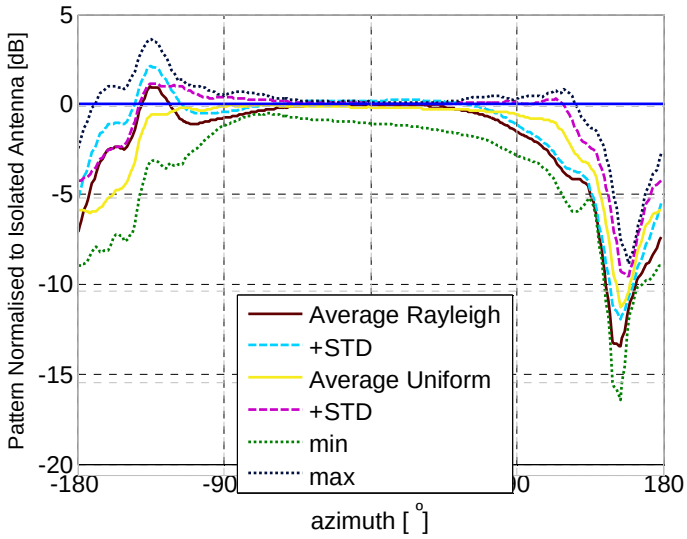

Figure C.4. Patch radiation pattern statistics near the head.

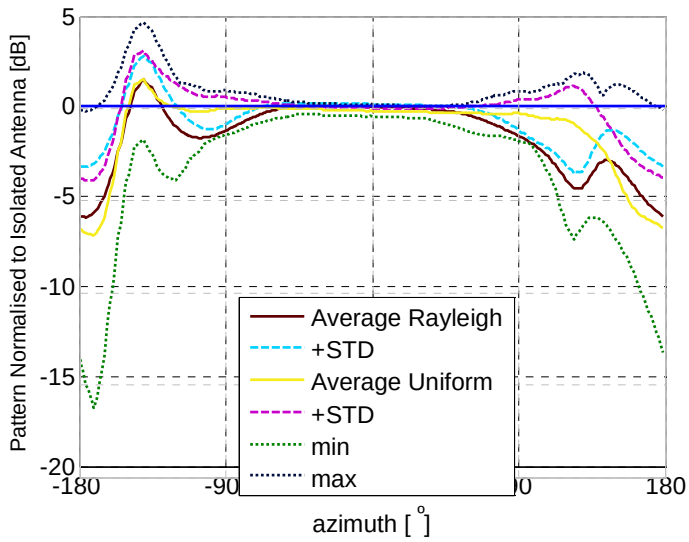

Figure C.5. Patch radiation pattern statistics near the arm.

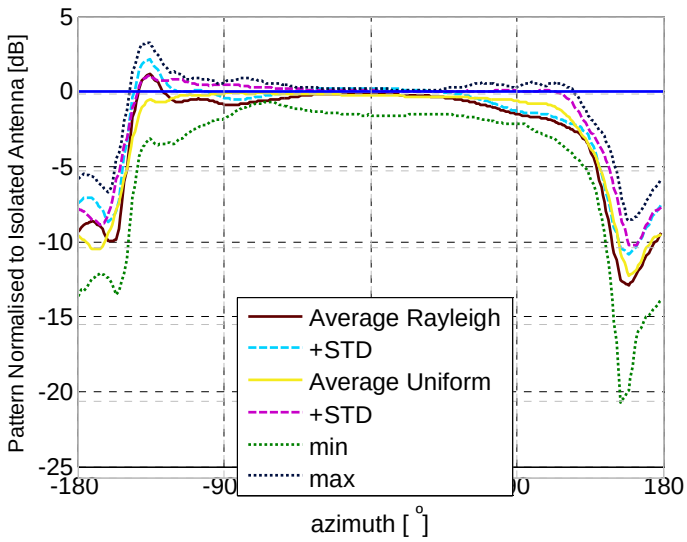

Figure C.6. Patch radiation pattern statistics near the leg.

Annex D

Classes of On-Body Links

This Annex contains the classification of on-body links for the different transmitter placements.

The classification of on-body links adopted for the different TX placements are shown from Figure D.1 to Figure D.9. Note that the following convention is used: TO_F: TX 1, WA_F: TX 2, HE_F: TX 3, HE_B: TX 4, TO_F: TX 5, WA_F: TX 6, TO_F: TX 7, WA_F: TX 8, TO_F: TX 9. The cell colours identify the classes, SYM: blue, LOS: red, NLOS: light blue, QLOS: orange. The numbers in italic identify the order number of the pair of RXs.

		RX							
	TX 1	2	3	4	5	6	7	8	9
RX	2		*1*	*2*	*3*	*4*	*5*	*6*	*7*
	3			*8*	*9*	*10*	*11*	*12*	*13*
	4				*14*	*15*	*16*	*17*	*18*
	5					*19*	*20*	*21*	*22*
	6						*23*	*24*	*25*
	7							*26*	*27*
	8								*28*
	9								

SYM
LOS
NLOS
QLOS

Figure D.1. Classes for TX on TO_F.

		RX							
	TX 2	1	3	4	5	6	7	8	9
RX	1		*1*	*2*	*3*	*4*	*5*	*6*	*7*
	3			*8*	*9*	*10*	*11*	*12*	*13*
	4				*14*	*15*	*16*	*17*	*18*
	5					*19*	*20*	*21*	*22*
	6						*23*	*24*	*25*
	7							*26*	*27*
	8								*28*
	9								

Figure D.2. Classes for TX on WA_F.

		RX							
	TX 3	1	2	4	5	6	7	8	9
RX	1		*1*	*2*	*3*	*4*	*5*	*6*	*7*
	2			*8*	*9*	*10*	*11*	*12*	*13*
	4				*14*	*15*	*16*	*17*	*18*
	5					*19*	*20*	*21*	*22*
	6						*23*	*24*	*25*
	7							*26*	*27*
	8								*28*
	9								

Figure D.3. Classes for TX on HE_F.

		RX							
	TX 4	1	2	3	5	6	7	8	9
RX	1		*1*	*2*	*3*	*4*	*5*	*6*	*7*
	2			*8*	*9*	*10*	*11*	*12*	*13*
	3				*14*	*15*	*16*	*17*	*18*
	5					*19*	*20*	*21*	*22*
	6						*23*	*24*	*25*
	7							*26*	*27*
	8								*28*
	9								

Figure D.4. Classes for TX on HE_B.

		RX							
	TX 5	1	2	3	4	6	7	8	9
RX	1		*1*	*2*	*3*	*4*	*5*	*6*	*7*
	2			*8*	*9*	*10*	*11*	*12*	*13*
	3				*14*	*15*	*16*	*17*	*18*
	4					*19*	*20*	*21*	*22*
	6						*23*	*24*	*25*
	7							*26*	*27*
	8								*28*
	9								

Figure D.5. Classes for TX on HE_L.

		RX							
	TX 6	1	2	3	4	5	7	8	9
RX	1		*1*	*2*	*3*	*4*	*5*	*6*	*7*
	2			*8*	*9*	*10*	*11*	*12*	*13*
	3				*14*	*15*	*16*	*17*	*18*
	4					*19*	*20*	*21*	*22*
	5						*23*	*24*	*25*
	7							*26*	*27*
	8								*28*
	9								

Figure D.6. Classes for TX on HE_R.

		RX							
	TX 7	1	2	3	4	5	6	8	9
RX	1		1	2	3	4	5	6	7
	2			8	9	10	11	12	13
	3				14	15	16	17	18
	4					19	20	21	22
	5						23	24	25
	6							26	27
	8								28
	9								

Figure D.7. Classes for TX on AB_L.

		RX							
	TX 8	1	2	3	4	5	6	7	9
RX	1		1	2	3	4	5	6	7
	2			8	9	10	11	12	13
	3				14	15	16	17	18
	4					19	20	21	22
	5						23	24	25
	6							26	27
	7								28
	9								

Figure D.8. Classes for TX on AB_R.

		RX							
	TX 9	1	2	3	4	5	6	7	8
RX	1		1	2	3	4	5	6	7
	2			8	9	10	11	12	13
	3				14	15	16	17	18
	4					19	20	21	22
	5						23	24	25
	6							26	27
	7								28
	8								

Figure D.9. Classes for TX on TO_B.

References

[Abra65] Abramowitz,M. and Stegun,I., *Handbook of Mathematical Functions: with Formulas, Graphs, and Mathematical Tables*, Dover Publications, New York, NY, USA, 1965.

[AlHD07] Alomainy,A., Hao,Y. and Davenport,D.M., "Parametric Study of Wearable Antennas with Varying Distances from the Body and Different On-Body Positions", in *Proc. of IET Seminar on Antennas and Propagation for Body-Centric Wireless Communications*, London, UK, Apr. 2007.

[AIKT11] Aoyagi,T., Iswandi, Kim,M., Takada,J., Hamaguchi,K. and Kohno,R., "Body Motion and Channel Response of Dynamic Body Area Channel", in *Proc. of EuCAP'2011 - European Conf. on Antennas and Propagation*, Rome, Italy, Apr. 2011.

[ATTK12] Aoyagi,T., Takada,J., Takizawa,K., Yazdandoost,K., Li,H., Hernandez,M., Hamaguchi,K. and Miura,R., "Propagation Characteristics for 2.45 GHz Dynamic Wearable WBAN using Multiport VNA", in *Proc. of ISMICT 2012 - 6th Int. Symp. on Medical Information and Communication Technology*, La Jolla, CA, USA, Mar. 2012.

[Bala97] Balanis,C.A., *Antenna Theory: Analysis and Design*, John Wiley & Sons, USA, 1997.

[Blue10] Bluetooth Core Specification v4.0, Bluetooth SIG, June 2010 (http://www.bluetooth.com).

[Burb92] Burberry,R.A., *VHF and UHF Antennas*, Peter Peregrinus Ltd., London, UK, 1992.

[CaMe06] Castela,A.M. and Medeiros,C., *Reconfigurable Antenna for Multi Services* (in Portuguese), Graduation Report, Instituto Superior Tecnico – Technical University of Lisbon, Lisbon, Portugal, June 2006.

[CaRR04] Carneiro,G., Ruela,J., and Ricardo,M., "Cross-layer design in 4G wireless terminals", *IEEE Wireless Communications*, Vol. 11, No. 2, Apr. 2004, pp. 7-13.

[CCSc09] Cotton,S., Conway,G. and Scanlon,W., "A Time-Domain Approach to the Analysis and Modeling of On-Body Propagation Characteristics Using Synchronized Measurements at 2.45 GHz", *IEEE Transactions on Antennas and Propagation*, Vol. 57, No. 4, April 2009, pp. 943-955.

[ChTa08] Chang,W. and Tarng,J., "Frequency-Space-Polarization on UWB MIMO Performance for Body Area Network Applications", *IEEE Antennas and Wireless Propagation Letters*, Vol. 7, 2008, pp. 577-580.

[CoSc07a] Cotton,S. and Scallon,W., "Spatial Diversity and Correlation for Off-Body Communications in Indoor Environments at 868 MHz", in *Proc. of VTC Spring 2007 - IEEE Vehicular Technology Conf.*, Dublin, Ireland, April 2007.

[CoSc07b] Conway,G.A. and Scanlon,W.G., "Low-Profile Microstrip Patch Antenna for Over-Body Surface Communication at 2.45 GHz", in *Proc. of IWAT '07 - Intl. Workshop on Antenna Technology: Small and Smart Antennas Metamaterials and Applications*, Cambridge, UK, Mar. 2007.

[CrEv97] Crumley,G.C. and Evans,N.E., "An Experimental RF Transponder for Biomedical Signal Acquisition", in *Proc. of IEE Coll. on RF and Microwave Circuits for Commercial Wireless Applications*, London, UK, Feb. 1997.

[COST10] *COST Action 2100 - Pervasive Mobile & Ambient Wireless Communications*, 2010 (http://www.cost2100.org/).

[COST12] *COST Action IC1004 – Cooperative Radio Communications for Green Smart Environments*, 2012 (http://www.ic1004.org/).

[CSTe12] *CST – Computer Simulation Technology*, *CST*, 2012 (http://www.*CST*.com).

[DERM11] D'Errico,R., Rosini,R. and Maman,M., "A Performance Evaluation of Cooperative Schemes for On-Body Area Networks Based on Measured Time-Variant Channels", in *Proc. of ICC 2011 - IEEE Int. Conf. on Communications*, Kyoto, Japan, June 2011.

[DFVH09] Dricot,J.M., Ferrari,G., Van Roy,S., Horlin,F. and Doncker,P., *Outage, Local Throughput, and Achievable Transmission Rate of Narrowband Body Area Networks*, TD(09)939, in *Proc. of COST2100 – 9th Management Committee Meeting*, Vienna, Austria, Sep. 2009.

[FDRD05a] Fort,A., Desset,C., Ryckaert,J., Doncker,P., Biesen,L. and Donnay,S., "Ultra Wide-band Body Area Channel Model", in *Proc. of ICC 2005– IEEE Int. Conf. on Communications*, Seoul, Korea, May 2005.

[FDRD05b] Fort,A., Desset,C., Ryckaert,J., Doncker,P., Biesen,L. and Wambacq,P., "Characterization of the Ultra Wideband Body Area Propagation Channel", in *Proc. of ICU 2005 – IEEE Int. Conf. on Ultra-Wideband*, Zurich, Switzerland, Sep. 2005.

[FDWB07] Fort,A., Desset,C., Wambacq,P. and Biesen,L., "Indoor body-area channel model for narrowband communications", *IET Microwaves, Antennas & Propagation*, Vol. 1, No. 6, Dec. 2007, pp. 1197-1203.

[FoGa98] Foschini,G.J. and Gans,M.J., "On Limits of Wireless Communications in a Fading Environment when Using Multiple Antennas", *Wireless Personal Communications*, Vol. 6, No. 3, Mar. 1998, pp. 311-335.

[FRDD06] Fort,A., Ryckaert,J., Desset,C., Doncker,P. and Wambacq,P., "Ultra-Wideband Channel Model for Communication Around the Body", *IEEE Journal on Selected Areas in Communications*, Vol. 24, No. 4, Apr. 2006, pp. 927-933.

[Gabr96] Gabriel,C., *Compilation of Dielectric Properties of Body Tissues at RF and Microwave Frequencies*, Brooks Air Force Technical Report, AL/OE-TR-1996-0037, San Antonio, TX, USA, 1996.

[GGSV09] Gorce,J.M., Goursaud,C., Savigny,C., Villemaud,G., Errico,R., Dehmas,F., Maman,M., Ouvry,L., Miscopein,B. and Schwoerer,J., *Cooperation mechanisms in BANs*, TD(09)862, in *Proc. of COST2100 8th Management Committee Meeting*, Valencia, Spain, May 2009.

[GHBN11] Gallo,M., Hall,P., Bai,Q., Nechayev,Y., Constantinou,C. and Bozzetti,M., "Simulation and Measurement of Dynamic On-Body Communication Channels", *IEEE Trans. on Antennas and Propagation*, Vol. 59, No. 2, Feb. 2011, pp. 623-630.

[GKHH12] Ghanem,K., Khan,I., Hall,P. and Hanzo,L., "MIMO Stochastic Model and Capacity Evaluation of On-Body Channels", *IEEE Trans. on Antennas and Propagation*, Vol. 60, No. 6, June 2012, pp. 2980-2986.

[Glas89] Glassner,A.S., *An Introduction to Ray Tracing*, Academic Press, New York, NY, USA, 1989.

[GROW12] *Group for Research on Wireless*, INOV / IST, 2012 (http://grow.inov.pt).

[Haba02] Habash,R., *Electromagnetic Fields and Radiation: Human Bioeffects and Safety*, Marcel Dekker Inc., New York, NY, USA, 2002.

[HaHa06] Hall,P. and Hao,Y., *Antennas and Propagation for Body-Centric Wireless Communications*, Artech House, Norwood, MA, USA, 2006.

[HaRa98] Hao,Y. and Railton,C.J., "Analyzing Electromagnetic Structures with Curved Boundaries on Cartesian FDTD Meshes", *IEEE Trans. on Microwave Theory and Techniques*, Vol. 46, No. 1, Jan. 1998, pp. 82-88.

[HDSZ10] Hiertz,G., Denteneer,D., Stibor,L., Zang,Y., Costa,X.P. and Walke,B., "The IEEE 802.11 Universe", *IEEE Communications Magazine*, Vol. 48, No. 1, Jan. 2010, pp. 62-70.

[HeUl10] Henneberg,M. and Ulijaszek,S., "Body Frame Dimensions are Related to Obesity and Fatness: Lean Trunk Size, Skinfolds, and Body Mass Index", *American Journal of Human Biology*, Vol. 2, No. 1, Feb. 2010, pp. 83-91.

[HFSS10] *HFSS - 3D Full Wave Electromagnetic Field Simulation*, ANSOFT, 2010 (http://www.ansoft.com/products/hf/hfss/).

[HHNA07] Hall,P., Hao,Y., Nechayev,Y., Aomainy,A., Constantinou,C., Parini,C, Kamarudin,M., Salim,T., Hee,D., Dubrovka,R., Owadally,A., Song,W., Serra,A., Nepa,P., Gallo,M. and Bozzetti,M., "Antennas and Propagation for On-Body Communication Systems", *IEEE Antennas and Propagation Mag.*, Vol. 49, No. 3, June 2007, pp. 41-58.

[Hine96] Hines,J.W., "Medical and Surgical Applications of Space Biosensor Technology", *Acta Astronautica*, Vol. 38, No. 4-8, Feb./Apr 1996, pp. 261-267.

[ICNI98] ICNIRP, *Guidelines for Limiting Exposure to Time-Varying Electric, Magnetic, and Electromagnetic Fields (up to 300 GHz)*, ICNIRP, Report 0017-9078/98, Germany, 1998.

[IEEE08] IEEE, *Channel Models for WBANs - NICT*, IEEE P802.15 Working Group for Wireless Personal Area Networks, IEEE P802.15-08-0416-04-0006, USA, Nov. 2008.

[IEEE09] IEEE, *Channel Model for Body Area Network*, IEEE P802.15 Working Group for Wireless Personal Area Networks, IEEE P802.15-08-0780-09-0006, USA, Apr. 2009.

[IEEE12] IEEE, *Standard for Local and Metropolitan Area Networks - Part 15.6: Wireless Body Area Networks,* Feb. 2012 (http://www.ieee802.org/15/pub/TG6.html).

[IFAP12] "An Internet Resource for the Calculation of the Dielectric Properties of Body Tissues", Institute for Applied Physics, Italian National Research Council, (http://niremf.ifac.cnr.it/tissprop/).

[InSm02] Ingalls,M. and Smith,D., "Microstrip Antennas for GPS Applications", in *Proc. of PLANS 2002 - IEEE Position Location and Navigation Symp.*, Palm Springs, CA, USA, Apr. 2002.

[IOSU04] Ishido,R., Onishi,T., Saito,K., Uebayashi,S. and Ito,K., "A Study on the Solid Phantoms for 3-6 GHz and Evaluation of SAR Distributions Based on Thermographic Method", in *Proc. of EMC'04 - Int. Symp. on Electromagnetic Compatibility*, Sendai, Japan, June 2004.

[ITLa13] IT Lisbon – Antennas and Propagation Laboratories, 2013, (http://www.it.pt/lab_detail_p.asp?id_laboratory=6).

[Jova05] Jovanov,E., "Wireless technology and system integration in body area networks for m-health applications", in *Proc. of 27th Annual Intl. Conf. of the IEEE Engineering in Medicine and Biology Society*, Shanghai, China, Sep. 2005.

[Kago90] Kagoshima,K., "Analysis of a directional antenna existing near a lossy dielectric cylinder", in *Proc. of IEEE Antennas and Propagation Society Int. Symp.,* Dallas, TX, USA, May 1990.

[KeFC09] Keshmiri,F., Fort,A. and Craye,C., "Analysis of Wave Propagation for BAN applications", in *Proc. of EuCAP'2009 – 3th European Conf. on Antennas and Propagation*, Berlin, Germany, Mar. 2009.

[KGTP10] Karapistoli,E., Gragopoulos,I., Tsetsinas,I. and Pavlidou,F.N., "An overview of the IEEE 802.15.4a standard", *IEEE Communications Magazine*, Vol. 48, No. 1, Jan. 2010, pp. 47-53.

[KhHa10] Khan,I. and Hall,P., "Experimental Evaluation of MIMO Capacity and Correlation for Narrowband Body-Centric Wireless Channels", *IEEE Trans. on Antennas and Propagation*, Vol. 58, No. 1, Jan. 2010, pp. 195-202.

[KhUH11] Khan,I., Ullah,I. and Hall, P., "Transmit-receive diversity for 2×2 multiple-input multiple-output channel in body area networks", *IET Microwaves, Antennas & Propagation*, Vol. 5, No. 13, June 2011, pp. 1589-1593.

[KHGN08] Khan,I., Hall,P., Guraliuc,A. and Nepa,P., "Reciprocity and Repeatability of Diversity Measurements for On-Body Communication Channels at 2.45 GHz", in *Proc. of IEEE Antennas and Propagation Society Int. Symp.*, San Diego, CA, USA, July 2008.

[KHNA10] Khan,I., Hall,P., Nechayev,Y. and Akhoondzadeh-Asl,L., "Multiple Antenna Systems for Increasing On-Body Channel Capacity and Reducing BAN-to-BAN Interference", in *Proc. of iWAT 2010 - Int. Workshop on Antenna Technology*, Lisbon, Portugal, Mar. 2010.

[KnPN96] Knoblauch,R., Pietrucha,M. and Nitzburg,M., "Field Studies of Pedestrian Walking Speed and Start-up Time", *Transportation Research Record 1538*, Transportation Research Board, National Research Council, Washington, D.C., USA, 1996, pp. 27-38.

[Kuma80] P. Kumaraswamy, "A generalized probability density function for double-bounded random processes", *Journal of Hydrology*, Vol. 46, No. 1-2, Mar. 1980, pp. 79–88.

[KYNH07] Khan,I., Yu,L., Nechayev,Y. and Hall,P., "Space and Pattern Diversity for On-Body Communication Channels in an Indoor Environment at 2.45 GHz", in *Proc. of EuCAP 2007 - European Conf. on Antennas and Propagation*, Edinburgh, Scotland, Nov. 2007.

[LBMB07] Latre,B., Braem,B., Moerman,I., Blondia,C., Reusens,E., Joseph,W. and Demeester,P., "A Low-delay Protocol for Multihop Wireless Body Area Networks", in *Proc. of MobiQuitous 2007 - 4th Annual Intl. Conf. on Mobile and Ubiquitous Systems: Networking & Services*, Philadelphia, PA, USA, Aug. 2007.

[LDOD11] Liu,L., DErrico,R., Ouvry,L., Doncker,P. and Oestges,C., "Dynamic Channel Modeling at 2.4 GHz for On-Body Area Networks", *Advances in Electronics and Telecommunications*, Vol. 2, No. 4, Dec. 2011, pp. 17-27.

[LiDO08] Liu,L., Doncker,P. and Oestges,C., "Fading Correlation Measurement and Modelling on the Front and Back side of a Human Body", TD(08)642, in *Proc. of COST 2100 - 6th Management Meeting*, Lille, France, Oct. 2008.

[Loyk01] Loyka,S.L., "Channel Capacity of MIMO Architecture using the Exponential Correlation Matrix", *IEEE Communication Letters*, Vol. 5, No. 9, Sep. 2001, pp. 369-371.

[LVMM04] Latré,B., Vermeeren,G., Moerman,I., Martens,L., Demeester,P., Louagie,F. and Donnay,S., "Networking and Propagation Issues in Body Area Networks", in *Proc. of SCVT 2004 – Symp. on Communications and Vehicular Technology*, Gent, Belgium, Nov. 2004.

[Lytl71] Lytle,R.J., "Far-field Patterns of Point Sources Operated in the Presence of Dielectric Circular Cylinders", *IEEE Transactions on Antennas and Propagation*, Vol. 19, No. 5, Sep. 1971, pp. 618-621.

[Matl12] *Matlab R2009b*, Mathworks, 2012 (http://www.mathworks.com/).

[MaCo12] Mackowiak,M. and Correia,L.M., "Towards a Radio Channel Model for Off-Body Communications in a Multipath Environment", in *Proc. of European Wireless 2012 – 18th European Wireless Conf.*, Poznań, Poland, Apr. 2012.

[Moli05] Molisch,A.F., *Wireless Communications*, IEEE Press/John Wiley and Sons, West Sussex, UK, 2005.

[MSRN11] Mellah,M.A., Sibille,A., Roblin,C., Nedil,M. and Denidni,T.A., "Statistical Modelling of the Antenna–Head Interaction", *IEEE Antennas and Wireless Propagation Letters*, Vol. 10, Apr. 2011, pp. 454-457.

[NEWC10] *NEWCOM++ - Network of Excellence in Wireless COMmunications++*, 2010 (http://www.newcom-project.eu/).

[OeCl07] Oestges,C. and Clerckx,B., *MIMO Wireless Communications*, Elsevier Academic Press, Oxford, UK, 2007.

[OlMC11] Oliveira,C., Mackowiak,M. and Correia,L.M., "Challenges for Body Area Networks Concerning Radio Aspects", in *Proc. of European Wireless 2011 – 17th European Wireless Conf.*, Wien, Austria, April 2011.

[Orfa96] Orfanidis,S.J., *Optimum Signal Processing, An Introduction*, Prentice-Hall, EnglewoodCliffs, NJ, USA, 1996.

[PaJa03] Park,S. and Jayaraman,S., "Enhancing the Quality of Life Through Wearable Technology", *IEEE Engineering in Medicine and Biology Magazine*, Vol. 22, No. 3, May/June 2003, pp. 41-48.

[Path82] Pathak,P.H., "Uniform Geometrical Theory of Diffraction", in *Proc. of Applications of Mathematics in Modern Optics*, San Diego, CA, USA, Aug. 1982.

[PeRG01] Peymann,A., Rezazadeh,A.A. and Gabriel,C., "Changes in the Dielectric Properties of Rat Tissue as a Function of Age at Microwave Frequencies", *Physics in Medicine and Biology*, Vol. 46, No. 6, 2001, pp. 1617-1629.

[Pose12] *Poser*, 2012 (http://*Poser*.smithmicro.com/*Poser*.html).

[PrHa11] Prabh,K.S. and Hauer,J.H., "Opportunistic Packet Scheduling in Body Area Networks", in *Proc. of EWSN2011 - 8th European Conf. on Wireless Sensor Networks*, Bonn, Germany, Feb. 2011.

[Proa01] Proakis, J.G., *Digital Communications*, Mac Graw Hill, New York, USA, 2001.

[QiMo06] Qiu,X. and Mohan,A.S., "The Performance of a CPW-fed Printed UWB Antenna for Wireless Body-Worn Application", in *Proc. of IEEE Antennas and Propagation Society Int. Symp.,* Albuquerque, NM, USA, July 2006.

[RDMH04] Ryckaert,J., Doncker,P., Meys,R., Hoye,A. and Donnay,S., "Channel model for wireless communication around human body", *Electronic Letters*, Vol. 40, No. 9, Apr. 2004, pp. 543-544.

[ReTa12] Reichman,A. and Takada,J., "Body Communications", in Roberto Verdone and Alberto Zanella (eds.), *Pervasive Mobile & Ambient Wireless Communications*, Springer, London, UK, 2012.

[RJVM07] Reusens,E., Joseph,W., Vermeeren,G., Martens,L., Latré,B., Moerman,I., Braem,B. and Blondia,C., "Path Loss Models for Wireless Communication Channel along Arm and Torso: Measurements and Simulations", in *Proc. of IEEE Antennas and Propagation Society Int. Symp.*, Honolulu, HI, USA, June 2007.

[Robe95] C. Robert, "Simulation of truncated normal variables", *Statistics and Computing*, Vol. 5, No. 2, June 1995, pp. 121–125.

[ROHD10] Roy,S., Oestges,C., Horlin,F. and Doncker,F., "Comprehensive Channel Model for UWB Multisensor Multiantenna Body Area Networks", *IEEE Transactions on Antennas and Propagation*, Vol. 58, No. 1, Jan. 2010, pp. 163-170.

[RoLa12] Rowel,C. and Lam,E., "*Mobile Antenna Design*", *IEEE Antennas and Propagation Magazine*, Vol. 54, No. 4, Aug. 2012, pp. 14-58.

[Sadi00] Sadiku,M., *Numerical Techniques in Electromagnetics*, CRC Press, Prairie View, TX, USA, 2000.

[SaHu03] Salonen,P. and Hurme,H., "A Novel Fabric WLAN Antenna for Wearable Apllications", in *Proc. of IEEE Antennas and Propagation Society Int. Symp.*, Columbus, OH, USA, June 2003.

[SaRK04] Salonen,P., Rahmat-Samii,Y. and Kivikoski,M., "Wearable Antennas in the Vicinity of Human Body", in *Proc. of IEEE Antennas and Propagation Society Int. Symp.*, Monterey, CA, USA, June 2004.

[ScEB99] Scanlon,W.G., Evans,N.E. and Burns,J.B., "FDTD Analysis of Closed-Coupled 418 MHz Radiating Devices for Human Telemetry", *Physics in Medicine and Biology*, Vol. 44, No. 2, 1999, pp. 335-345.

[ScEv01] Scanlon,W.G. and Evans,N.E., "Numerical Analysis of Bodyworn UHF Antenna Systems", *IEE Electronics and Communications Engineering Journal*, Vol. 13, No. 2, Apr. 2002, pp. 53-64.

[SEMC12] *SEMCAD X*, Speag – Schmid & Partner Engineering AG, 2012 (http://www.semcad.com).

[Sibi08] Sibille,A., "Statistical Antenna Modelling", in *Proc. of 29th URSI General Assembly*, Chicago, IL, USA, Aug. 2008.

[Taka08] Takada,J., "Static Propagation and Channel Models in Body Area", TD(08)639, in *Proc. of COST 2100 - 6th Management Meeting*, Lille, France, Oct. 2008.

[TCAB10] Thompson,W., Cepeda,R., Armour,S. and Beach,M., "Improved antenna mounting method for UWB BAN channel measurement", TD(10)11048, in *Proc. of COST 2100 - 11th Management Meeting*, Aalborg, Denmark, June 2010.

[Tela99] Telatar,E., "Capacity of Multi-Antenna Gaussian Channels", *European Transactions on Telecommunications*, Vol. 10, No. 6, Nov. 1999, pp. 585—595.

[ToHA93] Toftgärd,J., Hornsleth,S. and Andersen,J.B., "Effects on Portable Antennas of the Presence of a Person", *IEEE Trans. on Antennas and Propagation*, Vol. 41, No. 6, June 1993, pp. 739-745.

[TTHI08] Tesi,R., Taparugssanagorn,A., Hämäläinen,M. and Iinatti,J., "UWB Channel Measurements for Wireless Body Area Networks", TD(08)649, in *Proc. of COST 2100 - 6th Management Meeting*, Lille, France, Oct. 2008.

[VQLO12] Van Roy,S., Quitin,F., Liu,L., Oestges,C., Horlin,F., Dricot,J.M. and Doncker,P., "Dynamic channel modeling and validation for multisensory body area networks", *IEEE Transactions on Antennas and Propagation*, accepted Dec. 2012.

[VaAn87] Vaughan,R. and Andersen,J., "Antenna Diversity in Mobile Communications", *IEEE Trans. Vehicular Technology*, Vol. 36, No. 4, Nov. 1987, pp. 149-172.

[ViFa12] *Virtual Family*, IT'IS - Foundation for Research on Information Technologies in Society, 2012 (http://www.itis.ethz.ch/index/index_humanmodels.html).

[WADB07] Watteyne,T., Augé-Blum,I., Dohler,M. and Barthel,D., "AnyBody: a Self-Organization Protocol for Body Area Networks", in *Proc. of BodyNets'07 - 2nd ICST Intl. Conf. on Body Area Networks*, Florence, Italy, June 2007.

[Wait59] Wait,J., *Electromagnetic Radiation from Cylindrical Structures*, Pergamon Press, New York, NY, USA, 1959.

[WaJe04] Wallace,J.W. and Jensen,M.A., "Mutual Coupling in MIMO Wireless Systems: A Rigorous Network Theory Analysis", *IEEE Trans. on Wireless Communications*, Vol. 3, No. 4, July 2004, pp. 1317-1325.

[Wang08] Wang,Y., *Body-Centric Radio Propagation Channels: Characteristics and Models*, Ph. D. Thesis, Aalborg University, Aalbor, Denmark, Sep. 2008.

[Week64] Weeks,W.L., *Electromagnetic Theory for Engineering for Engineering Applications*, Wiley, New York, NY, USA, 1964.

[Weil77] Weiland,T., "A discretization model for the solution of Maxwell's equations for six-component fields", *Electronics and Communication*, Vol. 31, Mar. 1977, pp. 116-120.

[Whee07] Wheeler,A., "Commercial applications of wireless sensor networks using Zigbee", *IEEE Communications Magazine*, Vol. 45, No. 4, Apr. 2007, pp. 70-77.

[XDSB09] Xiao,S., Dhamdhere,A., Sivaraman,V., and Burdett,A., "Transmission Power Control in Body Area Sensor Networks for Healthcare Monitoring", *IEEE Journal on Selected Areas in Communications*, Vol. 27, No. 1, Jan. 2009, pp. 37-48.

[XFDT12] *XFdtd®*, REMCOM – Electromagnetic Simulation Software, 2012 (http://www.remcom.com).

[ZhHP05] Zhao,Y., Hao,Y. and Parini,C.G., "Two Novel FDTD Based UWB Indoor Propagation Models", in *Proc. of ICU 2005 - IEEE Int. Conf. on Ultra-Wideband*, Zurich, Switzerland, Sep. 2005.

[ZASW03] Zasowski,T., Althaus,F., Stäger,M., Wittneben,A. and Tröster,G., "UWB for Noninvasive Wireless Body Area Networks: Channel Measurements and Results", in *Proc. of IEEE Conf. on Ultra Wideband Systems and Technologies*, Reston, VA, USA, Nov. 2003.

[ZMAW06] Zasowski,T., Meyer,G., Althaus,F. and Wittneben,A., "UWB Signal Propagation at the Human Head", *IEEE Trans. on Microwave Theory and Techniques*, Vol. 54, No. 4, Apr. 2006, pp. 1836-1845.